

# A Digital Manufacturing Process For Three-Dimensional Electronics

Matthew Peter Shuttleworth

Submitted in accordance with the requirements for the  
degree of Doctor of Philosophy in Mechanical Engineering

The University of Leeds  
The School of Mechanical Engineering

January 2020



The candidate confirms that the work submitted is his own, except where work which has formed part of jointly authored publications has been included. The contribution of the candidate and the other authors to this work has been explicitly indicated below. The candidate confirms that appropriate credit has been given within the thesis where reference has been made to the work of others.

Chapter 5 includes elements from 3 jointly authored bodies of work:

**Paper 1:** Digitally Driven Process for the Fabrication of Integrated Flex-Rigid Electronics (Conference Proceedings)

**Paper 2:** Hybrid Additive Manufacture of Conformal Antennas (Conference Proceedings)

**Paper 3:** Light Based Synthesis of Metallic Nanoparticles on Surface-Modified 3D Printed Substrates for High Performance Electronic Systems (Journal Paper)

For publications details see the Academic Publications section of this thesis.

The authors work constitutes the design, printing, chemical modification and testing of all samples, except for the antennae in papers 2 and 3. These were manufactured by the author and Esfahani, M.N. but were designed and tested by Doychinov, V.

Wilkinson, N.J. and Hinton, J. provided technical support for the white light interferometry and pick and place equipment used in paper 3.

The work of Marques-Hueso, J., Jones, T.D.A., Ryspayeva, A. and Desmulliez, M.P.Y provided the basic understanding of the chemistry used in all 3 papers. Kay, R.W., Harris, R.A and Robertson, I.D. were supervisors on their respective papers.

This copy has been supplied on the understanding that it is copyright material and that no quotation from the thesis may be published without proper acknowledgement.

## **Abstract**

Additive manufacturing (AM) offers the ability to produce devices with a degree of three-dimensional complexity and mass customisation previously unachievable with subtractive and formative approaches. These benefits have not transitioned into the production of commercial electronics that still rely on planar, template-driven manufacturing, which prevents them from being tailored to the end user or exploiting conformal circuitry for miniaturisation. Research into the AM fabrication of 3D electronics has been demonstrated; however, because of material restrictions, the durability and electrical conductivity of such devices was often limited.

This thesis presents a novel manufacturing approach that hybridises the AM of polyetherimide (PEI) with chemical modification and selective light-based synthesis of silver nanoparticles to produce 3D electronic systems. The resulting nanoparticles act as a seed site for the electroless deposition of copper. The use of high-performance materials for both the conductive and dielectric elements created devices with the performance required for real-world applications.

For printing PEI, a low-cost fused filament fabrication (FFF); also known as fused deposition modelling (FDM), printer with a unique inverted design was developed. The orientation of the printer traps hot air within a heated build environment that is open on its underside allowing the print head to deposit the polymer while keeping the sensitive components outside. The maximum achievable temperature was 120 °C and was found to reduce the degree of warping and the ultimate tensile strength of printed parts. The dimensional accuracy was, on average, within 0.05 mm of a benchmark printer and fine control over the layer thickness led to the discovery of flexible substrates that can be directly integrated into rigid parts.

Chemical modification of the printed PEI was used to embed ionic silver into the polymer chain, sensitising it to patterning with a 405 nm laser. The rig used for patterning was a re-purposed vat-photopolymerisation printer that uses a galvanometer to guide the beam that is focused to a spot size of 155 µm at the focal plane. The positioning of the laser spot was controlled with an open-

sourced version of the printers slicing software. The optimal laser patterning parameters were experimentally validated and a link between area-related energy density and the quality of the copper deposition was found. In tests where samples were exposed to more than  $2.55 \text{ J/cm}^2$ , degradation of the polymer was experienced which produced blistering and delamination of the copper. Less than  $2.34 \text{ J/cm}^2$  also had negative effect and resulted in incomplete coverage of the patterned area. The minimum feature resolution produced by the patterning setup was  $301 \mu\text{m}$ ; however, tests with a photomask demonstrated features an order of magnitude smaller. The non-contact approach was also used to produce conformal patterns over sloped and curved surfaces.

Characterisation of the copper deposits found an average thickness of  $559 \text{ nm}$  and a conductivity of  $3.81 \times 10^7 \text{ S/m}$ . Tape peel and bend fatigue testing showed that the copper was ductile and adhered well to the PEI, with flexible electronic samples demonstrating over 50,000 cycles at a minimum bend radius of  $6.59 \text{ mm}$  without failure. Additionally, the PEI and copper combination was shown to survive a solder reflow with peak temperatures of  $249^\circ\text{C}$ . Using a robotic pick and place system a test board was automatically populated with surface mount components as small as 0201 resistors which were affixed using high-temperature, Type-V Tin-Silver-Copper solder paste.

Finally, to prove the process a range of functional demonstrators were built and evaluated. These included a functional timer circuit, inductive wireless power coils compatible with two existing standards, a cylindrical RF antenna capable of operating at several frequencies below  $10 \text{ GHz}$ , flexible positional sensors, and multi-mode shape memory alloy actuators.

## **Affiliations**

Matthew P. Shuttleworth, Reza N. Esfahani, Nathan Wilkinson, Jack Hinton, Russell A. Harris and Robert W. Kay

*Future Manufacturing Processes Research Group (FMPRG), School of Mechanical Engineering, University of Leeds, LS2 9JT, United Kingdom.*

Viktor Doychinov and Ian. D. Robertson

*Institute of Robotics, Autonomous Systems, and Sensing, School of Electronic and Electrical Engineering, University of Leeds, LS2 9JT, United Kingdom*

Tom D. A. Jones, Assel Ryspayeva, Jose Marques-Hueso & Marc P. Y. Desmulliez  
*School of Engineering & Physical Sciences, Nature Inspired Manufacturing Centre (NIMC), Heriot-Watt University, EH14 4AS, United Kingdom*

This thesis forms part of an overarching project entitled Photobioform II (EP/N018222/1 and EP/N018265/2) with a multidisciplinary team of collaborators. Printed substrates, chemistry formulations and analytical samples were passed between facilities, including visits and frequent meetings to ensure this multidisciplinary research vision was achieved. The specific inputs are listed below:

The author (Shuttleworth, M.P) and Esfahani, M.N. jointly developed the manufacturing apparatus and experiments to validate this digitally driven approach and provided samples and X-ray photoelectron spectroscopy for the team at Herriot-Watt, under the supervision of Harris, R.A. and Kay, R.W.

Doychinov, V. designed, simulated, and tested RF devices under the supervision of Robertson, I.D.

Wilkinson, N. supported the white-light interferometry aspect of this research and Hinton, J. assisted with solder dispensing, and pick and place assembly.

Marques-Hueso, J., Jones, T.D.A. and Ryspayeva, A. contributed to the chemical modification process under the supervision of Desmulliez, M.P.Y. and discovered a method to accelerate the process as discussed in Section 6.1.

All the review, design and experimental work presented in this thesis is that of the author, with the exception of Section 5.2. where the antenna designs, simulation and testing were performed by Doychinov V. and Robertson I.D. from the School of Electronic and Electrical Engineering at the University of Leeds but the functional samples were manufactured by M. P. Shuttleworth.

## **Acknowledgements**

Throughout the writing of this doctoral thesis I have received a great deal of support and assistance. Firstly, I would like to thank my supervisor Robert Kay who has guided and motivated me for the last three and half years. His passion for the project has helped to keep me determined and encouraged my continued development as an academic and an engineer.

I would also like to acknowledge all my peers and the staff of Future Manufacturing Process Group at the University of Leeds; in particular Mohammadreza Esfahani, Jack Hinton and Nathan Wilkinson. Their input during the project has been invaluable and allowed me to progress the research to where it is today.

I would like to thank Lee Wetherill for his assistance during the manufacture of components for the various machines in this work and Camille Hammersley for her guidance around the metrology and measurement of samples.

Additionally, I would like to extend my gratitude to all the collaborative partners at Herriot-Watt University and the School of Electrical Engineering at the University of Leeds for their involvement with Photobioform.

Finally I wish to thank my family; especially my parents, who throughout university career have supported me unconditionally, but most importantly my amazing wife Angela for her continued confidence in my abilities that has helped pull me through the toughest times during this PhD.



# Table of Contents

<b>Affiliations .....</b>	<b>iv</b>
<b>List of Figures .....</b>	<b>x</b>
<b>List of Tables .....</b>	<b>xvii</b>
<b>List of Abbreviations.....</b>	<b>xviii</b>
<b>Academic Publications .....</b>	<b>xx</b>
<b>1 Introduction .....</b>	<b>1</b>
1.1 Background and Motivation.....	1
1.2 Research Purpose.....	8
1.2.1 Aims and Objectives .....	8
1.2.2 Photobioform Project .....	10
1.3 Thesis Structure .....	11
<b>2 Additive Manufacture of Electronics .....</b>	<b>13</b>
2.1 Additive Manufacturing .....	13
2.2 Polymer Fused Filament Fabrication .....	14
2.2.1 Extrusion System .....	14
2.2.2 Motion Platform .....	18
2.2.3 Feedstock Materials .....	20
2.2.4 The Challenges of High-Temperature Printing .....	22
2.3 Direct Write of Functional Circuits.....	26
2.3.1 Inkjet Printing.....	27
2.3.2 Aerosol Jet Printing.....	28
2.3.3 Laser-Induced Forwards Transfer .....	29
2.3.4 Pump and Extrusion Printing.....	30
2.3.5 Conductive Material Inks .....	32
2.4 Multi-Material Printing .....	33
2.5 Hybrid-Additive Manufacture of Electronic Devices .....	35
2.5.1 Vat Photopolymerisation.....	35

2.5.2	Material Extrusion.....	36
2.5.3	Material Jetting.....	40
2.5.4	Additive Laser Structuring.....	41
2.6	Conclusions .....	43
<b>3</b>	<b>High-Temperature FFF Printing.....</b>	<b>50</b>
3.1	PEI Printing Feasibility Study .....	50
3.2	Design and Build .....	54
3.2.1	Motion Platform.....	56
3.2.2	Print-Head .....	58
3.2.3	Build Environment.....	59
3.2.4	Printer Control Systems .....	62
3.2.5	Calibration.....	64
3.3	Chamber Characterisation.....	66
3.4	Printed Part Performance Testing.....	68
3.4.1	Dimensional Accuracy .....	71
3.4.2	Tensile Strength.....	75
3.4.3	Warping.....	77
3.4.4	Flexible Printing .....	81
3.5	Summary.....	83
<b>4</b>	<b>Surface Metallisation and Functionalisation.....</b>	<b>85</b>
4.1	Process Flow .....	85
4.2	Process Development.....	88
4.2.1	Surface Modification Chemistry.....	88
4.2.2	Nanoparticle Reduction Parameters .....	90
4.2.3	Conformal and High-Resolution Patterning.....	100
4.2.4	Ion Removal.....	103
4.3	Conductor Characterisation .....	104
4.3.1	Plating Thickness and Conductivity.....	104
4.3.2	Temperature Response.....	108
4.3.3	Adhesion Testing.....	109
4.4	Flexible Electronics Fatigue Performance Testing .....	110

4.4.1	Experimental Setup .....	110
4.4.2	Fatigue Testing Results .....	113
4.5	Surface Mount Assembly .....	114
4.5.1	Solder Dispensing and Component Placement .....	116
4.5.2	Solder Reflow Process .....	117
4.6	Summary .....	120
<b>5</b>	<b>Process Applications.....</b>	<b>123</b>
5.1	Functioning Circuitry .....	124
5.2	Wireless Power and Communications .....	125
5.2.1	Transmission Coil .....	126
5.2.2	Pill Capsule Antenna .....	129
5.3	Flexible Devices.....	134
5.3.1	Flexible Positional Sensor.....	134
5.3.2	Embedded Shape Memory Actuation .....	138
5.4	Summary .....	142
<b>6</b>	<b>Conclusions and Future Work .....</b>	<b>143</b>
6.1	Conclusions.....	143
6.2	Future Work .....	147
	<b>References.....</b>	<b>150</b>
	<b>Appendix A.....</b>	<b>182</b>
	<b>Appendix B.....</b>	<b>183</b>
	<b>Appendix C.....</b>	<b>186</b>
	<b>Appendix D .....</b>	<b>196</b>
	<b>Appendix E.....</b>	<b>199</b>
	<b>Appendix F .....</b>	<b>200</b>

## List of Figures

Figure 1.1:	PCB manufacture process flow.....	2
Figure 1.2:	Electronic system showing the main parts .....	2
Figure 1.3:	Illustration demonstrating how advances in packaging technology can reduce the size of an IC.....	3
Figure 1.4:	Schematic of how a multilayer PCB can be layered, showing three double-sided PCB's used to create a six-layer PCB .....	4
Figure 1.5:	Proposed process flow for combining FFF of PEI with chemical modification and laser-based patterning to create 3D electronic devices compatible with surface mount solder reflow .....	10
Figure 1.6:	Summary of thesis structure .....	11
Figure 2.1:	Components of a typical FFF extrusion system: a) extruder. b) hotend .....	15
Figure 2.2:	FFF test piece with ringing artefacts [49] .....	16
Figure 2.3:	Illustration of error introduced by layer-based manufacturing ....	17
Figure 2.4:	Simplified Cartesian machine configuration.....	18
Figure 2.5:	Simplified delta machine configuration .....	20
Figure 2.6:	Pyramid of polymeric materials. Adapted from [75], Polymer abbreviations can be found in [76] .....	21
Figure 2.7:	Details of the Stratasys heat curtain design. The curtain is item 132, circled in red [86] .....	24
Figure 2.8:	Zonal heating system for localised heating of high-temperature polymers mid-print. Reproduced from [88].....	25
Figure 2.9:	Classification of direct-write methods [96].....	26
Figure 2.10:	Drop-on-demand inkjet printing using a) thermal and b) piezoelectric print heads. Adapted from [98] .....	27
Figure 2.11:	Aerosol jet print head schematic. Adapted from [106] .....	28
Figure 2.12:	Schematic showing the main elements of a LIFT system. Adapted from [122].....	29

Figure 2.13: Illustration of an air-backed syringe dispenser .....	31
Figure 2.14: Schematic of the FEAM process. Reproduced from [199] .....	38
Figure 2.15: Examples of 3D-MID devices, a) a smartphone antenna. b) combined structural and electrical carrier [216].....	42
Figure 3.1: Custom printer for studying high-temperature printing.....	51
Figure 3.2: Visual inspection of buckling on the aluminium bed .....	52
Figure 3.3: Comparison of flat PEI samples produced a) in ambient air and b) a heated build volume after being heated to their $T_g$ .....	53
Figure 3.4: Air temperature above a print bed heated to 150 °C with respect to height above the bed (adjusted for ambient conditions).....	54
Figure 3.5: HTID frame design details.....	57
Figure 3.6: Details of the print-head design.....	59
Figure 3.7: Schematic of chamber material stack-up and locations.....	60
Figure 3.8: Schematic detailing the HTID's control architecture .....	63
Figure 3.9: The completed build of the HTID .....	66
Figure 3.10: Chamber temperature response to different heater set points over 60 minutes .....	67
Figure 3.11: Layout of the dimensional accuracy test sample .....	72
Figure 3.12: Deviation from nominal on square features .....	73
Figure 3.13: Average feature circularity for the benchmark printer and HTID.	74
Figure 3.14: Close-up images showing the surface finish of features produced on both printers .....	75
Figure 3.15: Dimensions of an ASTM D638 Type-I tensile testing sample. L is the length between the start of the radii and G is the gauge length .....	75
Figure 3.16: Slicer output of one layer of the tensile test samples.....	76
Figure 3.17: UTS of coupons printed on the HTID at varying chamber temperatures and benchmark printer at 90 °C. Error bars show standard deviation over five samples) .....	77

Figure 3.18: Laser scanning setup used to acquire surface data and generate warp profiles .....	78
Figure 3.19: Point cloud data showing surface deviation for parts printed at a) ambient b) 90 °C and c) 120 °C chamber temperatures. d) The RMSD vs. chamber temperature .....	80
Figure 3.20: PEI samples after heating to their glass transition and peak SAC solder reflow temperatures.....	81
Figure 3.21: Illustration of how hatch orientation in FFF parts can affect tensile strength based on extrudate direction. a) hatch aligned. b) hatch rotated 90° each layer.....	82
Figure 3.22: Technical drawing of a flexible substrate.....	82
Figure 3.23: Substrate with integrated flexible region shown flat and compressed into an arc with an approximately 6.6 mm bend radius at the peak.....	83
Figure 4.1: Illustration of the chemical modification reactions a) hydrolysis and cleaving of the imide ring. b) displacement of potassium ions with silver ions .....	86
Figure 4.2: Copper plating setup .....	88
Figure 4.3: Visual inspection of how increasing the exposure to KOH alters the subsequent silver reduction reaction.....	90
Figure 4.4: PEI surface modification process flow .....	90
Figure 4.5: Illustration of slicing software scanline definitions .....	91
Figure 4.6: Actual laser power output compared to the selected setting in software, standard deviation = 0.06 mW.....	92
Figure 4.7: Effect of increasing the number of laser passes on the copper deposition. Left half of each panel shows post patterning colour from AgNP reduction. Right shows the plated copper.....	94
Figure 4.8: Closeup of a blistered sample a) before and b) after testing for adhesion.....	95

Figure 4.9: Suspected thermal damage to the substrate from excessive UV irradiation.....	95
Figure 4.10: Effect of hatch spacing on the copper deposition. Left half of each panel shows post patterning colour from AgNP reduction. Right shows plated copper.....	96
Figure 4.11: Effect of laser scanning speed and power on the copper deposition. Left half of each panel shows post patterning colour from AgNP reduction. Right shows the plated copper. Value below each panel is the $E_A$ in $J/cm^2$ .....	97
Figure 4.12: Repeat tests of selected laser parameters. The red rings indicate a defect in the copper from the underlying print .....	98
Figure 4.13: Test piece showing the minimum achievable feature size of the patterning rig.....	99
Figure 4.14: Illustration of laser focal terminology.....	100
Figure 4.15: Illustration of how a curved surface leads to a distortion of the projected pattern.....	100
Figure 4.16: Rotary jig that allows a part to be indexed for patterning around the diameter in small segments.....	101
Figure 4.17: Demonstration of conformal patterning, producing a copper spiral on a conical surface .....	101
Figure 4.18: Copper patterned conformally onto a double curved surface, across multiple stair-step artefacts.....	102
Figure 4.19: Silver micropatterning on PEI filament.....	102
Figure 4.20: SEM image of nanoparticles on the surface of a PEI sample .....	103
Figure 4.21: EDX image showing the selective presence of silver nanoparticles on the surface of the substrate.....	103
Figure 4.22: Ion removal process flow .....	104
Figure 4.23: Design of the sample used for evaluating thickness and conductivity.....	105

Figure 4.24: White light interferometry scans showing copper deposition a) in the middle of an FFF extrudate and b) in the trough between two adjacent extrudates. The dotted red line indicates the point at which two hatch lines meet .....	107
Figure 4.25: Sample undergoing 4-point probing to characterise conductivity .....	107
Figure 4.26: Average (red) and range (grey) of temperature responses for five copper strips heated from 30 °C to 170 °C .....	109
Figure 4.27: Copper plated sample a) before and b) after ASTM D3359 peel test .....	110
Figure 4.28: Samples used for fatigue testing .....	111
Figure 4.29: Image of the linear buckling rig used in fatigue testing .....	111
Figure 4.30: Side view of the linear buckling rig illustrating a sample in the a) uncompressed and b) fully compressed states .....	112
Figure 4.31: Plot showing the normalised resistance of copper strips over 50,000 cycles.....	113
Figure 4.32: Close-up of a crack in the substrate that propagated through the copper track leading to component failure .....	114
Figure 4.33: Test board design to demonstrate surface mount soldering capabilities a) schematic. b) Final board pre-soldering with a close-up of the vision alignment fiducials.....	115
Figure 4.34: Fisnar F7400NVL robotic dispensing machine.....	116
Figure 4.35: Reflow profile for the SMD4300SNLI0T5 solder paste [252] .....	118
Figure 4.36: Solder test board without components after reflow, to verify solder wettability .....	119
Figure 4.37: SMD components solder reflowed onto a PEI test board using SAC solder paste. Close-up of a 0.6 mm × 0.3 mm capacitor (left) and 160 pad BGA component (right).....	119
Figure 4.38: Process overview detailing key stages, parameters and approximate times .....	120



Figure 5.1: Concept render of a smart prosthetic demonstrating the potential benefits of this research .....	123
Figure 5.2: Butterfly demonstrator, showing the integration of rigid, flexible and conformal patterning with a fine-pitch SMD package soldered to its back .....	123
Figure 5.3: Printed, functional 555 timer circuit that causes an LED to blink when powered .....	125
Figure 5.4: 555 Timer circuit connected to a 5 V DC supply, showing the blinking LED a) off and b) on.....	125
Figure 5.5: Illustration of how a polyurethane plug is formed in the vias.....	126
Figure 5.6: Close-up of copper plated on to the inside of a through-hole via	127
Figure 5.7: Final induction loop with plated through-hole via.....	127
Figure 5.8: Power transmission plot for an additively manufactured transmission coil .....	128
Figure 5.9: Planar antenna used as a performance benchmark for the pill capsule .....	130
Figure 5.10: Simulated return loss against the actual result for the planar antenna .....	130
Figure 5.11: Final conformal pill capsule antenna .....	131
Figure 5.12: Measured return loss for the planar and conformal pill capsule antennas .....	132
Figure 5.13: Simulated 3D radiation pattern from the pill capsule antenna....	133
Figure 5.14: Simulated (solid lines) and measured (dotted lines), horizontal and vertical radiation patterns for the conformal pill capsule antenna.....	134
Figure 5.15: Stitched microscope image of a positional sensor's conductive elements .....	135
Figure 5.16: Sample loaded into the compression rig with the laser used for measuring bend radius turned on .....	136

Figure 5.17: Normalised output from the positional sensor grouped by applied compression, highlighting the burn-in, usable and drift phases.	136
Figure 5.18: Boxplot for the positional sensor, showing the change in resistance at discrete compressions over $20 \times 10^3$ cycles.....	137
Figure 5.19: Proof of concept for embedding Nitinol wire into Flexible additively manufactured components .....	139
Figure 5.20: Multi-region Nitinol actuator, showing the shape memory wire and the circuit used to achieve localised heating.....	140
Figure 5.21: Demonstration of SMA actuator moving continuously through its full range and selectively to each of the eight possible configurations. The coloured lines indicate which segments have been heated and therefore actuated .....	141

## List of Tables

Table 2.1:	Seven ASTM/ISO additive manufacturing process categories and their operation [11] .....	13
Table 2.2:	Conductivities for metals typically used as conductors in electronics .....	33
Table 2.3:	Summary of processes for producing AM Electronics, with bulk metal conductivity for comparison .....	46
Table 2.4:	Polymer name abbreviations .....	49
Table 3.1:	High-temperature printing system design requirements.....	55
Table 3.2:	Heater temperature setting and corresponding chamber temperatures .....	68
Table 3.3:	Side-by-side comparison of the HTID and benchmark FFF printers .....	69
Table 3.4:	Print parameters for both printers .....	70
Table 3.5:	Dimensional accuracy test sample dimensions .....	72
Table 3.6:	Dimensional accuracy test plan.....	73
Table 4.1:	Surface modification parameters from literature [32] .....	88
Table 4.2:	Default slicing software parameters .....	91
Table 4.3:	Experimentally determined laser patterning settings .....	99
Table 4.4:	White-light interferometry scan results.....	106
Table 4.5:	Solder test board components and sizes .....	115
Table 5.1:	Power transmission and efficiency of AM inductive transfer coils at different standards .....	128

## List of Abbreviations

3D-MID	3D-Moulded Interconnect Device
ABS	Acrylonitrile Butadiene Styrene
ADC	Analogue-to-Digital Converter
Ag	Silver
Ag <sup>+</sup>	Silver Ions
AgNO <sub>3</sub>	Silver Nitrate
AM	Additive Manufacturing
ASTM	American Society for Testing and Materials
BGA	Ball-Grid Array
CAD	Computer-Aided Design
CNC	Computer Numerical Control
Cu	Copper
DI	Deionised
DPN	Dip-Pen Nanolithography
DW	Direct Write
EPSRC	Engineering and Physical Sciences Research Council
FDM	Fused Deposition Modelling
FEAM	Fibre Encapsulation Additive Manufacturing
FFF	Fused Filament Fabrication
FIB	Focused Ion Beam
HTID	High-Temperature Inverted Delta
IC	Integrated Circuit
IJP	Inkjet Printing
IR	Infrared
ISO	International Organization for Standardization
KOH	Potassium Hydroxide
LDS	Laser Direct Structuring
LED	Light Emitting Diode
LIFT	Laser-Induced Forward Transfer
MEMS	Micro-Electromechanical System
MOD	Metallo-Organic Decomposition

MWCNT	Multi-Walled Carbon Nanotubes
NFP	Nanofountain Pen
NP	Nanoparticle
PCB	Printed Circuit Board
PEEK	Polyether Ether Ketone
PEI	Polyetherimide
PI	Polyimide
PID	Proportional, Integral and Derivative
PLA	Polylactic Acid
PPSU	Polyphenylsulfone
PVP	Polyvinylpyrrolidone
ROM	Range of Motion
SAC	Tin (Sn) Silver (Au) Copper (Cu)
SCARA	Selective Compliance Assembly Robot Arm
SL(A)	Stereolithography
SMA	Shape Memory Alloy
SMD	Surface Mount Device
SMU	Sourcemeater Unit
SSR	Solid-State Relay
$T_g$	Glass Transition Temperature
UE	Ultrasonic Embedding
UTS	Ultimate Tensile Strength
UV	Ultraviolet
VNA	Vector Network Analyser
VP	Vat Photopolymerisation

## Academic Publications

### Journal Papers

Esfahani, R.N., **Shuttleworth, M.P.**, Doychinov, V., Wilkinson, N.J., Hinton, J., Jones, T.D.A., Ryspayeva, A., Robertson, I.D., Marques-Hueso, J., Desmulliez, M.P.Y. Harris, R.A. and Kay, R.W. Light Based Synthesis of Metallic Nanoparticles on Surface-Modified 3D Printed Substrates for High Performance Electronic Systems. *Additive Manufacturing*. DOI: 10.1016/j.addma.2020.101367

Marques-Hueso, J., Jones, T.D.A., Watson, D.E., Ryspayeva, A., Esfahani, M.N., **Shuttleworth, M.P.**, Harris, R.A., Kay, R.W. and Desmulliez, M.P.Y. Spinach-based photo-catalyst for selective plating on polyimide-based substrates for micro-patterning circuitry. *Chemical Engineering Research and Design*. 2020, 153, pp.839–848. DOI: 10.1016/j.cherd.2019.10.044

Ryspayeva, A., Jones, T.D.A., Khan, S.R., Esfahani, M.N., **Shuttleworth, M.P.**, Harris, R.A., Kay, R.W., Desmulliez, M.P.Y. and Marques-Hueso, J. Selective Metallization of 3D Printable Thermoplastic Polyurethanes. *IEEE Access*. 2019, 7, pp.104947–104955. DOI: 10.1109/ACCESS.2019.2931594

Ryspayeva, A., Jones, T.D.A., Esfahani, M.N., **Shuttleworth, M.P.**, Harris, R.A., Kay, R.W., Desmulliez, M.P.Y. and Marques-Hueso, J. A rapid technique for the direct metallization of PDMS substrates for flexible and stretchable electronics applications. *Microelectronic Engineering*. 2019. DOI: 10.1016/j.mee.2019.03.001

Ryspayeva, A., Jones, T.D.A., Esfahani, M.N., **Shuttleworth, M.P.**, Harris, R.A., Kay, R.W., Desmulliez, M.P.Y. and Marques-Hueso, J. Selective Electroless Copper Deposition by Using Photolithographic Polymer/Ag Nanocomposite. *IEEE Transactions on Electron Devices*. 2019. DOI: 10.1109/TED.2019.2897258

Jones, T.D.A., Ryspayeva, A., Esfahani, M.N., **Shuttleworth, M.P.**, Harris, R.A., Kay, R.W., Desmulliez, M.P.Y. and Marques-Hueso, J. Direct metallisation of polyetherimide substrates by activation with different metals. *Surface and Coatings Technology*. 2019. DOI: 10.1016/j.surfcoat.2019.01.023

Marques-Hueso, J., Jones, T.D.A., Watson, D.E., Ryspayeva, A., Esfahani, M.N., **Shuttleworth, M.P.**, Harris, R.A., Kay, R.W. and Desmulliez, M.P.Y. A Rapid Photopatterning Method for Selective Plating of 2D and 3D Microcircuitry on Polyetherimide. *Advanced Functional Materials*. 2018, **28**(6), p.1704451. DOI: 10.1002/adfm.201704451

### **Conference Proceedings**

Wilkinson, N.J., Lukic-Mann, M., **Shuttleworth, M.P.**, Kay, R.W., and Harris, R.A. Aerosol Jet Printing for the Manufacture of Soft Robotic Devices, *In: 2019 2nd IEEE International Conference on Soft Robotics (RoboSoft)*. IEEE, 2019, pp.496–501. DOI: 10.1109/ROBOSOFT.2019.8722766

Ryspayeva, A., Jones, T.D.A., Hughes, P.A., Esfahani, M.N., **Shuttleworth, M.P.**, Harris, R.A., Kay, R.W., Desmulliez, M.P.Y. and Marques-Hueso, J. PEI/Ag as an Optical Gas Nano-Sensor for Intelligent Food Packaging, *In: Proceedings of the IEEE Conference on Nanotechnology*. 2019, pp.1–4.

DOI: 10.1109/NANO.2018.8626269

**Shuttleworth, M.P.**, Esfahani, M.N., Harris, R.A., Kay, R.W., Doychinov, V., Robertson, I.D., Marques-Hueso, J., Jones, T.D.A., Ryspayeva, A. and Desmulliez, M.P.Y. Hybrid Additive Manufacture of Conformal Antennas, *In: 2018 IEEE MTT-S International Microwave Workshop Series on Advanced Materials and Processes for RF and THz Applications, IMWS-AMP 2018*. IEEE, 2018, pp.1–3. DOI: 10.1109/IMWS-AMP.2018.8457128

**Shuttleworth, M.P.**, Esfahani, M.N., Marques-Hueso, J., Jones, T.D.A., Ryspayeva, A., Desmulliez, M.P.Y., Harris, R.A., and Kay, R.W. A New Digitally Driven Process for the Fabrication of Integrated Flex-Rigid Electronics, *In: Proceedings of the 29th Annual International Solid Freeform Fabrication Symposium*. 2018, pp.347–346.

### **Journal Cover Pages**

Marques-Hueso, J., Jones, T.D.A., Watson, D.E.G., Ryspayeva, A., Esfahani, M.N., **Shuttleworth, M.P.**, Harris, R.A., Kay, R.W. and Desmulliez, M.P.Y. Flexible Electronics: A Rapid Photopatterning Method for Selective Plating of 2D and 3D Microcircuitry on Polyetherimide (Advanced Functional Materials 6/2018). *Advanced Functional Materials*. 2018, **28**(6), p.1870041. DOI: 10.1002/adfm.201870041

# 1 Introduction

## 1.1 Background and Motivation

The invention of electronics has been transformative to almost all aspects of modern everyday life. This technology underpins the products and services in many sectors, including robotics, aerospace, medical, power generation, and consumer electronics. The integration of these systems allows us to create 'smart' devices that require less human interaction or can assist with more complicated tasks. Consumer electronics are widespread throughout society and in 2017 the global market was valued at \$1.172 Billion, growing at a rate of 6.2% per year, with a forecasted value of \$1,787 Billion by 2024 [1]. An electronic system is an assembly of three main parts:

- Electronic Components
- Printed Circuit Boards
- Solder Interconnects

Electronic components are discrete packaged modules that provide various functions in electrical circuits. These can be complex integrated circuits (IC)s that perform intelligent applications such as processing and memory, or less sophisticated passive devices like resistors, capacitors, and inductors. Components have two or more terminals for connecting into the system and are available in a variety of mounting styles and sizes depending on the application.

Power and signals are routed between the elements of the system using a printed circuit board (PCB), a series of conductive tracks that are clad directly onto a dielectric substrate. Simple PCB's are typically manufactured using photolithography techniques to etch the tracks into sheets of copper laminated FR4 fibre-reinforced epoxy [2]. The process starts by coating the laminate in a liquid etch-resist, onto which a rigid photomask is placed, and UV light is shone through. This selectively cures the resist and when the board is washed, the pattern of the circuitry is left behind. An etching stage removes the unwanted copper and finally the remaining resist is stripped leaving a complete PCB. This is summarised in Figure 1.1.



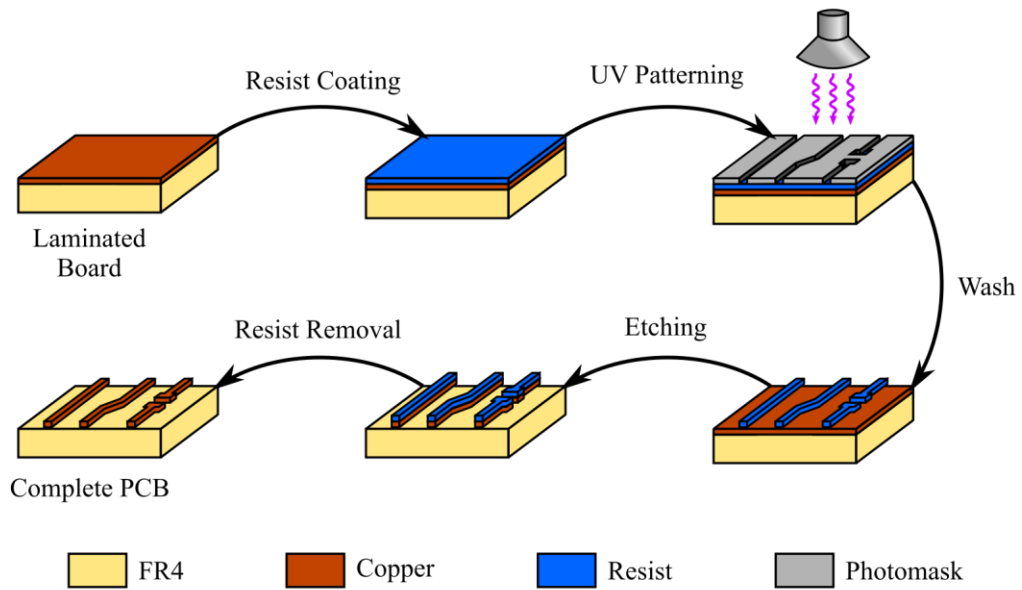


Figure 1.1: PCB manufacture process flow

At the interface with the components, the tracks typically have a larger surface area called a bond-pad. Components are placed on the pads and solder interconnects are used to form mechanical and electrical connections. Solder is a mixture of metallic particles and flux resin that simultaneously cleans the bond surfaces and forms a eutectic alloy when sufficiently heated [3]. As it cools the solder solidifies, creating a strong yet ductile joint that allows the assembly to withstand thermal expansion as well as shocks and vibrations [4] that may be experienced during use. Figure 1.2 shows an example of an electronic system, highlighting its main parts.

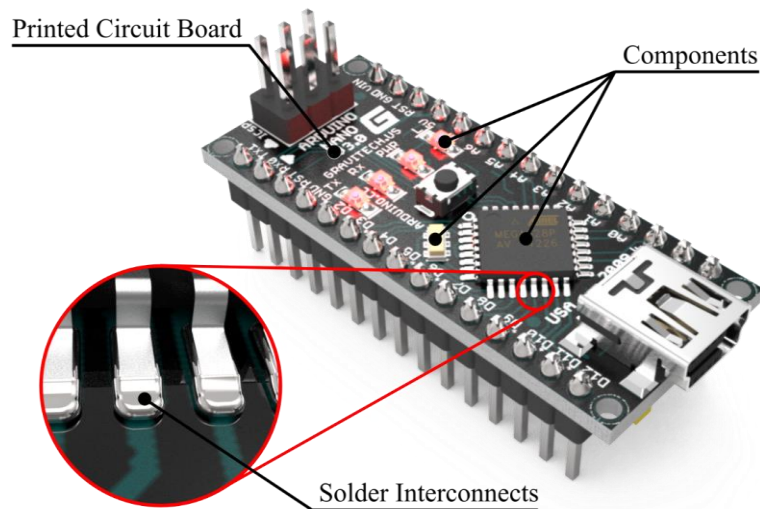


Figure 1.2: Electronic system showing the main parts

Over the last 50 years, electronics have undergone a rapid evolution towards increasing the density of devices, which has helped make them computationally faster, lowered power consumption and improved portability. This was evident with Moore's Law, a trend predicting that the number of components on an IC would double every two years [5]. To-date Moore's Law has remained true, resulting in significantly smaller IC's; however, there is a fundamental limit on the minimum transistor size, meaning that Moore's Law will eventually break-down [6]. This is a major driver in the advancement of packaging and PCB technologies which are required to ensure that the trends in increased miniaturisation, performance and functionality can continue.

This reduction has caused the minimum bond-pad size to continually shrink and seen the development of new IC packaging methods with smaller footprints (see Figure 1.3). The core of an IC is the silicon die, which has the components to make the chip function etched into it. In early IC's, the die was mounted in a plastic housing with leads protruding from it, that are wire-bonded to the silicon. The components are through hole mounted to PCB's, whereby the leads are passed through the board and soldered in place. This progressed into surface mount devices (SMD) [7] that are similar in construction; however, the leads are soldered to pads on one side of the board. More recently chip-scale, direct attach methods such as flip-chip and ball-grid array (BGA) [8, 9] have emerged where the pads reside underneath the component itself and the bare die is soldered to the PCB.

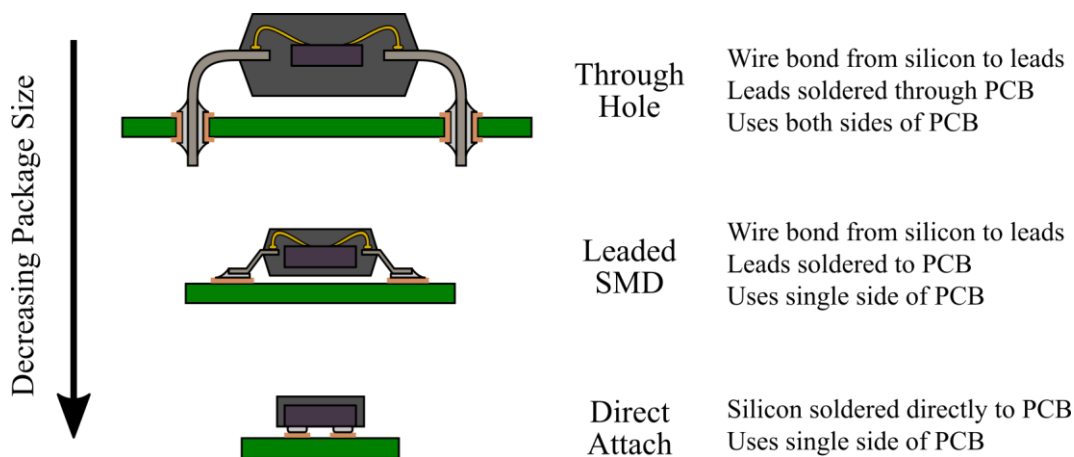
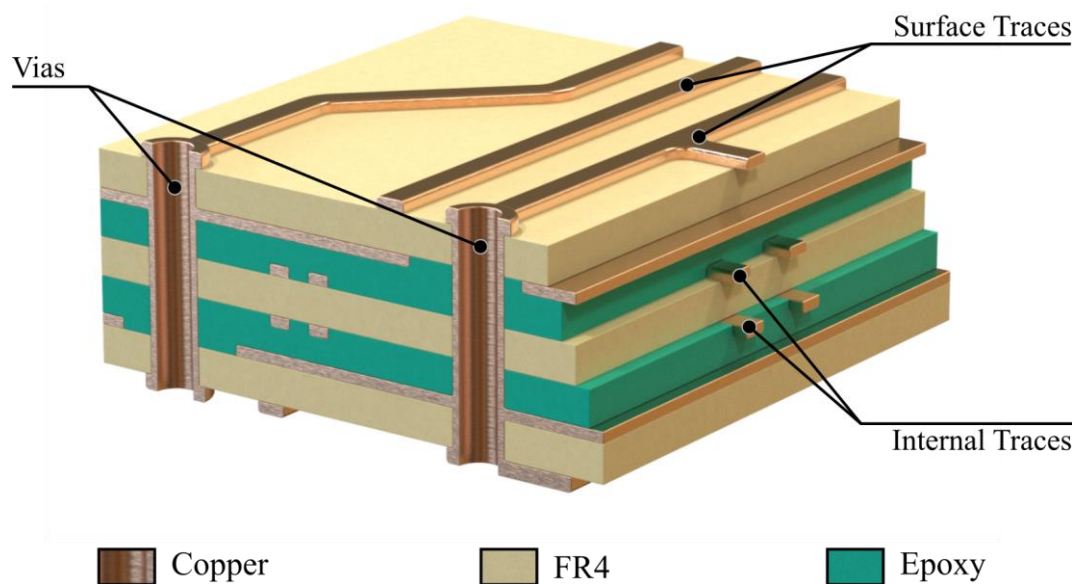


Figure 1.3: Illustration demonstrating how advances in packaging technology can reduce the size of an IC.

The option to have components mounted to the surface led to the invention of double-sided PCBs with vertical connections called vias, that allow electricity to pass through the board. Furthermore, multiple double-sided boards can be laminated together with epoxy to create multilayer boards with three-dimensional routing (see Figure 1.4). The vias are formed by drilling holes in the PCB and electroless plating them with copper to make them conductive [10]. In its current state, PCB manufacturing is an advanced field capable of producing densely populated, high-fidelity circuits that relies heavily on template-based photolithography.



*Figure 1.4: Schematic of how a multilayer PCB can be layered, showing three double-sided PCB's used to create a six-layer PCB*

These processes are optimised for mass-production where the design remains unchanged; however, the rigid photomasks mean that the boards that are produced must be planar. This inherent rigidity removes a dimension that could be used for miniaturisation by creating conformal circuits, although this has been partially overcome through the advent of flexible PCB's. These are a film based printed circuits that have copper etched on to a polyimide (PI) film and are used to form connections between moving or out of plane boards. These are not a perfect solution however, as the use of additional connectors for interfacing introduces new manufacturing complexities and potential failure points. Furthermore, as with rigid boards they are fabricated using photomasks which are expensive, preventing any degree of end-user customisation.

One alternative is to use digitally driven processes like Additive Manufacturing (AM), which use computer-controlled hardware, making them agile and flexible as well as removing the need for physical templates. The ISO/ASTM standard [11] defines AM as:

*“The process of joining materials to make parts from 3D model data, usually layer upon layer, as opposed to subtractive manufacturing and formative manufacturing methodologies.”*

More commonly known as 3D printing, this style of manufacturing was commercialised in 1987 by 3D Systems [12] and has since become a crucial element of Industry 4.0 [13].

These processes enabled the production of complex, three-dimensional geometries that were unachievable using conventional machining and forming methods. Because of this, AM has found applications in high-value sectors such as the manufacture and repair of bulk metallic parts for aerospace [14]. In comparison to electronics, AM is a recent development with a comparatively low market value of \$11.7 Billion in 2019; however, this is expanding rapidly with a compound annual growth rate of 25.7% [15]. Moreover, by 2025, it is estimated that 28% of the market share will be used to produce next-generation consumer electronics [16].

In isolation, AM processes are restricted to single material classes, i.e., polymers, metallics, or ceramics; meaning parts requiring contrasting material properties in one device, such as PCB's, are difficult to additively manufacture. To overcome this challenge, multiple avenues have been researched including multi-material printing, hybrid AM and additive structuring. Despite offering significant advancements in customisability and geometric flexibility, when compared to conventional PCB's each made compromises in one or more of the following areas:

- Electrical conductivity
- Substrate material properties
- Compatibility with existing packaging techniques
- Reliability/Durability
- Miniaturisation
- Cost
- Speed
- Efficiency

For example, many of the processes added high-performance conductors to substrates with poor thermal or mechanical properties that restricted them to prototyping applications. These trade-offs made them inappropriate for use in modern consumer electronics and are explored in detail in Chapter 2.

As dielectric substrate materials imide-based polymers are ideal, with excellent mechanical, thermal and chemical properties which have already led to them being widely adopted in the electronics industry. An approach that has explored using these materials as a base for additively applying high conductivity, copper circuitry is the chemical modification and selective metallisation of polyimide (PI) materials.

The concept of metallising PI was demonstrated by Ikeda et al. in 2001 [17]. The group used potassium hydroxide (KOH) to hydrolyse PI resin which cleaves imide rings and allows copper ions to be adsorbed. These were photochemically reduced to form copper nanoparticles (NP)s using UV irradiation and a titanium oxide catalyst. By introducing a quartz photomask, the copper could be selectively reduced to form individual tracks. In 2003 the same process was modified to enable silver metallisation [18], using silver nitrate ( $\text{AgNO}_3$ ) instead of copper. This approach did not require a photocatalyst for the reduction, simplifying the process.

With these approaches the films were often just a few hundred nm thick and produced conductivities significantly lower than those of bulk metals [17, 19]. It

has been shown however, that modified surfaces could be used as a seed site for subsequent plating [20, 21], increasing the overall conductivity.

In 2008 Ng et al. demonstrated this and used electroless copper plating to reach conductivities of  $3.20 \times 10^7$  S/m [22], or approximately 1.9 times lower than bulk copper. While still lower than bulk copper, it was an order of magnitude greater than existing hybrid DW processes and only bettered by wire embedding processes that used with a raw copper wire as a feedstock. Details of these process can be found in Chapter 2.

A key driver behind the research was to improve the conductor adhesion over DW approaches that rely on micro-roughening to anchoring to the surface [17]. This is seldom considered in AM electronics literature, but is important for the long-term reliability of electronics systems. Poor conductor adhesion could result in delamination [23] and premature failure as the device experiences vibrations, shocks and thermal expansion during every-day use. Selective metallisation techniques have shown good adhesion to the underlying layers, with bond strengths as high as 2 kN/m reported [24].

Light-based reduction has also demonstrated high resolutions, producing features between 500 nm [18] and 30  $\mu$ m [25] in width. It should be noted however, that in these reports a photomask was used to achieve these delicate features, introducing the same issues experienced by conventional PCB manufacture.

Other research has used UV lasers to directly pattern onto treated substrates [26, 27]. Lasers are a flexible processing method and depending on the application, the power, beam profile, and focal distance can be optimised to suit the substrate. By mounting the optics onto computer numerical controlled (CNC) axes, it is possible to trace paths over complex 3D geometries, allowing them reach areas not immediately accessible by the beam. Moreover, lasers have achieved high resolutions, with line widths approaching 5  $\mu$ m [28] with scope for further miniaturisation. This is controlled by the Rayleigh criterion diffraction limit [29] which dictates that with suitable hardware the 405 nm UV

light used by these processes could be focussed to a spot approaching 203 nm in diameter.

The predominant substrate material for these processes has been PI films [30, 31]; however, a laser-based approach has also been demonstrated on polyetherimide (PEI) [32] a polymer with similar properties to PI. Unlike PI, PEI parts has been additively manufactured using material extrusion processes, although they are difficult process and typically require expensive hardware. The challenges and existing approaches for the AM of PEI parts are discussed in depth in Chapter 2. To-date, chemical modification of PEI has not been applied to additively manufactured parts and is the main gap in the existing research that this thesis has expanded on.

## **1.2 Research Purpose**

### **1.2.1 Aims and Objectives**

This body of work aimed to develop a digitally driven manufacturing approach for additively fabricating high-performance, three-dimensional, flexible electronics devices durable enough for real-world applications. This was achieved through the hybridisation of additively manufactured PEI with chemical modification, digital light-based patterning, and copper plating. These were delivered through six key objectives:

1. Engineering a low-cost fused filament fabrication printer capable of printing PEI.
2. Printing flexible electronics directly into rigid parts without the need for additional connection hardware.
3. Establishing the chemical treatment and light exposure parameters required for patterning and copper plating printable grades of PEI.
4. Evaluating the mechanical, electrical and fatigue performance of fabricated circuits.
5. Attaching existing fine-pitch SMD components using high-temperature soldering methods.

6. Fabricating demonstrators that showcase the key characteristics and how they act as building blocks for next-generation electronics.

Objective 1; the design of a PEI printer, was not essential to the process as existing machines existed that can produce parts from this material; however, the decision to do so was driven by their expense and restrictive print settings. By building a custom machine with an alternative design this work looked to reduce the barrier to-entry and introduce added design freedoms, such as using thinner layers to print flexible features. Objective 2; the integration of these flexible regions into rigid bodies for electronics applications had not previously been explored, adding novelty to the work, and removing the need for additional connectors that were required to connect rigid and flexible circuitry. Objective 3 was the main enabler for this technology and allowed the chemical modification to be applied to 3D printed PEI, which to-date had only been demonstrated on sheet and film materials. Whilst there are existing approaches for additively manufacturing electronics, this work made use of high-performance polymers and copper plating that provided good mechanical, thermal and electrical performance. This led to the formation of objectives 4 and 5, to verify the applicability of the process for real-world use and compatibility with solder reflow processing; a technique that has not previously been used with AM electronics. Finally, as the process introduced new capabilities for electronic designs, objective 6 looked to better illustrate their potential.

The proposed process hybridised additive manufacture and chemical modification of PEI with laser-based patterning, the schematic of which is detailed in Figure 1.5. Fabrication started by additively manufacturing the substrate from PEI using fused filament fabrication (FFF), which was then treated using the two-stage chemical modification process from Section 4.2.1. With silver adsorbed into the polymer, a UV laser source scanned over the surface, triggering a photoreduction and converting ions into NP's. The entire component was then washed to remove unreduced ions and plated using electroless copper deposition to increase the conductivity. Solder and components were placed, and the assembly was heated in a reflow oven to form the interconnects and complete the process.



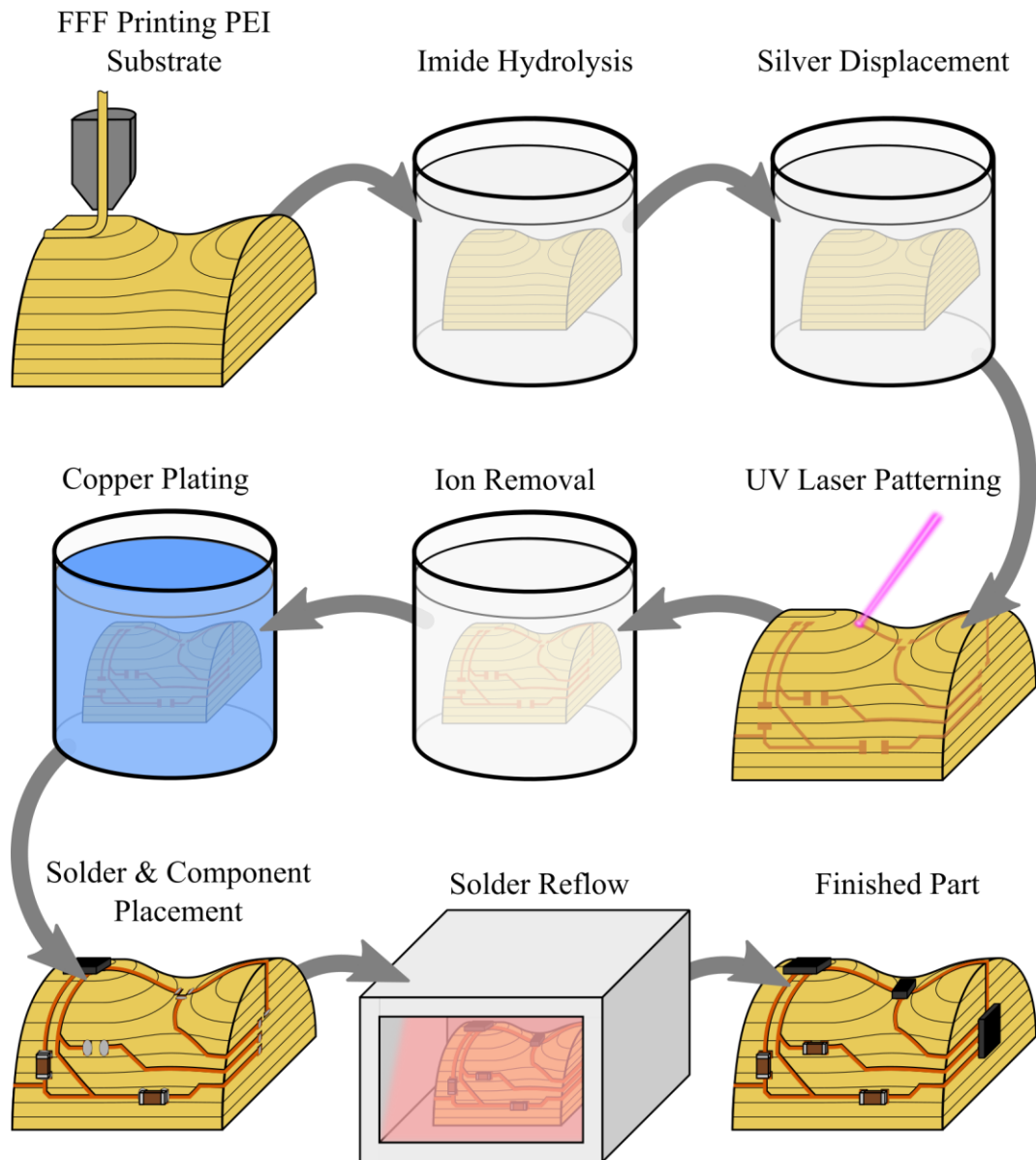


Figure 1.5: Proposed process flow for combining FFF of PEI with chemical modification and laser-based patterning to create 3D electronic devices compatible with surface mount solder reflow

### 1.2.2 Photobioform Project

This thesis directly supported a wider project entitled Photobioform which aimed to develop bio-inspired manufacturing process for selectively patterning metals onto non-conductive substrates using light-harvesting complexes to accelerate the reduction of metal ions. Photobioform was funded by four Engineering and Physical Sciences Research Council (EPSRC) grants: EP/L022133/1, EP/L022192/1, EP/N018265/1, and EP/N018265/2. The project was a collaborative effort with Herriot-Watt University and three industrial sponsors working in prosthetics, circuit technology and metrology. The work in

this thesis complemented Photobioform by applying it to additively manufactured parts and introducing fully digital, template less patterning.

### 1.3 Thesis Structure

The chapters of this thesis each addressed a different aspect of the process development and validation which are summarised in Figure 1.6.

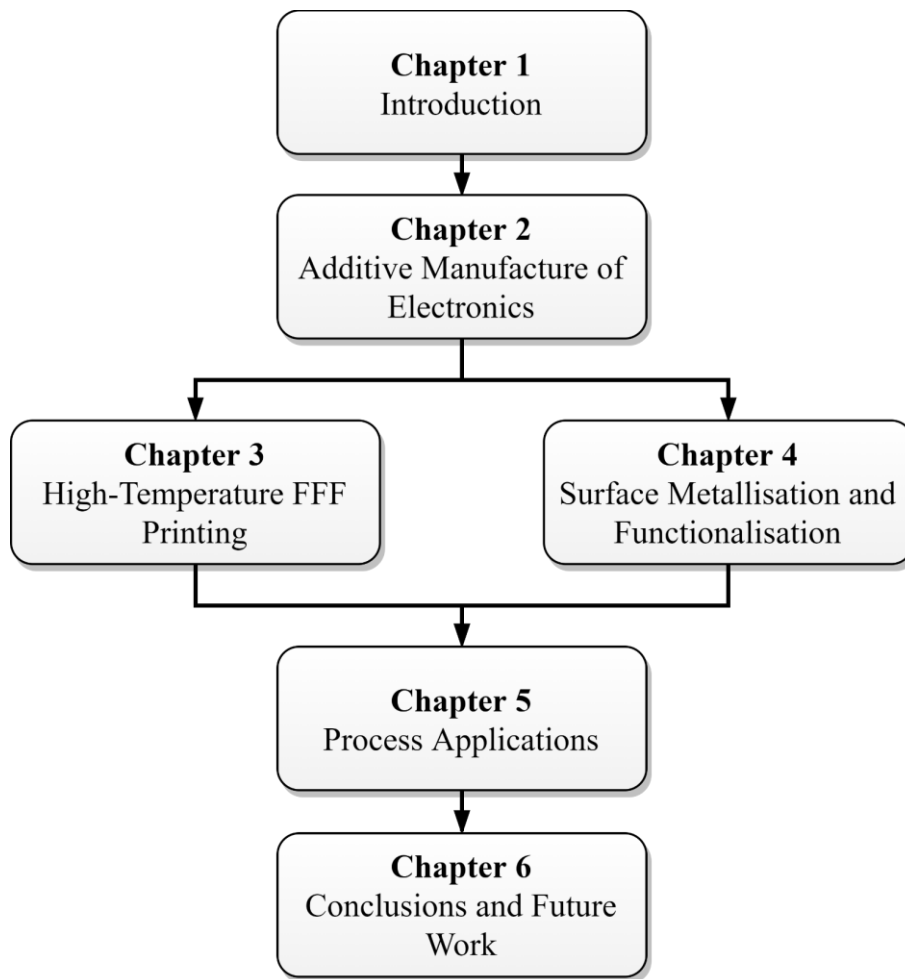


Figure 1.6: Summary of thesis structure

Chapter 2 started with detailed background research into additive, direct write (DW) and hybrid manufacturing that focused on electronics systems. Initially the review investigated the fused filament fabrication (FFF) of polymer materials. FFF was selected as the printing method as the hardware is easy to modify and, while challenging, is capable of printing PEI making it compatible with the chemistry described previously. This transitioned into exploring approaches for depositing electronics on to pre-formed and AM substrates. The

review helps to direct the thesis and guide experiments and decisions throughout.

Chapters 3 and 4 developed the process and characterised the substrates and circuitry. Chapter 3 details the design and build of a low-cost inverted FFF printer for producing the PEI substrates which were then mechanically and dimensionally tested to validate their suitability. Chapter 4 investigated the patterning and functionalisation of the PEI, by finding the optimal chemical treatment and UV dosages to successfully plate the surface. The conductor was then characterised to understand its electrical performance and fatigue life. At the end of the chapter an automated component placement and solder reflow workflow was developed.

Chapter 5 took the working process and demonstrated the different building blocks for next generation electronics systems. This included the creation of functioning electronic devices, integration of sensors, structurally embedded actuators and 3D antennas for wireless power and communication.

Finally, Chapter 6 outlined the main conclusions of the research and recommended future work, with a consideration for wider applications and process optimisation and improvement.

## 2 Additive Manufacture of Electronics

This chapter explored how AM has been applied to the production of electronic systems. Because the substrate material; PEI, can only be printed using FFF, the review focussed specifically on this AM technique and the difficulties of working with high-performance polymers. To investigate the deposition of conductors, the scope broadened into further additive and hybrid approaches as the materials are not restricted to a single process. Additionally, each technique has unique advantages and disadvantages that help illustrate the novelty of this thesis. For reference, at the end of the conclusions in Section 2.6 all the reviewed approaches for additively manufacturing electronics are summarised in Table 2.3, with the abbreviations of polymer names in Table 2.4.

### 2.1 Additive Manufacturing

ISO/ASTM standard 52900:2015 defines AM as, “The process of joining materials to make parts from 3D model data, usually layer upon layer, as opposed to subtractive manufacturing and formative manufacturing methodologies” [11]. The standard also divides AM into seven process categories based on their operating mechanisms, as detailed in Table 2.1.

Table 2.1: Seven ASTM/ISO additive manufacturing process categories and their operation [11]

Process Category	Description
Binder Jetting	A liquid binding agent is selectively deposited to join powder materials
Directed Energy Deposition	Focused thermal energy is used to fuse materials by melting as they are being deposited
Material Extrusion	Material is selectively dispensed through a nozzle or orifice
Material Jetting	Droplets of build material are selectively deposited
Powder Bed Fusion	Thermal energy selectively fuses regions of a powder bed
Sheet Lamination	Sheets of material are bonded to form a part
Vat Photopolymerisation	Liquid photopolymer in a vat is selectively cured by light-activated polymerisation

Despite their operational differences, all the AM processes have a similar workflow that starts by taking a digital design file and converting them into a triangulated mesh representing their outer surface. The mesh is then loaded into specially designed software called a slicer, which splits the surface into vertically stacked layers and works out the optimal order of operations for printing each. The software also produces any machine and material-specific commands such as processing temperatures or tool changing operations. With the finalised machine code ready, the design is transferred to the printer, which automatically builds the part without operator intervention. Once the build is complete, the part can be removed and, depending on the chosen AM category, post-processed to finish the part [33].

## **2.2 Polymer Fused Filament Fabrication**

Fused filament fabrication comes under the material extrusion category and was the generic name given to Stratasys' fused deposition modelling (FDM) process developed by Scott Crump in 1989 [34]. Rapid growth and development of FFF printers came primarily as a result of the University of Bath's open-source Replicating Rapid Prototyper or RepRap project [35]. The concept was to design a machine capable of printing most of its structure, and only using widely available parts in place of those that could not be printed. FFF was selected as the core technology because it requires no specialist parts such as lasers and can process a broad range of low-temperature thermoplastics, allowing more significant proportions of the original machine to be reproduced.

FFF printers heat a thermoplastic polymer and extrude it through a digitally controllable nozzle, which selectively deposits the material one layer at a time. Once a layer is completed, the nozzle moves up relative to the part and prints the next layer, repeating until the whole object has been built.

### **2.2.1 Extrusion System**

The extrusion system starts with the material feed mechanism, commonly referred to as the extruder, which depending on the format of the feedstock being used, can vary in its operation. The most common feedstock style in use today is a filament, which is typically fed using a set of pinch rollers with a high

friction surface, or teeth that bite into the plastic (see Figure 2.1 a). The intention is to apply as much driving force to the material without deforming or misshaping it as this can have consequences on the extrusion characteristics later in the system [36, 37]. Pelletised materials have been experimented with as they are often the rawest form a polymer can be purchased in, reducing the operating costs. To move the pellets from a hopper to the nozzle, pistons [38] or augur screws [39–41] have been employed; however, few designs have seen practical applications as the hardware is often bulky and difficult to fit to a motion platform. One notable exception was the ARBURG Freeformer [42], that used an auger to feed pelletised material to a nozzle and a plunger to dispense individual droplets, building up layers in a manner comparable to 2D inkjet printers. To overcome the bulk of the extrusion system, the Freeformer kept the print-head static and moved print-bed.

If high print speeds are required, the feed rate of the material must increase to keep the flow consistent. This comes with increase in force required to extrude the polymer, limiting the achievable print speed before the rollers begin to slip. Go and Hart [43] managed to achieve approximately a “10-fold greater build rate than commercial desktop FFF systems” [43] by using a threaded filament and rotating nut. Because the thread has a large contact area, the force that can be applied before the plastic deforms is higher than that of a roller. This was coupled with a laser pre-heater, which melts the polymer faster than a conventional heater, lowering its viscosity and allowing it to pass through the nozzle easier.

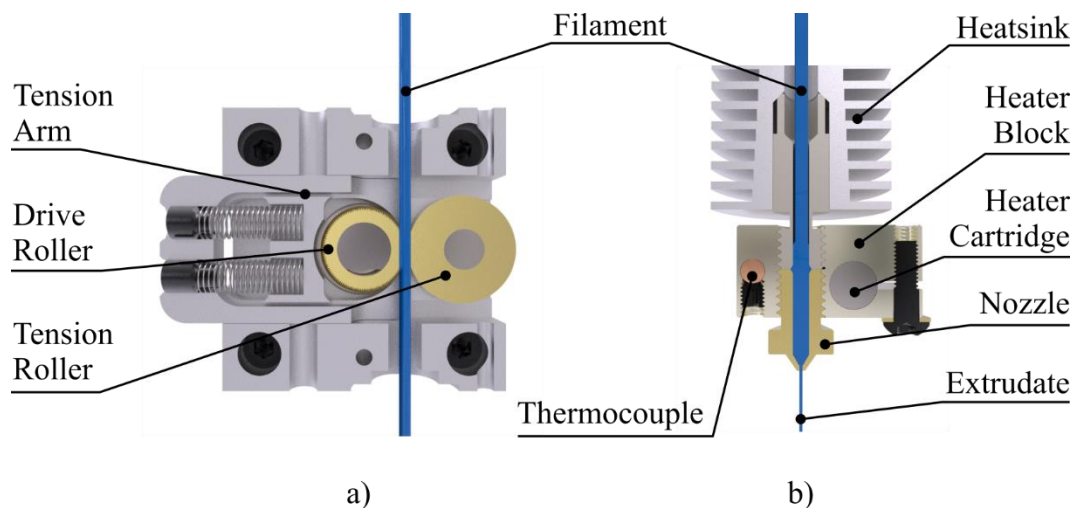
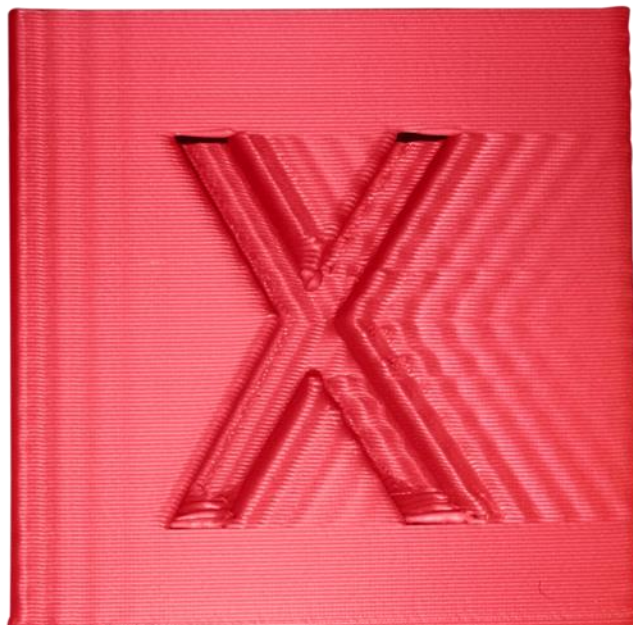


Figure 2.1: Components of a typical FFF extrusion system: a) extruder. b) hotend

In addition to providing a driving force, the extruder must accurately control the flow rate of the material from the nozzle [44, 45]. Failure to do so can lead to misshapen extrudates with blobs where the material has been over-extruded or necking where too little is dispensed [46, 47]. Direct drive extruders place the extruder on the print head, providing the shortest possible filament path, reducing friction and compression, improving the response at the nozzle. Alternatively, the feed system can be fixed to a static portion of the printer and connected to the nozzle via a length of guide tube referred to as a Bowden tube. Bowden setups have the disadvantages associated with a longer filament path, but by lowering the mass of the print head, higher speeds and accelerations can be achieved. Ringing artefacts [48], which appear as a ripple in the surface finish (see Figure 2.2) wherever the print head changes direction abruptly are also reduced. They are caused by flexibility in the motion platform components allowing the print head to oscillate and can be damped by stiffening the printer and lowering the print-heads mass.



*Figure 2.2: FFF test piece with ringing artefacts [49]*

The final stage of the extrusion system is the hotend, where the material is heated until it liquifies, before being compressed through a narrow orifice in the nozzle to form the extrudate (see Figure 2.1 b). To melt the polymer, a heater cartridge is installed into the same block of metal as the nozzle. The liquification temperature is monitored by a temperature probe, which is used as the feedback

element of a control loop. The heater assembly is attached to the print-head via a heatsink, which prevents thermal energy from travelling into the printer and keeps the molten material restricted to the liquefier [50].

The size of the nozzle dictates the minimum X-Y feature size that can be produced, with smaller nozzles producing narrower lines. The finest extrudate width reported was of the order of 100  $\mu\text{m}$  [51], although commercial printers were often sold with a 400  $\mu\text{m}$  nozzle and the option to upgrade to nozzles as small as 125  $\mu\text{m}$  [52]. The width of the printed line is not the same as the nozzle diameter due to the effects of die swelling, which can cause between 1.2 and 1.5 times radial expansion [51]. Die swell is not a constant characteristic either and varies depending on the material, extrusion speed and liquefier temperature [53]. Finer nozzles also lead to an increase in back-pressure [54], that must be overcome by the extruder, placing a limit on resolution improvements by using smaller nozzles. The pressure can be minimised by printing slower, reducing the mass flow rate of material through the nozzle. The resolution in the Z-axis is controlled by the height of each layer, which for typical FFF systems range between 20 and 330  $\mu\text{m}$  [55, 56].

Layering in Z also introduces an artefact known as stair-stepping (see Figure 2.3) which occurs on any surface that is not perpendicular to the layers as the slope must be interpolated, introducing error.

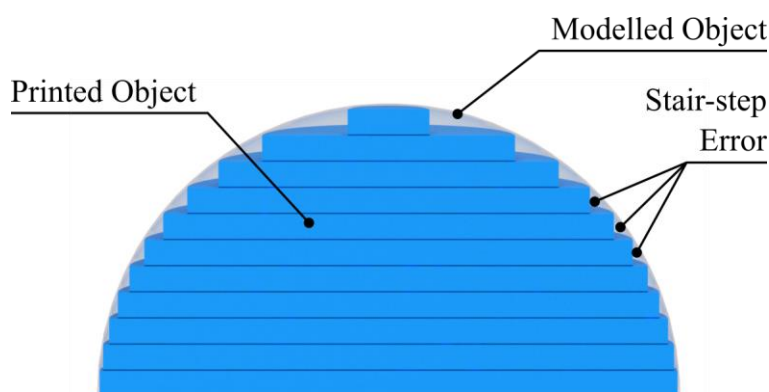


Figure 2.3: Illustration of error introduced by layer-based manufacturing

On vertical and horizontal surfaces, there is no approximation, but on shallow angles, the aliasing becomes particularly noticeable. This can be minimized by printing thinner layers at the expense of longer build times. The layer-based



nature means that parts exhibit mechanical anisotropy, with notably lower tensile strength when loaded through the build axis. This can be minimised by printing thin layers that are compressed more onto previous material, increasing the bond area and reducing the size of voids. [57–59].

### 2.2.2 Motion Platform

How an FFF printer positions the nozzle is determined by the configuration of the axes. The two main layouts in use today are Cartesian and delta systems. Cartesian machines consist of three linear translational stages aligned in the X-, Y- and Z-axes that directly move the print head relative to the bed, as illustrated in Figure 2.4. This style of printer is the most popular in use today [60], with the majority of professional and consumer designs being based around this architecture. The simple, orthogonal approach allows Cartesian systems to be built into a very rigid frame with minimal effort, which benefits how repeatably the print head can be positioned and reduces vibrations that introduce print artefacts such as ringing.

The added rigidity also allows the gantries to carry substantial loads, making them well suited for use with direct-drive extruders.

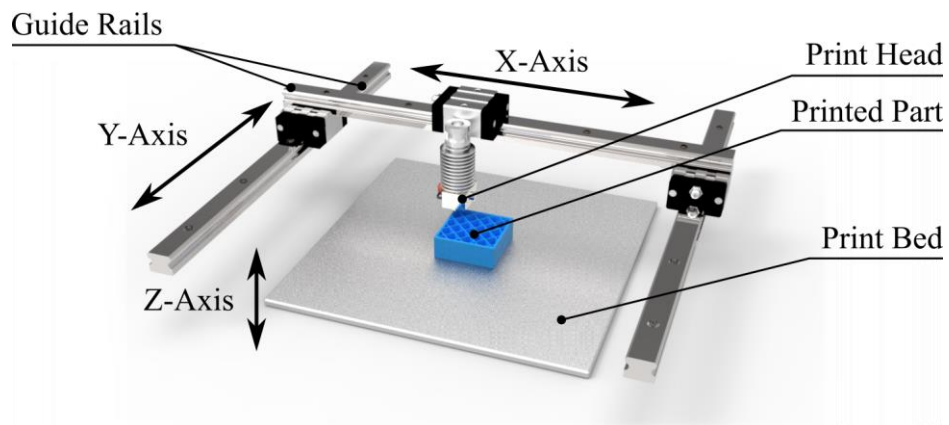


Figure 2.4: Simplified Cartesian machine configuration

The serial nature of the layout means that at least one of the axes must be carried by another, increasing the total moving mass, reducing the achievable acceleration. To counter this, variants such as the H-Bot and Core X-Y [61, 62] systems were developed, which decouple the heavy motors from the moving hardware and instead rely on longer, continuous lengths of timing belt to

position the axes. Alternatively, Mendel style Cartesian printers whereby the Z-axis is used to carry the extruder allowing X-Y movements to be inertially isolated. This is possible in 3D printers as while printing, the Z-axis only moves a single layer thickness at a time and does not need to accelerate rapidly.

Delta robots were initially developed in 1985 by Raymond Clavel, for rapidly positioning lightweight parts in industrial settings [63]. In most AM applications, delta robots use arms connected to sliders on three towers laid out in a triangular pattern (see Figure 2.5) to position an effector in 3D space. In comparison to cartesian printers, delta setups are mechanically more straightforward and easier to assemble [64], albeit more difficult to control. The complexity in delta printers is software-based due to the inverse kinematics [65] required to calculate the slider positions for desired movements at the head. These calculations are computationally intensive, particularly as effector speeds increase. These can be approximated to minimise processing times [66], although the result is less positional accuracy at the effector. Modern electronics have largely resolved this issue with commercially available, low-cost, high-performance 32-bit control boards such as the Smoothieboard 5XC and Duet [67, 68] becoming increasingly popular.

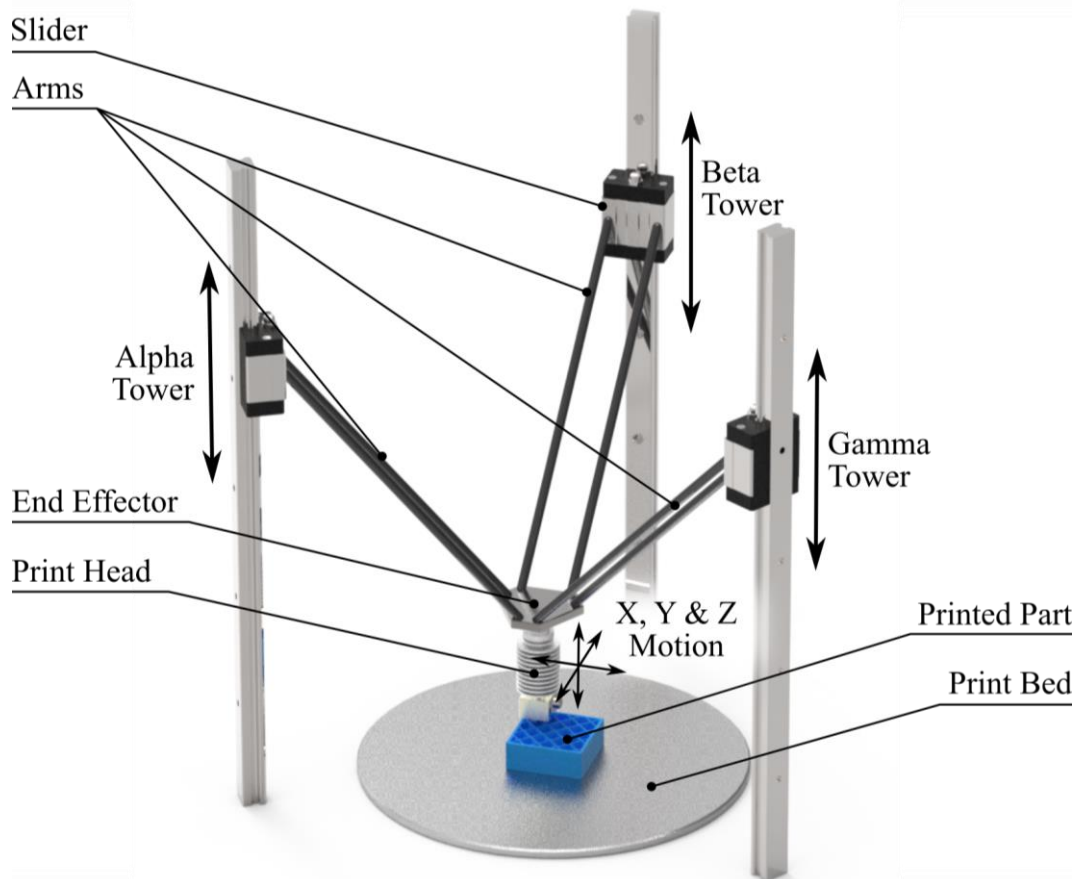


Figure 2.5: Simplified delta machine configuration

The key advantage for delta systems is they have a much lighter effector and can usually reach accelerations far beyond that of cartesian machines [69, 70], increasing their potential print speed. This comes at the cost of maximum payload and the force than can be exerted at the print head; however, in FFF applications this is not a concern as tool force is minimal. Despite this, delta designs often opt for Bowden extruders, to maximise their potential acceleration.

There are alternative architectures such as selective compliance assembly robot arm (SCARA) and polar printers; however, these are almost entirely restricted to hobbyist projects and outside the scope of this work.

### 2.2.3 Feedstock Materials

To allow them to be formed into filaments and then re-melted for printing the polymers used in FFF are usually amorphous and semi-crystalline thermoplastics. The most common materials in use today are polylactic acid (PLA) and acrylonitrile butadiene styrene (ABS) [71, 72] as they have low glass

transition temperatures ( $T_g$ ) making them easy to extrude. Based on their global consumption and typical properties, thermoplastics can be categorised into one of three categories (see Figure 2.6): commodity, engineering and high-performance polymers [73, 74].

- **Commodity Polymers:** Low  $T_g$ 's and therefore operate around ambient temperatures. They are low-cost, account for the largest proportion of the global consumption and are typically used in packaging materials.
- **Engineering Polymers:** Moderate service temperatures and better mechanical strength with elevated costs. Global consumption is approximately 1/30<sup>th</sup> of commodity polymers, and they are used in general engineering applications.
- **High-Performance Polymers:** Service temperatures greater than 200 °C and provide the best mechanical characteristics. They are expensive and therefore have a global consumption 1/600<sup>th</sup> of commodity polymers. They are reserved for use in specialist applications.

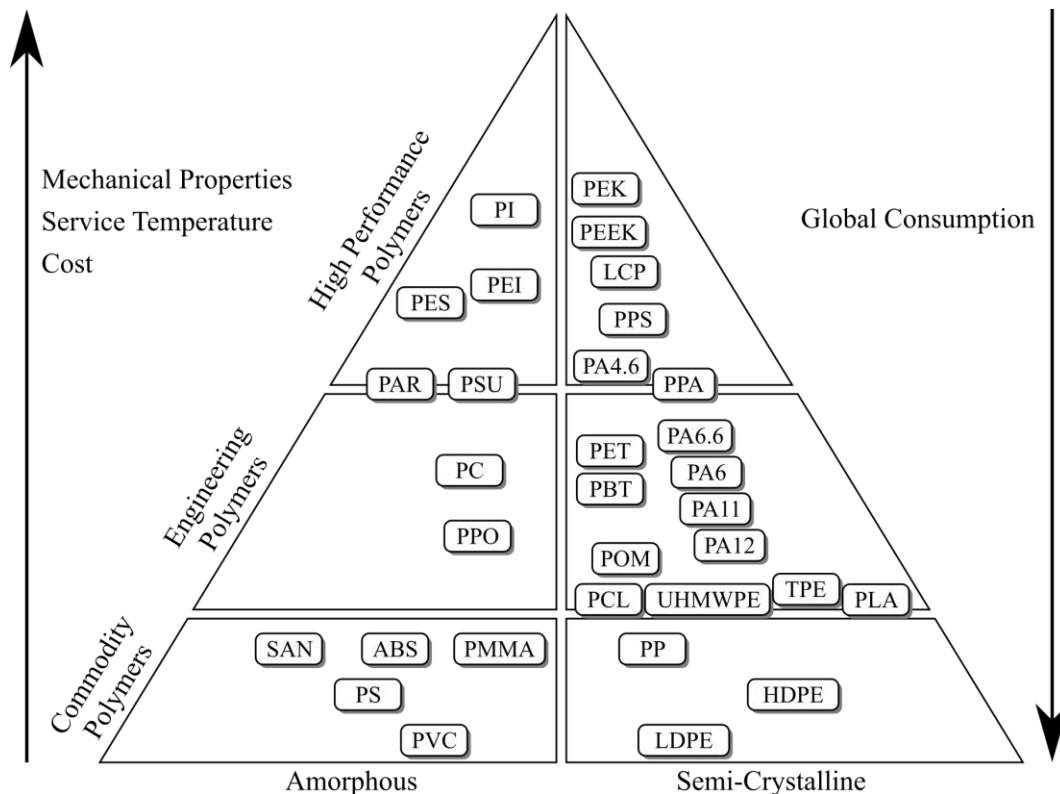


Figure 2.6: Pyramid of polymeric materials. Adapted from [75], Polymer abbreviations can be found in [76]

#### **2.2.4 The Challenges of High-Temperature Printing**

For the manufacturing approach suggested in Section 1.2.1, substrates made from high-performance polymers were desirable as they provide a high thermal resistance, preventing deformation during solder reflow. More importantly, both are available in the filament form usually required for the extrusion system. Some typical polymers include polyetherimide (PEI); also known as ULTEM, polyphenylsulfone (PPSU) and polyether ether ketone (PEEK). The printing process for these materials is fundamentally the same as FFF of low-temperature polymers; however, due to their high thermal resistance, the equipment needs to withstand higher temperatures.

The first challenge is reaching and maintaining the correct nozzle temperature, which can vary from 360 °C for some grades of PEI [77] and up to 410 °C for PEEK [78]. The nozzle temperature has a noticeable impact on the interlayer adhesion of printed parts, with higher extrusion temperatures leading to greater interlayer flow of the polymer, fewer voids, and better overall bonding. For semi-crystalline polymers such as PEEK and PPSU this effect is limited however, as the extrusion temperature also dictates the final morphology of the parts, altering their ductility and tensile strength as a result [79, 80]. Because of this the heaters must be both more powerful and better controlled than those used in low-temperature printers.

A common defect among FFF parts is warping, which is induced by thermal gradients throughout the part and across the build environment. This leads to uneven cooling of the plastic and a build-up of internal stresses that can deform the part as they try to relax [81–83]. In commodity and lesser engineering polymers such as PLA and ABS, the print temperatures and resulting thermal gradients are moderate, so the magnitude of the stresses is minimal. Any warping that does occur can be minimised by improving the parts adhesion to the build platform. This may be achieved by adding bed adhesion aid such as brims and rafts that maximise the contact with the build plate, securely fixing it in place. Alternatively the surface of the print bed can be modified through roughening or the application of materials such as PI tape or ABS-acetone

solutions [84] that the feedstocks adhere to more readily. For high-performance polymers, even if the warping is controlled through mechanical fixation, these stresses can introduce delamination between the printed layers, reducing the overall mechanical strength of the component [85]. The alternative is to regulate the temperature of the air surrounding the print to reduce thermal gradients and limit stress build up in the first place.

In 2004 Stratasys filed a patent [86] for a design for a cartesian style printer that operated inside a sealed oven, allowing them to directly control the ambient print temperatures (see Figure 2.7). This design became the Stratasys Fortus 450mc, an industrial grade printer capable of producing parts from high-temperature polymers including PEI. The chamber temperatures used by the Fortus 450mc were not published; however, an alternative machine with a similar configuration; the miniFactory Ultra, indicated that such designs can reach chamber temperatures as high as 250 °C [87]. As well as PEI, the miniFactory Ultra was marketed as being able to print other high-performance polymers including PPSU and PEEK.

A machine designed to operate inside an oven has additional requirements because the delicate electronics, motors, and mechanical components need isolating from the heat. Linear bearings, belts, and pulleys used in motion platforms rarely have operating temperatures greater than 120 °C, and motors are often lower at 100 °C. Stratasys' solution used a heat resistant curtain that moved with the print head, keeping the motion platform parts outside of the build area. In Figure 2.7 this feature is labelled as item 132 in the patent drawing.

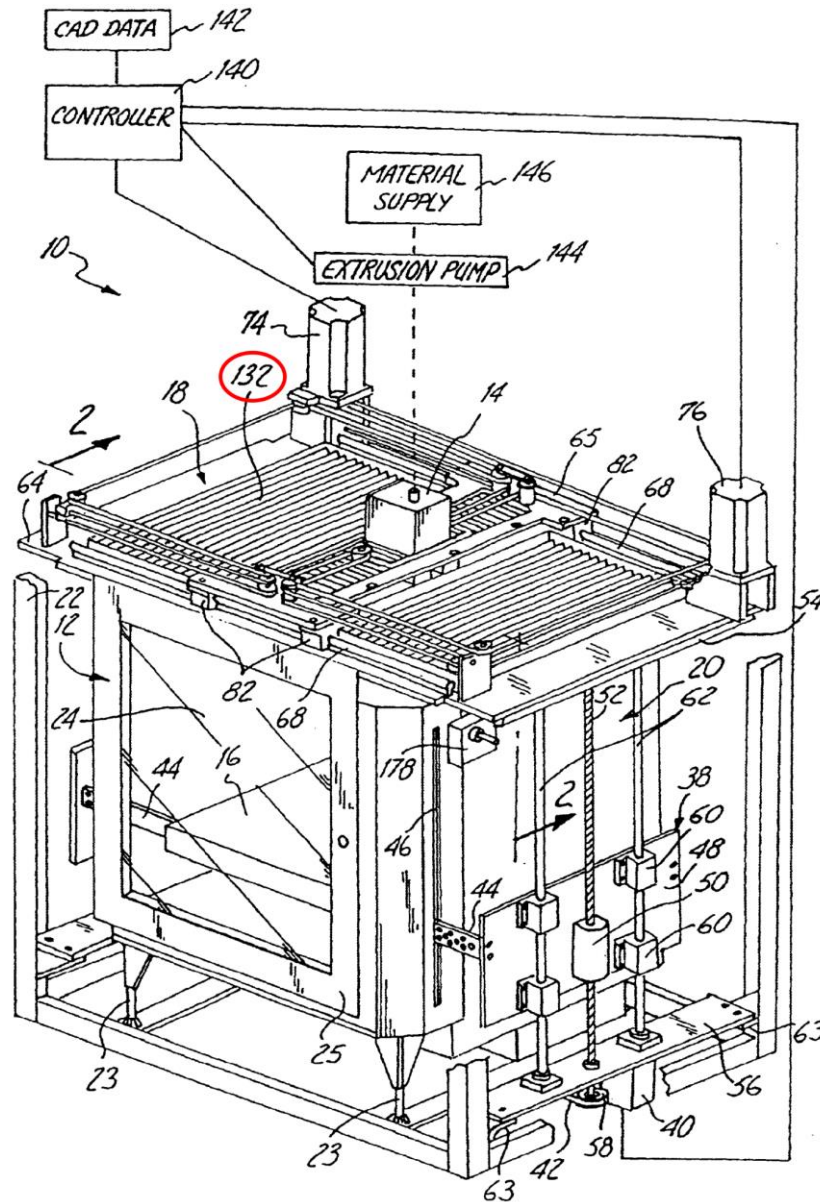
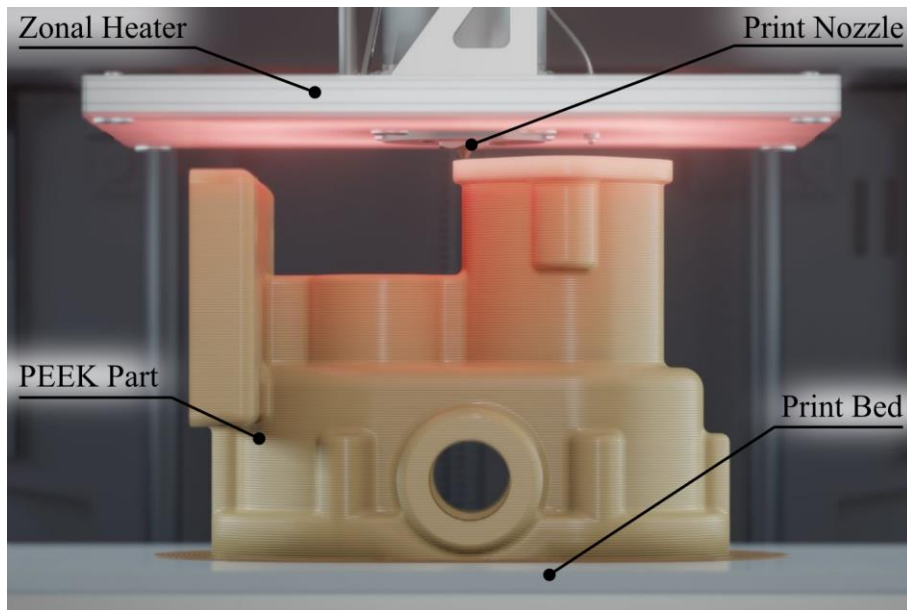


Figure 2.7: Details of the Stratasys heat curtain design. The curtain is item 132, circled in red [86]

An alternative approach from Apium Additive Technologies, used a localised zone heater mounted that moved with the print nozzle to create a region of 180 °C air surrounding the uppermost layers [88]. This provided the necessary heat for full crystallisation of semi-crystalline polymers and allowed gradual cooling from the high extrusion temperatures. The manufacturer also suggested that because only upper layers were kept above the polymers  $T_g$ , the parts were more rigid during printing. The result was improved surface quality and tighter tolerances because of less part deflection occurring at the nozzle while depositing new layers. Figure 2.8 illustrates the zonal heating approach.



*Figure 2.8: Zonal heating system for localised heating of high-temperature polymers mid-print. Reproduced from [88].*

Both methods added expense and complexity to the printer which drove the release of lower-cost machines, that used lower chamber temperatures rather than protecting the motion platform. Machines such as the Funmat HT from Intamsys and 850p from Tractus used motion platforms designs similar to consumer-grade, desktop printers but operated entirely inside an insulated chamber. These configurations coupled with enclosure heaters allowed them to reach temperatures up to 90°C [89, 90]; keeping them within the upper limit for most of the electronics. These temperatures produce higher thermal gradients, increasing the likelihood of print failure, reduced mechanical strength and warping.

A promising approach tested by NASA used focused heating of PEI [91] by adding 420 W IR heat lamps positioned towards the centre of the bed of a conventional FFF printer (Taz 4, Lulzbot). The entire printer was housed in an enclosure to further increase and stabilise the ambient build temperature. Through visual inspection, it was noted that parts printed with additional heating showed no signs of warping or delamination. The effect on mechanical performance was not evaluated. Their research also highlighted that the filament should be kept dry before it is extruded. If moisture is allowed to remain in the



filament, it can vaporise during extrusion, forming voids that lead to increased porosity and reduced mechanical strength [92, 93].

### 2.3 Direct Write of Functional Circuits

Direct-write (DW) is a broad spectrum of processes that functionalise surfaces by printing materials onto a pre-formed substrate. Previous attempts have been made to define DW [94, 95]; however, they fail to adequately distinguish between DW and AM. A more suitable definition is provided by Hon, Li, and Hutchings [96]:

*“Direct writing denotes a group of processes which are used to precisely deposit functional and/or structural materials on to a substrate in digitally defined locations. DW is distinguished from conventional AM in terms of the following characteristics:*

- *The track width ranges from sub-microns to millimetres.*
- *The range of materials deposited can include metals, ceramics, and polymers, electronically and optically functional materials as well as biological materials including living cells.*
- *The substrate is an integral part of the final product.”*

These processes can be broken down into distinct categories based on how they deposit material; these are summarised in Figure 2.9.

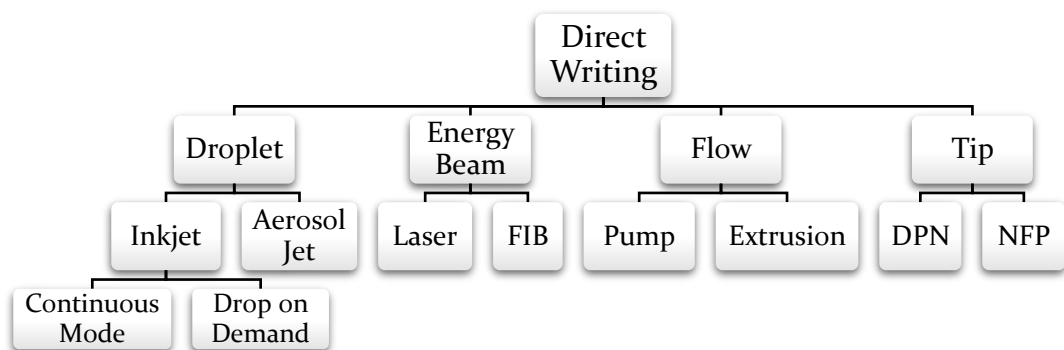


Figure 2.9: Classification of direct-write methods [96]

Three of these processes: Focussed Ion Beam (FIB), Dip-Pen Nanolithography (DPN), and Nanofountain Pen (NFP) were targeted at nanoscale features, which were beyond the scope of this work and therefore, omitted for conciseness [96].

### 2.3.1 Inkjet Printing

Inkjet printing (IJP) is a droplet based DW method that has two modes of operation. Continuous IJP was rarely used in electronics manufacture as it recirculates ink, which can lead to feedstock contamination [97]. This is avoidable by discarding the ink, but metallic inks can be expensive, so this is undesirable. The alternative is drop-on-demand, which can be broken down into thermal and piezoelectric configurations, as illustrated in Figure 2.10.

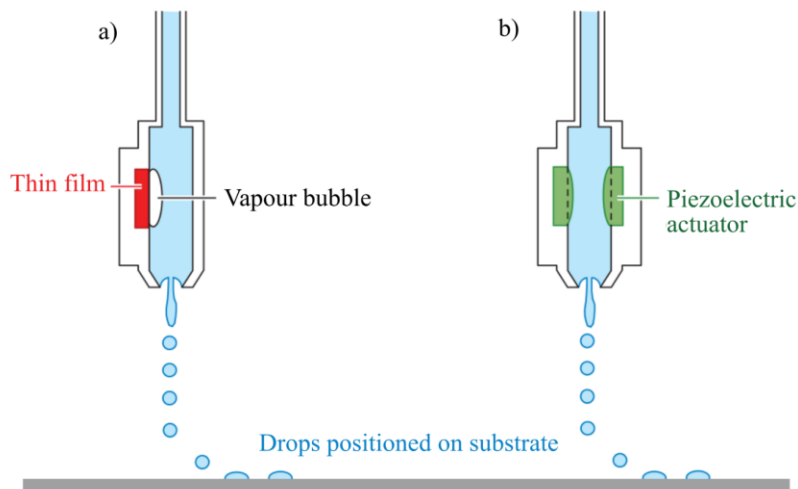


Figure 2.10: Drop-on-demand inkjet printing using a) thermal and b) piezoelectric print heads. Adapted from [98]

In both methods, drops are jettisoned by sending a pressure pulse through the ink behind the nozzle. In thermal print heads (Figure 2.10 a), the pulse is generated using a heater to vaporise a small quantity of the material, causing a bubble to form and rapidly collapse [97]. In piezoelectric setups (Figure 2.10 b), a ceramic actuator oscillates to create the pulse [99, 100]. Dispensing discrete droplets of conductive ink gives IJP a spatial resolution as low as  $70\ \mu\text{m}$  [101], although it should be noted that the wettability of the ink can have a significant effect on this. Work in 2006 showed that different substrate materials could reduce the resolution of an IJP process three-fold [102]. The location of the deposition is adjusted by moving the nozzle over the area to be patterned using a computer-controlled stage. This allowed the head to be dynamically swept over contoured surfaces; however, the small nozzle standoff height [98] coupled with the relatively large head size [103] has prevented the patterning of steep gradients or tight, concave features. Because of this, IJP electronics were usually

planar, with more focus on flexible [104, 105], rather than three-dimensional devices.

### 2.3.2 Aerosol Jet Printing

As with IJP, Aerosol Jet Printing (AJP) deposits discrete droplets of ink from a nozzle onto a substrate. Figure 2.11 shows the schematic of a typical aerosol jet head.

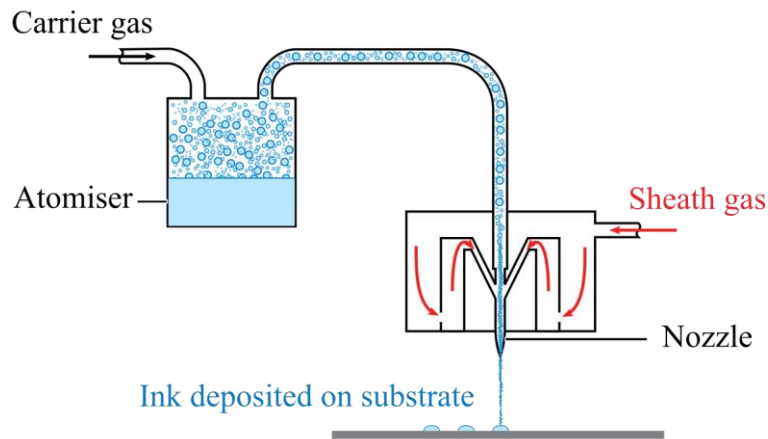


Figure 2.11: Aerosol jet print head schematic. Adapted from [106]

Initially, the ink is aerosolised in an atomiser, forming a cloud of functional particles and solvent. A carrier gas is then passed into the atomiser chamber, transporting the aerosol to the print nozzle, where it is focused using a sheath gas, before impacting the substrate [106]. The use of a sheath gas provided advantages in both resolution and stand-off height compared to IJP, with reported minimum feature sizes of 20  $\mu\text{m}$  [107, 108] and nozzle clearances as high as 15 mm [109]. Furthermore, the nozzle does not have to be perpendicular to the deposition surface and can tolerate inclinations up to 45°, reducing the need for expensive translational stages with four or more degrees of freedom [110].

For electronics manufacture, AJP has seen use on PEI and ceramic substrates [110]; however, it has seen more use in flexible and transparent electronic devices. The substrate of choice for flexible AJP devices is Kapton [111, 112], a PI film that is regularly used to mass-manufacture existing flexible circuits [113]. A key concern with flexible AJP electronics is cracking in the conductor after repeated bend cycling. This was shown to be an issue by Reboun et al., who

compared the bending endurance of samples produced using AJP, screen printing, and copper foil etching and found that AJP silver ink on Kapton tape had significant reductions in electrical performance after as little as 1,000 cycles. This is in direct contrast to etching processes, which achieved 10,000 cycles without any significant change [114]. Mahajan et al. [111] improved upon this, reaching 10,000 cycles without failure at a 5 mm bend radius by embedding the tracks in an epoxy resin. To-date, AJP has seen use in micro-scale printed electronic components, with applications in sensing [115–117], organic LEDs [109], and photovoltaics [118, 119] rather than system-level circuitry.

### 2.3.3 Laser-Induced Forwards Transfer

Laser-Induced Forward Transfer (LIFT) is a set of non-contact processes that work by focusing a laser onto a transparent precursor coated with a functional material. This forms a pocket of vapour that jettisons a droplet towards the substrate below. Depending on the specific configuration, a galvanometer scanner or an X-Y stages were employed to position the laser (see Figure 2.12). The use of a laser means that LIFT has produced high resolutions, with features as fine as  $0.5\ \mu\text{m}$  demonstrated from metallic inks [120, 121].

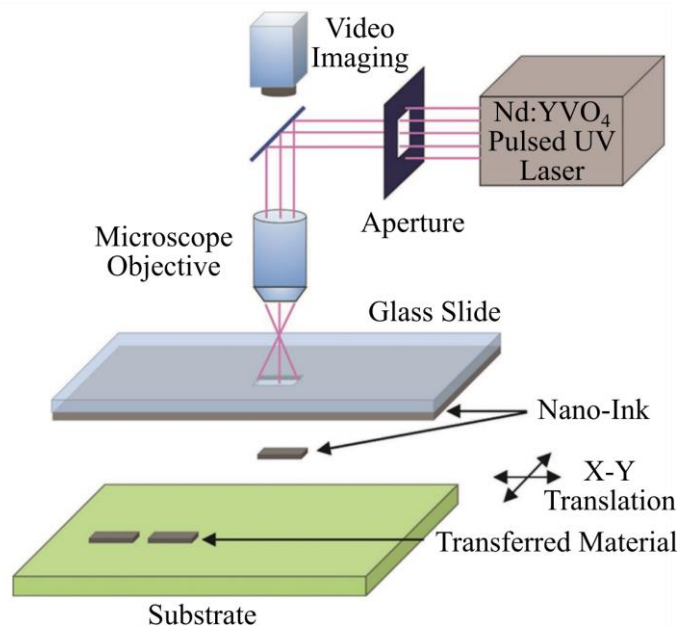


Figure 2.12: Schematic showing the main elements of a LIFT system. Adapted from [122]

The standoff between the deposition apparatus and the substrate is lower than other non-contact methods at approximately  $100\ \mu\text{m}$  [123], making conformal

patterning impractical. Instead, Piqué et al. focused on embedding electronics within the substrate, using the LIFT laser to micromachine cavities into a flat PI sheet before placing components. LIFT was then used to create tracks and interconnects [124]. In later work this was expanded on by using a ribbon with electrical components affixed to it and using LIFT to eject the components onto the substrate [125]. In both reports, the components were fixed in place by spin-coating a layer of PI resin over the top surface of the fabricated devices. The author also indicates that the process could theoretically produce multi-layer circuits; however, this is yet to be demonstrated. All of these characteristics make LIFT a very scalable process that could be used to rapidly prototype electronics in small quantities and mass-manufacture them using roll-to-roll techniques [122]. Because lift can produce patterns on a wide range of scales, it has been used to produce structures for devices such as micro-batteries and sensors [123] as well as tracks in larger circuits [126]. A further modification to the process allowed Wang et al. to produce voxels rather than discrete particles, which when stacked allowed them to create 3D structures and bridges. The suggested application was as an alternative to wire bonding on bare silicon die, which was supported by experimental data showing that they were more resistant to vibration induced fatigue [127].

#### **2.3.4 Pump and Extrusion Printing**

Basic pump and extrusion setups can be created by mounting an air-backed syringe of material to a translational stage (see Figure 2.13). As the syringe moves relative to the bed, pressure is applied to the back of the material which extrudes through a nozzle. The final feature size is primarily determined by the nozzle used, and to-date the smallest track width reported is 0.6  $\mu\text{m}$  [128]. Additional control over the deposition can be achieved by adding high-precision pressure controllers or screw-driven pumping systems [129].

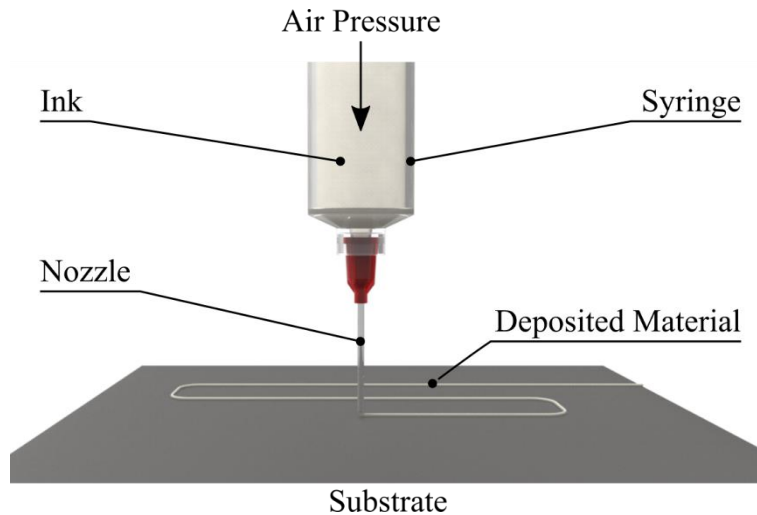


Figure 2.13: Illustration of an air-backed syringe dispenser

Unlike the previous DW processes, these methods rely on the deposition nozzle contacting the surface of the substrate, meaning that some geometries will restrict tool head access. This can be minimised by using high-aspect ratio nozzles that keep the bulky deposition hardware away from the part. A more significant issue is that the nozzle must track the surface correctly to maintain deposition shape and prevent it from impacting the substrate.

In 2011, Adams et al. successfully used a pressure-backed syringe to print conformal silver antennas on both convex and concave domes [130]. To enable fabrication at the extremes of the hemisphere, a bent nozzle was employed, reducing the effective angle between the surface and the material flow. More recently, these processes have been shown to work on freeform and even moving surfaces by placing fiducials on the substrate and using optical tracking to correct the printer's trajectory [131]. Although contact approaches often add complexity as a precise standoff has to be controlled, Muth et al. used this to their advantage and produced electronics embedded inside flexible elastomers [132]. This was achieved by dragging the nozzle through an uncured elastomer while simultaneously depositing a carbon loaded conductive grease and post-curing the whole assembly. By controlling how the conductive is cured, material extrusion can also produce freestanding structures, as demonstrated by Skylar-Scott et al. [128]. Their method used a laser, focused on the deposition point to instantaneously solidify a metallic paste as it was extruded, which conveniently sinters the conductor simultaneously. This has the benefit of enabling patterning

onto thermally sensitive substrates such as flexible PET sheets. In 2013 paste extrusion with a 30  $\mu\text{m}$  nozzle was applied to fabricating micro-battery architectures using multiple inks [133]. The result was a battery measuring just 2.1 mm  $\times$  2.1 mm  $\times$  1.5 mm, with a combined power and energy density that surpassed other examples at the time.

### 2.3.5 Conductive Material Inks

For producing electronics, the inks or pastes used are composed of conductive elements such as metals or carbon dispersed in carrier solvents. The metals typically printed were silver [102, 107, 126, 127, 133-141], copper [143-148], and gold [149, 150] on account of them being the three most conductive elements. Because of their inert nature, silver and gold are easy to process in ambient conditions [151]; however, both are very costly. Copper will oxidise readily upon exposure to air but is comparatively inexpensive, which has driven the development of copper inks coated with a shell to prevent oxidation during deposition [147, 148]. Carbon inks tend to offer conductivities several orders of magnitude lower than their metallic counterparts [101, 132, 152]; however, they are inexpensive and easy to process.

The conductive particles used existed in one of two forms, nanoparticles (NP)s [134, 153] or compounds that undergo metallo-organic decomposition (MOD) [154, 155]. Both needed drying to remove the carrier solvent and then sintered to reach their full conductivity [151]. In MOD inks, sintering triggered the decomposition of the precursor into its final metallic state.

For hot-air convection sintering, typical processing temperatures were 150 – 250  $^{\circ}\text{C}$  [102, 107, 127], although higher temperatures produced better conductivities [141, 156], with some values higher than 400  $^{\circ}\text{C}$  [130, 136, 150]. At these temperatures, glass and ceramics were the only suitable substrates as they are unaffected by the extreme heat; but they are also challenging to manufacture, adding complexity to the process. Lower temperatures at the substrate have been achieved by using Ohmic [157, 158], microwave [159], pulsed photonic sintering [160, 161] to heat the inks locally.

The conductivity of the tracks is not necessarily dictated by the deposition method used, as droplet, energy, and flow-based DW process have all demonstrated conductivities within 1.2 – 3.2 times lower than bulk silver at  $6.30 \times 10^7$  S/m [102, 127, 130]. For reference throughout this review, Table 2.2 contains the conductivities for metals typically used as conductors in electronics manufacture.

*Table 2.2: Conductivities for metals typically used as conductors in electronics*

<b>Bulk Material</b>	<b>Conductivity (S/m)</b>
Silver	$6.30 \times 10^7$
Copper	$5.96 \times 10^7$
Gold	$4.10 \times 10^7$

## 2.4 Multi-Material Printing

Multi-material printing involves the use of a single printer that uses the same deposition method to build both the insulating and conductive elements of a circuit. In 2012 Leigh et al. used a commercially available FFF printer with three print heads to extrude both a dielectric PLA filament and a custom, carbon-loaded ABS filament [162]. A key benefit of their approach was the ability to embed conductive elements inside the object, rather than just on the outer surfaces.

Typically, carbon-loaded filaments exhibited conductivities several orders of magnitude lower [162, 163] than bulk copper [164] with Kwok et al. reporting a value of 200 S/m [165]. The electrical performance has been improved by increasing the carbon loading [165]; however, the resistance was still comparatively high. When used in conjunction with PLA, this limits the technology to low power devices as ohmic heating [166] will soften and melt the low  $T_g$  substrate. Kim et al. improved on previous work by electroplating copper to the carbon filament, increasing its conductivity more than two orders of magnitude. In addition, the plating had the added effect of reducing the surface roughness by 77%, reducing parasitic losses in an additively manufactured antenna [167].



Another issue with multi-material FFF is that the Young's Modulus of FFF parts is significantly reduced at the materials interfaces [168] where they fail to fuse correctly. This has led to poor adhesion between the substrate and the conductor resulting in delamination and breaks in the circuit [165]. Furthermore, the resolution of FFF processes is limited by the size of the nozzle, with Leigh et al. successfully demonstrating a relatively large 1.5 mm nozzle [162].

Vat photopolymerisation approaches can produce significantly finer features than FFF, and in 2017, Mu et al. used multi-material digital light processing (DLP) technology to produce conductive elements by dispersing Multi-Walled Carbon Nanotubes (MWCNT)s into a UV curable resin. To allow multiple polymers to be processed, the printer had separate conductive and dielectric resin vats, and the part was removed and cleaned between entering each. The parts produced had a layer thickness of just 19.05  $\mu\text{m}$  [169] and could contain complex, multi-layered circuitry. Being carbon-based, the conductivity was poor at 0.027 S/m, limiting the potential practical applications.

Also, in 2017, multi-material inkjet printing was used to produce 40  $\mu\text{m}$  features [170] with a conductivity of  $1 \times 10^7$  S/m [156]; or 5.9 times lower than bulk silver, from a combination of silver and acrylic inks. Notably, the selected ink produced conductivities twice as high by curing it at 150  $^{\circ}\text{C}$ ; however, the author demonstrated experimentally that the substrate cannot survive the elevated temperature. A similar configuration has been commercialised by Nano Dimensions Ltd. and achieved multi-layer conformal electronics. The Dragonfly LDM system used proprietary, UV curing silver and thermoset polymer inks to produce a minimum track thickness of 17  $\mu\text{m}$  at a width of 100  $\mu\text{m}$  [171]. The stated conductivity of the silver tracks was between 3 and 20 times lower than bulk copper [172], and while compatible with hand soldering, low-temperature solders were recommended [173].

The use of low  $T_g$  of polymers is prevalent in current multi-material processes [156, 162, 163, 165, 169], this has prevented the use of solder to attach components. Solder is beneficial as it forms a metallurgical bond between components and the circuit, offering enhanced mechanical strength at low

resistances [174]. Processes, that have incorporated discrete electronic components have relied on the terminals being pressed directly into the conductor with no permanent attachment. This may not be an issue; however, no work has demonstrated the reliability of this approach.

## **2.5 Hybrid-Additive Manufacture of Electronic Devices**

Hybrid-AM processes are defined as “the use of AM with one or more secondary processes or energy sources that are fully coupled and synergistically affect part quality, functionality, and/or process performance” [175]. By using different processes for building, feedstocks can be more varied in their formulation; this enables the co-deposition of a wide range of specialised materials. Typically, the AM processes have been used to form the substrate material, and the secondary processes applied or inserted the conductors.

Of the categories, only vat photopolymerisation, material extrusion and material jetting have been successfully demonstrated. Binder jetting was used in one example [176]; however, the mechanical performance of binder jetted parts [177, 178] limit its potential applications. Sheet lamination has seen no use in the direct manufacture of electronics, but because these process produce little heat when bonding materials, they have been used for embedding delicate electronic components in structures [179–182]. Directed energy deposition techniques have not been used for electronics manufacture.

### **2.5.1 Vat Photopolymerisation**

#### **2.5.1.1 Direct Writing onto Stereolithography Parts**

One of the most explored hybrid approaches for producing AM electronics is the combination of extrusion DW with stereolithography. Vat photopolymerisation (VP), is a category of processes that use liquid photo-curing polymer resins in a vat and cures them selectively using light [11]. A large proportion of research into this combination of techniques has come from the University of Texas in El-Paso and has been in development since 2005 [183]. Their method worked by printing until the point where electronics are to be deposited, and lowering the resin vat, exposing the part. This was then cleaned with isopropanol to remove residues before an air-backed syringe deposited silver ink which was cured using the VP

laser. Finally, the vat was returned, and the print continued, embedding the circuitry. Once a print was complete, the silver ink could also be patterned on the outside surfaces, allowing both conformal and embedded circuitry to be produced. By printing channels in the resin substrate to constrain the ink, the smallest track width achieved was 254  $\mu\text{m}$  [184].

The group also showed the ability to place electrical components and print over them by leaving cavities in the substrate. There were then connected to by extruding silver ink through holes in the top surface and onto the component terminals [185]. This method only allowed a single layer of embedded components as there would be no way to connect to layers deeper inside the substrate. In 2016 Wasley et al. [186, 187] improved on this and built stacked, multi-layer devices by depositing silver epoxy in an ascending spiral, to create freestanding pillars. These were formed mid-print and acted as vias, connecting to elements that would have been printed over in other approaches. Additionally, the printed tracks had almost twice the resolution at 134  $\mu\text{m}$  wide, allowing them to connect to bare die flip chip components [188]. A drawback of the conductive epoxy they used was a low conductivity, approximately 200 times lower than that of bulk silver. This was due to the limited thermal stability of VP resins, which cannot withstand the curing temperatures required to achieve higher conductivities. This could be mitigated by using localised curing methods [158, 189] which have been shown to lower the overall curing temperatures for inks written onto VP components. Ultimately however, low thermal performance of the substrate restricted VP-based electronics to prototyping applications.

## **2.5.2 Material Extrusion**

### **2.5.2.1 Direct Write onto FFF Parts**

In 2013, Optomec Inc. demonstrated AJP of a silver conductive ink combined with FFF of PEI [190] to produce a wing with integrated electronics. The device included a T-slot antenna, printed strain gauges and was capable of handling 10 W of power to drive two DC motors. Before the jetting could take place, to alter the wetting characteristics of the ink and fill any gaps, the surface was grit blasted and smoothed using an undisclosed dielectric undercoat [110, 191]. This

was required to improve the adhesion of the ink and prevent it from wicking along the hatch of the FDM parts [192]. The best resolution was 150  $\mu\text{m}$  with a conductivity of  $1.56 \times 10^5 \text{ S/m}$ . The surface finish of FFF parts meant that higher viscosity inks with less tendency to spread were likely to produce finer details. Printing of these is better suited to pump and extrusion based DW processes, which was the method used in the Voxel8 developer printer, an FFF printer that could also deposit conductive inks onto sloped and conformal surfaces [193].

### 2.5.2.2 Metal Injection into FFF Parts

Metal injection processes start by using FFF to print parts from ABS, PLA, or polyurethane, with voids left for the metal which are backfilled to create conductive paths. There were two bodies of work, and each used different low-melting point metallic alloys instead of inks as the conductive material. The first injected Galinstan, which is a conductive liquid at room temperature [194]; while the second, used a eutectic bismuth, indium, lead, tin alloy that melts at  $57.8 \text{ }^\circ\text{C}$  [195]. This required the part to be held at an elevated temperature during the injection, thus allowing it to flow successfully. This alloy needed solidify to become conductive which limited its current carrying capacity. This was demonstrated when localised ohmic heating of the alloy caused the conductor to melt, forming a break in a timer circuit. The filling stage also introduced manufacturing difficulties and required careful process control to remove air bubbles in the metal, that led to uneven filling and further breaks in the tracks [196]. This also influenced the minimum channel size, which was a square cross-section of  $0.8 \text{ mm} \times 0.8 \text{ mm}$ , dictated by the narrowest gap that could be used without the blockages due to print defects.

Both FFF-based injection methods have been interfaced with electronic components for manufacturing multilayer, active systems with actuators and sensors [194, 195, 197]. In the literature, there is little electrical characterisation; however, the conductivity of Galinstan is  $2.3 \times 10^6 \text{ S/m}$  [198] so it is reasonable to assume the performance was similar. This would produce a conductivity 25.9 times lower than bulk copper.

### 2.5.2.3 Wire Embedding into FFF Parts

Wire embedding technologies aim to produce additively manufactured electronics with the same conductivity as bulk metals. Two competing approaches have been explored, ultrasonic embedding (UE) and fibre encapsulation additive manufacturing (FEAM). UE worked by placing the conductor on top of the substrate and then using an ultrasonic horn to press the wire into the polymer. This was performed after the part was printed, producing circuits on the surface, or between layers, embedding the conductors within. The FEAM approach deposited the wire during the FFF printing by using a digitally controlled feed system to pass the wire into the extrudate, parallel to the direction of travel [199], see Figure 2.14. When the desired amount of wire had been placed, a cutter was used to sever the feed. This method could only place material within layers and therefore, could not produce, conformal circuitry.

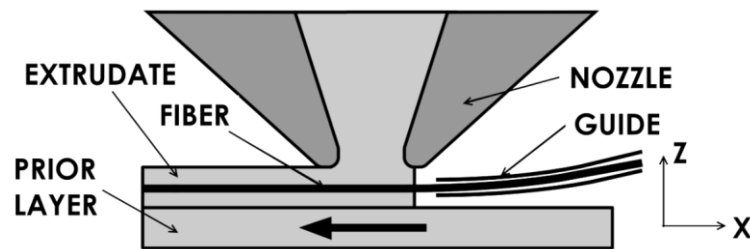


Figure 2.14: Schematic of the FEAM process. Reproduced from [199]

Both processes were shown to produce multilayer systems by adding conductive vias to electrically couple the layers. UE achieved this by inserting a U-shaped piece of copper over the intersection of two wires and relied on mechanical interference to form a connection. To work optimally the wires had to run parallel, although a displacement of 0.3 mm and angular misalignment of 40° could be tolerated. Beyond this the connection began to break-down. The advantage was that by using the same material as the conductor there was no drop in conductivity through the vertical axis [200]. FEAM used multi-material FFF to deposit a conductive polymer between wires to form the vertical interconnects. This could handle wires that crossed at all angles however, the conductivity was diminished. Because the connection is over a short distance and can be expanded to produce a large contact area, the author indicated that the increase in resistance was negligible. The reported values were 110 mΩ

between layers and 250 m $\Omega$  within the same layer, although the author predicted that 40 m $\Omega$  is possible with further optimisation [201].

The substrate material selection was less critical for these processes as elevated temperatures were not required to post-process the conductor. Both processes could manufacture parts from additively manufactured ABS, and the UE system also demonstrated polycarbonate and PEI. The resolution of a UE circuit was not dictated by polymer print quality as the embedding was executed after a layer was printed. The minimum feature size was dictated by the wire diameter used, which ranged from 50 to 320  $\mu\text{m}$  [202]. For FEAM, the smallest diameter wire used was 127  $\mu\text{m}$ , but because the wire had to be encapsulated in the extrudate, it had to follow the toolpath of the FFF nozzle with a documented resolution of 450  $\mu\text{m}$  [203]. This also meant that printing complex circuits was difficult and required advance toolpath planning algorithms; however, no such technique was discussed. This complication was supported by the nature of the components demonstrated using FEAM, which were either continuous coils [201] or simple test pieces with two wires crossing [204].

UE could also use of copper mesh feedstock and has been used to create ground planes for producing antennas [205]. UE has also demonstrated the ability to produce conformal electronics by feeding the wire coaxially through the ultrasonic horn while dynamically manipulating the substrate [206]. While copper is suited to soldering techniques, neither approach tests this, likely because of the low melting points of the polymers used.

#### **2.5.2.4 Multi3D**

Multi3D was a system developed at the University of Texas in El-Paso which hybridised several of their earlier technologies including wire embedding and syringe extrusion of silver inks. The first variant of the system took advantage of high-temperature FFF, ink extrusion, ultrasonic wire embedding and micromachining [207]. To provide suitable mechanical and thermal resistance substrates were FFF printed from PEI, which was then machined to improve the minimum feature resolution from 6 mm to just 2 mm with a 1% error. Machined channels were also used to improve the edge definition and prevent short-

circuiting of silver extrusion features; however, the most significant impact was found to be related to the raster-to-raster air gap. By printing the solid layers of the FFF part closer together, thus minimising any gaps between extrudates, the ink wicked less and did not connect to adjacent tracks. This combined with the machining produced an average minimum track width for the silver of 506  $\mu\text{m}$ . Electrical components could also be placed into cavities in the PEI and printed onto with silver ink; an approach used to produce a functioning CubeSat module [208]. The first version also used the UE wire embedding technology from earlier work, with a minimum copper wire diameter of 80  $\mu\text{m}$ . It was not until the second-generation Multi3D system that wire embedding became more utilised, as this unit also incorporated a laser welding head [209] that enabled the connection of the wires to electrical components. The reported conductivities using this technique were  $8.47 \times 10^6$  S/m for the silver and  $5.88 \times 10^7$  S/m for the copper. The second-generation system had a substantially different architecture, foregoing the all-in-one approach of its predecessor and used a robotic arm to move the build platform around various stations within a room. The reported advantage was that the system was more flexible [210] and could be easily adapted to add or remove various manufacturing tools.

### **2.5.3 Material Jetting**

#### **2.5.3.1 Conductive Ink Injection into Material Jetted Parts**

Material jetting processes have some of the best resolutions of any AM techniques, making them well suited for printing complex structures within objects. Wu et al. [211] capitalised on this to create channels in acrylic parts and backfill them with conductive silver ink. The finest reported printing resolution was 30  $\mu\text{m}$ ; however, there were limitations because of the injection process. The primary constraint was channel diameter as if it was too narrow the viscosity of the ink prevented it from spreading sufficiently through the part. This led to a minimum diameter of 400  $\mu\text{m}$ , although improved results were achieved at 600  $\mu\text{m}$ . The inks needed curing at room temperature as the dielectric does not provide enough thermal stability for high-temperature curing. As a result the conductivities were relatively low at  $1.96 \times 10^5$  S/m. The process was used to produce fully encapsulated passive devices such as induction coils, resistors, and

capacitors. These were combined to create a functional screw cap for food containers that uses capacitance and an inductive loop to measure the spoiling of the contents of the container wirelessly.

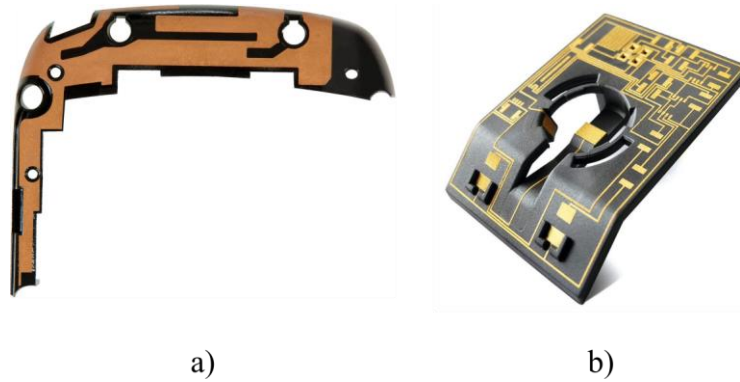
### **2.5.3.2 Direct-Writing onto Material Jetted Parts**

In 2015, Chang et al. [212] recognised that electronics produced using NP inks were incompatible with most additively manufactured dielectrics, requiring sintering temperatures outside their thermal envelope. By using AJP to deposit a silver ink onto a flexible transfer film, they were able to produce tracks with a conductivity 1.9 times lower than bulk silver. This was then pressed onto a material jetted substrate with an adhesive layer applied, transferring the sintered ink onto the part which can be printed over to fully-encapsulate the circuit. The author also shows how, because the film was flexible, that patterns can be applied to non-planar geometries by producing a circuit on an additively manufactured aortic valve. This process also demonstrated embedded devices such as the strain gauges, but its practicality for electronic systems is restricted by the poor thermal characteristics of the acrylic-based substrate.

### **2.5.4 Additive Laser Structuring**

Additive laser structuring was not strictly a hybrid AM process, however; it combined injection moulding with selective metal plating to produce 3D circuitry and has in limited applications been applied to AM parts. The advantages of 3D electronics have already been realised by industry in the form of 3D-Moulded Interconnect Devices (3D-MID), which are employed across multiple sectors including automotive, medical, and consumer electronics [213]. An important advantage is space-saving, with some mobile phones using 3D-MID's to sweep antennas around the chassis of the devices, saving space on the PCB [214]. There were multiple approaches for manufacturing 3D-MID's, several of which feature the limitations of being template driven; however, they have been produced using digitally driven, additive laser structuring. The most prevalent technique, which in 2014 accounted for 50% of the 3D-MID market, was LPKF's Laser Direct Structuring (LDS) [215].





*Figure 2.15: Examples of 3D-MID devices, a) a smartphone antenna. b) combined structural and electrical carrier [216]*

LDS was a three or four-stage process that started by using injection moulding to form the 3D substrate from a wide range of polymers including: ABS, PEI and PEEK [217]. The chosen polymer was blended with a laser-activated structuring additive; that was then ablated with a laser and forms a catalytic surface that encouraged the formation of metallised tracks in subsequent electroless plating stages. The optional final stage was to prepare the surface for component bonding by either additional plating or mechanically smoothing the conductors. The recommended track width and pitch reported by LPKF was 150  $\mu\text{m}$  at a spacing of 200  $\mu\text{m}$ , although 100  $\mu\text{m}$  was achievable with careful process optimisation [218]. The use of a laser as the patterning tool allowed freeform surfaces to be patterned; however, injection moulding is template based, meaning that once chosen, the geometry was fixed.

LPKF overcame this with a now discontinued process; Proto-Paint LDS, whereby a paint containing the structuring additive was applied to the surface of an additively manufactured component. This was then processed like its moulded counterpart. The most significant concern with this approach is durability, as the conductor adhesion was only that of the bond between the paint and the polymer [215].

Alternatively, Amend et al. used selective laser sintering AM with a powdered structuring additive blended into the polymer build material. After printing, the part was selectively irradiated with a laser to generate the surfaces that initiate electroless plating. A notable complication introduced by the SLS was that the fusing laser could expose the plating additive in areas that were not supposed to

be plated. To prevent this, printed parts required infiltration with paint to seal the additive before exposure to the ablative laser [219]. Additionally surface roughness can affect how electrical components bond to LDS parts [215] and the granular surface produced by SLS printing may introduce difficulties when trying to surface mount electronics.

## **2.6 Conclusions**

In the past two decades a multitude of methods for additively manufacturing polymer-based electronics have been explored, and are summarised in Table 2.3, with the abbreviations for the polymers names in Table 2.4. The demonstrated approaches have shown potential, introducing new design freedoms and techniques for producing 3D electronic devices. From a hardware standpoint multi-material printing was the simplest approach, which, through material jetting, has demonstrated the ability to produce complex, fine feature electronics. However, multi-material printing was fundamentally limited by the need to use similar materials for successful fabrication, compromising on both conductive and dielectric performance. These characteristics meant that it was best used in prototyping applications.

For functional devices, hybrid-AM showed the most promise, but each technique compromised on a different aspect to achieve their goal, most commonly in substrate performance. Many of the processes focused on AM techniques that used materials lacking in either thermal stability or mechanical strength. This was in part due to the traditionally cost-prohibitive nature of the AM processes required to manufacture parts from high-performance polymers. In recent years; because of patent expiration, several new systems with heated build chambers and suitable print-heads have reached the market, lowering the barrier-to-entry. Despite this, high-performance polymer AM was only used in two different processes.

With regards to conductor performance, DW and injection of silver inks have dominated the literature, readily illustrating high resolutions, complex internal and conformal structures as well as connectivity to electrical components. The drawback of metallic inks; however, was that to reach a conductivity comparable

to current PCB's; high-temperature sintering outside the thermal limits of the polymers used was required. Localised sintering approaches have been employed with varying degrees of effectiveness. Furthermore, little testing was performed on the adhesion between the substrates and printed tracks so conclusions cannot be drawn about their durability for use in real-world applications.

Wire embedding and the Multi3D processes have provided both, excellent substrate performance and conductivity by combining PEI substrates and bulk copper wire. Additionally, laser welding has been used to provide a strong bond between the circuit and electrical components, although further validation of the effectiveness of this method is required. Because wire embedding uses a continuous fibre, complex circuitry with multiple branches off a single track cannot be manufactured. This could be possible if multiple short lengths of wire were placed and electrically joined but was not discussed in the literature.

Finally, while most of the processes demonstrated some form of connection to electrical components, the majority relied on directly printing onto the bond pads. This removed the benefits of using solder joints which are highly conductive yet ductile, allowing them to absorb shocks and relative thermal expansion.

For the hybrid manufacturing process described in this thesis, chemical modification was used as the ideal method for producing the conductive tracks. This was chosen as it has previously been shown produce tracks with conductivities 1.86 times lower than bulk copper [22], with 2 kN/m of adhesion to the substrate [24] and a resolution of 5  $\mu\text{m}$  [28]. This decision also informed the choice of PEI as substrate material, which is simultaneously compatible with the chemical modification and AM fabrication while offering the requisite mechanical and thermal properties for a robust electronic circuit carrier. FFF was the only process by which PEI could be additively manufactured and therefore, the method used throughout the thesis.

The traits of the substrate and conductor coupled with patterning by a digitally translatable 405 nm laser source, meant that a process capable of creating

complex, 3D electronic devices, compatible with solder reflow technology and suitable for applications beyond prototyping could be realised. This research exploits a gap in the current state-of-the art, whereby no existing approach can cater to all these requirements in a single package.

Table 2.3: Summary of processes for producing AM Electronics, with bulk metal conductivity for comparison

	Substrate		Conductor				Notes	Refs		
	Process	AM	Materials	Process	Conformal	Materials			Best-Case Conductivity (S/m)	Finest Feature Size
Direct-Write onto pre-formed substrates	N/A	No	Alumina, Carbon, Glass fibre reinforced epoxy, PET, PI, PTFE	IJP	See Notes	Carbon, Copper, Gold, Silver	$4.95 \times 10^7$	70 $\mu\text{m}$	Due to ink spreading, conductor resolution decreases as wettability increases. Large print head typically prevents conformal patterning, but this has been achieved with continuous IJP.	[97-104, 135, 139, 140, 146-152, 155, 158]
			Alumina, Glass fibre reinforced epoxy, PET, PI, Silicon	AJP	Yes	Aluminium, Conductive Polymers, Silver	$3.16 \times 10^7$	20 $\mu\text{m}$	Due to ink spreading, conductor resolution decreases as wettability increases. Similar processing window to IJP but with greater standoff therefore regularly used for conformal patterning.	[106-118]
			PEI, PI, Silicon, Quartz	LIFT	No	Copper, Gold, Silver	$5.26 \times 10^7$	0.5 $\mu\text{m}$	Electronics successfully embedded into substrate by machining pockets with the transfer laser. Can handle higher metal loading than AJP and IJP so ink spreading is less of a concern.	[119-126, 136, 142, 144, 145]
			Alumina, Glass, PET, PI, Silicon, Silicone Rubber, Skin	Pump & Extrusion	Yes	Carbon, Silver	$2.00 \times 10^7$	0.6 $\mu\text{m}$	Relies on nozzle contact with the substrate so requires high aspect ratio nozzles for the print head to avoid the part. Contact introduces the risk of crashing the nozzle during deposition.	[127-132, 136, 138, 141, 156, 157]

<b>Multi-Material</b>	FFF	Yes	ABS, PLA	FFF	Yes	Carbon, Copper, Graphene	$2.00 \times 10^2$	1.5 mm	Typically, low conductivity however, > 100 × increase in conductivity shown by using carbon filament as an electrode for metal electroplating	[161–166]
	VP	Yes	Acrylic-based resin	VP	Yes	Carbon	$2.70 \times 10^{-2}$	19 μm	Demonstrated working, low voltage electronics but was limited by Ohmic heating due low conductivity.	[168]
	IJP	Yes	PVP, Undisclosed UV curable thermoset polymer [171]	IJP	Yes	Silver	$1.74 \times 10^7$	17 μm	Process has been commercialised. Components can be soldered to parts but requires low temperature soldering techniques.	[155, 169–172]
<b>Hybrid</b>	VP	Yes	Acrylic-based resin	DW	Yes	Silver	$1.43 \times 10^5$	134 μm	Widely researched method that has demonstrated 3D, conformal and embedded multilayer electronics. Soldering not possible due to low thermal resistance of substrates.	[182–187]
		Yes	PEI, PLA	DW	Yes	Silver	$1.56 \times 10^5$	150 μm	High wettability of inks caused wicking along the hatch lines of FFF parts. Grit blasting and surface coating needed to produce continuous tracks.	[110, 189–192]
	FFF	Yes	ABS, PLA, Polyurethane	Metal Injection	See Notes	Galinstan, Sn-Bi-In Alloy	$2.30 \times 10^6$	800 μm	Can create internal 3D electronics but must be fully encapsulated so not conformal. Air bubbles from filling can form breaks in tracks.	[193–197]
		Yes	ABS, PEI, Polycarbonate	Wire Embedding	Yes	Copper	$5.80 \times 10^7$	50 μm	Two approaches: feed wire into filament mid-print or embed after using ultrasonic energy.	[198–205]

<b>Hybrid</b>	Yes	PEI	DW + Wire Embedding (Multi3D)	Yes	Copper, Silver	Copper: $5.88 \times 10^7$ Silver: $8.47 \times 10^6$	Copper: 80 $\mu\text{m}$ Silver: 506 $\mu\text{m}$	Air-backed syringe extrusion of silver ink with ultrasonic copper wire embedding. more than two AM techniques. Used laser welding to attach electrical components to conductors.	[206–209]
	Yes	Acrylic	Conductive Ink Injection	See Notes	Silver	$1.96 \times 10^5$	400 $\mu\text{m}$	Can create internal 3D electronics but must be fully enclosed so not conformal.	[210]
	Material Jetting	Transfer film: PFA, PTFE Yes Final Substrate: Acrylic-based polymers	DW	Yes	Silver	$3.31 \times 10^7$	Not Given	Prints first onto a low-energy transfer film before pressing the pattern onto an adhesive coated substrate. Can be fully encapsulated or wrapped around conformal surfaces.	[211]
<b>Laser Structuring</b>	See Notes	Injection Moulded: ABS, COP, LCP, PA, PBT, PC, PEEK, PET, PPE, PPO  Laser Sintered: Nylon (PA-12)	Electroless Plating	Yes	Copper, nickel, gold, tin	$3.46 \times 10^7$	100 $\mu\text{m}$	Typically for injection moulded substrates. Two examples of AM substrates however, these produced limited adhesion of tracks of required additional infiltration to prevent unwanted copper deposits.	[212–214, 216–218]

<b>Bulk Metal Conductivities</b>	Silver	$6.30 \times 10^7$
	Copper	$5.96 \times 10^7$
	Gold	$4.10 \times 10^7$

Table 2.4: Polymer name abbreviations

<b>Abbreviation</b>	<b>Polymer</b>
<b>ABS</b>	Acrylonitrile Butadiene Styrene
<b>COP</b>	Cyclic Olefin Copolymer
<b>LCP</b>	Liquid-Crystal Polymer
<b>PA</b>	Polyamide
<b>PBT</b>	Polybutylene terephthalate
<b>PC</b>	Polycarbonate
<b>PEEK</b>	Polyether Ether Ketone
<b>PEI</b>	Polyetherimide
<b>PET</b>	Polyethylene Terephthalate
<b>PFA</b>	Perfluoroalkoxy Alkane
<b>PI</b>	Polyimide
<b>PPE</b>	Polyphenylene Ether
<b>PPO</b>	Polyphenylene Oxide
<b>PTFE</b>	Polytetrafluoroethylene
<b>PVP</b>	Polyvinylpyrrolidone



### **3 High-Temperature FFF Printing**

While there are commercially available systems for the FFF of PEI, they are typically expensive to purchase and have restricted user-definable print settings such as minimum layer height or nozzle size. Lower cost, more open units also exist, but they sacrifice the maximum chamber temperature which introduces the potential for warping and reduce the overall part strength. To overcome these restrictions, this chapter outlines the design and build of a novel high-temperature polymer FFF printer and compares it to a commercial system. The performance was evaluated by characterising the dimensional accuracy, mechanical strength, and resistance to warping of the parts it produced.

#### **3.1 PEI Printing Feasibility Study**

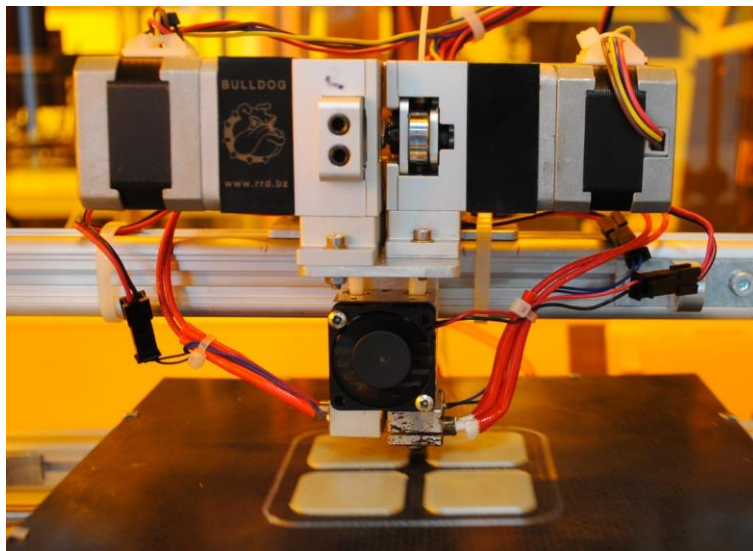
The feasibility study started with a customised 3-axis Cartesian printer based on an existing chassis (K8200, Velleman). The chassis was selected as it has an open design that allows for easy access and modification to the hardware. The frame was built from aluminium extrusion, making affixation of additional components simple. The printer's kinematics use a bed that translates in both X and Y on a pair of stacked gantries, while the print head moves in just the Z-direction. The printer was multi-material capable and had two matching direct-drive extruders (XL, Bulldog). Each used a hobbed brass drive gear attached to a stepper motor and a 3:1 reduction planetary gearbox. The hotends (V6, E3D) were all-metal, air-cooled variants with a 0.4 mm nozzle, 40 W heater cartridges, and PT100 probes for temperature control. The heated bed on the initial build was an aluminium clad PCB heater with an integrated NTC-100 thermistor and was secured to the X-Y gantries using screws in all four corners. Under the screws were bed levelling springs that exert an upward force and allow the height at each corner to be manually adjusted without the need for tools. As standard, the printer comes with a 1.5 mm thick, sanded carbon fibre print surface that is attached to the bed using clips. The electronics were based on an 8-bit microcontroller (MEGA 2560, Arduino). All axes were driven using 1.8° stepper motors with the drivers configured to produce 16 microsteps. The X and Y axes were connected using belts and 30 tooth pulleys that had a GT2 tooth

profile. The Z-axis used a leadscrew with a 2 mm pitch. This gave a theoretical resolution in X-Y of 18.75  $\mu\text{m}$  and Z of 0.625  $\mu\text{m}$ , which were calculated using Equations (3.1) and (3.2) respectively.

$$\text{Resolution} = \frac{\text{Step Angle} \times \text{Tooth Count} \times \text{Belt Pitch}}{360 \times \text{Microsteps}} \quad (3.1)$$

$$\text{Resolution} = \frac{\text{Step Angle} \times \text{Lead Screw Pitch}}{360 \times \text{Microsteps}} \quad (3.2)$$

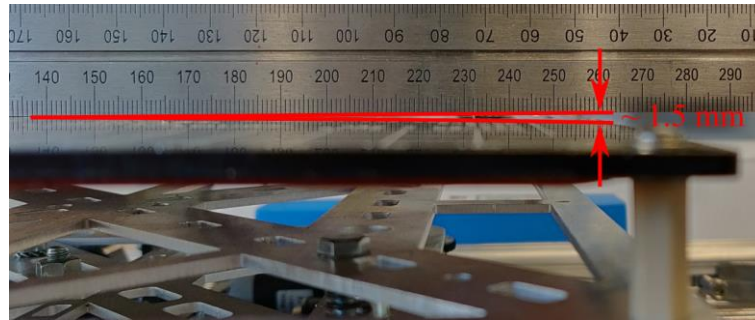
To carry any loads, all the axes ran on cylindrical guide rods and homing was performed using microswitches at the axis extremes. All the axes use linear bearings on cylindrical guide rods. The default heated bed was only capable of reaching 80  $^{\circ}\text{C}$ , which is 60  $^{\circ}\text{C}$  lower than the manufacturers recommended minimum for PEI printing [77]. This was upgraded by bonding a 500 W silicone heater mat to the underside of an aluminium plate which reaches a peak temperature of 200  $^{\circ}\text{C}$  and a continuous operating temperature of 150  $^{\circ}\text{C}$ . Figure 3.1 shows the modified FFF printer.



*Figure 3.1: Custom printer for studying high-temperature printing*

The first attempts to print PEI consisted of producing a grid of four 30 mm  $\times$  30 mm  $\times$  1 mm flat samples. These small samples allowed the quality of the first layer of prints in different areas of the bed to be quickly evaluated and-retested. The nozzle and bed temperatures were set to 365  $^{\circ}\text{C}$  and 150  $^{\circ}\text{C}$  respectively and the prints adhered well to the sanded carbon fibre surface. Additionally, at 1 mm

thick there were no signs of warping or shrinkage once parts were removed from the bed and cooled down. What was observed however, was uneven part thickness, with a tendency to print thinner away from the centre of the bed. Upon visual inspection, the aluminium bed would buckle due to thermal expansion (see Figure 3.2).



*Figure 3.2: Visual inspection of buckling on the aluminium bed*

The buckle produced approximately 1.5 mm of vertical deviation at the edges of the bed, increasing the nozzle clearance and layer thickness. The rigid mounts at the corners of the bed prevent lateral expansion and force the plate to bow upwards. This was resolved by changing to slotted mounts that do not restrict the expansion and replacing the carbon fibre with a sheet of 3 mm thick borosilicate glass. The cast glass expands evenly and therefore should not warp during heating. As the glass is smooth, the PEI manufacturer advised adding a layer of PI tape and polyvinylpyrrolidone (PVP) adhesive [77] to improve print adhesion. The final configuration had minimal warp and had a 150 mm square printable area.

With the printer successfully producing parts, it was necessary to determine if they could handle the temperatures involved with a solder reflow process. It was predicted that due to the lack of a heated build environment, the parts would contain residual internal stresses and warp as they approached their  $T_g$ . The initial hypothesis was that if parts were kept sufficiently thin, the heat from the bed would warm the ambient air and reduce stress build up. To test this, samples were printed both on the modified printer and outsourced to an external print house. The equipment at the print house (Fortus 450mc, Stratasys) has a heated build volume and is designed specifically for printing high-temperature

thermoplastics. As a result, this offers the best possible baseline for the test. The samples were placed in a digitally controlled oven (LHT6030, Carbolite) and gradually heated to their  $T_g$  (186 °C), at which point they were removed and cooled to ambient conditions. Two of the coupons can be seen in Figure 3.3



*Figure 3.3: Comparison of flat PEI samples produced a) in ambient air and b) a heated build volume after being heated to their  $T_g$*

Parts from the customised printer shrank by 20% in both the X and Y directions and warped beyond practical use. This demonstrates that over distances as small as 1 mm, parts printed from PEI based materials are susceptible to higher levels of internal stress build-up when printed in ambient air. There are also indications of deformation on the outsourced part, with a total shrinkage of less than 2% in any direction. Despite the minimal change in size from the outsourced components, this could result in solder joint failure. To prevent the occurrence of this issue the resulting printer must be designed around printing a grade of PEI with a higher  $T_g$  (Thermax ULTEM 1010, 3DXTech).

To further quantify what was observed, a thermocouple was mounted to the z-axis above the bed and used to measure the air temperature. By moving the axis upwards and recording the average reading over 20 seconds, a temperature profile at different heights was gathered. The test was repeated five times and the average was used to generate Figure 3.4.

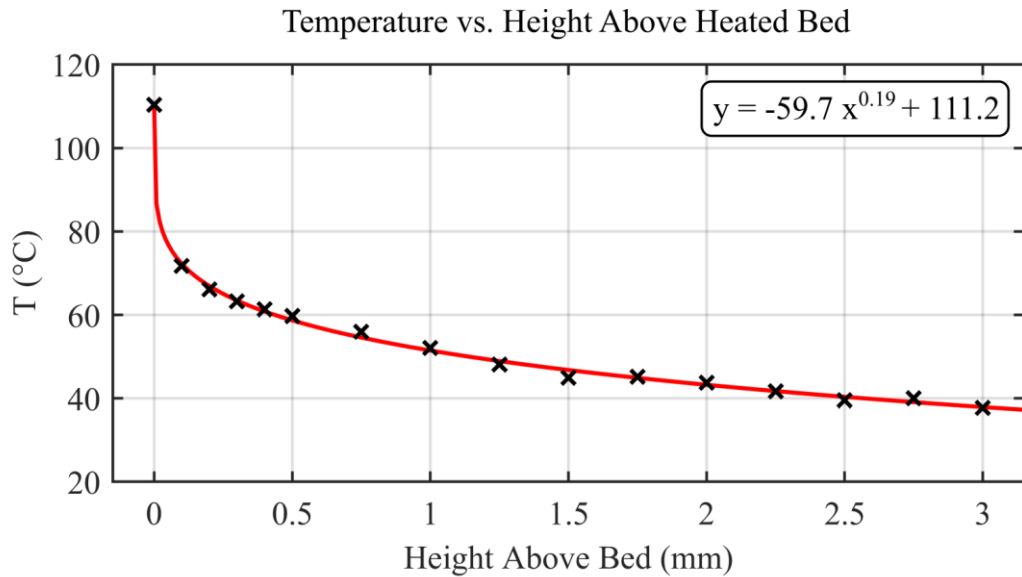


Figure 3.4: Air temperature above a print bed heated to 150 °C with respect to height above the bed (adjusted for ambient conditions)

The plot illustrates the severity of the thermal gradient, with a temperature drop of 40 °C in the first 100 µm, increasing to almost 60 °C at the full height of a 1 mm part. Additionally, the surface temperature of the bed is 40 °C cooler than the systems readout. This is because the temperature probe for the bed control is on the underside of the assembly, which acts as a heat sink and reduces the temperature at the print surface.

Another issue that was encountered with the custom printer was material feed jams in the air-cooled side of the hotend during material retractions. This occurred because the heatsink for the cold side draws warm air from the bed across its fins lowering its total cooling capacity. This allows a longer length of feedstock to be molten which during retractions is drawn up into the heatsink, solidifying and forming a solid plug. This causes print failures and as such an alternative cooling solution needs to be evaluated.

### 3.2 Design and Build

Table 3.1 shows the design requirements and drivers for a custom FFF printer capable of building parts from PEI filament (Thermax ULTEM 1010, 3DXTech). Temperature requirements were derived from industrial units with high-temperature, fully enclosed build environments, whereas positional accuracy relates to a benchmark printer (Funmat HT, Intamsys); described in Section 3.4. Other requirements stem from improvements this design looks to address.

Table 3.1: High-temperature printing system design requirements

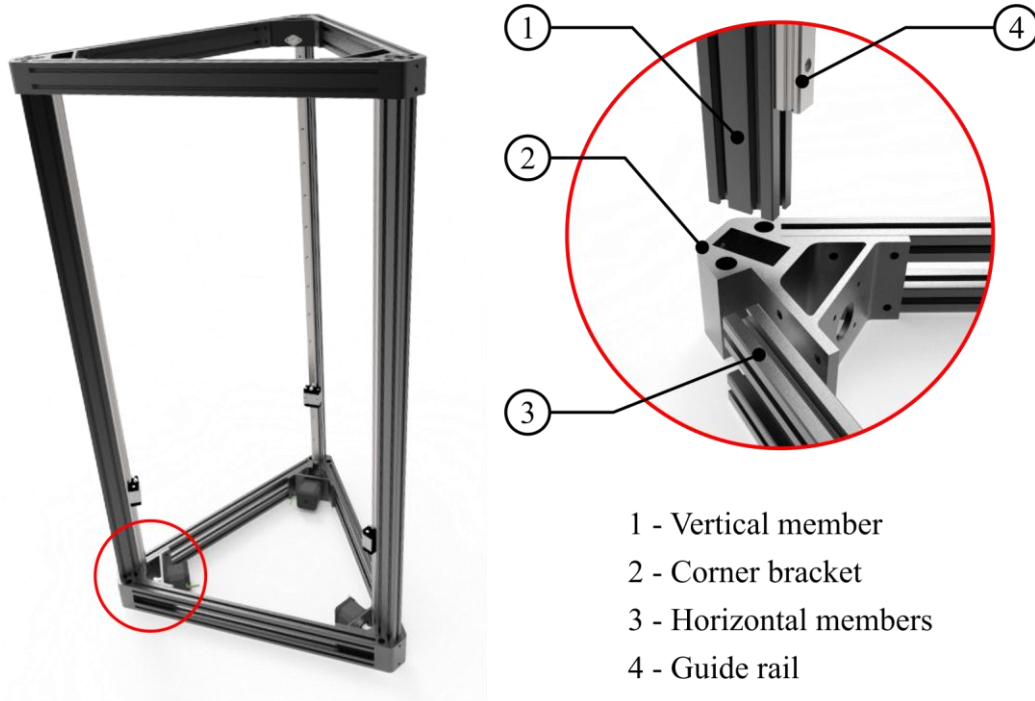
Feature	Requirement	Design Driver
Print Bed	Maintain a maximum temperature of 200 °C	Comparable to temperatures found in industrial systems
	200 mm diameter	Accommodates standard ASTM tensile test coupon (165 mm long)
	Remain flat during heating	For adhesion across the entire print-bed as found in the feasibility study
	Removable	Ease of use: Preparing bed and removing parts
Print Head	Maintain a maximum temperature of 400 °C	Maximum print temperature of the PEI filament
	Liquid cooled hotend	To prevent jamming during retractions as found in the feasibility study
	Nozzle diameter of 0.4 mm	Matches default PEI nozzle on benchmark printer
	Changeable nozzles	Improved maintainability and variable nozzle size
Build Volume	Capable of maintaining a maximum temperature of 200 °C at its centre	Comparable to temperatures found in industrial systems
Motion Platform	Positional accuracy of 12.5 µm or better in all three axes	Comparable or better than the benchmark system
	Must be isolated from the print temperatures	To protect electronics and bearings
Calibration	Automated and performed at build temperature	Safety and repeatability
Software	Open-sourced slicer	Enables modification of all base print parameters

To print PEI reliably, a heated build chamber is essential; however, this adds complexity and cost to the printer if the mechanics are to be fully enclosed. This work exploits the lower density of air that has been heated relative to its surroundings. By designing a chamber that is open on its underside, the heated air will be trapped in the build environment while allowing easy access to the print head. A machine with delta kinematics is well suited to such an application as the sensitive components reside at one end of the machine while the print-head is relatively compact and can reach into tighter spaces. The main alteration, when compared with a typical delta robot, is that the printing will have to occur inverted as the print bed will have to reside in the top of the printer to trap the heat. This leads to concerns with the effects of gravity on FFF printed parts, although previous studies have shown that this technology functions desirably in zero- and micro-gravity situations [220–222]. As the design will be an inverted delta configuration, from this point forward, the printer will be referred to as the high-temperature inverted delta (HTID).

### **3.2.1 Motion Platform**

For this printer, the main requirement of the motion platform is to keep the sensitive components isolated from the high-temperature environment. As discussed earlier, this is challenging for conventional Cartesian machines because of the proximity of linear motion components to the print head. For delta configurations, however, the print head is suspended by three pairs of arms and moves in all three axes, meaning the bed can remain stationary, removing the need for bearings and motors inside the build volume.

The frame of the HTID was based on an existing design (D300VS, UltiBots), which uses aluminium extrusion as the main structural members and pre-formed aluminium brackets for the corners. The geometry of the brackets ensured the alignment of the vertical towers which can have an impact the accuracy of delta machines. Aluminium extrusion is also widely available and contains t-nut slots, simplifying modifications such as attaching additional hardware for the chamber or routing heater cables. Details of the corner brackets can be seen in Figure 3.5.



*Figure 3.5: HTID frame design details*

To ensure smooth and accurate linear motion, linear guides (SVRJ24L-940, MISUMI) which span the full vertical height of the machine were used. While this is unnecessary for printing as they are longer than the range of motion (ROM), it allowed them to be used to set the height of the top frame relative to the bottom, ensuring parallelism. The sliders on the vertical towers were connected to motors that sit in the base of the printer using belts and pulleys. 6mm wide, Kevlar-reinforced belts with a GT2 tooth profile were used to remove backlash and improve repeatability. The loop of belt was passed around a 20-tooth drive pulley and a matching, toothed idler to reduce wear and the open ends terminated at a machined bracket mounted to the linear rail carriages.

The frame had an equilateral triangular base with sides measuring 590 mm in length, and a vertical height of 990 mm. This allowed a 200 mm circular build area to be traced by the effector while keeping its extremities within the inner dimensions of the extrusion. This left enough room for up to 20 mm of insulation on each side of the chamber while keeping its outer walls flush with the motion platform. The whole platform was bolted to a 10 mm aluminium plate to add mass to the base, reducing the likelihood of it toppling over.



The arms of the HTID were manufactured from unidirectional carbon fibre for stiffness and low mass. This was to reduce vibrations from directional changes which can leave ringing artefacts on FFF prints. The epoxy matrix of the carbon fibre was rated to 350 °C, meaning that it could withstand the desired chamber temperatures. To allow the arms to pivot stainless steel, universal joints were attached to each end of the arms with high-temperature epoxy. To ensure the length of all six arms was equal, they were held in a jig while the epoxy cured. Their length was set at 382 mm giving a 75° inclination of the arms when the effector is central. A steeper inclination reduces head stability but improves the reach that can be achieved with the chamber fitted. The brackets for the sliders and the end effector were milled from aluminium and designed to be self-aligning. The arms attached to these with M8 countersunk bolts and vibration resistant thread-locking fluid (242, Loctite) to prevent loosening due during operation.

### **3.2.2 Print-Head**

For printing PEI, the print head needed to reach a minimum temperature of 350 °C although preferably as high as 400 °C. To prevent jamming, the filament prior to the liquefier had to be kept cool to increase its rigidity. This was achieved by using a fully metal, water-cooled hotend system (Chimera Aqua, E3D) with an externally located radiator. To match the benchmark printer (Funmat HT, Intamsys) a 0.4 mm nozzle was selected. Two tapped holes drilled in the side of the print-head allowed a calibration probe to be mounted coaxially to the nozzle, the details of which are discussed in Section 3.2.5. The final print-head design can be seen in Figure 3.6.

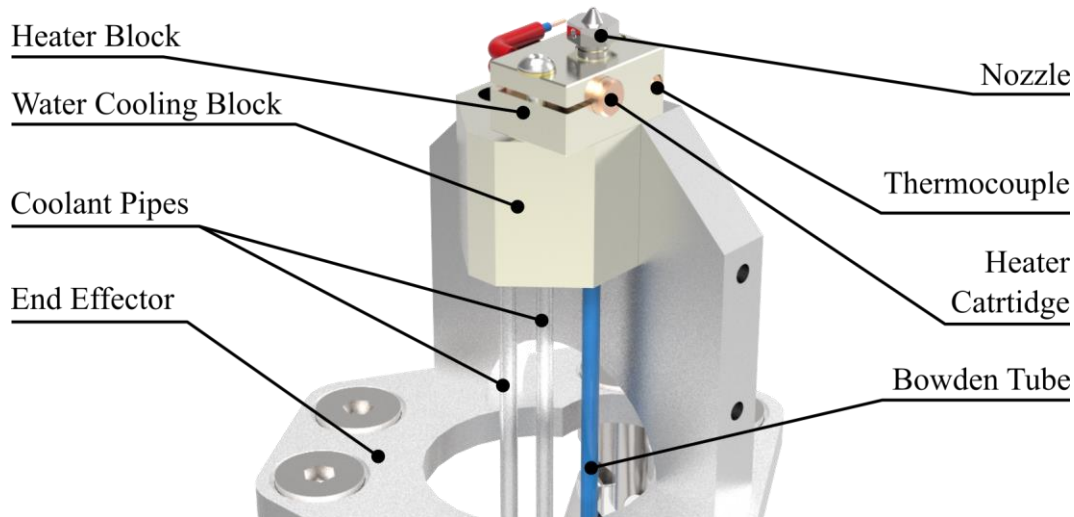


Figure 3.6: Details of the print-head design

To feed the filament, a stepper motor driven extruder (Titan, E3D) was mounted outside the chamber and connected to the hotend by a 500 mm Bowden tube. This configuration was chosen to keep the extruder motor sufficiently cool and has the additional benefit of a lowered print-head mass. A lower mass reduces the force required to accelerate and decelerate, enabling more rapid motions without the stepper motors losing their position.

### 3.2.3 Build Environment

#### 3.2.3.1 Insulation Layout

To provide the external structure of the chamber, 350 mm tall, 3 mm thick aluminium panels were fixed between the vertical towers, with a ceiling panel mounted flush with upper frame. One of the walls has a 200 mm × 250 mm cut-out for the aluminium door, which houses a 150 mm × 180 mm borosilicate glass viewing window. Heat will be lost from the chamber via conduction, convection, and radiation, which can be reduced by insulating the walls with reflective thermal insulators. For safety, the insulation must be able to withstand the design build temperature, with enough overhead to protect it in the event of a heater malfunction. A flame-retardant, 8 mm thick silicone sponge insulation (Silicone Sponge Sheet, TYM Seals & Gaskets) rated up to 300 °C was used to line the inside of the aluminium walls. An air gap of 6 mm was left between the foam and the walls to further insulate the chamber. Finally, a layer of aluminium foil was laid over the foam to reflect radiative heat back into the chamber. The

same layering was used on the door, with an opening for the window. The ceiling of the chamber has a 40 mm cavity above it which meant an additional sheet of foam and an increased air gap could be used. These were sealed with an additional aluminium plate.

The print bed was built from a 3 mm thick, 260 mm diameter aluminium heat spreader with the heater directly bonded to it. The bed mounts to the ceiling plate of the chamber with three standoffs located to give enough clearance for a 200 mm build area at its centre. To allow the bed to expand and contract without warping, the mounting holes were radially slotted and spring washers were used. A borosilicate glass print surface aided in maintaining bed flatness during prints. The arrangement used for the chamber and bed can be seen in Figure 3.7.

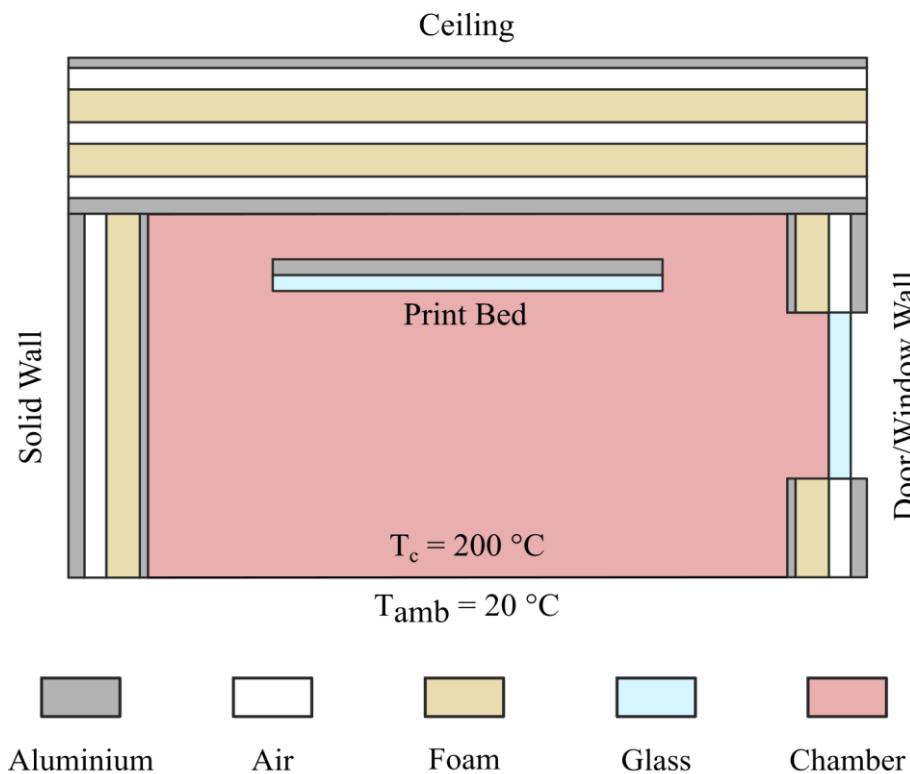


Figure 3.7: Schematic of chamber material stack-up and locations

### 3.2.3.2 Heater Requirements

To provide heating, the chamber made use of a finned strip heater and the bed used a wire-wound silicone mat. These were chosen for their form factor and maximum temperature ratings; fitting comfortably into the structure of the HTID while being able to withstand the required temperatures. To select suitable heating equipment, the power required to heat the build volume and

the print bed from ambient temperatures (20 °C) were first calculated using Equation (3.3) [223]:

$$P = \rho C_p V \frac{\Delta T}{t} \quad (3.3)$$

Where:

- $P$  is the required power in W
- $\rho$  is the density of the material being heated in kg/m<sup>3</sup>
- $C_p$  is the specific heat capacity of the material being heated in J/kg.K
- $V$  is the volume being heated in m<sup>3</sup>
- $\Delta T$  is the desired temperature change in K
- $t$  is the desired heat up time in s

To provide values for a worst-case scenario, the bed and heater were treated separately, removing combined heating effects. For the chamber, the internal air volume well as the immediate internal surfaces were included in the power calculation. For the bed, the glass build surface and aluminium heat spreader were used. This showed the chamber and bed power requirements to be 220.3 W and 105.9 W, respectively. The dimensions and thermal properties used can be found in Appendix A.

These calculations do not include the losses that are experienced in real-world applications. To provide a more realistic set of power requirement the heat flux due to conduction, convection and radiation were also be accounted for using Equations (3.4) to (3.6) [223]:

$$Q_{Conduction} = -kA \frac{T_2 - T_1}{t} \quad (3.4)$$

$$Q_{Convection} = hA(T_2 - T_1) \quad (3.5)$$

$$Q_{Radiation} = \varepsilon\sigma A(T_2^4 - T_1^4) \quad (3.6)$$

Where:

- $Q$  is the heat flux in W
- $k$  is the thermal conductivity in W/m.K
- $A$  is the surface area for heat loss in  $m^2$
- $T_x$  is the temperature in K
- $h$  is the convective heat transfer coefficient in W/m<sup>2</sup>.K
- $\varepsilon$  is the emissivity of the surface
- $\sigma$  is the Stefan-Boltzmann constant ( $5.67 \times 10^{-8}$  W/m<sup>2</sup>.K<sup>4</sup>)

The values for the conductive heat transfer coefficients involve further calculations that have been omitted for brevity, however the relevant equations and calculations can be found in Appendix B. The overall heat losses were calculated using the details specified previously and predicted a total heat loss of 352.8 W from the chamber and 196.4 W from the bed.

Adding the ideal power requirements and estimated losses indicated that the chamber and the bed heaters needed to output at least 573.2 W and 302.3 W respectively to maintain the target temperatures. The heaters selected for the printer were a 750 W finned strip heater (FSH-121-240V, Omega) and a 375 W silicone heater mat (200 mm Circular Wire-Wound, Holroyd Components). These leave approximately 25% overhead on each, allowing them to operate with a margin of safety. To prevent the chamber heater from heating stagnant air and overheating, a fan coupled to a manifold was added that circulates air across the heater's fins. Because the fan contains a motor that cannot withstand the temperatures produced by the heater, it was situated outside of the build environment and attached to the manifold using a silicone pipe.

### **3.2.4 Printer Control Systems**

The schematic in Figure 3.8 shows the control system that was developed to control the various systems in the HTID.

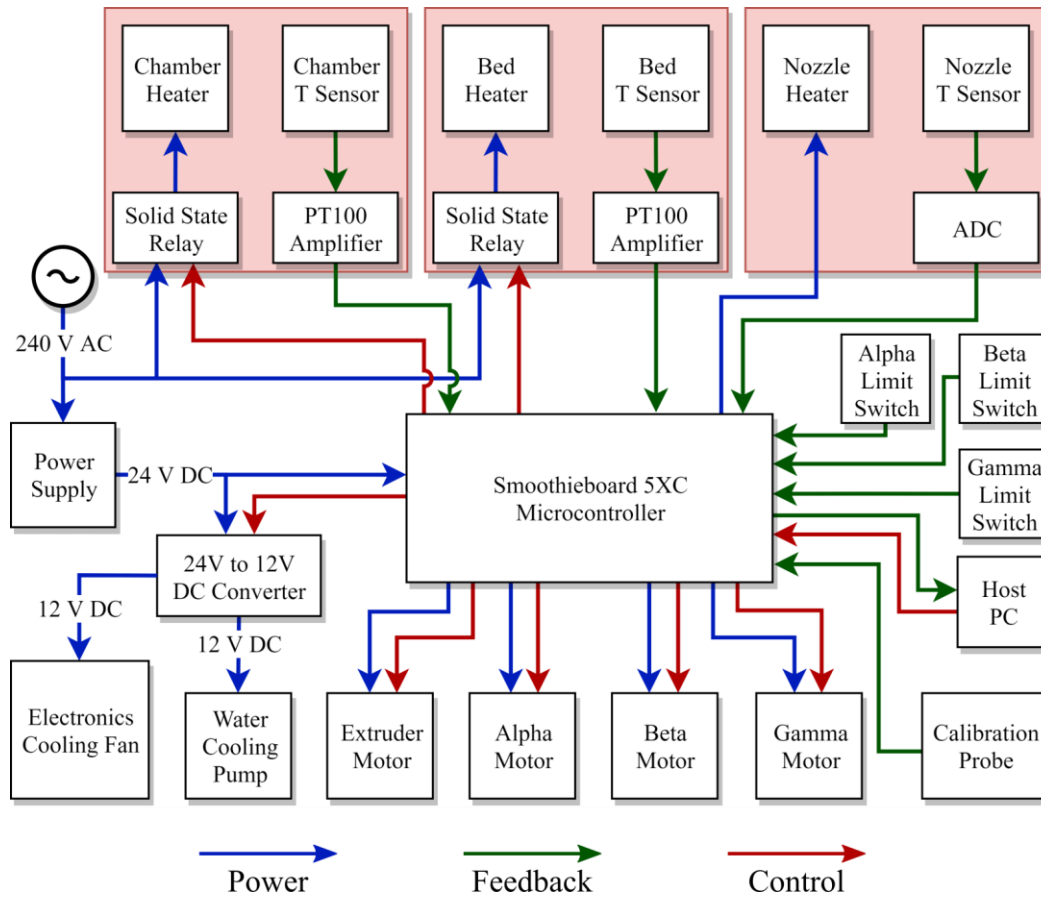


Figure 3.8: Schematic detailing the HTID's control architecture

To manage the motion platform, heaters and parse G-Code sent to the printer, a suitable control board is required. The chosen control board (Smoothieboard 5XC) is a 32-bit model, with open-source firmware heavily adapted for controlling delta robots. Communication with the board was performed from a host PC using a USB connection. The control board uses five pre-installed stepper-motor drivers, capable of producing 32 microsteps from each stepper motor. These in conjunction with  $0.9^\circ$  step angle stepper motors and 20 tooth GT2 pulleys mean that the sliders of the HTID have a theoretical positional resolution of  $3.125 \mu\text{m}$ . This can be calculated using Equation (3.1).

The 40 W heater used in the print-head draws approximately 1.7 A so was powered directly from an on-board MOSFET. Both the chamber and bed heaters were supplied with 240 V AC power, which the controller cannot natively handle. Instead, each was wired to a solid-state relay (SSR) with the switching signal connected to the controller and powered via a 240 V AC bus.

The control board provides individual proportional, integral, and derivative (PID) temperature management for each heater. PT100 probes are well suited for measuring the system temperatures, as they have a fast response time and are accurate within the operating range of all three heaters. To read the PT100's, the signal needed amplification; however, the controller only supports two external amplifiers. This was mitigated by using a K-Type thermocouple in the print-head with an analogue-to-digital converter (ADC) to produce a signal for the PID loop. To provide rapid heating without overshoot the control board auto tuned the PID gains for each heater at their ideal operating temperature. For the bed this was 150 °C, the print head 380 °C and chamber 270 °C. While the chamber can be used at a range of temperatures, 270 °C was the safe upper limit, therefore the PID gains were tuned for this setting.

The power for motors, pumps, electronics cooling fan and logic circuitry were provided by a 24 V, 400 W power supply. A switching DC to DC converter was used to step the 24 V down to 12 V for the coolant pump. This also allows the pump to be disabled while pre-heating the print-head to improve warm-up times. The maximum possible power draw from the AC supply is 1.5 kW which equates to 6.25 A at 240 V AC therefore, the entire system could be run from a single wall plug with a 13 A fuse.

### **3.2.5 Calibration**

To ensure that the nozzle to print bed clearance remains consistent, the bed must be flat and parallel to the X-Y plane of the motion platform. In low-cost printers, the flatness is often achieved by clipping a sheet of cast borosilicate glass to the build platform which expands uniformly without warping when heated. For tuning parallelism, they use screws at three points to adjust overall height and inclination. This process is performed by positioning the nozzle over a screw and sliding a feeler gauge between it and the bed. The screw is then adjusted until a light drag from the nozzle can be felt on the gauge. This is repeated until the feel is the same at each screw.

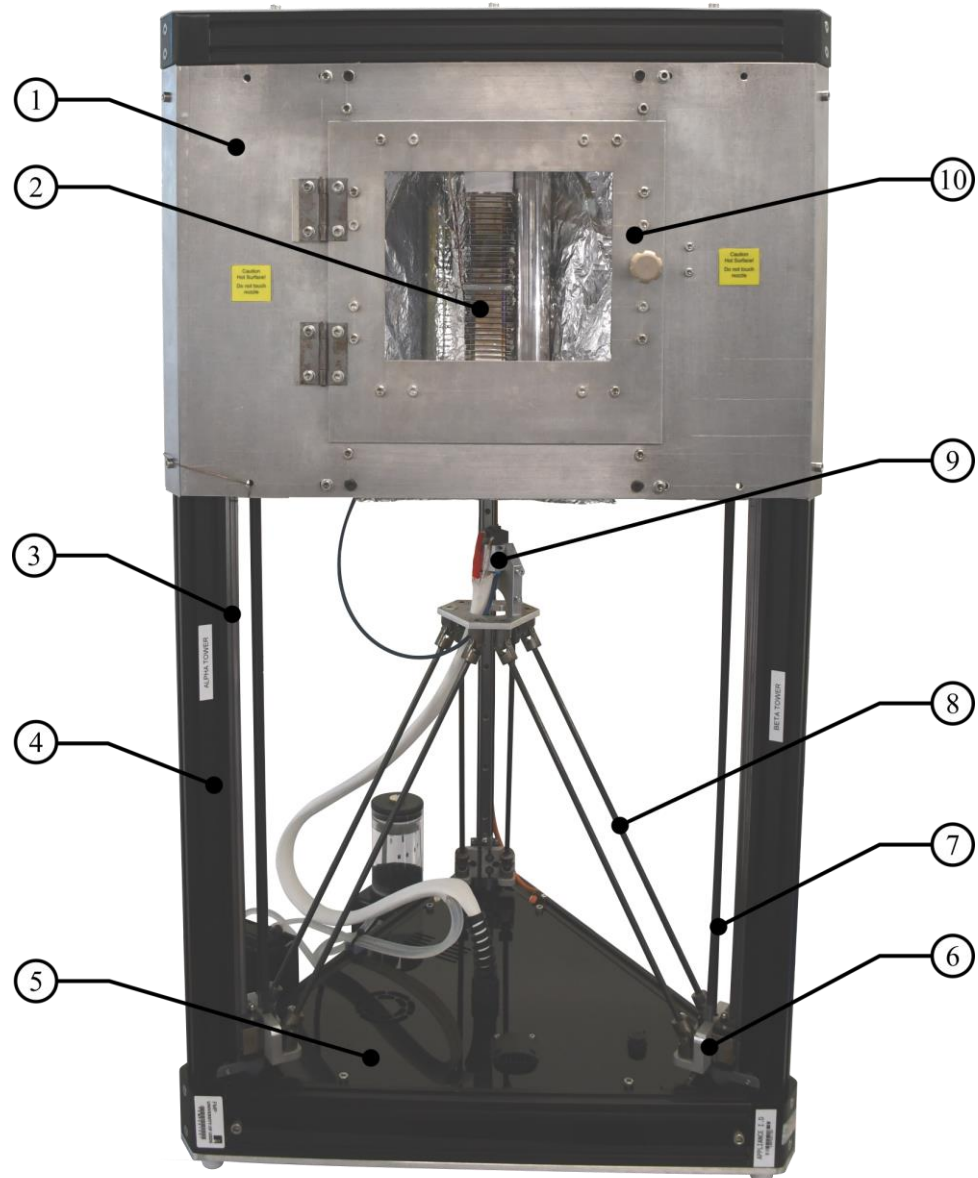
While effective on lower temperature printers, the HTID needed to be calibrated at its operating temperatures to reduce inaccuracies due to thermal expansion.

The solution was to use a touch probe mounted above the nozzle, that automatically measures the Z-axis offset between the nozzle and the bed. The probe consisted of a microswitch (TZ-1G, Omron) on an aluminium bracket that when bolted to the print-head, aligned the switch coaxially to the nozzle. When not in use, the probe was removed and disconnected from the system.

The control board also used the probe to automatically correct for inaccuracies in the printer's assembly. The first routine trimmed the end-stop locations by homing all three sliders and probing a point above each limit switch. This was used to calculate the Z-axis offset of each switch and apply a correction factor for each in the firmware. This was then repeated until the difference between successive readings was less 30  $\mu\text{m}$ . With the end-stops trimmed, the second routine calibrated the arm radius variable in the kinematic model. This parameter dictates how flat the nozzle tracks, with an incorrect value resulting in the nozzle moving in the Z-direction during X-Y only moves. While calibrating the HTID would probe the centre of the bed as well as three points on a circle and measure their height relative to each other. I would then predict the correct arm radius and re-probe, repeating this process until the points were within 15  $\mu\text{m}$  of each other.

Before printing the HTID also performed a 25-point grid calibration, measuring the height of the bed at 25 points to generate a surface map of distortions in the print surface. Based on the readings the HTID automatically applied vertical translations to X-Y moves, keeping the nozzle clearance consistent. The completed build of the HTID is shown in Figure 3.9.





- |                         |                     |
|-------------------------|---------------------|
| 1 - Chamber             | 6 - Slider (×3)     |
| 2 - Chamber Door/Window | 7 - Belt (×3)       |
| 3 - Guide Rail (×3)     | 8 - Arms (×3 Pairs) |
| 4 - Towers (×3)         | 9 - Print Head      |
| 5 - Electronics Bay     | 10 - Chamber Heater |

Figure 3.9: The completed build of the HTID

### 3.3 Chamber Characterisation

The heating equipment was characterised via two key parameters: how long the chamber took to reach a stable temperature, and what heater output was needed to reach the desired temperature.

The HTID cannot measure the chambers air temperature directly, but instead controls the temperature of the finned strip heater. To measure the actual temperature of the chamber, a K-Type thermocouple connected to a data logger

was mounted in place of the nozzle, and the print-head was moved to the centre of the designed build volume. To mimic printing conditions, the bed temperature was set to 150 °C at the same time as the chamber was turned on and the printer was left to stabilise for one hour. This was performed at five different temperature settings in 25 °C increments down from the safe upper limit of 270 °C. The results of this test are shown in Figure 3.10.

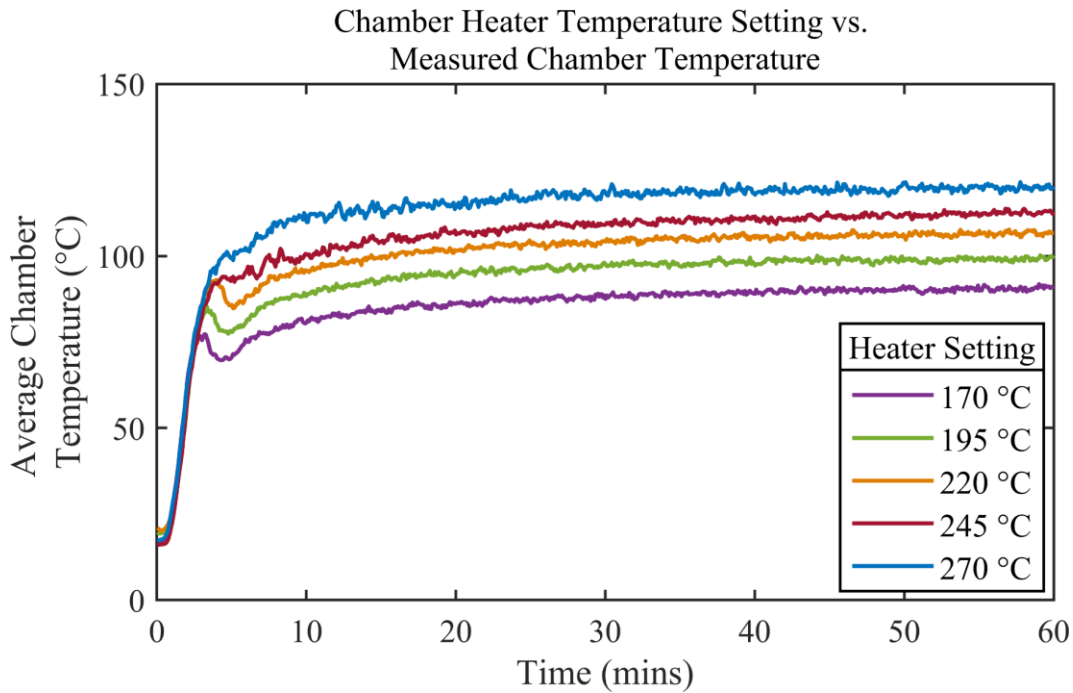


Figure 3.10: Chamber temperature response to different heater set points over 60 minutes

What this shows is that the initial warm-up, before the PID control starts to restrict the heater to limit overshoot, occurs in under five minutes regardless of temperature setting. For the lower temperatures, the chamber reaches 98% of its stable value in this time but then dips as the heater cuts off. This is not seen in two higher temperature plots as they are closer to the tuned value of the PID loop. For each test, the temperature continues to rise gradually for approximately 30 minutes at which point they plateau. After this point the readings were assumed to be stable and averaged to produce Table 3.2.

Table 3.2: Heater temperature setting and corresponding chamber temperatures


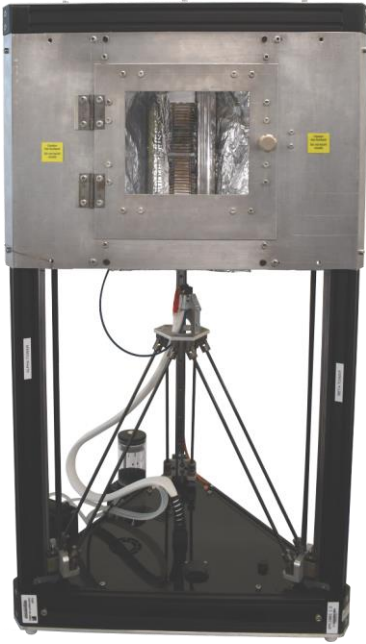
<b>Heater Temperature Setting</b>	<b>Average Chamber Temperature</b>
170 °C	90.3 ± 1.5 °C
195 °C	98.9 ± 1.7 °C
220 °C	106.6 ± 1.9 °C
245 °C	112.2 ± 1.6 °C
270 °C	119.7 ± 2.8 °C

What the data shows is that the current configuration can reach higher temperatures than typical desktop-grade high-temperature FFF printers, regardless of the open nature of its design. There is an inefficiency in the HTID's chamber design preventing it from reaching 200 °C as intended. This is likely due to the fan drawing cooler ambient air into the chamber, producing additional heat losses that were not accounted for in the calculations. The result is a reduction in designed operating temperature of 80 °C and an additional 10 minutes to warm up and stabilise. Additionally, the temperature gradient between the bed and the chamber air will be significantly reduced compared to the tests in the initial study. Throughout the chamber characterisation, there were no signs of electronics overheating such as skipped steps from the motors or unexpected shutdowns. A handheld thermocouple was used to periodically probe the bed and electronics bays and the recorded temperature never exceeded 60 °C.

### 3.4 Printed Part Performance Testing

To evaluate the performance of PEI parts printed on the HTID, a series of tests were carried out against a benchmark printer (Funmat HT, Intamsys). The benchmark is a consumer grade, desktop printer capable of using the same grade of PEI required by the chemical modification process. It has a cartesian configuration with a direct drive extruder attached to an X-Y gantry, while the print bed translates in the Z-axis using a leadscrew. These all operate inside an enclosed, heated build environment which limits the maximum chamber temperature to 90 °C. A side-by-side comparison of the HTID and the benchmark can be seen in Table 3.3.

Table 3.3: Side-by-side comparison of the HTID and benchmark FFF printers

	Intamsys Funmat HT	High-Temperature Inverted Delta
Image of printers (approximately to scale)		
<b>Configuration</b>	Cartesian	Delta
<b>Printer Size</b>	540 mm × 500 mm × 650 mm	590 mm × 530 mm × 990 mm
<b>Build Volume</b>	260 mm × 260 mm × 260 mm	Ø 200 mm × 350 mm
<b>Min Layer Height</b>	50 µm	50 µm ‡
<b>T<sub>Chamber</sub> Max</b>	90 °C	120 °C
<b>T<sub>Bed</sub> Max</b>	150 °C †	200 °C
<b>T<sub>Nozzle</sub> Max</b>	450 °C	500 °C
<b>Positional Accuracy</b>	X/Y: 12.5 µm Z: 1.25 µm	X/Y: 3.13 µm Z: 3.13 µm
<b>Max Print Speed</b>	300 mm/s	Not Tested
<b>Print Bed Material</b>	3 mm Borosilicate Glass	3 mm Borosilicate Glass
<b>Extruder Type</b>	Direct Drive	Bowden Tube
<b>Nozzle Diameters</b>	0.4, 0.6, 0.8 mm	0.25, 0.3, 0.4, 0.6, 0.8 mm
<b>Calibration</b>	Manual: bed inclination	Automatic: end-stop trim, arm radius, nozzle clearance, bed inclination, bed flatness
<b>Slicer</b>	INTAMSUIT	Any open source slicer

† The datasheet states 160 °C however, the printer could not successfully pre-heat to this temperature

‡ This is the smallest value tested, the true minimum could be different

To ensure the benchmark printer operated as the manufacturer intended, all G-Code files were created using the slicer it was packaged with (INTAMSUIT 3.4.0, Intamsys). Additionally, the slicer is based on an open sourced slicing engine (CuraEngine, Ultimaker) and produces G-Code compatible with the HTID. This allows both machines to share the same files, removing potential part variation from differences introduced by the slicer. Because the printers have different bed shapes and origin locations, after the G-Code files were generated a translation was applied to all the X-Y coordinates using a MATLAB script. By performing this operation after the file was generated, the toolpaths and print parameters remained unchanged, but the print became centred on the bed. As the benchmark printer was designed to print PEI, the slicer contains default settings optimised this application. These were used to produce all G-Code files and are detailed in Table 3.4. The chamber temperature and bed adhesion aids were altered on a test-by-test and per-printer basis. These settings are detailed in each test description.

*Table 3.4: Print parameters for both printers*

<b>Print Parameter</b>	<b>Value</b>
Nozzle diameter	0.4 mm
Layer height	0.15 mm
First layer height	0.3 mm
Top and bottom thickness	1.2 mm
Wall thickness	0.8 mm
Hatch pattern	Grid
Hatch angle	$\pm 45^\circ$
Infill density	20%
Infill pattern	Grid
Infill angle	$\pm 45^\circ$
Print speed	50 mm/s
Travel speed	120 mm/s
Nozzle temperature	380 °C
Bed temperature	150 °C
Chamber Temperature	See Individual Test Specifications
Bed Adhesion Aids	See Individual Test Specifications
Bed preparation	PI tape and PVP adhesive

The PEI filament (Thermax ULTEM 1010, 3DXTech) had a 1.75 mm diameter and came pre-loaded onto 500 g spools. Following the material handling procedures found in the literature [91, 93, 224], the PEI was stored in a vacuum desiccator when not in use and a dry box filled with desiccant during printing. If material ooze from the nozzle was found to be greater than 10 mm/min, the filament was dried in an oven at 161 °C for 1 hour [91] to reduce the moisture content. For both printers, the bed was prepared by affixing a layer of 100 mm wide PI tape the borosilicate glass and applying a thin layer of PVP glue on top. Before printing, the nozzle clearance of both printers was calibrated as per their specification.

The tests performed covered three key areas:

- Dimensional accuracy
- Tensile strength
- Warping

Dimensional accuracy and tensile tests were performed on parts from both printers as a baseline for the printing performance of the HTID compared to another printer. The effectiveness of the HTID's heated chamber was subsequently validated through further tensile and warp testing at different chamber temperatures.

### **3.4.1 Dimensional Accuracy**

When measuring the dimensional accuracy of a machine, Moylan et al. [225] suggest there are two main approaches: directly taking measurements from the moving parts or indirectly measuring parts produced by them. The direct approach has the benefit of getting accurate results with little influence from external factors; however, taking readings can be complicated as the measurement devices may impinge on the machine or interfere with safety features such as enclosures or interlocks [225].

Indirect methods use dimensional accuracy samples, designed with features that test aspects of a machine's performance. For 3D printers, these will typically consist of a flat base with a variety of shapes and sizes of features such as slots, holes, bosses and overhangs printed onto it [226, 227]. When designing a

sample, it is important to consider the aspects being evaluated as these dictate which features to use and the complexity of the sample [228]. Square sided features are useful for testing X-Y deviation from the CAD dimensions, whereas round features allow cross-axis performance to be validated by measuring their circularity. The sample used for testing both printers consisted of a 45 mm × 45 mm × 6 mm base with series of through-holes and 8 mm tall square and round bosses. The layout and dimensions of which can be seen in Table 3.5 and Figure 3.11.

Table 3.5: Dimensional accuracy test sample dimensions

Feature Type	ID	Size
Square Boss	SB4	4 mm × 4 mm
	SB6	6 mm × 6 mm
	SB8	8 mm × 8 mm
Square Hole	SH4	4 mm × 4 mm
	SH6	6 mm × 6 mm
	SH8	8 mm × 8 mm
Circular Hole	CH4	Ø 4 mm
	CH6	Ø 6 mm
	CH8	Ø 8 mm
Circular Boss	CB4	Ø 4 mm
	CB6	Ø 6 mm
	CB8	Ø 8 mm

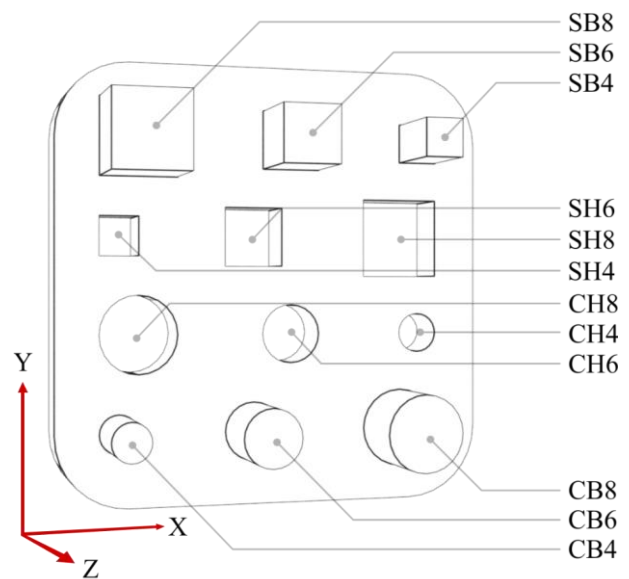


Figure 3.11: Layout of the dimensional accuracy test sample

For these experiments, the parts were printed with the settings in Table 3.4 and a chamber temperature of 90 °C for both machines. Additionally, it is important to avoid warping in dimensional accuracy samples as it can prevent correct measurements from being obtained [229]. To reduce warping, an 8 mm wide brim was added to the parts during printing and removed before measuring. In total, five samples from both printers were measured on an automated coordinate measuring machine (LEGEX, Mitutoyo). Each feature was measured at three different vertical locations to account for imperfections in the surface finish. The details of the measurements that were taken can be seen in Table 3.6.

Table 3.6: Dimensional accuracy test plan

Feature Type	Measurement Type	Measurement Direction	Z-Height (mm)
Square Bosses (SB4, SB6, SB8)	External Width Across Flats	X and Y Axes	8
			10
			12
Square Holes (SH4, SH6, SH8)	Internal Width Across Flats	X and Y Axes	2
			3
			4
Circular Bosses (CB4, CB6, CB8)	External 6-Point Circularity	X-Y Plane	8
			10
			12
Circular Holes (CH4, CH6, CH8)	Internal 6-Point Circularity	X-Y Plane	2
			3
			4

Where Z = 0 mm is at the print-bed facing surface

Before plotting the measured values were subtracted from the nominal CAD dimensions to find their deviation. For each printer, the X and Y deviations on for a single square feature were combined across all five samples to create a 30-point box plot. This was repeated for all other square features and plotted on the same axes to form Figure 3.12.

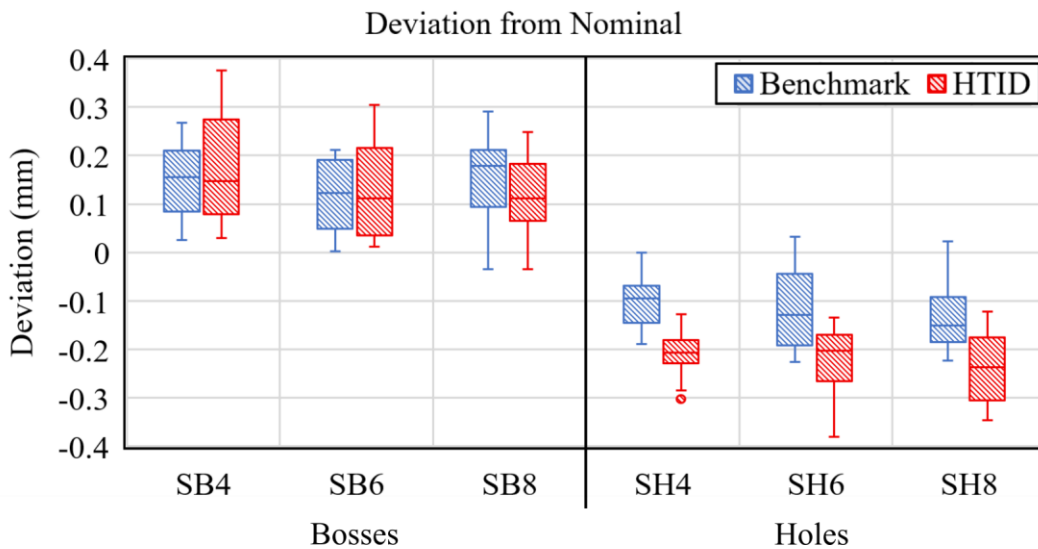


Figure 3.12: Deviation from nominal on square features

Both printers performed similarly when building square bosses, with no significant difference in their deviations between feature sizes. For square holes however, the benchmark printer produced approximately half the average



deviation, at -0.12 mm compared to -0.22 mm on the HTID. The deviation was consistent, rather than proportional to the feature size and always took the printed dimension outside the nominal. This suggested that the toolpath and true nozzle locations were offset, which was likely due to using the benchmark printer's slicer configuration for a different printer. Furthermore, the average deviation was not centred on zero, indicating that parts are being scaled. On delta machines this is usually caused by a mismatch between the measured and actual diagonal arm lengths.

For each printer, the circularity values for a single feature were averaged over all five samples. These were then plotted as a bar graph with error bars to produce Figure 3.13.

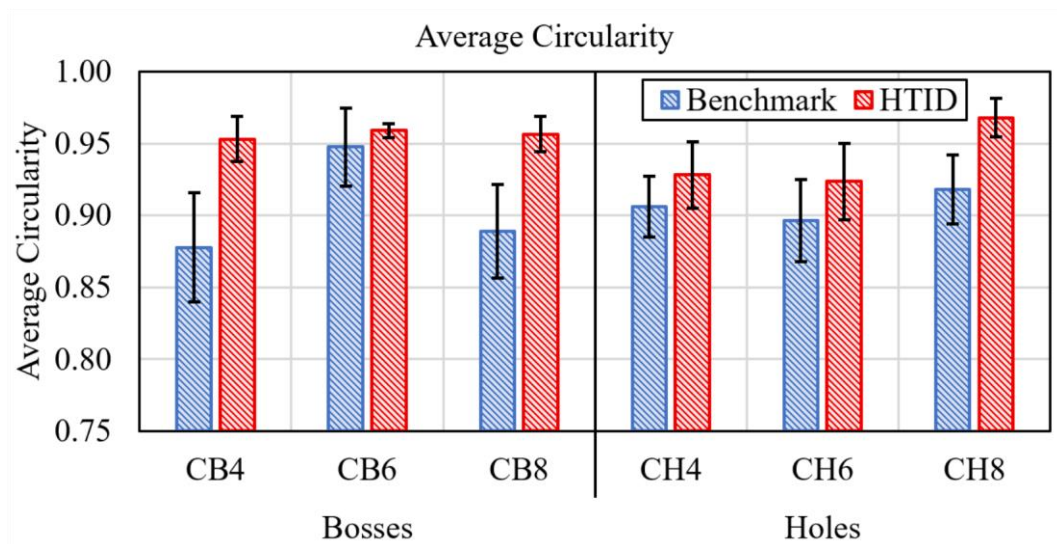


Figure 3.13: Average feature circularity for the benchmark printer and HTID

The HTID consistently produced features that were more circular than those of the benchmark printer, with the average circularity being 5% higher. In Cartesian machines, a lower circularity would indicate one axis performing differently to the other. With delta kinematics, all the axes are coupled; therefore, in the event of one slider moving incorrectly the Z-axis, shifts and the print fails rather than a reduction in circularity. As illustrated in Figure 3.14, there was a marked improvement in the finish of samples produced by the HTID with more uniform and distinct layering and edges. Despite the Bowden configuration, the HTID also suffered less from stringing as the head moved between bosses.

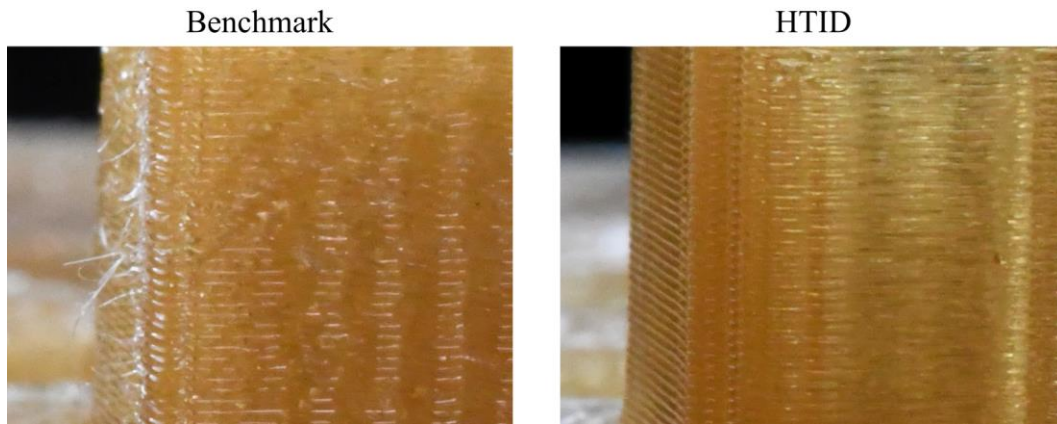


Figure 3.14: Close-up images showing the surface finish of features produced on both printers

### 3.4.2 Tensile Strength

Amongst the literature [220, 230–233], ASTM D638 [234], or the equivalent ISO 527 [235] are the most commonly used standards for tensile testing. This work followed the Type-I variation of the standard as it is the recommended approach for most rigid plastics and the test piece fitted within in the build volume of both printers. The dimensions of the sample are shown in Figure 3.15.

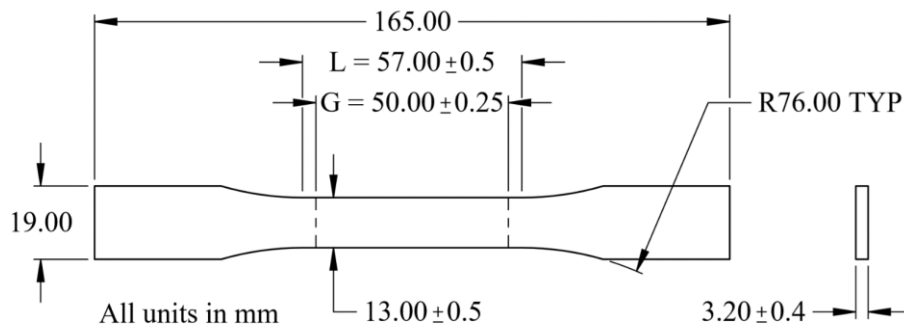
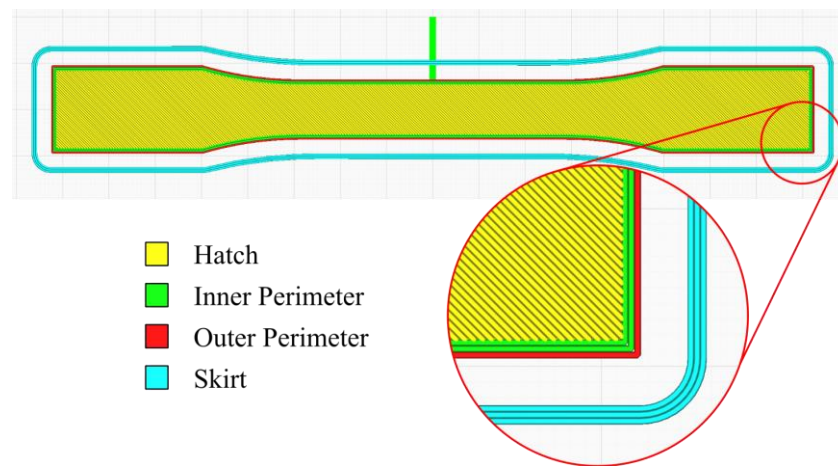


Figure 3.15: Dimensions of an ASTM D638 Type-I tensile testing sample.  $L$  is the length between the start of the radii and  $G$  is the gauge length

Within the field of AM, previously work has assessed how different printing parameters affect the mechanical performance of parts produced using FFF. The studies found that parameters including layer height [230, 232, 233, 236, 237]; nozzle diameter [236]; shell thickness [232, 236]; build orientation [231]; and hatch pattern, angle and density [230, 232, 233, 238] had measurable impacts on the mechanical properties. As this was a comparison of the hardware, the main print parameters were kept the same on both printers and can be found in Table 3.4.

To establish how the chamber temperature influences mechanical strength, parts were produced on the HTID at the five chamber temperatures evaluated in Section 3.3. As a comparison, samples were also fabricated on the benchmark printer at 90 °C as this was the chamber temperature it was designed to print PEI at. Whilst these parts could be printed in many different orientations, it was chosen to have the largest face printed flat on the bed. This was to increase the contact area with the print surface and reduce the likelihood of the samples detaching during a print. The resultant slice pattern can be seen in Figure 3.16.



*Figure 3.16: Slicer output of one layer of the tensile test samples*

As per the test standard, five samples were manufactured for each different test condition. For calculating the ultimate tensile strength (UTS), three cross-sectional area measurements were taken from each sample and averaged prior to testing. These were calculated by measuring the width and thickness at the centre and 20 mm inboard either side of the gauge length using a micrometre (MDC-25SX, Mitutoyo). The tests were performed on a tensile test rig (3369, Instron) fitted with an extensometer for providing strain measurements in the gauge length, at a strain rate of 0.1 mm/(mm.min). The results for the HTID were plotted in Figure 3.17, with the average for the benchmark printer overlaid in green. The full set of stress strain curves can be found in Appendix C.

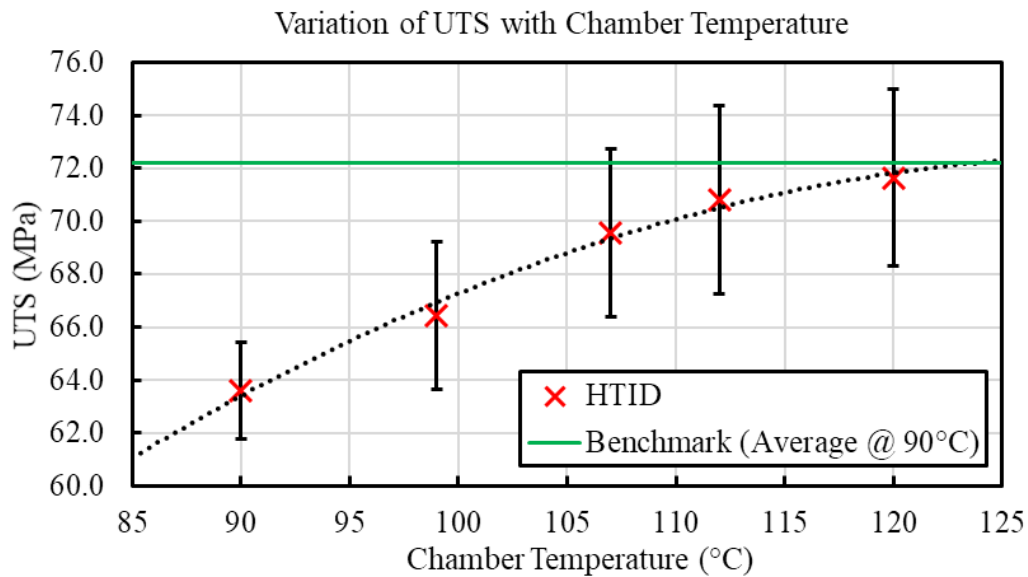


Figure 3.17: UTS of coupons printed on the HTID at varying chamber temperatures and benchmark printer at 90 °C. Error bars show standard deviation over five samples)

The plot showed that on average, as the temperature of the air inside the HTID build environment increased, so did the ultimate tensile strength of the parts. The polynomial trend of the data indicated that while increasing the temperature led to performance benefits there was an optimal value. Extrapolating this gave a predicted optimum value of 72.5 MPa at a temperature of 131.3 °C. This is close to the average value produced on the benchmark printer at 90 °C, suggesting that factors other than the chamber temperature were influencing the mechanical strength. One possibility might be a variation in temperature gradient throughout the X-Y plane of the chamber, introduced by the hot air manifold and blowing towards the corners of the heated chamber and producing localised hotspots.

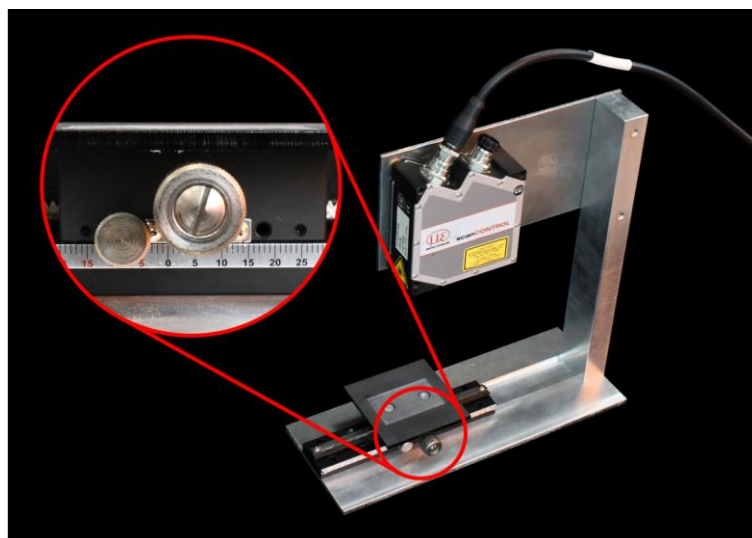
### 3.4.3 Warping

As with dimensional accuracy, previous literature [81, 82, 239] has used the measurement of additively manufactured test pieces to characterise warping performance. These were usually thin rectangular samples which, once allowed to cool to ambient temperature, have the print bed facing surface profile measured for vertical deviation. To measure how the HTID's heated chamber affected warping, 30 mm × 50 mm × 3 mm rectangular coupons were printed using the settings in Table 3.4, while varying the chamber temperature. Three chamber temperatures were used: ambient, 90 and 120 °C. Ambient was chosen

as the lowest temperature to set a baseline for printing PEI without the aid of a heated environment. This temperature also dictated the sample size, which fitted within the printable region found in the feasibility study, reducing the chance of parts detaching from the bed mid-print. 90 and 120 °C were selected as they represent the minimum and maximum chamber temperatures the chamber was characterised for. To ensure the repeatability of the test, three samples were printed at each chamber condition, nine in total.

For generating the profiles, a laser scanning rig was built using a 2D profilometer (ScanCONTROL 2900-50, Micro-Epsilon) and a manually controlled linear axis with a ten division Vernier scale (XWGI40, Misumi). The scanner has an operating window of 70 to 120 mm away from measurement face and a vertical resolution of 4 µm [240]. To give the setup the maximum scanning height the scanner was positioned 120 mm above the translational axis.

The aluminium base had a step machined into it, against which the axis was aligned. The same step was used for aligning the vertical member, which holds the scanner and ensures perpendicularity. The bed was CNC laser cut from an acrylic sheet and has a recess machined into it for holding coupons in place during measurements. Countersunk bolts were used to centre the bed on the table below. Figure 3.18 shows the final configuration.



*Figure 3.18: Laser scanning setup used to acquire surface data and generate warp profiles*

To improve the consistency of the scan data and prevent the laser scattering through the translucent PEI, parts were coated with indelible ink. When taking readings, the samples were placed with the warped (print bed facing) surface towards the laser and positioned so that one of the edges was directly under the laser. Once captured the table was moved  $1 \pm 0.1$  mm along the part and another profile was recorded. This procedure was repeated until the full surface had been profiled. MATLAB was used to create a surface map which was automatically levelled to remove the effects of part rotation and converted to deviation from the highest point on the surface.

To quantify how much of the total surface had warped away from the nominal value of zero, the RMSD for the entire surface was calculated for each sample using Equation (3.7) [241].

$$\text{RMSD} = \sqrt{\left(\sum_{i=1}^m \frac{x_i - \bar{x}}{m}\right)^2 + \left(\frac{\sum_{i=1}^m x_i}{m} - Y_{CAD}\right)^2} \quad (3.7)$$

Where:

- $m$  is the number of measurements
- $x_i$  is the measurement value
- $\bar{x}$  is the mean of the measurements
- $Y_{CAD}$  is the nominal value from the CAD

The first term is the variance, or how close the measurements are to each other, and the second term is the deviation from the nominal. For a perfect surface, the measurements would be identical (zero variance) and match the design (zero deviation) producing an RMSD of 0. Figure 3.19 shows surface maps from three samples printed at different chamber temperatures and the trend in RMSD for all samples. All additional warping profiles can be found in Appendix D.

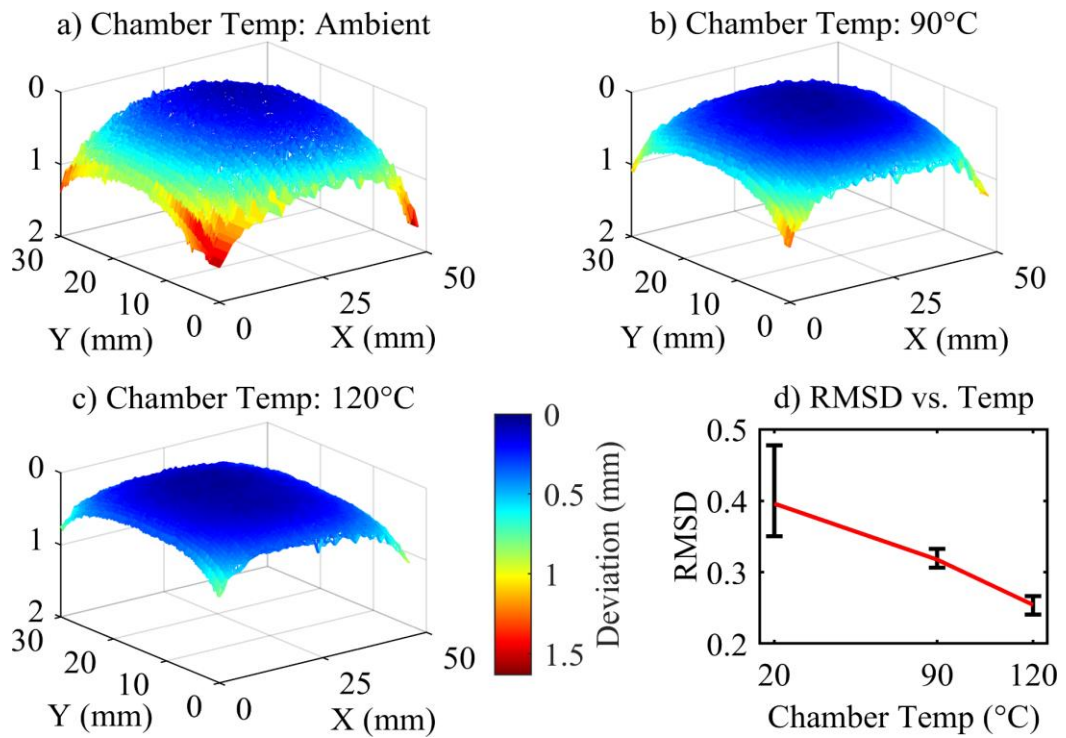


Figure 3.19: Point cloud data showing surface deviation for parts printed at a) ambient b) 90 °C and c) 120 °C chamber temperatures. d) The RMSD vs. chamber temperature

What the results show is that by increasing the air temperature in the chamber, the degree of warping away from the bed can be reduced, with a 36% reduction in the average RMSD over the three settings. This does not remove warping all together, with approximately 1 mm of deflection occurring at the extremities of the samples.

To test if components on the HTID could withstand a solder reflow without shrinking or warping, 30 mm × 30 mm × 1 mm samples were printed out of PEI filament, using the settings from Table 3.4 and a chamber temperature of 120°C. The parts were then subjected to the test from Section 3.1 at the polymers  $T_g$  (218 °C), and again at the peak reflow temperature (249 °C) of the solder paste that will be used (see Section 4.5.2 for details). The samples after testing can be seen in Figure 3.20.



*Figure 3.20: PEI samples after heating to their glass transition and peak SAC solder reflow temperatures*

The parts were measured using Vernier callipers (CD-6" ASX, Mitutoyo) and showed less than 0.5% shrinkage in any direction regardless of temperature. Furthermore, there was no perceivable deformation to the samples. The only caveat is that the samples softened at this temperature and therefore must cool below their  $T_g$  before being handled. This softening may also cause deflection of unsupported structures such as overhangs, reducing the maximum overhang angle that can be used in parts that require soldering. For self-supporting structures however, parts printed on the HTID from this grade of PEI (Thermax ULTEM 1010, 3DXTech) can withstand a solder reflow process.

#### **3.4.4 Flexible Printing**

Whilst PEI is typically used to manufacture rigid parts when printed, when the thickness of the material reduces so does its stiffness. By coupling this with the layer-based nature of FFF, the thickness of a substrate can be tailored; therefore, printing regions with varying thickness should enable parts with rigid and flexible characteristics to be produced.

An important characteristic of FFF printing that may influence the working life of flexible parts is a distinct mechanical anisotropy that occurs within a layer of part. This occurs because the cross-sectional area and degree of polymer fusion where two extrudates meet is lower than along the length of a single extrudate. Because of this a single layer of an FFF part will resist tensile loading along the hatch lines better than across them [242]. Figure 3.21 illustrates how this effect scales as more layers are added.



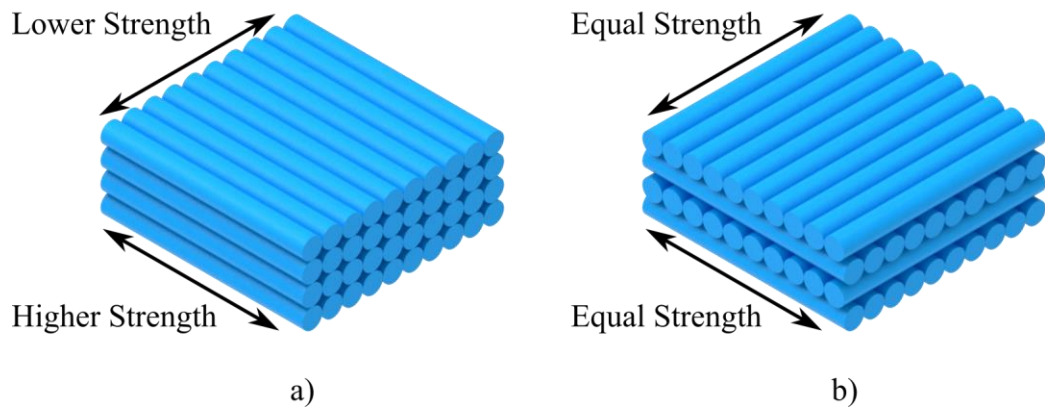


Figure 3.21: Illustration of how hatch orientation in FFF parts can affect tensile strength based on extrudate direction. a) hatch aligned. b) hatch rotated 90° each layer

What this shows is that if the hatch is aligned throughout the structure, anisotropy will occur in the X-Y plane as well as the Z-axis. By rotating the direction of the hatch perpendicular to the previous layer, the part can be made equally strong under tension in both the X and Y axes, although the Z axis will still suffer from lower performance. To prevent the flexible parts splitting along the hatch, samples were printed with a raster angle that rotated by 90° after each layer.

To test the ability to print flexible PEI parts, a substrate consisting of two 1 mm thick rigid sections connected by a 100  $\mu\text{m}$  thick flexible ribbon was manufactured. To make the centre section flexible, the first two layers were printed at a height of 50  $\mu\text{m}$  each, which then increased to 150  $\mu\text{m}$  for the remaining 8 layers to reduce the print time. The dimensions are detailed in Figure 3.22.

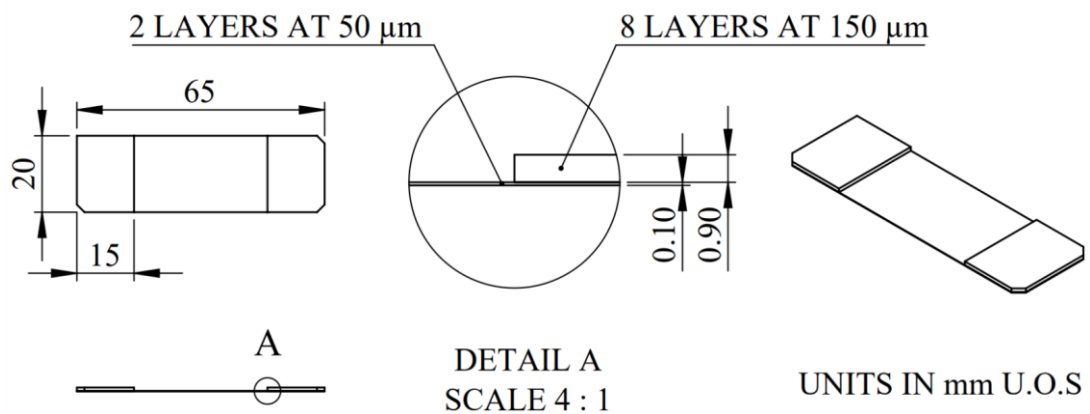


Figure 3.22: Technical drawing of a flexible substrate

These substrate designs were later used as the base design for several test pieces and functional demonstrators including a durability test (Section 4.4) and a flexible positional sensor (Section 5.3.1). Characterisation of these substrates was coupled with performance testing of flexible copper conductors and can be found in the fatigue performance experiments from Section 4.4. Figure 3.23 shows an example of a printed substrate and demonstrates how the flexible region was deflected into an arc by compressing it along its length.

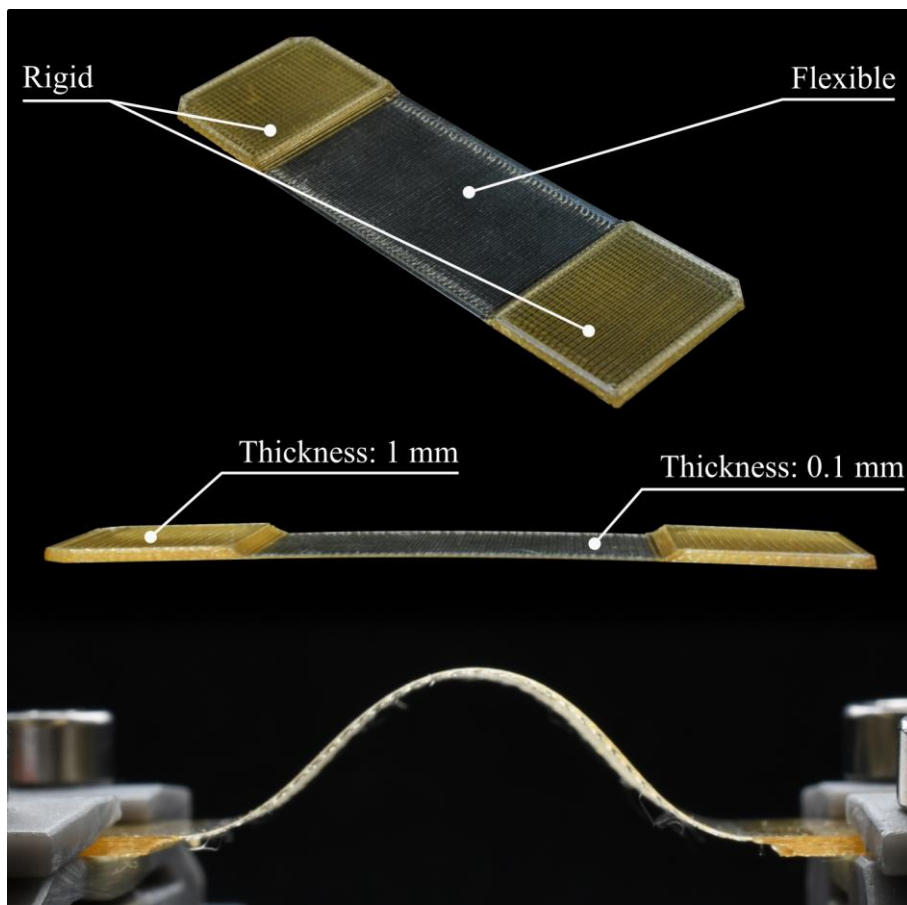


Figure 3.23: Substrate with integrated flexible region shown flat and compressed into an arc with an approximately 6.6 mm bend radius at the peak

### 3.5 Summary

This chapter set out to build a low-cost 3D printer capable of printing PEI, without the complexity of a fully enclosed build chamber. The resulting machine was tested to validate its thermal performance as well as the quality of parts that it produced.

Overall, the deviation on parts produced by the HTID were comparable to those on the benchmark system, except for holes which it tended to undersize more.

To correct of this, a recommended toolpath offset of 0.1 mm inwards should be applied to the slicer an offset to reduce the error. The slight scaling that was also noticed might be correctable with iterative tuning of the diagonal arm length parameter in the kinematic model.

While the HTID fell short of the initial design temperature, the maximum achievable temperature inside the build environment was greater than alternative desktop printers. This could be improved by using a fan designed for hot exhaust flows and recirculating-air from within the chamber.

The use of a heated chamber has been shown to positively impact both the UTS and warping characteristics of PEI components. As expected, a higher temperature raised the UTS. While warping was noticeably reduced, to remove it entirely, printing with additional build plate adhesion methods such as brims and rafts is advisable. Components were also exposed to the peak reflow temperature of SAC solder paste (249 °C) that they could be expected to withstand during a high-temperature hot-air reflow process. This showed that while above their  $T_g$ , they do not deform unless they are not allowed to cool sufficiently before handling.

Finally, by using precise z-axis control, substrates with flexible and rigid elements were demonstrated. This removed the need for additional connection hardware in devices that have moving elements such as hinges.

## 4 Surface Metallisation and Functionalisation

Whilst previous work has produced patterns on PEI [32], according to the published literature this has not been performed on printed parts. AM compatible PEI introduces challenges due to impurities such as additives and plasticisers that improve printability. The lower PEI content means that the existing chemical treatments must be modified to work effectively. This had a notable impact on the surface modification and as a result, reduction stages of the process. Section 4.2 discusses the experimental development of these stages to enable successful patterning of printed PEI, explores the achievable resolution and patterning capabilities and finally validates the removal of ion deposits.

Following the metallisation process development, the conductivity and adhesion of the copper plating to the substrate was evaluated to test its suitability for functional devices. This extended into the printing flexible circuitry and characterisation of their fatigue performance, before adding further functionality through the surface mounting and solder reflowing electrical components.

### 4.1 Process Flow

The process for activating PEI to allow the copper plating to form on its surface consisted of four main stages:

1. Surface modification
2. Nanoparticle reduction
3. Ion removal
4. Copper plating

The surface modification process started with a two-stage chemical dip that bonded silver ions ( $\text{Ag}^+$ ) into the polymer chain. The first step (Figure 4.1 a) was the hydrolysis of imide rings by submerging the PEI in concentrated aqueous potassium hydroxide (KOH). This broke a carbon-nitrogen bond and formed an ionised carboxyl group which bonds to positively charged potassium ions in the solution. After being removed and rinsed in deionised (DI) water, the parts were placed in silver nitrate ( $\text{AgNO}_3$ ) where a displacement reaction occurred (Figure

4.1 b), replacing the potassium ions for silver ions. The suitable chemical formulations and processing conditions for modifying AM compatible PEI were developed in Section 4.2.1

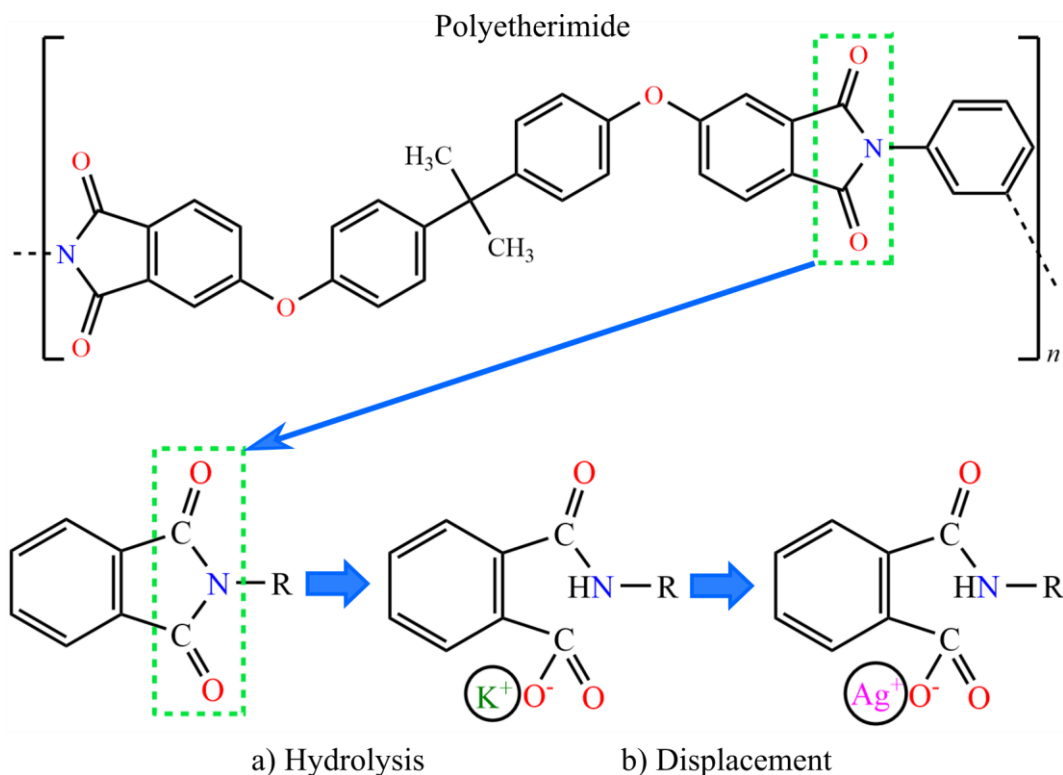


Figure 4.1: Illustration of the chemical modification reactions a) hydrolysis and cleaving of the imide ring. b) displacement of potassium ions with silver ions

The modified surfaces readily acted as a seed site for the copper plating, but to produce patterns, selectivity needed to be introduced. This was performed by reducing the  $\text{Ag}^+$  in the regions to be plated to silver nanoparticles (AgNP)s in their zero-valent state. During a careful chemical wash in later stages, this difference in charge meant that the AgNP's were removed more slowly, allowing them to remain on the surface.

Previous work [32] has used photoreduction with a 405 nm UV source and photomasks to pattern the substrate. To make the process digital and remove the limitations of template-based patterning; this work used a UV laser that can scan across the surface to perform the reduction. The 405 nm wavelength required, was also used to cure the resin in many commercial vat-photopolymerisation printers. Of note, one consumer-grade printer (Form 1+, FormLabs) had an open-sourced slicer software (Open FL, FormLabs) that enabled modification of

patterning parameters that were usually pre-set. This allowed the unit to be exploited for circuit generation and pattern optimisation. The patterning hardware had a 405 nm diode laser with a maximum power rating of 120 mW, coupled to an X-Y galvanometer scanner for positioning of the laser spot. The optimisation of the laser parameters and the ability to pattern conformal surfaces at high-resolutions were discussed in Section 4.2.2 and 4.2.3 respectively.

With two forms of silver on the substrate, the remaining  $\text{Ag}^+$  that was not reduced needed removing. Marques-Hueso et al. [32] showed that a two-stage chemical dip of ammonium hydroxide and sulphuric acid was sufficient to remove the  $\text{Ag}^+$ . The 250 mL of 17.5% w/w ammonium hydroxide used was, diluted with DI water from a 35% w/w stock solution (Fisher Scientific). Substrates were submerged for 15 seconds at ambient temperature before being immediately transferred to an ultrasonic bath of DI water for 10 minutes. Following the ultrasonic cleaning, the samples were immersed in 250 mL of a 1 M sulphuric acid solution (Fisher Scientific) for 20 seconds before returning to the ultrasonic bath for 10 minutes. The verification of the washing stage and existence of AgNP's was discussed further in Section 4.2.4.

The chosen plating solution was a commercially available tartrate-based copper plating bath (Metex 9962, MacDermid Enthone) designed for precision plating of through-hole plated PCB's. The bath composition was selected primarily for its deposition type, ease of use, and relative safety compared to other formulations such as cyanide-based baths. The chosen bath formed a fine grain structure for filling small surface imperfections, making it suited to the surface of FFF components with gaps between the hatch and stair-stepped faces. Additionally, the composition was like that used by the LPKF-LDS process [243], which also uses silver seeding to initiate plating, improving the likelihood of successful deposition.

The bath chemistry was not modified and was performed in a 600 mL beaker on a hotplate with a stirrer. The hotplate made use of an external probe to control the temperature of the solution, which was kept at the optimal 24 °C specified

in the datasheet. Agitation was provided by a magnetic stir-bar running at 200 RPM and depending on the sample; they were suspended in the bath from an enamelled copper wire passed through a hole or held by a pair of locking tweezers in a clamp stand. The bath composition is detailed in Appendix E, and an example of the setup can be seen in Figure 4.2.

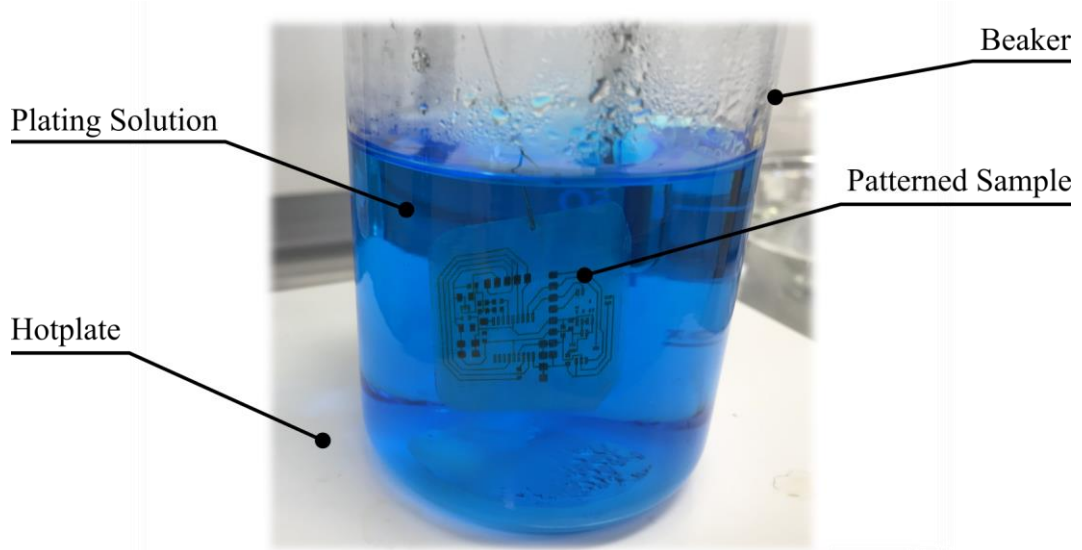


Figure 4.2: Copper plating setup

## 4.2 Process Development

### 4.2.1 Surface Modification Chemistry

All the surface chemistry was performed on a small scale and performed in beaker setups on hotplates. Initially, the chemistry was evaluated with the parameters in Table 4.1 from the work of Marques-Hueso et al. [32].

Table 4.1: Surface modification parameters from literature [32]

Stage	Chemical	Concentration	Temperature	Dip Time
Hydrolysis	KOH	15 M	50 °C	15 minutes
Displacement	AgNO <sub>3</sub>	0.1 M	Ambient	15 minutes

Equation (4.1) was used to calculate the required quantities of solid KOH to make solutions of prescribed concentrations.

$$m = \frac{cVm_a}{\% \text{ Purity}} \quad (4.1)$$

Where:

- $m$  = the mass of solid reagent required in grams
- $c$  = the desired concentration on moles
- $V$  = the desired volume of solution in litres
- $m_a$  = the atomic mass of the reagent

For 400 mL of a 15 M solution, 396.07 g of 85% pure KOH (Reagent Grade, Acros Organics) was gradually added to 200 mL of deionised water in a beaker that was being continually stirred on a magnetic hotplate/stirrer (AREC.X, Velp Scientifica). Once the KOH had dissolved, more DI water was added to bring the total volume up to 400 mL. With the solution mixed and heated to 50 °C, one PEI sample was submerged for 15 minutes and then rinsed with DI water. Following this, they were transferred to a 0.1 M AgNO<sub>3</sub> (Acros Organics) for a further 15 minutes before being rinsed once more. From the literature, as Ag<sup>+</sup> reduces it becomes brown in colour; however, after being exposed to UV light, there was no indication of the photoreduction. The hypothesis was that the lower purity of AM compatible filament required more aggressive conditions to initiate the hydrolysis reaction.

To test this, three samples were submersed in 15 M KOH that was heated to 80 °C, then removed, rinsed, and submersed in AgNO<sub>3</sub> as before. To simultaneously test the effect of submersion time, the samples were removed from the KOH at 15-minute intervals. Finally, they were irradiated and visually inspected for any indication of the photoreduction, the results of which can be seen in Figure 4.3.



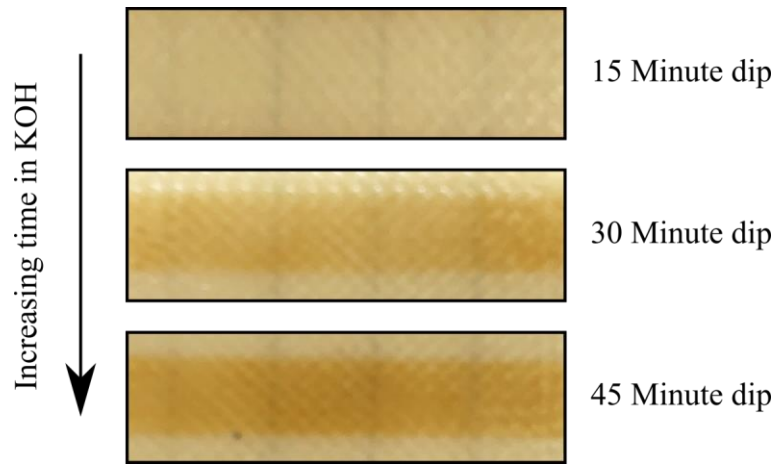


Figure 4.3: Visual inspection of how increasing the exposure to KOH alters the subsequent silver reduction reaction

This test showed that increasing the temperature was able to successfully start the hydrolysis; however, not within 15 minutes. After 30 minutes, a slight change in colouration can be seen, with more notable differences after 45 minutes. To keep the processing time minimal, the remaining experiments proceeded with a 30 minute, 80 °C KOH dip. The final PEI surface modification process flow is summarised in Figure 4.4.



Figure 4.4: PEI surface modification process flow

#### 4.2.2 Nanoparticle Reduction Parameters

To control the position of the laser, the pattern was modelled as a 0.1 mm thick, flat object in a CAD package (Solidworks 2016, Dassault Systèmes) and exported as an STL file. This was loaded into the slicer, which treats the part as a single layer. Individual lines of the raster could not be directly manipulated; however, the hatch spacing between the scanlines could be modified. The scanline terminology and default processing parameters are shown in Figure 4.5 and Table 4.2.

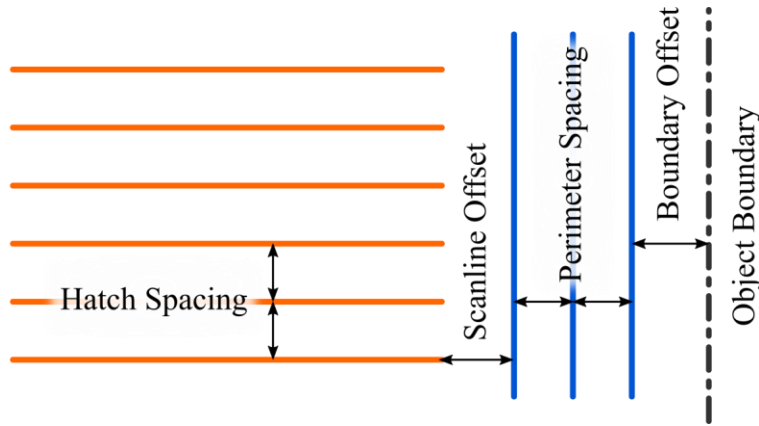


Figure 4.5: Illustration of slicing software scanline definitions

Table 4.2: Default slicing software parameters

Parameter	Default Value
Laser Power	50 mW
X-Y Scan Speed	800 mm/s
Hatch Spacing	80 $\mu\text{m}$
Perimeter Spacing	80 $\mu\text{m}$
Number of Perimeters	3
Perimeter Offset	120 $\mu\text{m}$
Boundary Offset	30 $\mu\text{m}$
Layer Thickness	0.1 mm
Number of Passes per Layer	1

The area-related energy density was used to compare the relative amount of UV exposure applied to different samples and is defined by Equation (4.2)[244]. An additional laser processing variable was the number of times the laser scanned the pattern onto the substrate. This effectively multiplied the UV exposure so to get the total area-related energy density Equation (4.3) was used.

$$E_A = \frac{P_L}{v_s H} \quad (4.2)$$

$$E_A = n_s \frac{P_L}{v_s H} \quad (4.3)$$

Where:

- $E_A$  is the area-related energy density in  $\text{J}/\text{m}^2$
- $P_L$  is the power of the laser in  $\text{W}$
- $v_s$  is the scan speed of the laser in  $\text{m}/\text{s}$
- $H$  is the hatch spacing in  $\text{m}$
- $n_s$  is the number of scans

The patterning rig used a diode laser to produce the 405 nm radiation. These units are compact and cheap which can lead to inaccuracies in their power ratings. Additionally, the beam passed through focal optics, reflects off three-mirrors and finally through a sheet of silicone bonded to acrylic before reaching the substrate. This absorbed a percentage of the UV energy; therefore, the actual power of the laser at the patterning face needed characterising.

To test this a power meter (S310C, Thorlabs) was placed on the bed of the patterning rig, set to measure 405 nm radiation, and zeroed. The rig then scanned a circular pattern continuously onto the power meter, which logged 300 readings at 0.1 s intervals. The test was repeated at power settings of 10 mW up to 60 mW in 10 mW increments. 60 mW was the maximum output of the laser. The readings for each setting were averaged and used to produce Figure 4.6.

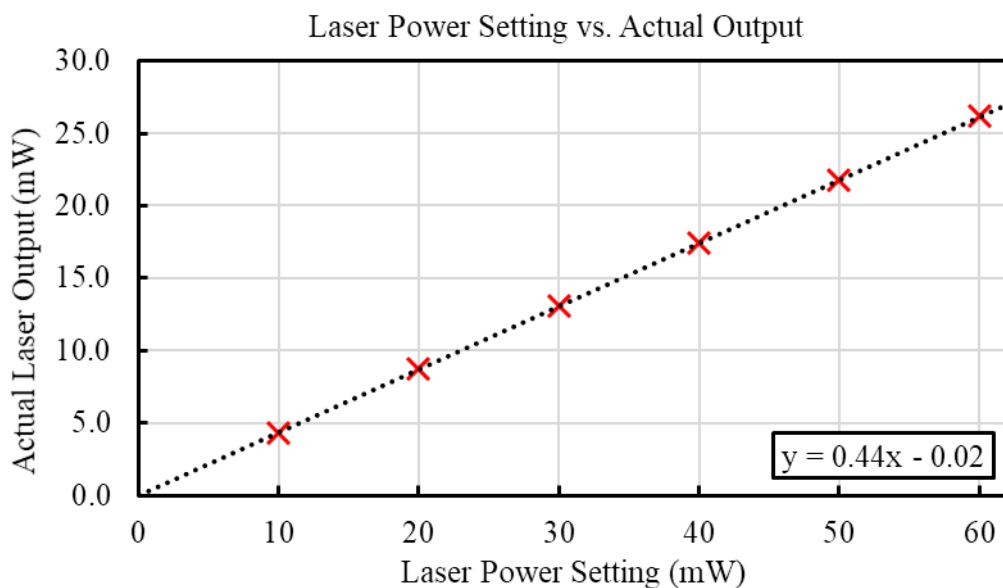


Figure 4.6: Actual laser power output compared to the selected setting in software, standard deviation = 0.06 mW

What the graph shows was a consistent 56% power drop at the patterning face relative to the value requested of the diode. The measured output showed a high degree of consistency, with a standard deviation for all settings of 0.06 mW.

The effect of each laser parameter was tested sequentially by patterning several test strips while varying one of the inputs. To remove the influence of variation in the surface modification process, all test strips for a given laser parameter were produced on the same substrate. Each experiment was performed once to find deduce the best parameter, which once established, was reproduced on five different substrates to test the repeatability. All samples were imaged using a digital camera (D7500, Nikon) and qualitatively assessed for the following criteria before and after patterning:

- Completeness of coverage
- Plating adhesion
- Changes in colouration
- Visual inconsistencies in the surface finish

Completeness of coverage was defined as the percentage of the patterned area with a coating of copper that prevented the underlying polymer being visible, regardless of imperfections. This was evaluated prior to adhesion testing, which was performed by placing a strip of masking tape (Scotch 250 Flatback, 3M) over the sample and peeling it back, removing loose copper deposits. This was a preliminary test; a more in-depth examination of the copper adhesion can be found in Section 4.3.3. The best result from each experiment was used as a baseline for each subsequent experiment. Colouration and visual imperfection were unquantified observations.

The hypothesis for all parameters was that an increase in exposure would equate to a higher degree of reduction; therefore, providing a more catalytically active surface for the copper plating. The expected outcome would be a darker colouration to the substrates before plating and more complete copper coverage after.

The first experiment varied the total number of laser passes. A single PEI sample was patterned with five, 10 mm × 40 mm strips. To alter the number of scans on each test strip, the passes per layer was set to one and the height of the CAD model was varied. For example, for 45 passes, the height of the part would be set to 4.5 mm with a layer thickness of 0.1 mm. The resulting slice would produce 45 layers and scan 45 times. Preliminary tests found that no plating would occur at less than 45 passes, so the experiment started here and incremented in steps of 10 passes. The results can be seen in Figure 4.10.

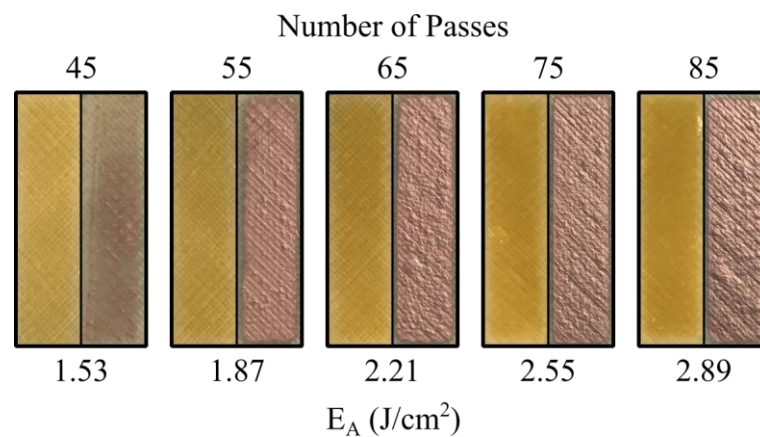


Figure 4.7: Effect of increasing the number of laser passes on the copper deposition. Left half of each panel shows post patterning colour from AgNP reduction. Right shows the plated copper

The results showed that a higher number of passes produced a darker colouration of the substrate and increased the copper coverage in the patterned region. At an energy density of 1.53 J/cm<sup>2</sup> there was minimal copper deposition; however, as the number of passes increased, the copper extends further into the edges and corners of the pattern, producing full coverage at 2.55 J/cm<sup>2</sup>. The highest exposure appeared to produce a similar result; however, in several areas there were raised blisters of copper. Figure 4.8 shows a discarded sample with extreme blistering after an accidental double exposure; note how the blisters appeared as ‘bumps’ in the copper surface. When a tape adhesion test was performed, these regions were found to be delicate and detach readily from the substrate, exposing the polymer beneath.

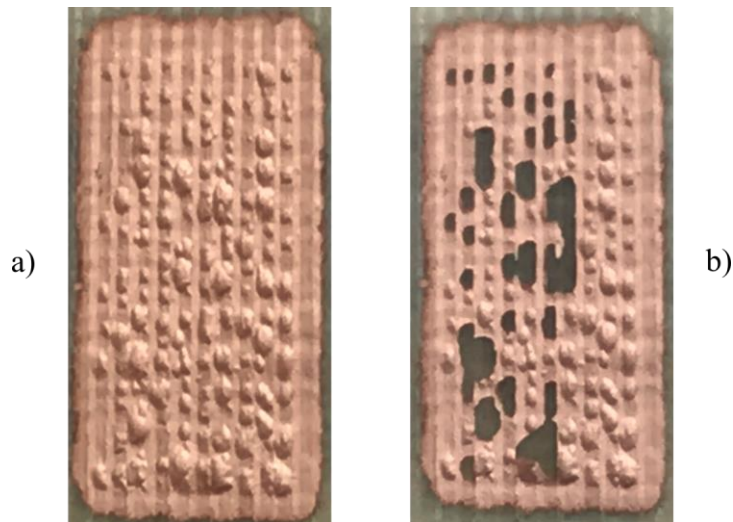


Figure 4.8: Closeup of a blistered sample a) before and b) after testing for adhesion

An optical microscope (BX53M, Olympus) configured for front-lit, polarised, brightfield observations was used to image samples prior to plating. This revealed that for samples exposed to more than  $2.55 \text{ J/cm}^2$  of UV radiation, there was bubbling of the PEI at the centre of the laser scanlines (see Figure 4.9). The indication was that while more exposure increased the surface activity and thus plating rate, it could lead polymer degradation and poor adhesion of the copper. As the deposition built up, the internal stresses overcame the lower adhesive force causing the surface to buckle, forming a raised blister of metal [245].

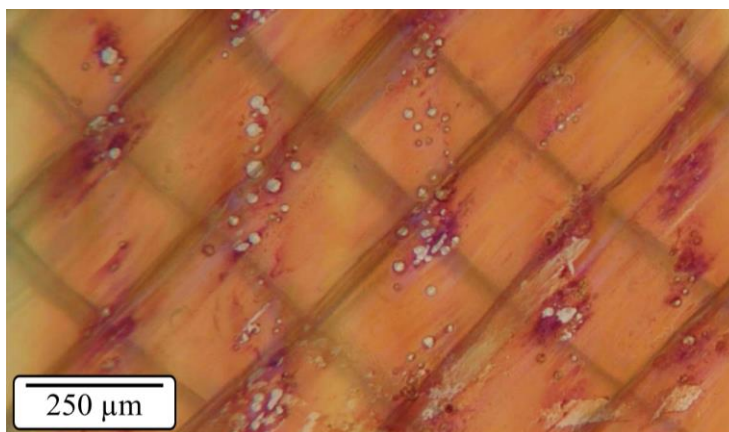


Figure 4.9: Suspected thermal damage to the substrate from excessive UV irradiation

With a value of 75 passes selected as best to progress with, the second parameter altered was the hatch spacing. To test this, the same style of the test piece was produced, with the hatch parameters altered from 60 to 140  $\mu\text{m}$  in increments of 20  $\mu\text{m}$ . 60  $\mu\text{m}$  was selected as the lowest value as the Open FL slicer will not

interpret spacings any smaller. This produced a range of energy densities from 1.46 to 3.40 J/cm<sup>2</sup>, the results of which can be seen in Figure 4.10.

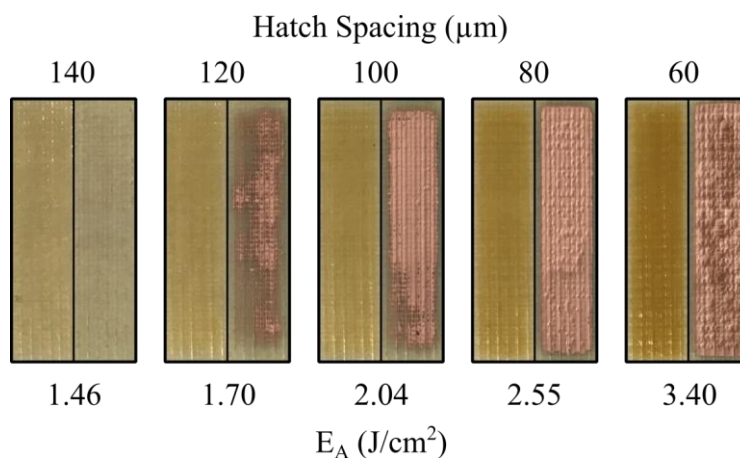


Figure 4.10: Effect of hatch spacing on the copper deposition. Left half of each panel shows post patterning colour from AgNP reduction. Right shows plated copper

The test showed best results at an energy density of 2.55 J/cm<sup>2</sup> from a an 80 μm spacing. As the energy density increased there was significant blistering; and as it decreased there was progressively inadequate coverage. In retrospect, this was understandable as the spacing between the scanlines would be largely dictated by the spot size of the laser. As this was fixed, larger spacings would produce areas without any exposure to the UV radiation and therefore, no plating. The implication of this was that the hatch spacing was best left at the manufacturer's specification.

Using the best settings from the previous experiments, the final experiment explored the impact of both the laser power and scanning speed simultaneously, allowing a wider range of energy densities to be evaluated with fewer samples. 10 mm × 25 mm, rectangles were patterned on a substrate in a grid format with increasing scan speed in one direction and increasing laser power in the other. The speed was varied from 600 to 1,000 mm/s in 100 mm/s increments and the power was increased from 17.4 to 21.8 and finally 24.5 mW. These settings produced a range of energy densities from 1.63 to 4.09 J/cm<sup>2</sup>. The results are shown in Figure 4.11.

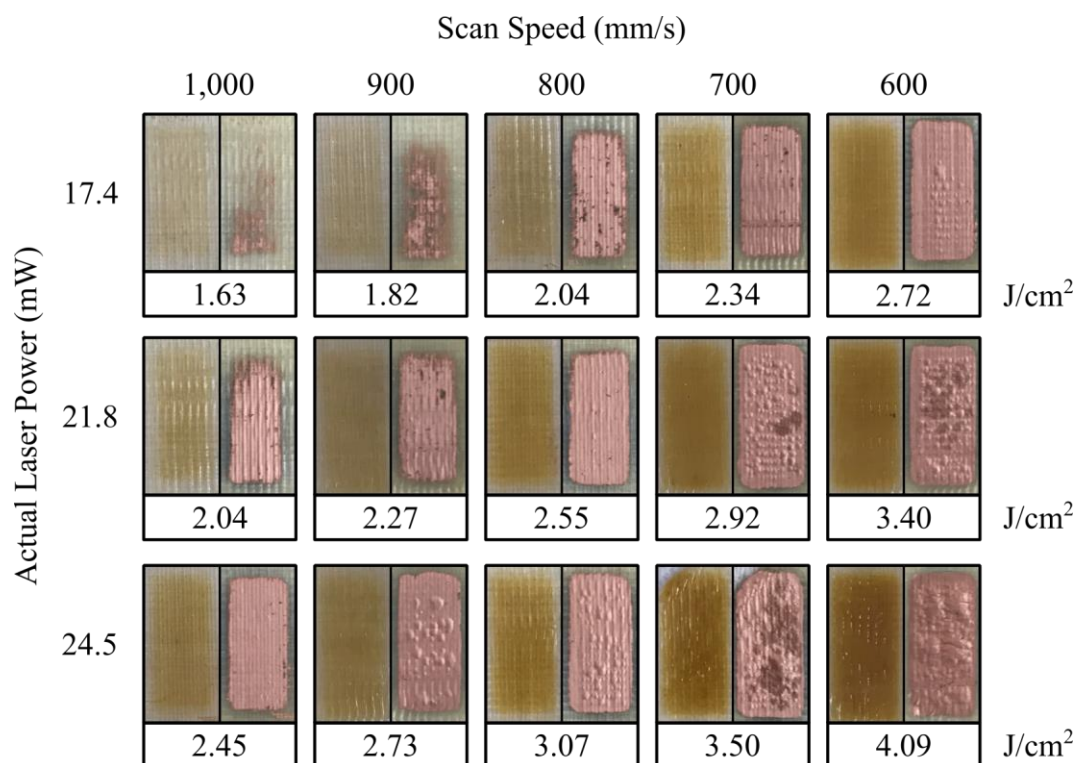
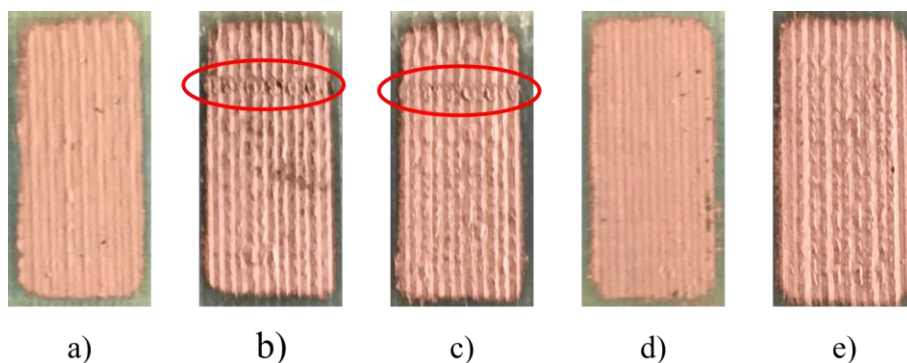


Figure 4.11: Effect of laser scanning speed and power on the copper deposition. Left half of each panel shows post patterning colour from AgNP reduction. Right shows the plated copper. Value below each panel is the  $E_A$  in J/cm<sup>2</sup>

The results confirmed the expected trend, with better copper coverage as the energy density increased. As with the previous tests, more exposure to UV radiation resulted in polymer degradation and blistering, that in the most extreme case covered the entirety of the test pattern. To avoid defects, the highest energy density that did not damage the substrate was selected for continued testing. This was found to be 2.55 J/cm<sup>2</sup>, occurring at a scan speed of 800 mm/s and a power of 21.8 mW. To test the repeatability of these settings, a single 10 mm × 25 mm rectangle was patterned onto five different samples. The results are shown in Figure 4.12.





*Figure 4.12: Repeat tests of selected laser parameters. The red rings indicate a defect in the copper from the underlying print*

What the repeats showed is that despite the same laser parameters there remained an element of variability in the final deposition. This was evident from the small areas of copper missing around the edges of samples a) and d) and was likely due to a lack of control in the plating bath setup. Additionally, there were notable score marks in the copper (highlighted in red) of samples b) and c) however, these were due to the nozzle of the 3D printer fouling on the parts mid-print. Whilst showing the presence of the mark, the copper on top did not lift from the surface and was well adhered.

With these settings, each of the five samples, the 2.5 cm<sup>2</sup> area took 75 minutes to pattern, equating to a patterning rate of 2 cm<sup>2</sup>/hour. Because of the sequential nature of the laser patterning, the total time to finish patterning would increase with the area to be patterned. Other findings from the Photobioform project mentioned in Chapter 1 could be applied to reduce the energy required for Ag<sup>+</sup> reduction, reducing patterning times and preventing polymer damage. The mechanisms behind this are explored further in Section 6.2. The final processing parameters selected from the tests are summarised in Table 4.3.

Table 4.3: Experimentally determined laser patterning settings

Parameter	Default Value
Laser Power	21.8 mW
Scan Speed	800 mm/s
Hatch Spacing	80 $\mu\text{m}$
Perimeter Spacing	80 $\mu\text{m}$
Number of Scans	75

After the parameters were finalised, a single sample was patterned with a series of parallel lines to test the minimum feature size the rig could produce. In the slicing software the smallest line width that could be accepted was 250  $\mu\text{m}$  at a pitch of 500  $\mu\text{m}$ . The sample was then patterned and plated before being placed under an optical microscope (BX53M, Olympus) configured for front-lit, polarised, brightfield observations, at a  $\times 5$  magnification. Linear dimensions were taken using the microscopes measurement software (Olympus Stream, Olympus) that uses a calibrated video feed to allow the operator to trace measurements directly onto the images. These can be seen in Figure 4.13.

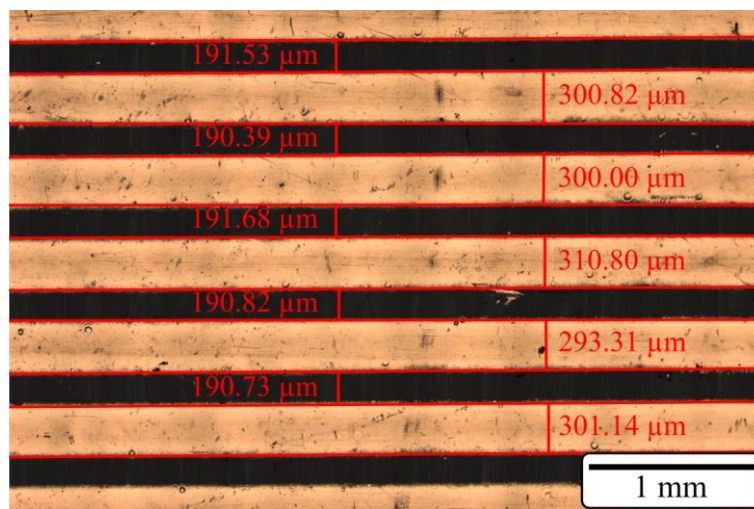


Figure 4.13: Test piece showing the minimum achievable feature size of the patterning rig

The test pattern showed that the process caused the patterned track width to expand by, on average, 51  $\mu\text{m}$ , producing a mean track width of 301  $\mu\text{m}$  and a standard deviation of 6  $\mu\text{m}$ . By adding a track width to the adjacent gap and then taking an average across all measurements, the average pitch was found to be undersized by 8  $\mu\text{m}$  at 492  $\mu\text{m}$ .

### 4.2.3 Conformal and High-Resolution Patterning

When a laser is shone through focal optics, it exhibits a focal depth [246] as opposed to a perfect point, as illustrated in Figure 4.14. As such, if the surface does not deviate out of this range, it will see minimal change in energy absorption.

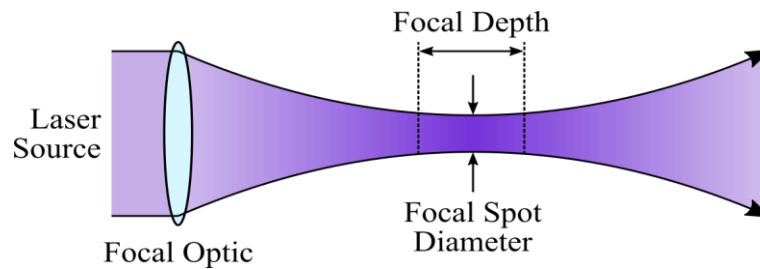


Figure 4.14: Illustration of laser focal terminology

This allowed the laser to pattern surfaces with defects and non-planar topologies without being refocused. Any distortion that occurred on extreme slopes as a result of projecting a 2D pattern onto a 3D surface, however, was not accounted for (see Figure 4.15).

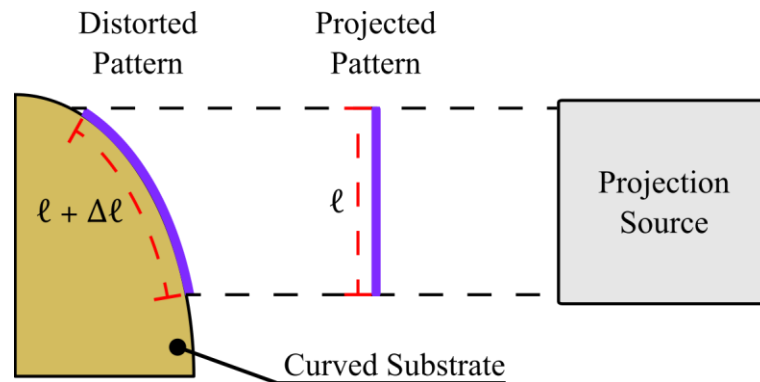
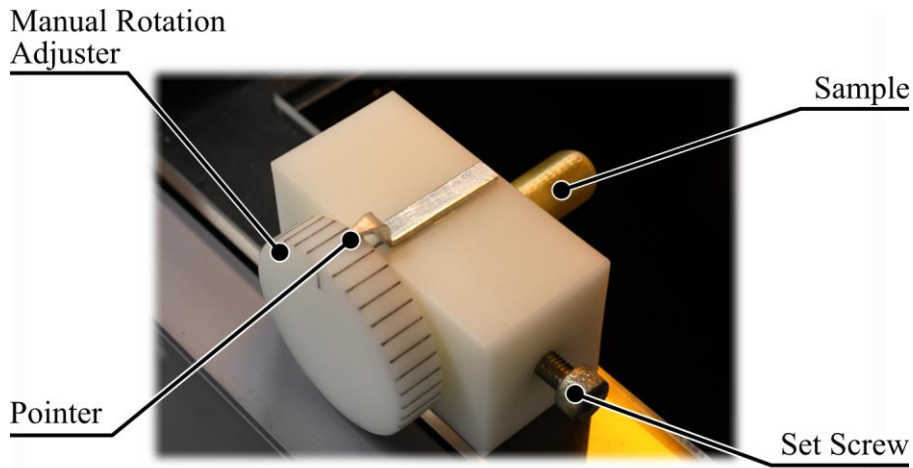


Figure 4.15: Illustration of how a curved surface leads to a distortion of the projected pattern

To prevent distortion when patterning cylindrical surfaces, a manual rotary jig that allowed the components to be indexed to one of 36,  $10^\circ$  increments was used (see Figure 4.17). For the applications in this work, patterns were split into  $30^\circ$  segments, which produces a maximum slope of  $15^\circ$  at the extremities and approximately 3.5% elongation of the pattern. This was a trade-off between distortion and the number of segments required, with smaller angles producing more accurate patterns at the expense of setup and alignment time.



*Figure 4.16: Rotary jig that allows a part to be indexed for patterning around the diameter in small segments*

Conical objects were also be patterned by tilting the angle of the rotational axis, such that it kept the face of the cone parallel to the laser. An example of a spiral track on a conical surface made from PEI is demonstrated in Figure 4.17.



*Figure 4.17: Demonstration of conformal patterning, producing a copper spiral on a conical surface*

The technique also allowed objects without rotational symmetry to be patterned provided they were sufficiently short in the Z-axis allowing the lasers depth of focus to account for the topology. This does introduce distortion to the pattern if the surface is heavily angled. Figure 4.18 shows a conformally patterned sample with a meandering track patterned onto a double curved surface and across multiple vertically stacked layers that were formed during the FFF printing.

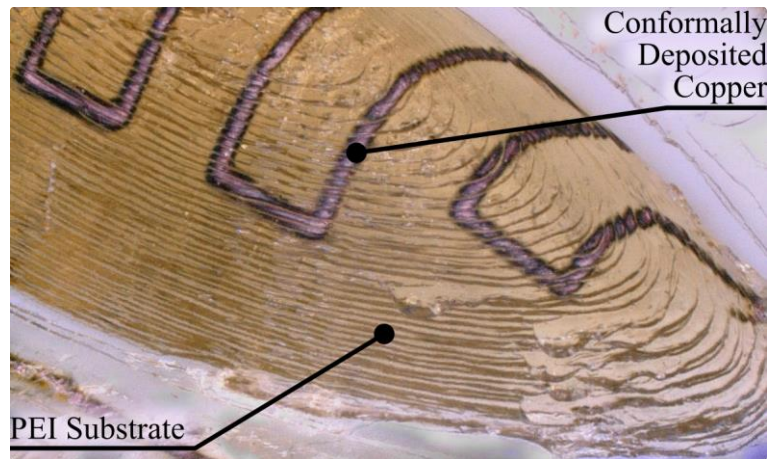


Figure 4.18: Copper patterned conformally onto a double curved surface, across multiple stair-step artefacts

The 155  $\mu\text{m}$  focal spot produced by the laser system in the Form 1+ limited the minimum feature size achievable in this body of work. With the use of improved hardware; however, it is theoretically possible to approach the Rayleigh criterion diffraction limit of  $\lambda/2$  [29], which equates to a feature size of 202.5 nm for this patterning wavelength.

To validate the feasibility of producing higher resolution features, a chrome-on-glass photomask was placed over a single length of treated PEI filament, and the laser was scanned across it to produce the silver pattern in Figure 4.19.

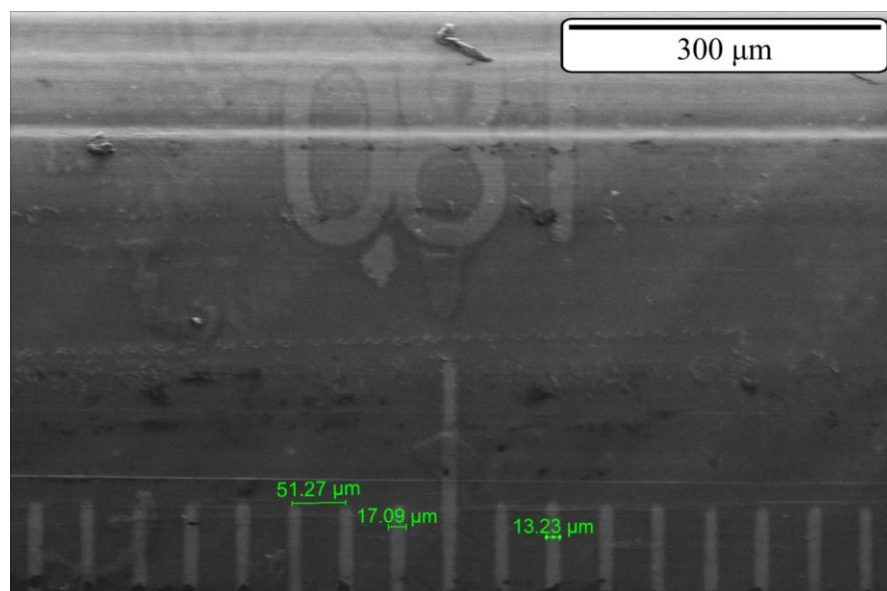


Figure 4.19: Silver micropatterning on PEI filament

The SEM image showed that while not template-less, it was possible to generate features an order of magnitude smaller using the chemical modification approach. The measured line widths were between 13 – 17  $\mu\text{m}$  or 23 times smaller

than using the current rig without a mask and at a pitch of approximately 50  $\mu\text{m}$  were fully resolved.

#### 4.2.4 Ion Removal

To verify the ion removal process described in Section 4.1 had worked successfully, a single sample was placed under a scanning electron microscope (SU8230, Hitachi) with a 15 kV accelerating voltage, 14.6 mm working distance and a  $\times 5,000$  magnification. Observations were made using the photodiode backscatter electron detector and energy-dispersive x-ray spectroscopy instruments (Aztec Energy EDX, Oxford Instruments). The results are shown in Figure 4.20 and Figure 4.21 respectively.

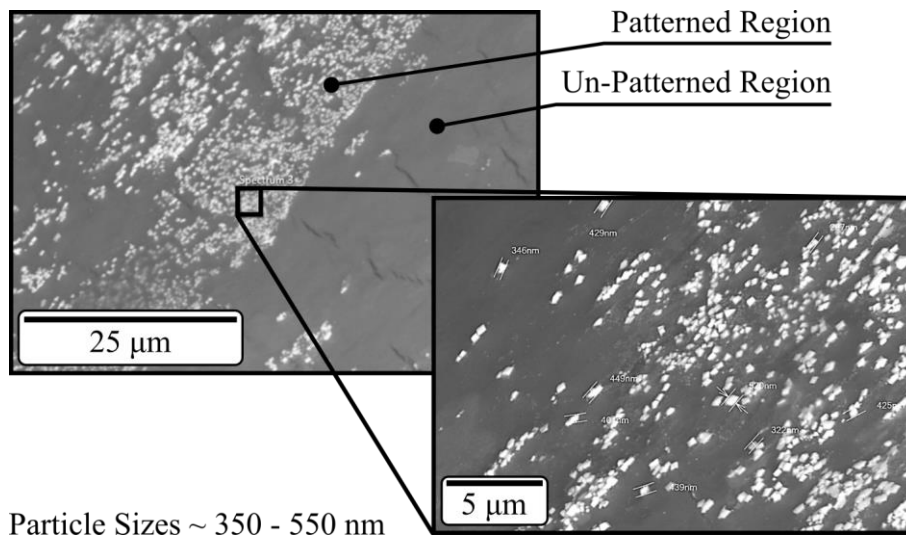


Figure 4.20: SEM image of nanoparticles on the surface of a PEI sample

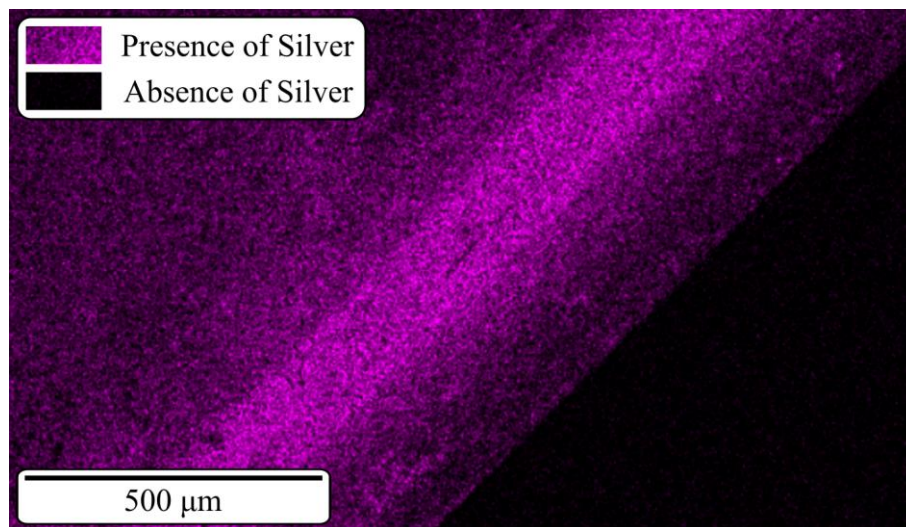


Figure 4.21: EDX image showing the selective presence of silver nanoparticles on the surface of the substrate

From the SEM image a distinct change in particle density between the patterned and un-patterned areas was seen. This was further supported by the EDX analysis which confirmed the persistence of silver in the patterned area and its removal elsewhere, indicating the chemical modification and washing stages worked as intended. The full ion removal process flow is summarised in Figure 4.22.

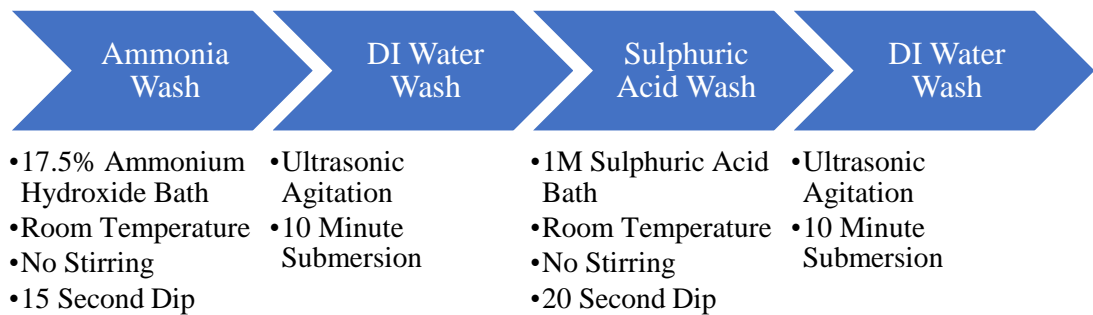


Figure 4.22: Ion removal process flow

### 4.3 Conductor Characterisation

As discovered in Chapter 2, existing approaches for digitally manufacturing electronics are often limited by the performance of the conductor. This section looked to evaluate the conductivity, adhesion and change in resistance due to temperature.

#### 4.3.1 Plating Thickness and Conductivity

When measuring the conductivity of materials with a low resistance such as metals, two-point probing methods are insufficient as the resistance of the test leads is comparable to the object being measured, introducing significant error. This was overcome by using four-point probes which use a second set of probes to calculate and remove the line resistance. To get the dimensionless material property of the conductor, the thickness of the material was also required.

A white-light interferometer (NP-FLEX, Bruker) was chosen for measuring the copper thickness; however, on the FFF substrates this is challenging as the surface is not perfectly flat but instead has an uneven topology due to the hatch, as such there is no definitive height to measure from. Ideally, a flat sheet of PEI would be used; however, this would be an unfair test as the grades available in

sheets differ from the printable variants. The difference in chemistry could have an impact on the final copper deposition affecting the results.

To overcome this, a sample was designed with tick marks (see Figure 4.23) that allow the step height between the copper and PEI directly next surrounding them to be measured in one image. To assess how the copper conformed to the hatch of the printed parts, ticks were spaced such that some were situated directly on hatch lines and others between them. The 20 mm diameter circle of copper in the centre of the part was for measuring the conductivity. This removes variation in the thickness of copper that could arise from using samples plated at different times or baths. For this test, a single sample was manufactured.

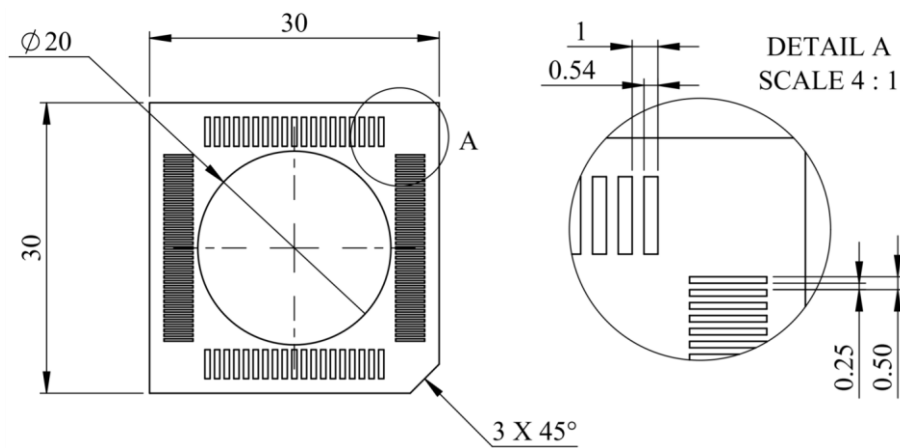


Figure 4.23: Design of the sample used for evaluating thickness and conductivity

Line scans were then taken across the width of the ticks and used to extract the average height across the centre of the copper and the minimum values either side. The average of the left and right minimum values was then subtracted from the height across the centre to find the thickness. This was repeated at ten sample locations around the substrate and used to produce the results in Table 4.4. All ten plots are available in Appendix F.



Table 4.4: White-light interferometry scan results

Sample	Avg. Max (μm)	Left Min (μm)	Right Min (μm)	Avg. Min (μm)	Thickness (μm)
1	2.257	1.727	1.749	1.738	0.519
2	2.474	2.109	2.099	2.104	0.37
3	3.182	2.41	2.671	2.5405	0.6415
4	2.46	1.75	1.558	1.654	0.806
5	2.358	1.699	1.804	1.7515	0.6065
6	2.213	1.644	1.747	1.6955	0.5175
7	2.311	1.876	1.801	1.8385	0.4725
8	0.205	-0.195	-0.189	-0.192	0.397
9	2.491	1.736	1.801	1.7685	0.7225
10	2.258	1.74	1.705	1.7225	0.5355
<b>Mean (μm)</b>					0.559
<b>Std. Dev. (μm)</b>					0.130

The average thickness measured on the sample was 0.559 μm with a standard deviation of 0.130 μm and was used later to calculate the bulk conductivity. By comparing area scans from features that run along an extrudate (Figure 4.24 a) and cross the boundary between two (Figure 4.24 b), it was also be seen that the copper successfully bridged artefacts arising from the printing process. This was an advantage as no additional surface smoothing was required to prevent broken connections.

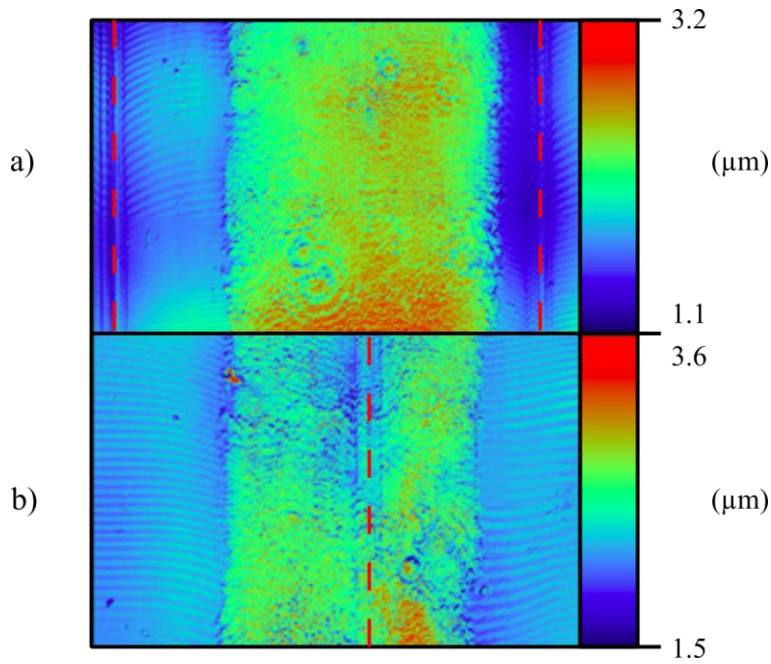


Figure 4.24: White light interferometry scans showing copper deposition a) in the middle of an FFF extrudate and b) in the trough between two adjacent extrudates. The dotted red line indicates the point at which two hatch lines meet

To measure the conductivity, the same sample was placed under a four-point probe (1 mm Spacing, 60g, Tungsten Carbide Tip,  $R_{\mu}$  100, Jandel Engineering Ltd.) connected to a sourcemeter unit (SMU) (2450, Keithley) configured to source 100 mA and measure the sheet resistance. The average of ten readings and the thickness found earlier was used to calculate the bulk conductivity using Equation (4.4). The probing setup is shown in Figure 4.25.

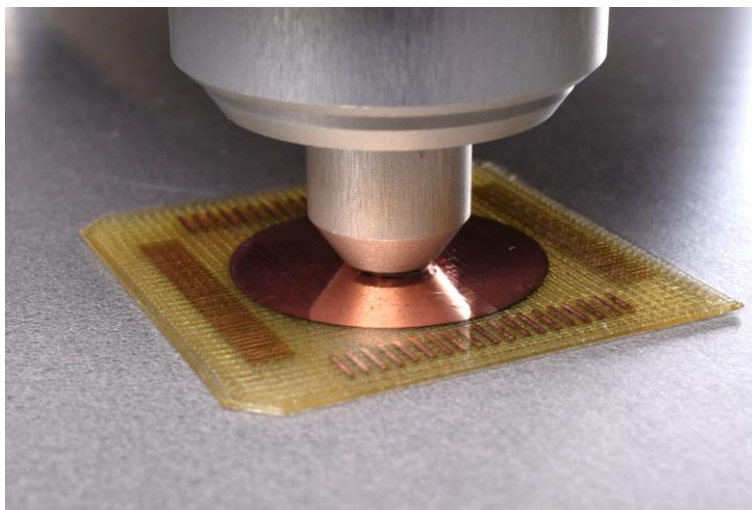


Figure 4.25: Sample undergoing 4-point probing to characterise conductivity

$$\sigma = \frac{C}{R_s t} \quad (4.4)$$

Where:

- $\sigma$  = Conductivity in S/m
- $C$  = Geometric correction factor
- $R_s$  = Sheet resistance in  $\Omega/\square$
- $t$  = Thickness in m

When taking measurements with a four-point probe, the geometry of the sample can affect the output. For a circular test area with a diameter 20 times greater than the tip spacing, a correction factor of 0.9788 must be applied [247]. From this, the measured conductivity was  $3.81 \times 10^7$  S/m or 1.56 times lower than that of bulk copper.

### 4.3.2 Temperature Response

The resistivity of copper naturally varies with temperature, and because of this, it is important to understand how heat will influence the performance of electronics manufactured using the process. To test the thermal response a 100 mm long copper test strip was patterned onto a flexible substrate printed from two, 50  $\mu\text{m}$  layers. At either end of the test strip 18-gauge, thermally insulated wires of equal length were soldered onto the bond pads and then potted with cyanoacrylate adhesive which acted as a strain relief. The sample had a K-Type thermocouple adhered to it and was taped to an aluminium heat spreader to distribute the heat evenly. The entire configuration was then placed inside a PID controlled oven (LHT6030, Carbolite) and the wires were passed through an access port in the roof. The thermocouple was attached to a digital multimeter (2110 5½ Digit, Keithley), and the sample to an SMU (2450, Keithley) for measuring the resistance of the sample. Both instruments were connected to a computer running LabVIEW which synchronously logged data every 2 seconds as the oven warmed up from 30 to 250 °C. The experiment was repeated on a total of five samples, and the resistance data was normalised by dividing all the results of each sample by the initial resistance. The maximum, minimum and

mean across the five samples was plotted against the temperature measured by the thermocouple to produce Figure 4.26.

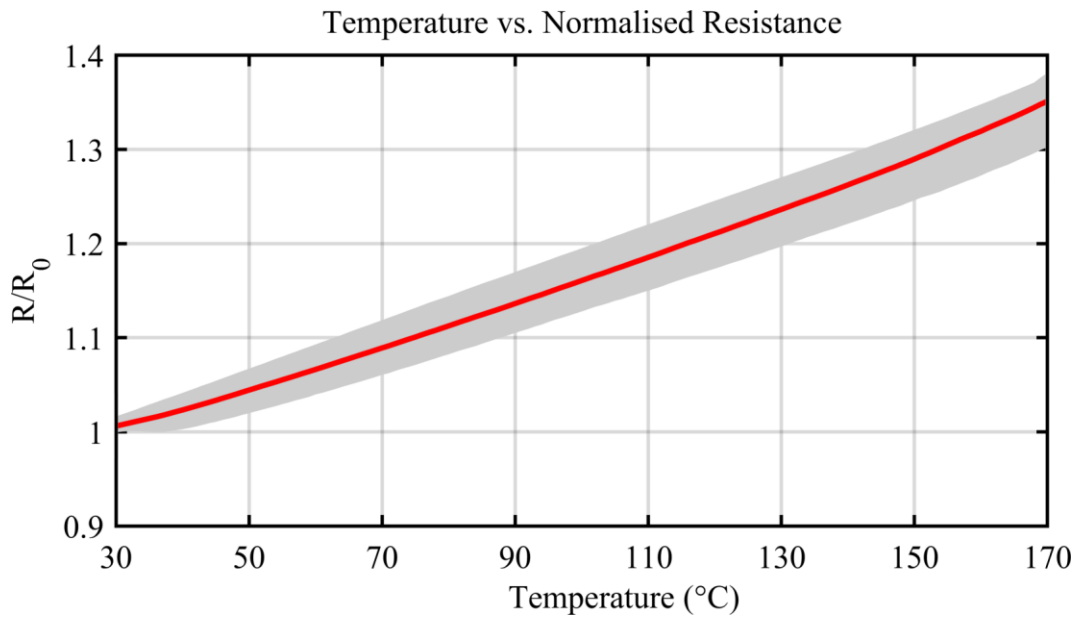


Figure 4.26: Average (red) and range (grey) of temperature responses for five copper strips heated from 30 °C to 170 °C

What was found was that the resistance of the samples increased linearly with the ambient temperature. Furthermore, the trend was consistent across several samples. Whilst the experiment was conducted up to 250 °C, no sample survived the heating because the solder between the copper, and the wires began to reflow and disconnect. Four of the samples reached 230 °C; however, one failed at 170 °C, so the data was clipped at this point.

### 4.3.3 Adhesion Testing

To test the adhesion performance of the electroless plated copper to the substrate, a cross-cut tape test was performed based on the ASTM D3359-Method B standard for testing coating adherence [248]. A 20 mm square of copper was plated onto a single sample before having 6 × 6 grid, spaced at 2 mm scored into the surface using a sharp stainless-steel blade. To provide a worst-case scenario, the patterning was performed on the glass-facing side of the printed sample; which, as found in the literature reduces the adhesion of materials through mechanical methods and relies purely on the chemical bonding [18]. A 25 mm wide strip of tape (Scotch 250 Flatback, 3M) was placed over the sample and smoothed down firmly using a pencil eraser. The tape was

then peeled back at 180° until all the copper was visible again and the result was visually assessed as per ASTM standard D3359. Figure 4.27 shows the sample with the cross-cut pattern before and after the peel test.

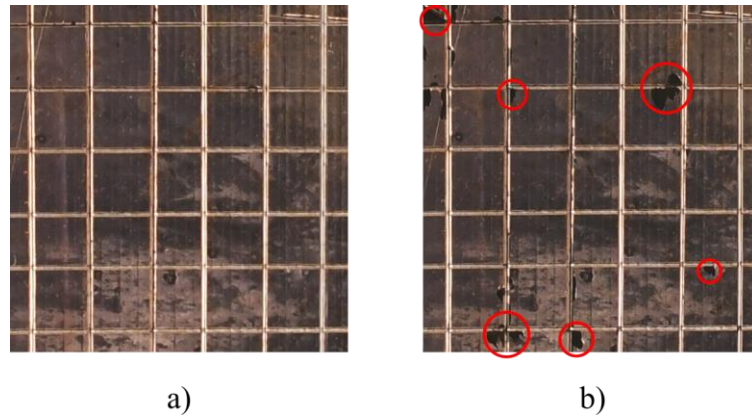


Figure 4.27: Copper plated sample a) before and b) after ASTM D3359 peel test

ASTM D3359 gives plating adhesion classification of 5B – 0B based on how much of the material remains attached to the substrate where 5B is all the material adheres and 0B is total removal. Based on Figure 4.27, the sample met the requirements for a 4B classification, with 5% or less of the plating removed by the tape.

#### 4.4 Flexible Electronics Fatigue Performance Testing

Arguably a more-appropriate method for validating the performance of electrical devices was to test situations closer to real-world applications. This section looked at testing the fatigue life of both the conductor and the substrate through linear buckling, a method that has been used previously to validate flexible AM electronics devices [104, 114, 128]. This test acted as a secondary validation of the adhesion strength between conductor and the dielectric, while also illustrating the ductility of the fine-grain copper deposition.

##### 4.4.1 Experimental Setup

A 100 mm long, U-shaped track was patterned onto the glass-facing side of the substrate design from Section 3.4.4. The track ran from one end to the other and back, terminating in a 5 mm × 5 mm square pads that were used to affix 18-gauge wires. These were connected electrically by hand soldering that was then coated in cyanoacrylate adhesive to act as a strain relief. Six samples were produced and can be seen in Figure 4.28

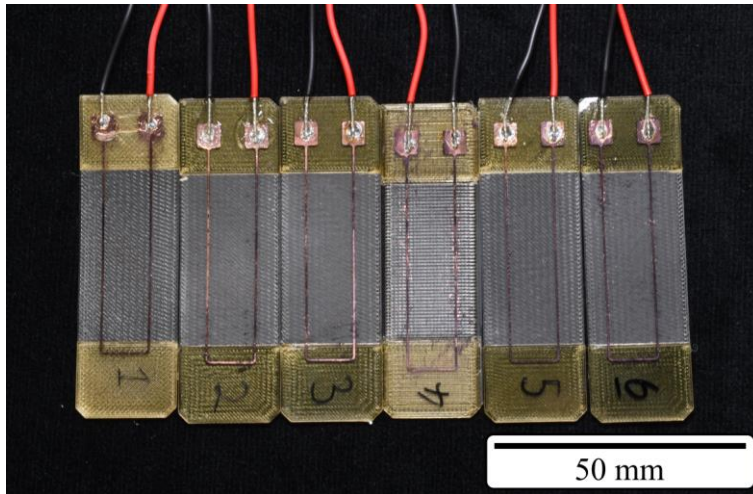


Figure 4.28: Samples used for fatigue testing

To ensure the fatigue testing was repeatable, an automated compression rig was built and is shown in Figure 4.29. The test rig consisted of a slider with a pair of linear bearings that runs along 8 mm diameter chrome hardened steel guide rods. The slider also housed a brass lead-nut that meshed with a single-start, 2 mm pitch leadscrew used to adjust its position. The setup was directly driven by 1.8° per step, stepper motor configured for quarter stepping, which using Equation (3.2), gave a theoretical positional resolution of 2.5  $\mu\text{m}$ . Test pieces were held in two clamps, one on top of the slider and a second on the static end of the rig that also housed a microswitch for homing. The system was controlled by an 8-bit microcontroller (Mega 2560, Arduino) which received commands from a LabVIEW program that also controlled the SMU (2450, Keithley). This was used for monitoring the resistance of the samples during the test.

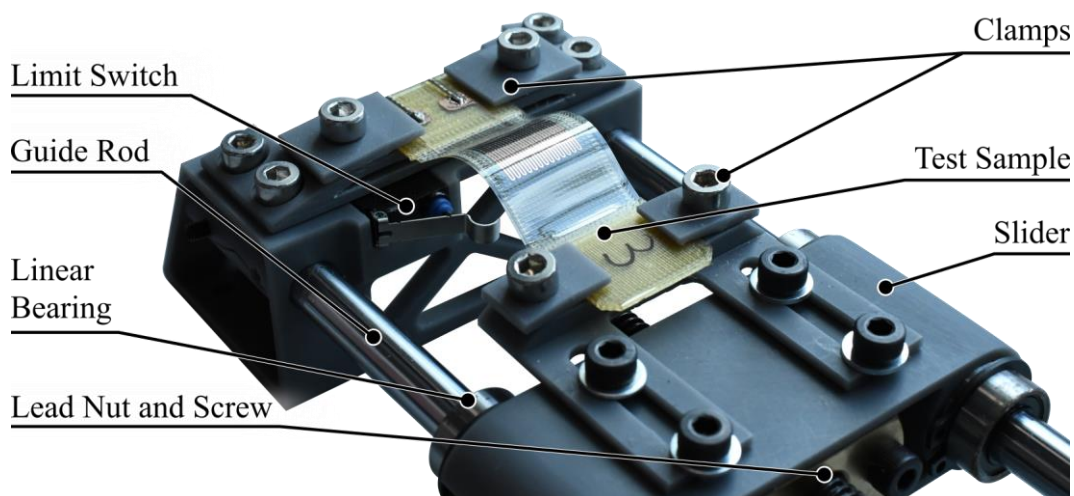


Figure 4.29: Image of the linear buckling rig used in fatigue testing

To perform the tests the rig was first zeroed, and the clamps moved 35 mm apart before a sample was loaded with the copper facing up. To prevent the bend in the samples reversing direction during the test, a 0.1 mm pre-load was applied, and the flexible region was manually deflected upwards. With the sample, loaded into the clamps, the wires were connected to the SMU and the cycling started. At a rate of 30 mm/s, the test cycle compressed the parts 5 mm and then retracted, measuring the resistance at zero compression after each cycle. This produced a minimum bend radius of 6.59 mm at the peak, as measured with a laser profilometer (ScanCONTROL 2900-50, Micro-Epsilon). The experiment was running for 50,000 cycles per sample and repeated across all six samples. After the tests had finished the results were normalised by dividing them by the resistance at the start of the test. To reduce the effects of temperature and humidity the experiment was conducted in an environmentally controlled laboratory. Figure 4.30 defines the relevant measurements of a sample loaded into the test rig in both the uncompressed and maximum compressed states

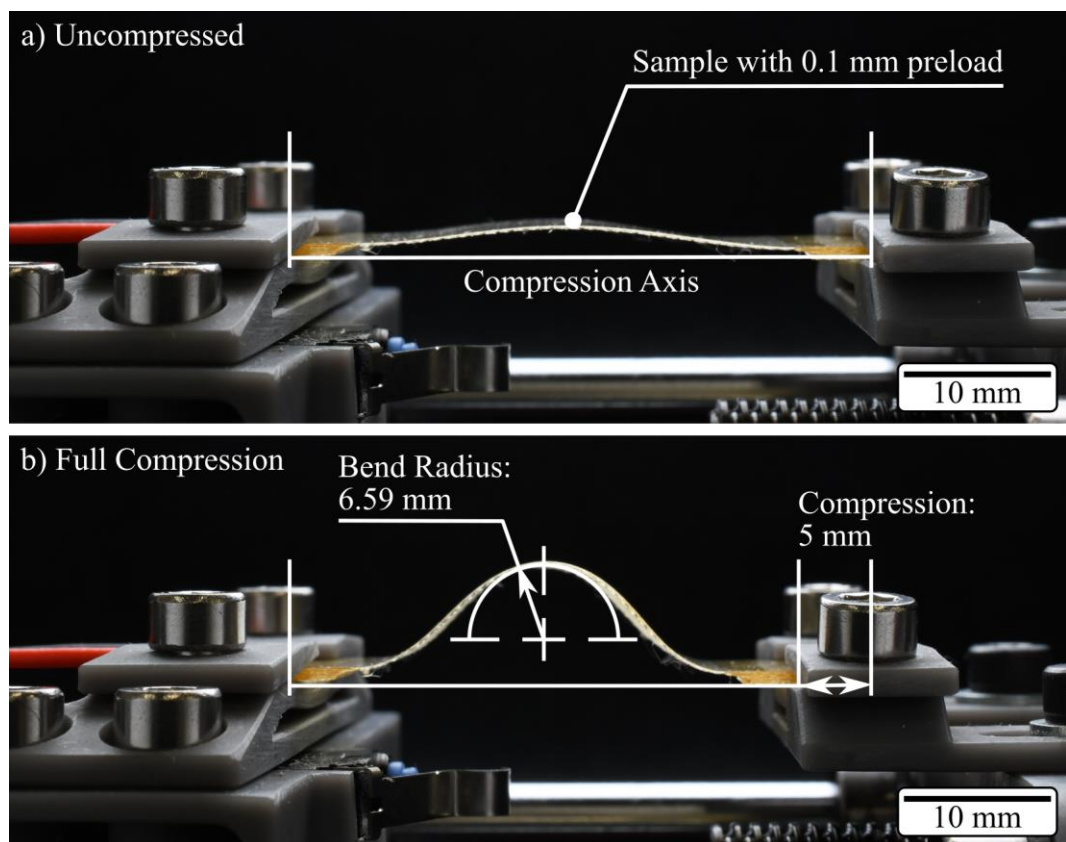


Figure 4.30: Side view of the linear buckling rig illustrating a sample in the a) uncompressed and b) fully compressed states

#### 4.4.2 Fatigue Testing Results

The average normalised resistance across the samples was plotted against the number of cycles to produce Figure 4.31. The error bars show the standard deviation of the sample set.

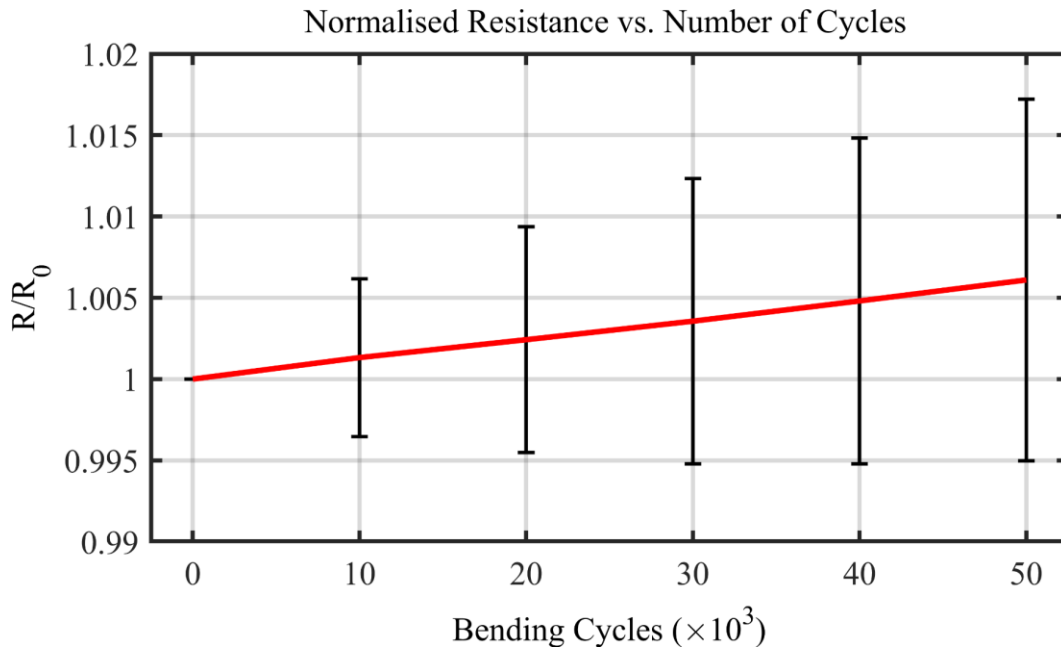
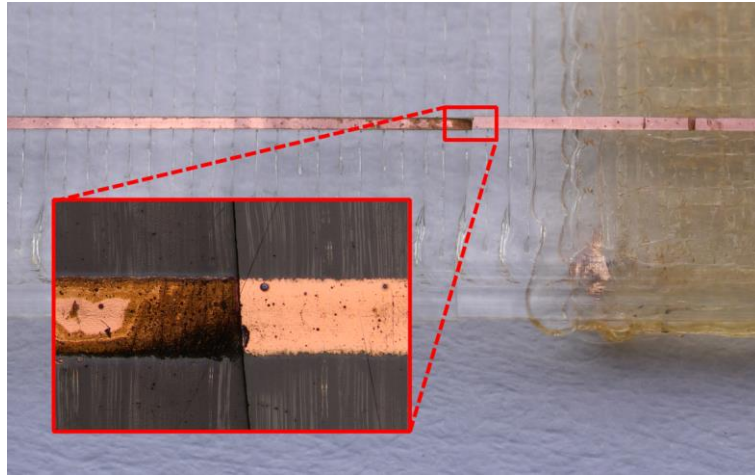


Figure 4.31: Plot showing the normalised resistance of copper strips over 50,000 cycles

The results showed that over 50,000 cycles, on average there was a 0.6% change in resistance over the initial value. This indicated that the conductor was ductile and can repeatedly elastically deform without cracking or delaminating from the substrate. During the standard testing window, no samples stopped functioning, so an extended test was undertaken to establish what the potential lifetime and the eventual failure modes of the devices were. In addition to the 50,000 cycles already undertaken, the samples were cycled until failure in 10,000 cycle blocks. It was found that the samples failed during the second set of further testing, surviving between 60 and 70,000 cycles. The failure mode seen in all 6 samples is pictured in Figure 4.32.





*Figure 4.32: Close-up of a crack in the substrate that propagated through the copper track leading to component failure*

The failure mode witnessed was a crack in the PEI that started at the perimeter of the part and then propagated along the hatch and severed the copper track. This failure mode may have been introduced by alignment of the hatch orientation and bending axes creating a weak spot that encouraged crack growth. In future testing rotating the hatch by 45° might increase the working life of the parts.

#### **4.5 Surface Mount Assembly**

Up to this point, the parts produced that had been electrically interfaced with had relied on hand-soldering techniques to attach test leads and used no electronic components. While this was suitable for laboratory-scale settings, for the process to be adaptable to the broader industry, it needed to be compatible with surface mount technology and solder reflow processes.

Since the introduction of the Waste Electrical and Electronic equipment directive in 2006 the use of leaded solder in all consumer and many commercial products has been banned. Leaded solders are typically easier to work with and reflow at lower temperatures; however, to show greater compatibility with current regulations this work focuses on using industry standard SAC solders.

To validate the ability to solder SMD components to parts produced using this approach, a test board was designed with pads for different component packages, ranging from two-pad components up to 160 pad ball-grid arrays (BGA)s. The details of the components and their location on the board are

illustrated in Figure 4.33 and Table 4.5. The board also used asymmetric fiducial markers for registration with the vision alignment system on the placement robot.

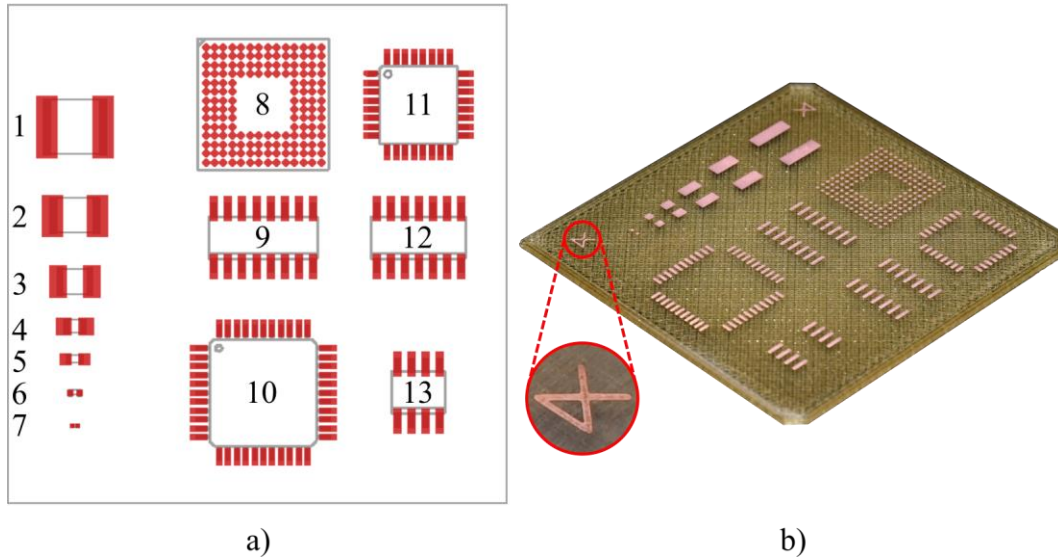


Figure 4.33: Test board design to demonstrate surface mount soldering capabilities a) schematic. b) Final board pre-soldering with a close-up of the vision alignment fiducials

Table 4.5: Solder test board components and sizes

ID	Component Footprint	Component Size or Pitch
1	2220 SMD	5.7 mm × 5 mm
2	1812 SMD	4.6 mm × 3.2 mm
3	1210 SMD	3.2 mm × 2.5 mm
4	0805 SMD	2.8 mm × 1.9 mm
5	0603 SMD	1.55 mm × 0.85 mm
6	0402 SMD	1.2 mm × 0.6 mm
7	0201 SMD	0.6 mm × 0.3 mm
8	160 Pad BGA	0.8 mm pitch
9	16 Pad SOIC	1.27 mm pitch
10	44 Pad TQFP	0.8 mm pitch
11	32 Pad TQFP	0.8 mm pitch
12	14 Pad SOIC	1.27 mm pitch
13	8 Pad SOIC	1.27 mm pitch

### 4.5.1 Solder Dispensing and Component Placement

As a continuation of the digitally-driven theme, a robotic dispensing machine (F7400NVL, Fisnar) (shown in Figure 4.34) was used to apply the solder paste as well as picking and placing the components onto the test board.

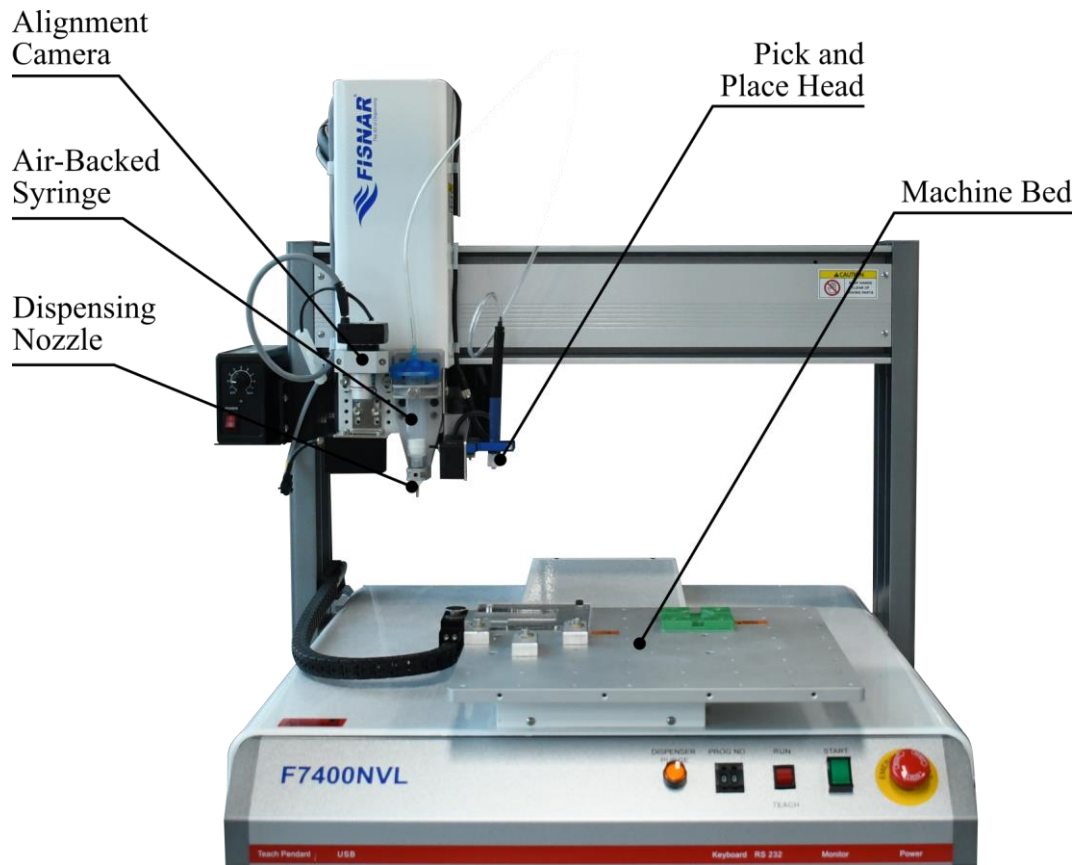


Figure 4.34: Fisnar F7400NVL robotic dispensing machine

The dispenser used an air-backed syringe like those discussed in Chapter 2 to dispense solder paste through Luer-lock nozzles. Tests with the dispenser showed that at the shortest possible dispense time of 0.1 seconds, the material tended to spread to a width approximately twice the diameter of the nozzle outlet. The smallest pads on the board are 400  $\mu\text{m}$  diameter circles on the BGA component so to prevent the material bridging between pads, a 27-Gauge (210  $\mu\text{m}$ ) tapered nozzle was selected. To achieve adequate material flow without blockages, the nozzle outlet should be at least five times larger than the maximum solder particle diameter [249, 250]. For the 210  $\mu\text{m}$  nozzle, this meant that the particles must be smaller than 42  $\mu\text{m}$ . As a result, a ‘Type V’ SAC solder paste was most suitable; with a maximum particle size of 30  $\mu\text{m}$  [250]. The

chosen paste (SMD4300SNL10T5, Chip Quik Inc.) was preloaded into 10 mL syringes that fitted the dispensing hardware. The solder paste did not have a working time like conductive epoxies but was refrigerated to prevent flux separation. Before use it was allowed four-hours to reach ambient temperature as per the manufacture's recommendation.

To control the dispensing location, a DXF schematic of the board was loaded into the robot's software, which automatically converted the pad positions into dispense points. Larger pads were modelled as a series of points 350  $\mu\text{m}$  apart so that when dispensed, they coalesce to form a continuous line. With the layout programmed, patterned boards were placed in a jig that was bolted to the bed of the robot. Fiducial markers and the vision alignment system on the robot were used to improve the accuracy of the dispensing and account for misalignment of the copper pattern or board placement. Once the parts true had been established the robot moved to each dispense point, automatically dispensing dots of solder paste.

For assembling components onto the board, the head was reconfigured with a vacuum pick-and-place tool with a 400  $\mu\text{m}$  orifice, allowing it to manipulate the smallest 0201 resistors. A jig was designed that holds both the substrate and the components in known positions that were programmed into the robot. The system then moved over the first component, descended, and turned on the vacuum, picking it up. The head was then raised, repositioned over the solder, and lowered, lightly pressing the component into the paste. Finally, the vacuum was switched off, and the sequence repeated autonomously until the board was fully populated.

#### **4.5.2 Solder Reflow Process**

To convert the solder from a viscous paste to a solid that bonds the components to the copper, it needed to go through a solder reflow process. The most straightforward approach is to use hot-air convection to heat the solder to the reflow temperature, allowing the solder particles to coalesce and diffuse into the pad [174], forming a strong yet ductile intermetallic bond. A typical hot-air reflow process has three main stages [251]:

**Preheat:** Evaporates any volatile solvents out of the paste to prevent them interfering with reflow.

**Soak:** Activates the flux, removing any oxides from the connections to produce a good bond as well as equalises the board and component temperatures to reduce expansion related stresses in the joint as it cools.

**Reflow:** Takes the solder into its liquid phase allowing it to wet to the pad and the component and form the intermetallic required for bonding.

After this, the part should be cooled quickly to return the solder to a solid. Figure 4.35 shows the recommended reflow profile for the paste used in this process.

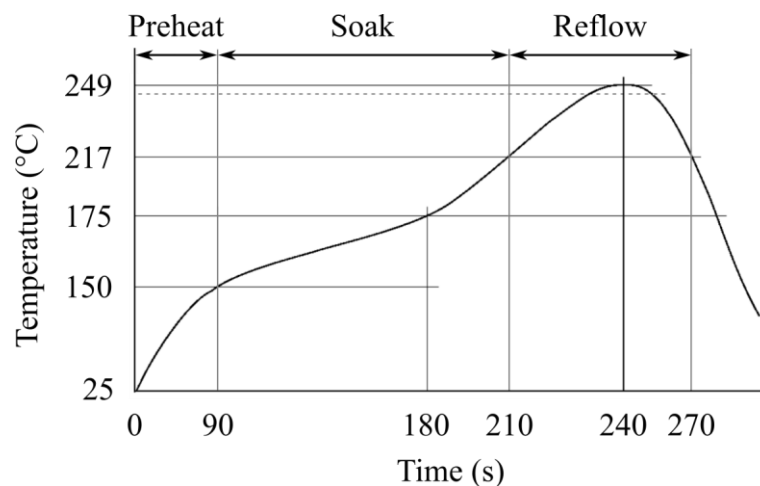


Figure 4.35: Reflow profile for the SMD4300SNLI0T5 solder paste [252]

This solder was chosen as it has a peak reflow temperature of 249 °C, which is at the high-end of SAC pastes and therefore more challenging to reflow.

Before committing to populating a board with components, a sample was produced with just solder (Figure 4.36 a) to verify that the reflow profile would successfully allow the solder to wet to the copper and flow into a metallic coating over the entirety of the pads without bridging. A convection oven with a programmable PID controller (LHT6030, Carbolite) was used to regulate the temperature during the reflow process. The oven could warm-up at the 1.7 °C/s rate required; however, the heavy insulation prevented it from cooling rapidly. To perform the cool-down, the door was opened to expose the part to ambient air. The resultant board is shown in (Figure 4.36 b)

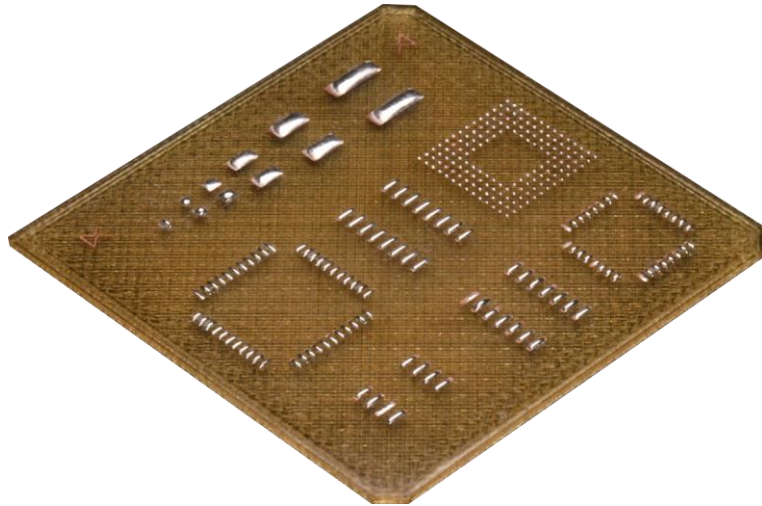


Figure 4.36: Solder test board without components after reflow, to verify solder wettability

The results of the test were promising, with no bridges between any of the pads and the solder wetted to the copper with almost complete coverage, rather than beading up on the surface. Based on this, a fully populated board was produced and is shown in Figure 4.37.

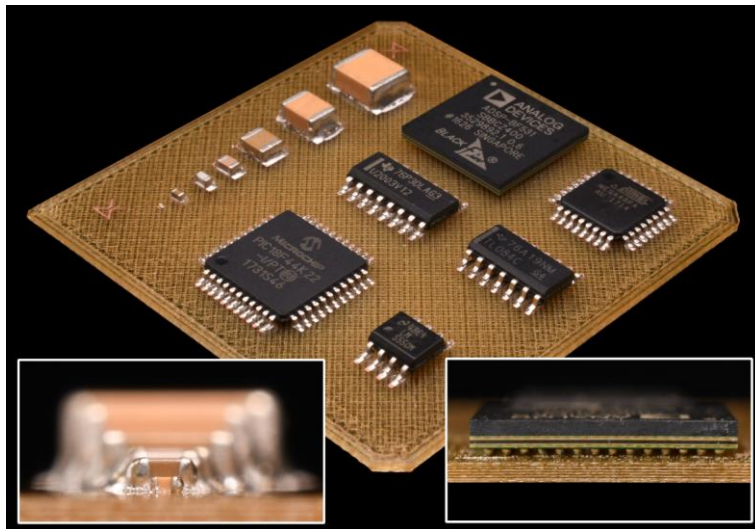


Figure 4.37: SMD components solder reflowed onto a PEI test board using SAC solder paste.  
Close-up of a 0.6 mm × 0.3 mm capacitor (left) and 160 pad BGA component (right)

The final piece was soldered to a satisfactory level for this work, with all the visible connections soldered to and un-bridged, forming fillets between the leads and the bond-pads. After soldering, a small degree of solder balling and beading was noticed. These appear in the form of solder balls near but not attached to the pads and a spattering of smaller solder balls on the surrounding substrate.

Both are caused by heating the solder too aggressively [253], causing the volatile components of the paste to expand rapidly, ejecting solder from the joint. This indicates that the solder reflow is not optimised; however, the main objective was to create a solid electrical connection between the copper and components which has been achieved. Additionally, the board did not exhibit any warping.

#### 4.6 Summary

Chapter 4 has shown the development of a full process for adding electronic circuitry and components to the surfaces of bare, additively manufactured, PEI substrates. This is summarised in Figure 4.38.

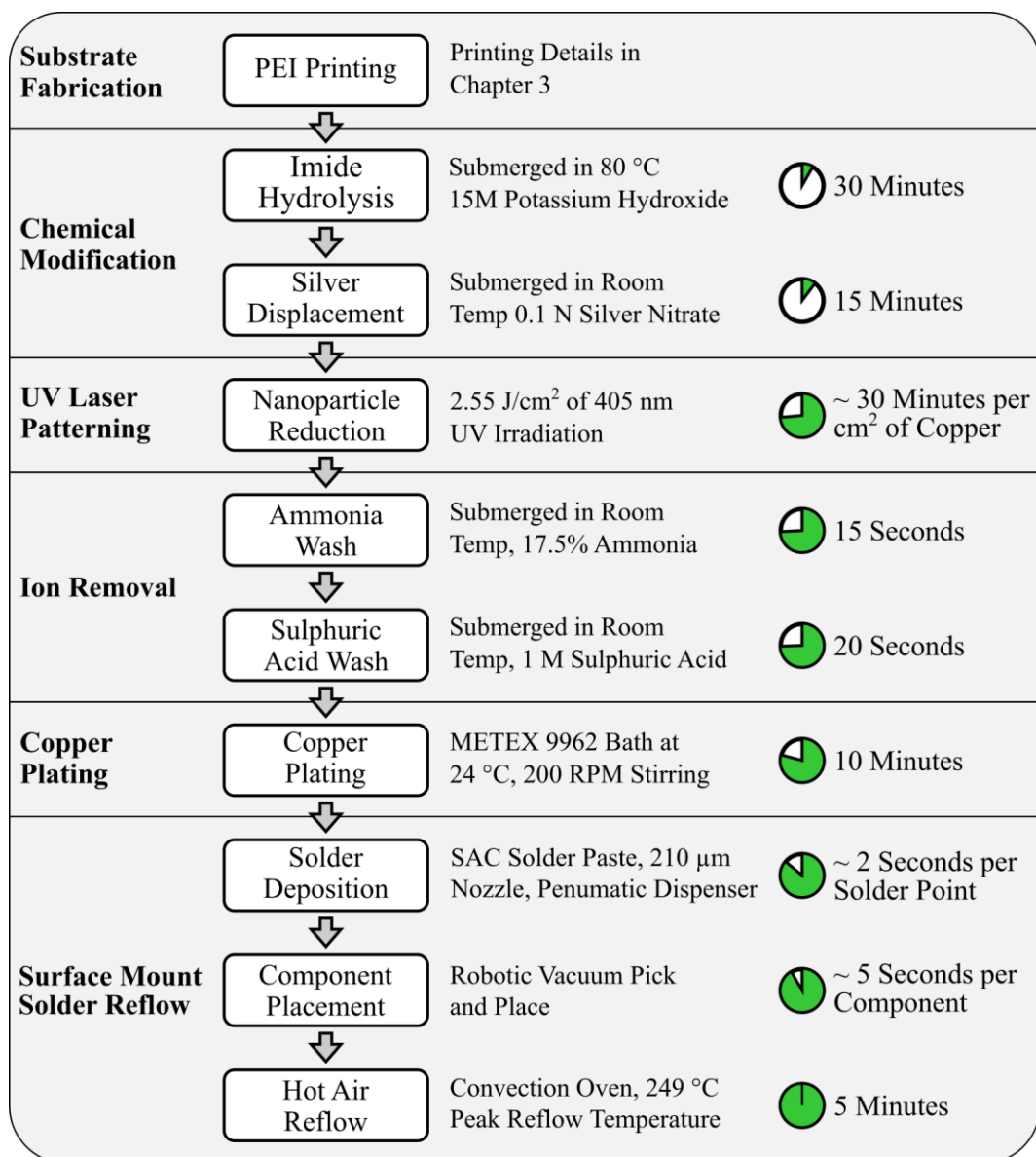


Figure 4.38: Process overview detailing key stages, parameters and approximate times

In the chemical modification stage, due to the lower concentration of PEI in the printable grades, more aggressive hydrolysis conditions than reported in the literature were required to break the imide rings. Additionally, it was found that the surface of the FFF parts could retain chemicals after each stage; therefore, to prevent cross-contamination, ultrasonic cleaning with DI water is necessary.

When patterning the circuitry, a higher UV dosage produced a more active seed for copper plating, improving the overall coverage. Conversely, overexposure degraded the polymer, causing blistering and delamination of the conductor. Experimental tests found that a balance was achieved at an area-related energy density of  $2.55 \text{ J/cm}^2$ . The patterning time was dictated by the copper plated area, with a  $1 \text{ cm}^2$  region patterning in approximately 30 minutes, limiting the method to smaller samples or low volumes. This is a significant drawback when compared with bulk exposure techniques as the pattern size does not impact the processing time, allowing them to scale more readily. The copper deposition was characterised with tape tests, white light interferometry and four-point probing. This showed the copper exhibited a strong mechanical bond to the substrate, with a thickness of 599 nm and a bulk conductivity 1.56 times lower than bulk copper. Importantly, the plating was capable of bridging over imperfection in the surface of the FFF parts, introduced by the printing method. As such they do not require mechanical removal before functionalisation.

Methods for patterning a range of complex features were demonstrated, including cylindrical and conical and swept surfaces without the need for refocussing the laser. The resolution of the hardware was limited by the quality of the optics, producing widths of  $301 \mu\text{m}$ ; however, the use of a photomask showed that the process can produce features 23 times smaller.

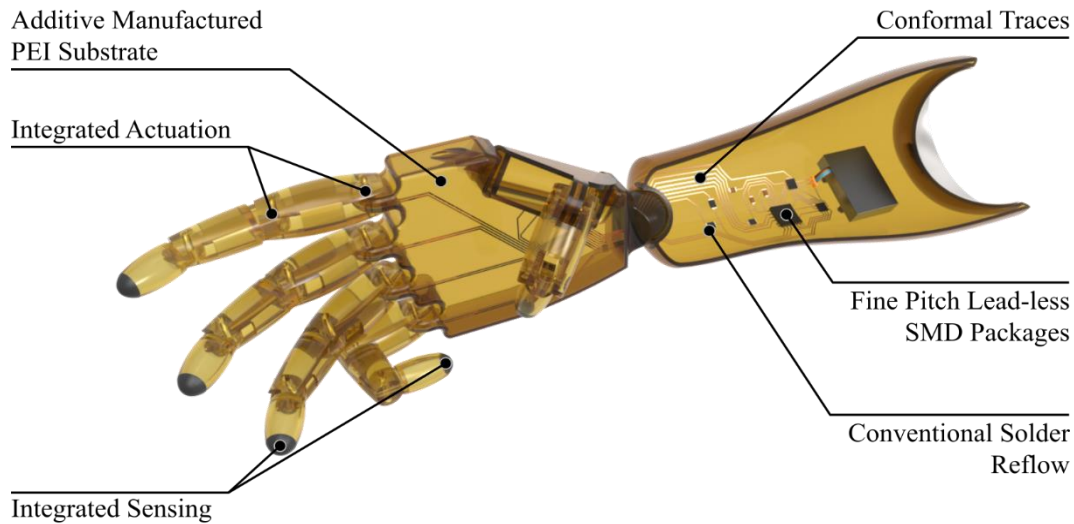
The real-world performance of the substrate-conductor system was evaluated by fatigue testing flexible electronic devices until failure. This showed that after 50,000 bend cycles the resistance of the conductor increased by 0.6% and total failure occurred at over 60,000 cycles. During the testing, the conductor substrate bond remained intact.



Finally, an approach for digitally populating and soldering components to the circuitry was successfully explored. By extruding a Type-V SAC solder paste through a 210  $\mu\text{m}$  tapered nozzle, sufficiently small solder balls were placed and used to attach leadless and BGA ICs with a pitch of 0.5 mm.

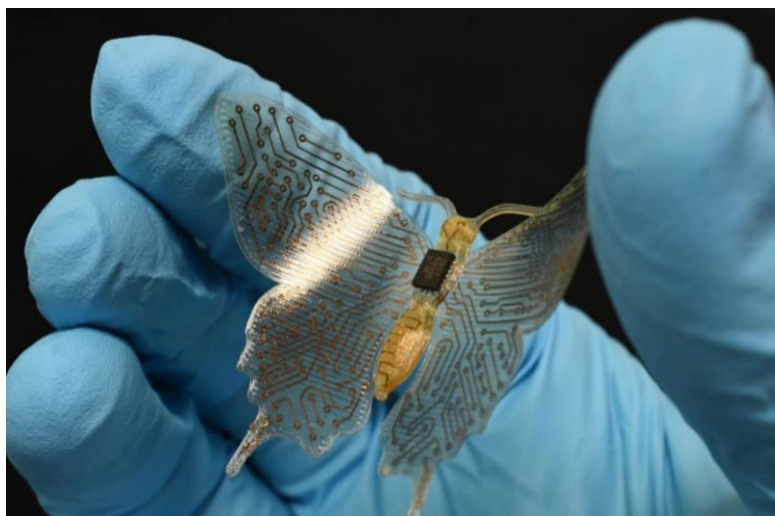
## 5 Process Applications

Initially, the attributes of this manufacturing process were explored in isolation; however, they could also be combined to produce complex, one-piece systems. For example, a device could take the form of a modern smart prosthetic as illustrated in Figure 5.1, whereby discrete PCB's can be removed and integrated directly into the structure.



*Figure 5.1: Concept render of a smart prosthetic demonstrating the potential benefits of this research*

Figure 5.2 shows a butterfly fabricated with the process that had an intricate 3D structure, a 49 mm, flexible wingspan and incorporated solder interconnects and conformal patterning. The IC on the abdomen had 12 pads at a 500  $\mu\text{m}$  pitch requiring high-resolution patterning and accurate, automated chip placement.



*Figure 5.2: Butterfly demonstrator, showing the integration of rigid, flexible and conformal patterning with a fine-pitch SMD package soldered to its back*

This was ultimately a non-functioning part and for illustration purposes only, but the remainder of Chapter 5 evaluates how the process could be used to create working devices and showcase their potential applications. This was performed by producing and characterising several functional devices, including:

- A functional electronic circuit
- 3D and double-sided wireless antennas
- Flexible sensors integrated into additively manufactured components
- Electrically controlled actuating structures

Because the samples were designed to illustrate the technical capabilities and potential applications rather than repeatability or reliability, many of them were one-off's. All work was that of the author, with the exception of Section 5.2 which was performed with the assistance of other researchers. Details of the collaboration can be found at the start of section 5.2.

## **5.1 Functioning Circuitry**

The fundamental requirement for this technology was to be able to digitally manufacture working electronic devices using SMD components that were attached using conventional SAC solder. To illustrate the combination of the key elements of an electronic device, a functional device was designed that included tracks, solder interconnects and active and passive IC's. The design consisted of an LED driven by a 555-timer circuit and was built onto a 30 mm × 30 mm PEI substrate. The circuit has six discrete SMD components: 1 × LED, 2 × resistors, 2 × capacitors and 1 × 555 timer in a layout that causes the LED to flash at a fixed rate of 1 Hz when a voltage is supplied. The final device was fabricated and can be seen in Figure 5.3 and is illustrated operating in Figure 5.4.

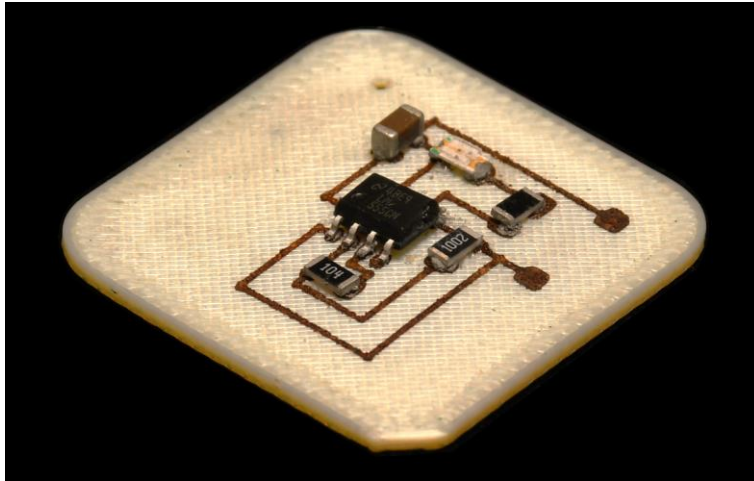


Figure 5.3: Printed, functional 555 timer circuit that causes an LED to blink when powered

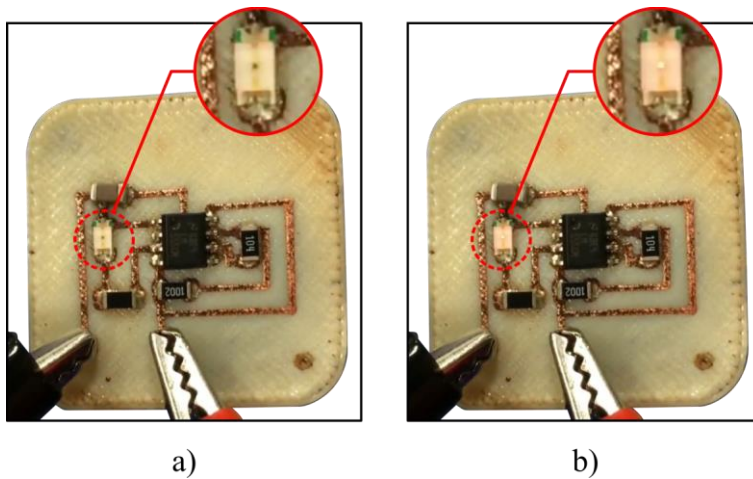


Figure 5.4: 555 Timer circuit connected to a 5 V DC supply, showing the blinking LED a) off and b) on

What could be seen was the LED on the functional board flashing at the designed rate of 1 Hz. This proved that the circuit carriers produced by this approach are durable enough to be populated and reflowed without affecting their function. Inspection of the sample showed no indication of damage to the tracks.

## 5.2 Wireless Power and Communications

As modern electronics become increasingly advanced, the need to remove the tethers that facilitate data and power transmission to electronic systems becomes more apparent. Robotic equipment for use in enclosed spaces such as pipelines or inside the human body become more flexible if they do not require wire harnesses to be transported behind them. Section 5.2 focused on using the

through-hole vias and conformal patterning methods from Chapter 4 and applied them to antenna fabrication.

The antenna design and testing were undertaken with the assistance of Viktor Doychinov and Ian Robertson from the School of Electronic and Electrical Engineering at the University of Leeds. Any graphs in Section 5.2 contain data produced by them.

### 5.2.1 Transmission Coil

To create devices such as an inductive transmission coil, spiral-shaped tracks connected to a power supply at either end were required. On a single-sided component, a wire could be soldered at the centre of the coil to attach one end of the track to the external circuitry; however, is an inelegant solution with an additional potential failure point.

To manufacture boards where tracks need to cross over one another, vias were necessary to allow vertical routing. The hole for the vias was printed into the substrate and chemically modified as normal; however, the laser could not be angled relative to the part to irradiate its surface. This meant that during the washing stage, all of the seeding material would be removed, preventing the copper deposition. It should be noted that un-washed surfaces can be metallised as the copper readily plates to  $Ag^+$ ; therefore, by protecting them during the wash, vias could be created. This was achieved by sealing the hole with a length of polyurethane filament pulled through the hole until it formed a plug (see Figure 5.5). Afterwards the part was then washed with the plug in-situ, which was removed prior to the final rinse and copper plating. An example of resulting via is shown in Figure 5.7.

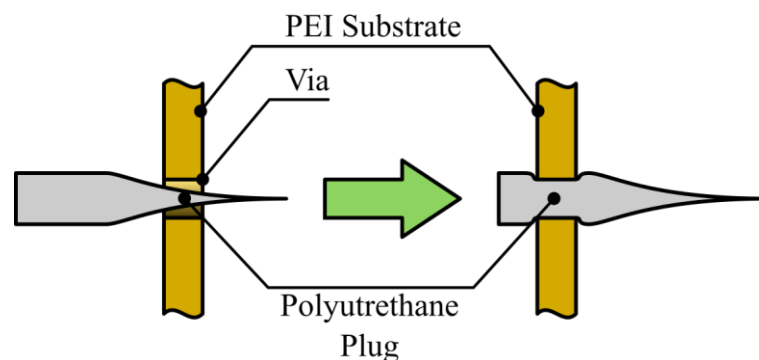
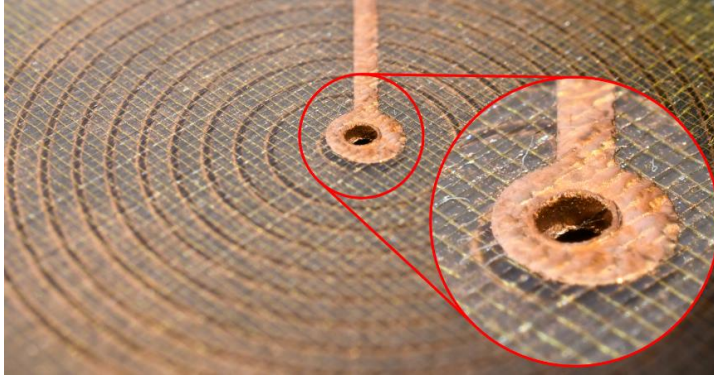
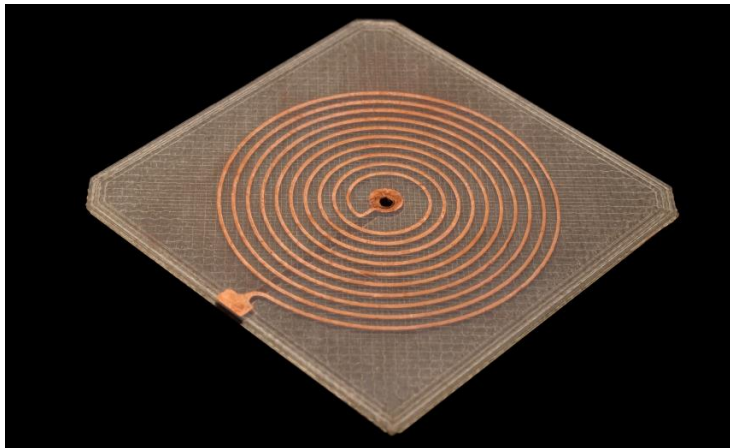


Figure 5.5: Illustration of how a polyurethane plug is formed in the vias



*Figure 5.6: Close-up of copper plated on to the inside of a through-hole via*

A matching pair of transmission coils were produced on 40 mm square, 1 mm thick, planar substrates with a 1.5 mm diameter hole printed into their centre. The spiral pattern had 10 turns at a 1 mm pitch with a bond-pad on one end and a 3 mm circular land that outlined the via. The opposite side of the sample was patterned with a single return track and a matching bond-pad and land. The sample is pictured in Figure 5.7.



*Figure 5.7: Final induction loop with plated through-hole via*

To test the performance of the coils, their inductance and power transmission at different frequencies were measured using a vector network analyser (VNA) (FieldFox N9917A, Keysight). The inductance was calculated from the reflectance coefficient and found to be a stable  $1.75 \pm 0.25 \mu\text{H}$  over a broadband frequency range of 50 kHz to 50 MHz. The power transmission was measured by connecting two coils; separated by 10 mm, to the network analyser and measuring the power transferred from one coil to the other. A reference of 0 dB was set and represented perfect, lossless power transfer. The results were used to

generate the plot in Figure 5.8, which shows how power transmission varies with frequency from 0 – 20 MHz.

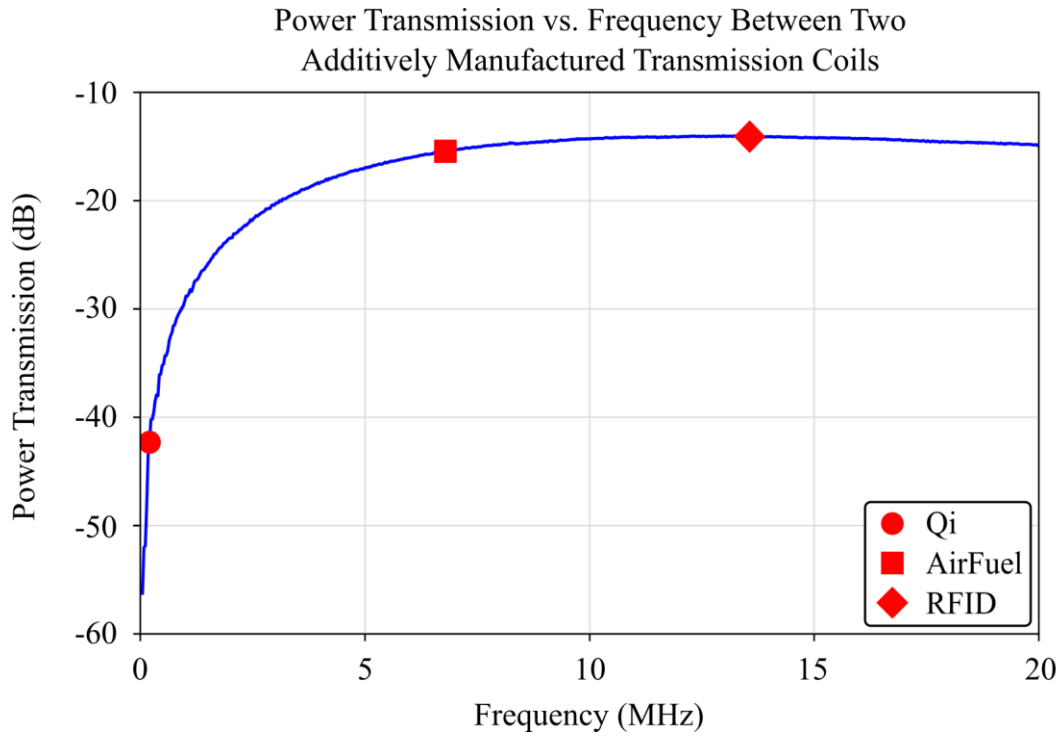


Figure 5.8: Power transmission plot for an additively manufactured transmission coil

The markers on the plot indicated the operating frequencies of three coil-based transmission standards: Qi, AirFuel and RFID. For reference, power transmission at these frequencies was converted to efficiency using Equation (5.1) and displayed in Table 5.1.

$$S_{21} = 10 \log \eta \quad (5.1)$$

Where:

- $S_{21}$  = Power transmission in dB
- $\eta$  = Efficiency

Table 5.1: Power transmission and efficiency of AM inductive transfer coils at different standards

Standard	Operating Frequency (MHz)	Power Transmission (dB)	Efficiency (%)
Qi	0.2	-42.3	0.005
AirFuel	6.87	-15.5	2.8
RFID	13.56	-14.1	4.0

While the coils performed markedly better at the higher-frequency AirFuel and RFID standards, the efficiency was still significantly lower than the 90% that is regularly achieved by wireless power delivery coils at similar separation distances [254]. This would be prohibitive to high-power transfer applications where the losses would result in excessive heating of the coils, but may be acceptable in low-power, short-range data transmission such as near-field communication.

The low efficiency was attributable to the density of the windings in the coil, which was limited by the minimum gap width the laser system could produce without the copper bridging during the plating process. Additionally, the copper plating has a low thickness, reducing the quantity of copper and further limiting the potential efficiency. If this process were to be used for wireless communication or power delivery, improvements in both areas would be necessary.

### **5.2.2 Pill Capsule Antenna**

To illustrate the space-savings that could be gained from conformal patterning, an ingestible pill capsule antenna was designed that could be used to transmit signals from within a patient. PEI has two notable advantages in this application. Firstly, it can be purchased in biocompatible grades, making it an appropriate choice for use in medical devices, and secondly, it has low relative permeability and loss tangents of 2.67 and 0.001 respectively, which improves antenna performance. The track design was a twin spiral monopole antenna, selected for its omnidirectional radiation pattern and was produced on both planar and cylindrical substrates. Before manufacturing the cylindrical sample, the planar version was used to verify the design worked as intended. The part had a form factor of 40 mm × 20 mm and can be seen in Figure 5.9.



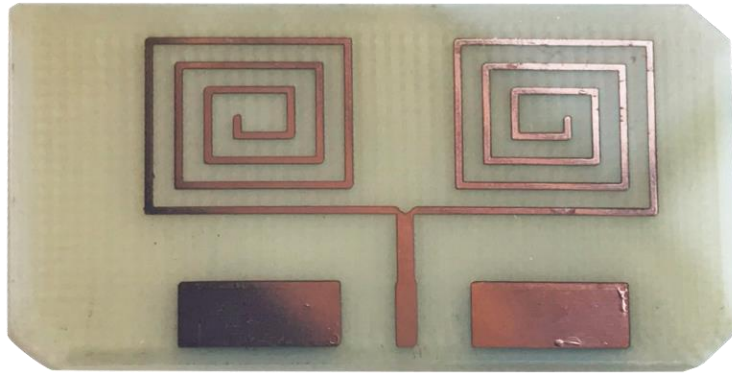


Figure 5.9: Planar antenna used as a performance benchmark for the pill capsule

For taking measurements, the planar antenna track had a flanged coaxial connector hand soldered to it for hooking it up to a VNA (FieldFox N9917A, Keysight). Before the tests were run, a short, open, load calibration was performed to account for parasitic losses in the cables and the VNA's circuitry. The return loss test ran a sweep across a broadband frequency range from 0.1 – 10 GHz, measuring the return loss at 801 frequency points. This test range was used to cover many of the communication standards that operate below 6 GHz, including Wi-Fi, cellular and medical frequencies. All characterisation tests took place inside an anechoic chamber to reduce external interference. For validation, the measured return loss was compared to simulations performed in a commercially available 3D electromagnetic simulation package (Electronics Desktop, ANSYS). The results can be seen in Figure 5.10.

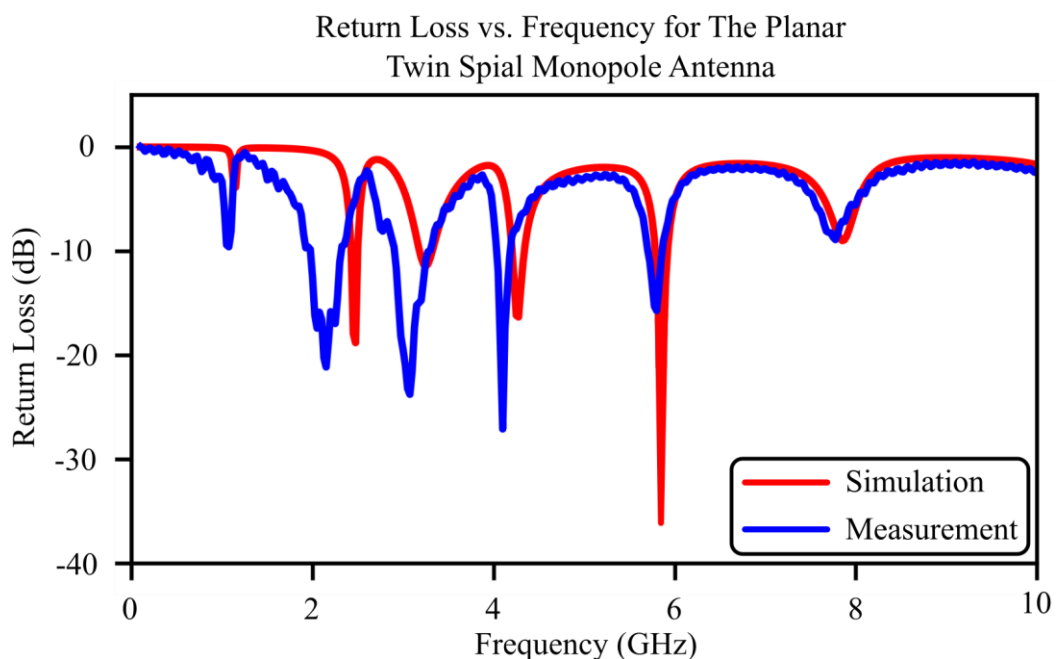


Figure 5.10: Simulated return loss against the actual result for the planar antenna

The shape of the plot was typical of monopole antennas, with multiple resonant frequencies throughout the broadband frequency range. There was good agreement between the simulation and the actual device, indicating that the antenna performed as designed. The variation between the two plots was likely due to parasitic losses in the connector used for interfacing with the antenna, as this was not modelled in the simulation.

With the design shown to function correctly, the conformal version was fabricated, onto a printed 20 mm tall, 11 mm diameter cylindrical casing with a hemispherical dome. At higher frequencies, surface roughness can negatively impact the return loss of antenna lines [255, 256] so to minimise the effect of layering artefacts a, 50  $\mu\text{m}$  layer height was used. The same twin monopole antenna track was wrapped around the outside of the capsule and is pictured in Figure 5.11.



*Figure 5.11: Final conformal pill capsule antenna*

To ensure that any losses that were unaccounted for in the design matched those of the pill capsule, an identical flanged coaxial connector was hand soldered onto the track. The conformal antenna was tested with the same parameters as the planar sample and resulting plot was overlaid onto the measured data for the planar sample (see Figure 5.12).

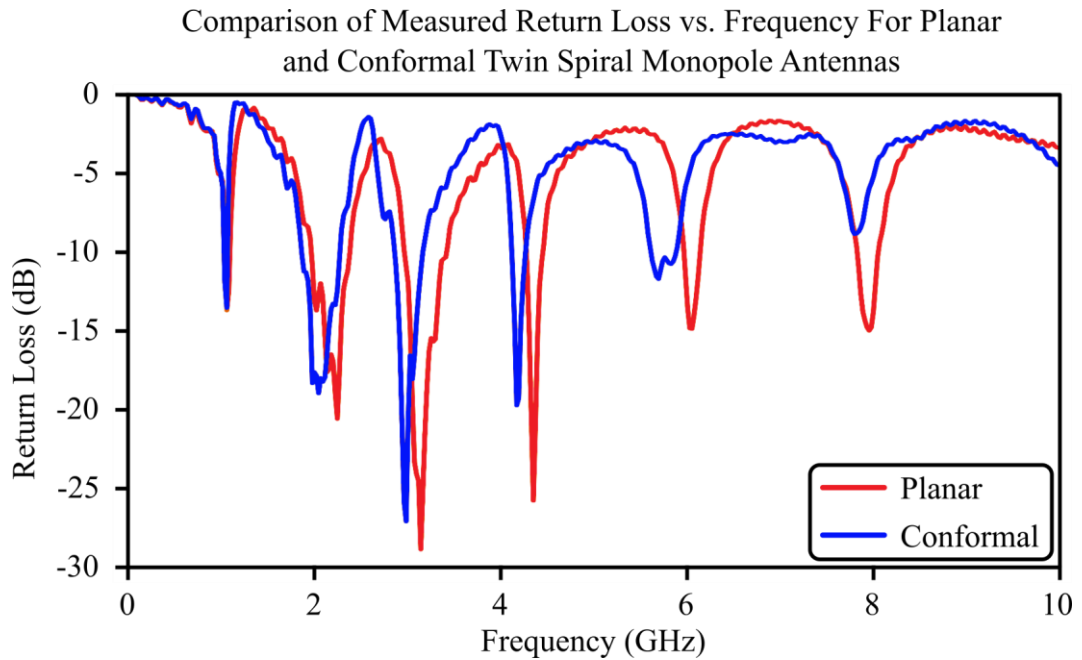


Figure 5.12: Measured return loss for the planar and conformal pill capsule antennas

The graph showed that both antennas performed similarly at all frequencies, suggesting that introducing conformality to the tracks had negligible impact on the overall function. This was particularly true at the first harmonic, which was indistinguishable between the two devices. Above 4 GHz the performance started to diverge, where the rougher surface from printing across layer lines introduced parasitic losses. For the conformal antenna, all the harmonics below 5 GHz, produced a good return loss that was than -10 dB, with the best performance of -27 dB at approximately 3 GHz. This was achieved while keeping the form factor of the capsule 45% narrower and 27% shorter, making it easier to ingest. Furthermore, the capsule was hollow and can therefore, protect any additional electronics that would be required. Conversely the open, planar part would need additional casings for protection, increasing its final size.

In addition to the return losses, the radiation pattern was simulated and shown to have a uniform, 360° coverage, as illustrated in Figure 5.13.

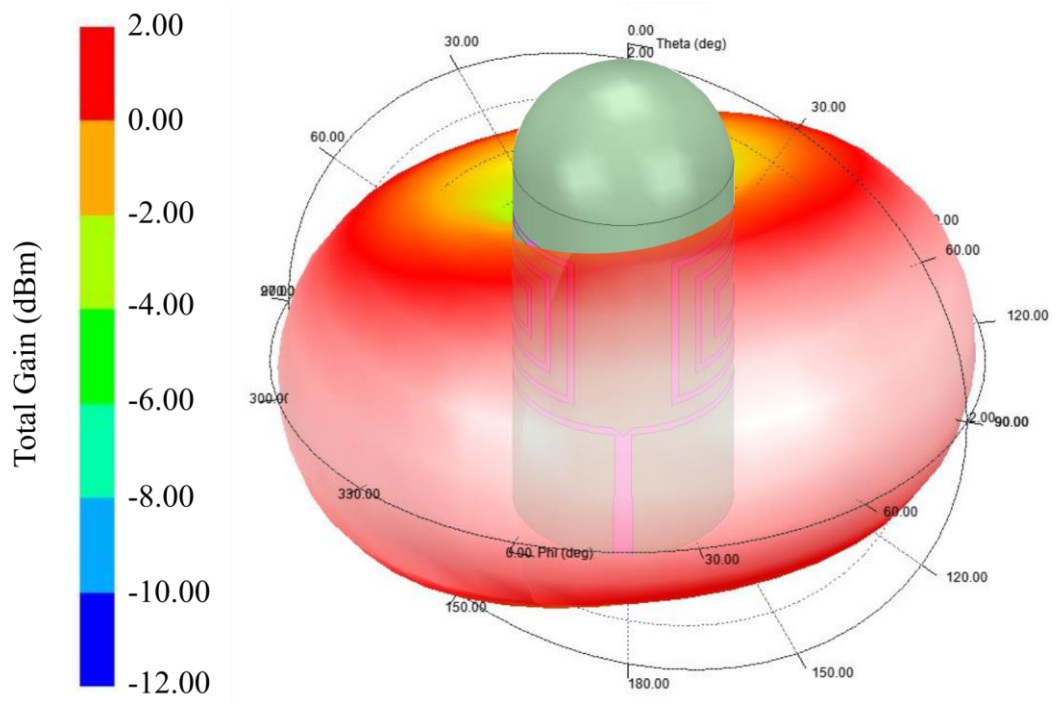


Figure 5.13: Simulated 3D radiation pattern from the pill capsule antenna

To validate the simulations, the radiation pattern was measured at the first resonant frequency (1.05 GHz). These measurements were performed using the far-field anechoic chamber facility at the University of Bradford, UK. The chamber was calibrated for a 0-dB reference level and a double-ridged, broadband horn antenna was used as the source antenna. The capsule antenna was rotated in  $5^\circ$  increments; however, due to the limitations of the chamber, the radiation pattern was only measured at a declination of  $90^\circ$  for azimuths ranging from  $-180$  to  $+180^\circ$ . The measured and simulated radiation patterns in vertical and horizontal polarisations are plotted in Figure 5.14.

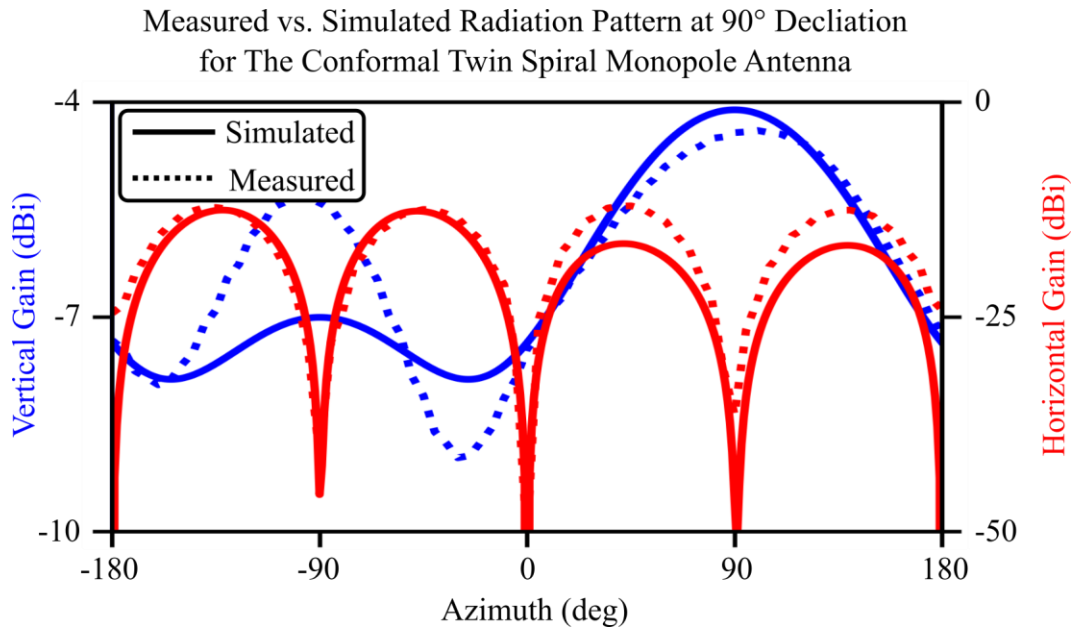


Figure 5.14: Simulated (solid lines) and measured (dotted lines), horizontal and vertical radiation patterns for the conformal pill capsule antenna

The comparison showed a close agreement between the simulated and measured results, with a perfect fit for the horizontal gain, and vertical gain, demonstrating that at the first harmonic, an omnidirectional coverage was achieved. There was some distortion to the vertical polarisation between 0 and -180° however, this was most likely caused by the relatively large, metallic connector affixed in this region.

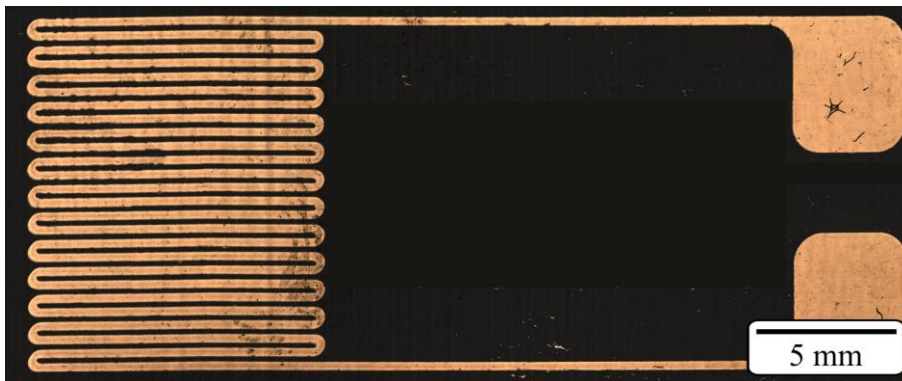
### 5.3 Flexible Devices

#### 5.3.1 Flexible Positional Sensor

An additional application that was explored with this manufacturing approach was the ability to integrate several types of sensors directly into the additively manufactured housing of devices. For example, patterning strain gauges into a smart structure to provide continual data for structural health monitoring. This could extend further to include patches of copper that use the temperature sensitivity explored in Section 4.3.2 as a low-profile thermometer. In this section, a sensor that could be directly assembled into additively manufactured articulating joints was designed and tested. The sensor operated on the same principle as a strain gauge, in that as the copper was deformed its resistance changed. By patterning the conductor onto a flexible substrate, as the object was

bent, the outer surface was placed in tension, causing the tracks to stretch and narrow fractionally, increasing the output resistance.

This demonstrator used a design with 32 meanders, modelled at 250  $\mu\text{m}$  wide with a 500  $\mu\text{m}$  pitch. They were patterned onto the same substrate type used in the fatigue testing (see Figure 3.22) with the meanders running parallel to the length of the substrate and the gauge section in the centre of the flexible region. This positioning maximised the area being stretched due to the sample buckling therefore, producing the greatest change in resistance. An example of the track used is illustrated in Figure 5.15.



*Figure 5.15: Stitched microscope image of a positional sensor's conductive elements*

As with the fatigue testing from Section 4.4, the sample had equal length, 18-Gauge wires hand-soldered to the pads and coated with cyanoacrylate adhesive and connected to an SMU (2450, Keithley). The same linear buckling rig was used, and the parts were loaded copper-side up with the clamps set 35 mm apart. They were then preloaded by 0.1 mm to prevent reflexing of the substrate during testing. Before the test was started a laser profilometer (ScanCONTROL 2900-50, Micro-Epsilon) was placed over the sample for measuring the bend radius at each compression. The rig was sent to each position and a profile was taken and processed in MATLAB to give the minimum bend radius at the centre of the flexible region. The setup is illustrated in Figure 5.16.

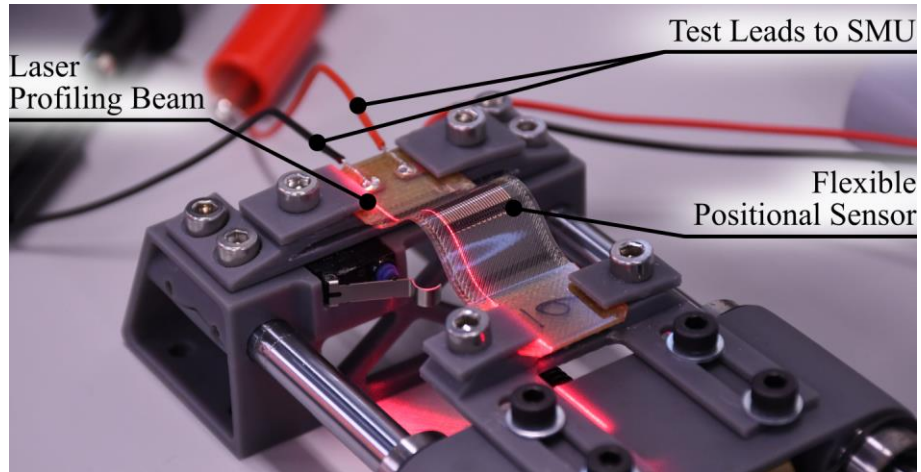


Figure 5.16: Sample loaded into the compression rig with the laser used for measuring bend radius turned on

The test cycle moved at 30 mm/s in 1.25 mm increments until a 5 mm compression was reached. At each interval, the SMU was triggered by LabVIEW to take five resistance readings and report the average. The current sourced was 10 mA and was kept active throughout the test without being shut-off between readings, to ensure the temperature increase from ohmic heating stayed constant. Based on the results in Section 4.4, was cycled 50,000 times to avoid over-fatiguing and due to the long, 26-day run-time, a single sample was tested. The raw output of the sensor normalised about the initial resistance over the full test window can be seen in Figure 5.17.

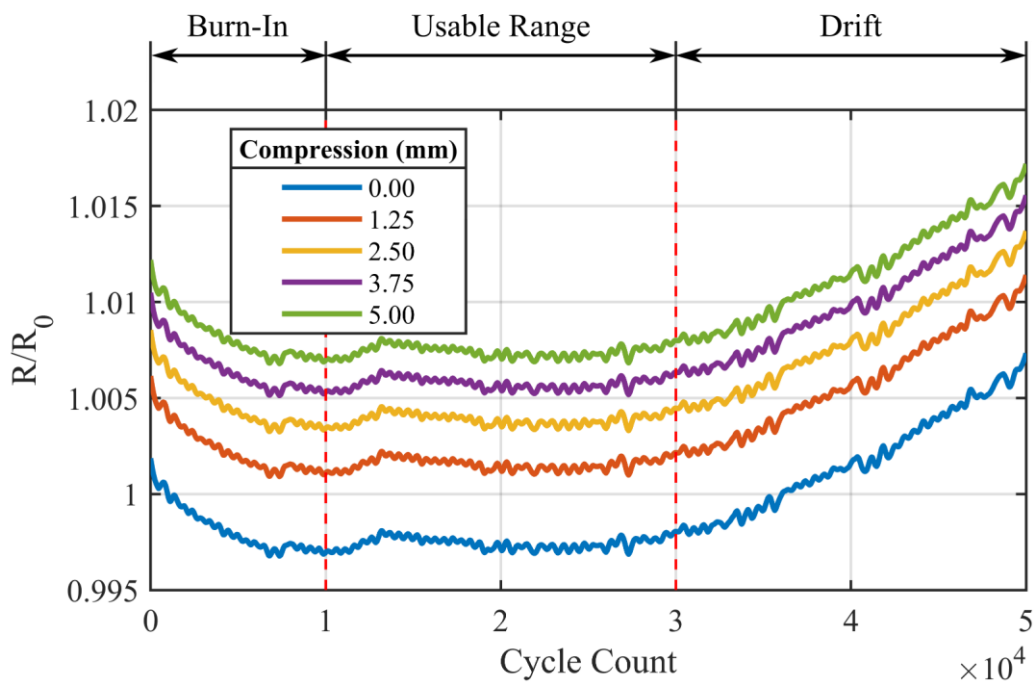


Figure 5.17: Normalised output from the positional sensor grouped by applied compression, highlighting the burn-in, usable and drift phases

What was seen were three distinct phases in the sensor's life: burn-in, a usable range, and finally drift. The reason for the burn-in phase over the first 10,000 cycles was unclear; however, changes to the copper's grain structure brought upon by the cyclic application of tensile forces could be the cause [257]. Over the next 20,000 cycles the sensor reached a plateau, where positional sensing could be achieved. Eventually, at 30,000 cycles drifting was experienced, and was likely due to work hardening and micro-cracking of the copper after repeated buckling. Additional SEM analysis should be used in the future to verify this.

Figure 5.18 shows the same data over the usable range of the sensor and grouped by applied compression. The distribution of variation across the 20,000 cycles is represented using boxplots and corresponding bend radii at the peak of the sample have been included.

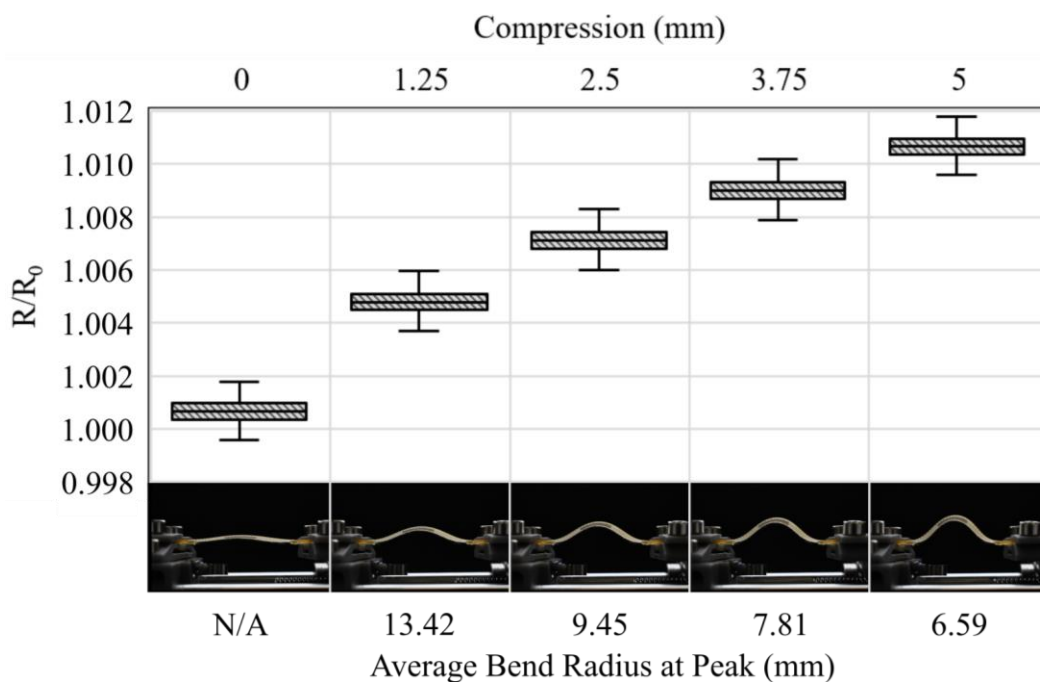


Figure 5.18: Boxplot for the positional sensor, showing the change in resistance at discrete compressions over  $20 \times 10^3$  cycles

The chart illustrates that for each bend radius, there was an upward trend in  $R/R_0$  as the bend radius decreased, with a tight grouping over the inter-quartile range. This demonstrated the viability of a compact and flexible positional sensor that could be used to measure the bend radius of a joint. Due to the drift there are data points that began to overlap, so such a sensor would either have a limited lifespan or would require increasingly periodic re-calibration.



### 5.3.2 Embedded Shape Memory Actuation

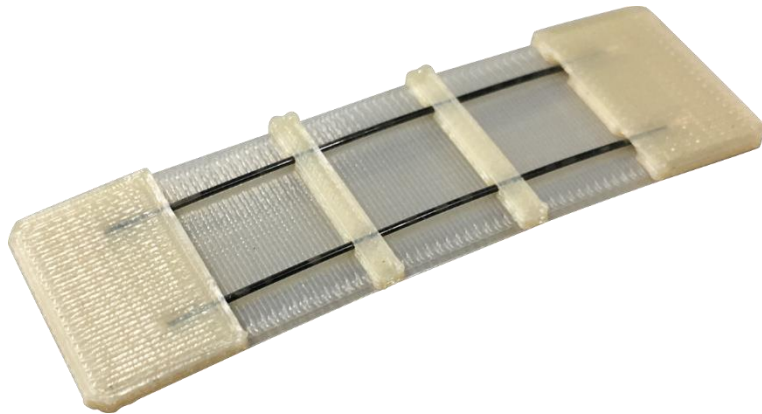
Whilst being able to print conformal electronics can save space, some situations may require the system to start in one form and transition to another. For example, the solar panels of a satellite may have to be folded for storage and launch, before being unfurled for maximum energy harvesting area once in-situ. This could be achieved using additional actuation hardware such as motors, jacks, and pulley systems; however, these take up space and add mass. This section looked to overcome these limitations by building low-profile, solid-state actuation directly into flexible PEI parts that could be controlled to take several different forms.

The concept of self-folding structures is not new, with notable bodies of work by Felton et al. [258, 259] who uses a pre-stretched polystyrene (PSPS) layer that shrunk when heated, causing their devices to change shape. The PSPS was laminated into a sandwich construction with paper and a flexible polyimide PCB that was used to controllably heat and shrink the PSPS. In locations where paper was removed from the laminate, the structure tended to fold about the cut and allowed the author to dictate the final shape of the device. As this approach used PCB's to heat the PSPS, it was fundamentally template-driven and thus had the geometric limitations.

AM of such structures has also been attempted with a significant focus on shape memory polymers [260, 261]. These materials can be printed in one form and then 'trained' to remember another so that when the heat is applied, they return to their original state. The main drawback of these polymers was that they exhibit signs of mechanical degradation after repeated cycling [262], rendering them unsuitable for critical applications and limiting them to prototype parts.

An alternative category of shape memory materials is shape memory alloys (SMA)s, which when plastically deformed, undergoes a solid-state phase change which converts the crystalline structure from a martensitic to an austenitic arrangement. When heat is applied, the alloy reverts to its martensitic phase which causes it to 'remember' its shape prior to deformation. By embedding SMAs into the rigid-flex parts demonstrated in this thesis, it was possible to

create lightweight actuating structures. Figure 5.19 shows a proof of concept, with a pair of Nitinol wires embedded into an additively manufactured PEI part.

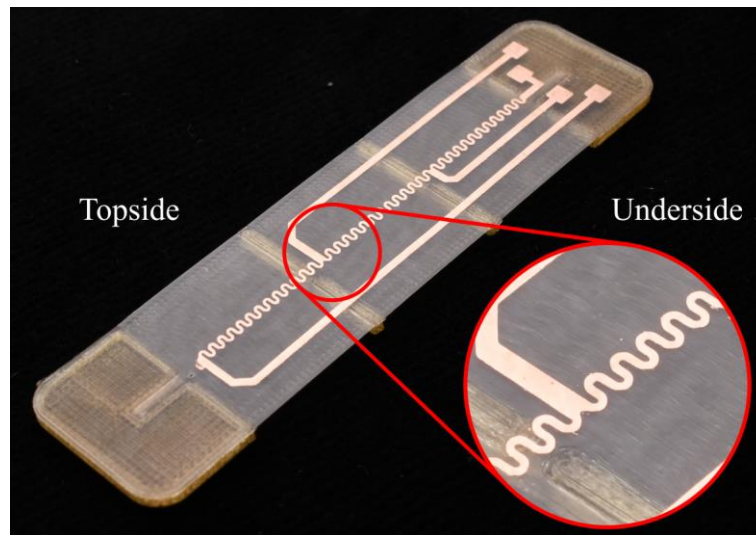


*Figure 5.19: Proof of concept for embedding Nitinol wire into Flexible additively manufactured components*

Nitinol, an alloy of nickel and titanium, is a commonly available SMA material. The wire used in this work (SmartFlex05, SAES Getters) was 500  $\mu\text{m}$  in diameter and had a maximum actuation force of 35 N. It could be formed into the shape to be remembered and held in a jig while heated to 500  $^{\circ}\text{C}$  to anneal it. When bent into any other shape after annealing, heating above 50  $^{\circ}\text{C}$  caused the wire to return to the shape it was set in. If no annealing was performed, the wire naturally straightened itself when heated. The proof of concept was produced by printing a typical rigid-flex substrate however cavities were left, into which the wire can be placed. Mid-way through, the print was paused, and the head raised to gain access to the part. The wires were then pressed into place, and the print was resumed, encapsulating them into the structure. The bridges on the part were required to keep the wires running close to the substrate and prevent them from deviating when heated. This part could be bent into any shape, yet when heat was applied to it with a hot-air gun, it returned to its flat form. This was a passive device requiring external input to actuate; however, using an approach similar to Felton et al. [258], a selectively deposited copper heating element was used to actuate the SMA.

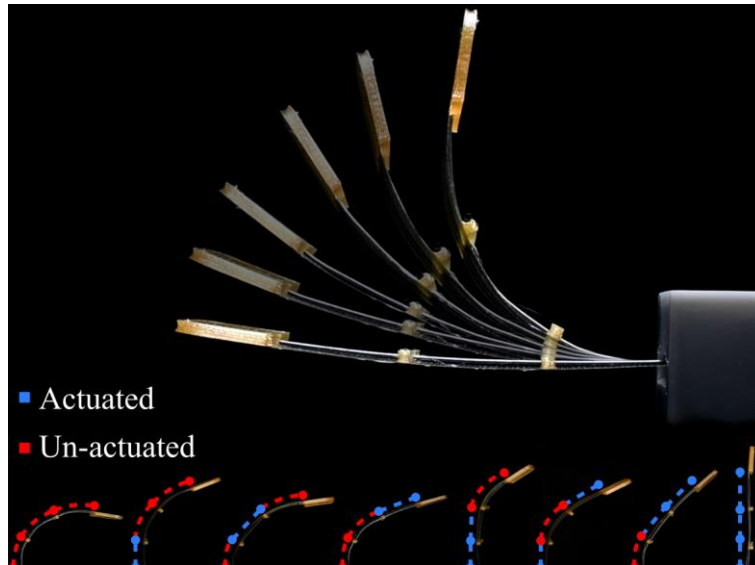
The design in Figure 5.20 uses the same mechanics as the previous part; however, it could be actuated by applying an electrical current to the copper tracks. The circuit had a narrow, repeating s-shaped track to increase its total

length and therefore, resistance. This was to ensure that the heating element would warm as opposed to the electrical connections. In addition, there were four electrical terminals that divide the heating element into three distinct regions, allowing specific segments to be targeted individually. By heating specific areas, the wire could be actuated into a total of eight configurations. To prevent the SMA wire short circuiting the heating element, the tracks were patterned onto the opposite side of the sample to the wire retention cavities. Whilst PEI is a poor thermal conductor; this design relied on the substrate being thin enough and the proximity of the wire being close enough to transfer the heat and trigger the actuation adequately.



*Figure 5.20: Multi-region Nitinol actuator, showing the shape memory wire and the circuit used to achieve localised heating*

To connect to the sample, 18-Gauge copper wire was hand-soldered to each of the four pads and attached to a programmable two-channel benchtop power supply (2220-30-1, Keithley). The setup was then clamped into a bench vice and manually bent into an arc of approximately 90°. The power supply was used to apply a current to the desired wires, heating the selected sections and causing it to deflect. Between each configuration, the wire was manually bent back to 90° and re-actuated. Figure 5.21 shows the sample first moving through its full range continuously and then selectively actuating into one of the eight possible configurations.



*Figure 5.21: Demonstration of SMA actuator moving continuously through its full range and selectively to each of the eight possible configurations. The coloured lines indicate which segments have been heated and therefore actuated*

The figure shows how this process could be used to develop actuating devices that require little space with no moving parts. Furthermore, they could be digitally controlled to take one of multiple forms.

There was a limitation in that if the wire was embedded during the print it must be trained into a flat form; otherwise, the print temperatures were enough to actuate the wire, causing it to deviate from the channels before they were encapsulated. It may be possible to use a wire with a higher actuation temperature; however, there is a greater chance of burning out the conductor or reaching the  $T_g$  of the PEI and melting the structure during operation. A more straightforward approach would be to design the part such that the wire can be set into the desired shape outside of the print and then threaded into cavities left for the component after the print had completed. Currently, motion in just one direction has been demonstrated as most SMA's do not return to their previous form when cooled, although bidirectionality can be achieved by using antagonistic pairs of SMA's [263] or bias springs [264]. Because this process allowed structures to have a tuneable stiffness by controlling their thickness, it may be possible to amalgamate a type of bias-spring into the structure by having a hinge that partially resists motion and acts as a spring.

## **5.4 Summary**

Chapter 5 set out to illustrate how the novel developments in electronics manufacture from the process described in this thesis have brought about improvements in various application areas. Using high-performance PEI substrates, for the first-time conventional SAC solder has been used to mount SMD electronic components to functional devices. The combination of AM and non-contact, laser-based patterning has enabled the integration of antennas into 3D geometries, where previously they would have to be flexible and wrapped around the structure. This coupled with the ability to embed solid state actuation directly into components offered advances space saving and design simplification. Finally, unlike some existing AM electronics fabrication methods, all these benefits were realised in a single device.

## 6 Conclusions and Future Work

### 6.1 Conclusions

This thesis has developed a digital fabrication method for high-performance three-dimensional electronic devices by combining the benefits of high-performance polymer AM and selective light-based copper deposition. The approach improves on previous bodies of work which typically compromised on either conductivity or durability which limited their application to prototyping. There were several key findings that underpinned the process.

The first was the parameters that enabled successful chemical modification of additively manufacturable PEI. It was shown that stronger hydrolysis conditions than previously reported; with a 15M KOH bath at a temperature of 80 °C and submersion times greater than 30 minutes, were required to achieve hydrolysis of the PEI. This was significant because it enabled the seeding of printable high-performance polymers, which had previously only been performed on sheet materials, not 3D geometries. During the treatments it was found that avoiding cross-contamination was essential to avoid staining or undesirable copper deposits on the samples. Ultrasonic washing for 10 minutes in de-ionised water was discovered to be effective at clearing remaining chemicals that had been trapped in the hatch off FFF parts. The main limitation of the testing method was that only the impact on the reduction of silver ions was explored rather than how this influenced the final copper deposits. Additionally, because the inspection was visual, the degree of hydrolysis is not fully understood. Use of more advanced methods like Fourier-transform infrared spectroscopy would have given a quantifiable measure of the surface imide content and therefore, completeness of hydrolysis.

The second finding was that increasing the exposure of treated PEI to 405nm radiation improved copper coverage to an extent, but overexposure led to polymer degradation and raised blistering of the copper, weakening its bond. The ideal processing window was found to be an area related energy density between 2.34 J/cm<sup>2</sup> and 2.55 J/cm<sup>2</sup>, which was controlled by varying the speed, power, and number of passes of the patterning laser. This was also varied using

the hatch spacing; however, altering the spacing between laser passes without matching the lasers spot size could result in un-patterned areas between scanlines. The importance of this finding was that it prevented unnecessary weakening of the copper adhesion and gave an indication of the processing times that can be expected when using a laser patterning technique. For the explored approach, the patterning rate was found to be approximately  $2 \text{ cm}^2/\text{hour}$  and the size of the pattern directly controls the processing time, resulting in a poor process scalability. There are two potential approaches for improving the scalability: increasing the reduction rate and selective bulk exposure. Improvements in reduction rates have already been development by the collaborative partners [32, 264, 265] of the Photobioform project through the application of a plant-based extract to the substrates before patterning. Using this they were able to increase the rate of reaction by an order of magnitude without altering the UV exposure. By lowering the energy requirement, this technique may also help reduce the chances of polymer degradation. Alternatively, patterning hardware based on digital micromirror devices that can project an entire pattern simultaneously could be used instead of galvanometer scanning. Bulk exposure would remove the relationship between time and pattern size meaning that large circuits would take no additional time over smaller circuits. Another observation was a variability in the plating quality, and because single samples were used to establish the processing window this variability cannot be attributed to any one stage.

The next finding was that the fine-grain electroless copper deposition was able to successfully bridge the hatch line and stair-step induced topology of the FFF parts. This was central to the process as it ensured the conductor could conform to the surface of 3D geometries without breaks in the tracks. Furthermore, this was produced without the need for additional post-processing such as grit-blasting to remove surface features that have been required in previous examples with FFF PEI substrates. Four-point probe and white light interferometry measurements of the conductor found a bulk conductivity of  $3.81 \times 10^7 \text{ S/m}$  at a thickness of 559 nm. Except for wire embedding, this was better than the alternative hybrid AM approaches published to-date and on-par with laser direct

structuring. Tape peel testing of the copper showed good adhesion to the polymer, a result later supported by fatigue testing of flexible devices. After 50,000 cycles of bending, the copper remained attached to the substrate and due to its ductility showed less than 1% change in resistance.

Regarding the AM of PEI, it was found that by producing thin layers a flexible substrate could be created that could be bent to a radius of 6.7 mm and back more than 60,000 times before failing. The failure mode of all samples tested was crack propagation parallel to the bending axis along the hatch of the printed part. The indication was that this might not be the upper limit to fatigue performance and altering the hatch orientation so that it does not align to the bending axis might discourage crack formation. The printing of both rigid and flexible substrates as one is significant as it allows devices to be built as one-piece, simplifying designs, and removing connectors and potential failure points. Furthermore, this is a novel finding and has to-date not been demonstrated in the literature.

The final enabling scientific finding was that printable PEI can withstand a solder reflow at temperatures above its  $T_g$  with minimal deformation, provided it was printed in a heated build environment. This was shown to be true for a SAC solder reflow process with a peak temperature of 249 °C, on parts printed in a 120 °C build chamber. The significance of this was for the first time, AM electronics were compatible, conventional soldering methods and allowed a durable and highly conductive bond to be formed between all elements of an AM electronic device. Previously AM electronics have relied on conductive epoxies or DW of silver inks to connect to the bond pads of the components, both of which offer either lower conductivity or adhesion. The main limitation of the testing was the lack of verification using self-supporting geometries like overhangs or bridges that may sag when elevated above the polymers  $T_g$ . Additionally, sectioning of the solder joints would have helped validate their overall quality.

The additional achievements of this thesis were:

- The engineering of a low-cost, high-temperature FFF printer.



- The characterisation of mechanical, fatigue and electrical performance for the substrates and circuitry.
- The production of process demonstrators illustrating the building blocks for increased functionality including working circuits, conformal and double-sided RF antennae, flexible sensors, and embedded actuators.

The inverted, open chamber design of the FFF printer illustrated the potential of such designs for reducing the cost of high-temperature desktop AM. Parts produced demonstrated a dimensional accuracy close to existing designs but with fewer extrusion artefacts and an objectively higher quality surface finish. Increasing the temperature within the chamber was shown to improve the UTS of PEI parts whilst simultaneously reducing warping, although not eliminating it completely. Through selective control of substrate thickness rigid-flex boards were produced as a single assembly without the need for connectors or post processing. These substrates were fatigue tested in compression and found to withstand between 60 and 70 thousand cycles before showing signs of splitting near the step change in thickness.

The focal depth of the laser was used to successfully pattern curved and sloped surfaces without re-focussing the beam. The hardware was limited as only areas immediately visible to the optical path could be patterned and extreme slopes introduced distortion to designs. This was mitigated with the introduction of a manual rotary stage that was effective in producing continuous, 360° features. The inability to pattern faces parallel to the beam also introduced challenges when forming through-hole vias, as the seed site could not be readily formed. This was solved by sealing vias during the ion removal, leaving them for subsequent plating alongside the patterned regions. The configuration used also restricted the vertical change in height of patterns as it relied on the depth of focus of the laser which only extended a few mm either side of the central focus point. All three of these issues could be avoided by using a 4 or 5-axis setup that would allow the part to be moved relative to the laser. The smallest tracks produced were 301  $\mu\text{m}$  wide; however, the pattern in software was 250  $\mu\text{m}$ , indicating that either the plating builds outwards as well as upwards, or the laser

size and position is poorly calibrated. Going forward it would be important to measure and account for this, potentially leading to improvements in patterning accuracy and minimum feature size. Added experimentation with a photomask also demonstrated that the chemical modification approach could create features 23 times smaller with upgrades to the laser system.

The manufacturing approach reported in this thesis has overcome the main challenges previously restricting AM electronics. Devices produced have exhibited improvements in both conductivity and durability compared to previous methods, while retaining the geometric freedoms of digitally driven processing. Furthermore, novel functionality in the form of integrated flexible electronics, sensing and actuation have been demonstrated.

## **6.2 Future Work**

The focus of this research has been proving the feasibility of a new manufacturing process. While the building blocks for a transformative process have been successfully demonstrated, there are several key areas that could improve its applicability to industry.

As discussed in Section 4.2.3, the wavelength of light used can theoretically be focused to a minimum spot size of 202.5 nm; therefore, the density of circuitry can be increased. This would necessitate enhanced laser optics and software that provides additional control over laser positioning. Traditional PCB fabrication has made use of 3D routed multilayer boards to increase the density of circuitry. A repeat processing approach that accepts completed substrates and prints over them may be able to accomplish the same objective. Alternatively, it enables the embedding of electronics, which coupled with the characteristics of PEI could be used to manufacture devices for operating in harsh environments. Multilayer boards were briefly explored during the thesis however it was found that after the PEI hydrolysis, subsequent printing would not adhere to the treated material. Work by the collaborative partners on the Photobioform project has shown that reimidisation of the PEI can be performed which may overcome this challenge.

The advantages of conformal circuitry have been discussed at length; nevertheless, the configuration applied in this work could only pattern areas directly exposed to the optical path. By mounting the patterning hardware to four or five-axis stages fully 3D patterning could be realised, enabling the production of more complex devices. Being able to rotate relative to the path of the laser would also enable digitally driven manufacture of through-hole vias as opposed to the manual technique presently employed.

The thickness of the copper deposition was restricted by the bath formulation used for plating however, the surface chemistry will act as seed for a wide range of electroless plating baths. A dedicated composition should be able to increase the thickness, although using the existing metal as a precursor and re-plating with electrolytic copper might be a more effective route. Modification to the plating bath could also be exploited for introducing new metals and thus functionality; such as gold, for increased corrosion resistance and under bump metallisation. This could also be achieved through the selective synthesis of alternative metallic nanoparticles such as palladium, nickel, chromium and cobalt [265].

The soldering methods from Section 4.5 were not optimised for the substrate/conductor combination. Before the process could be adopted by industry, long-term characterisation such as accelerated aging needs to be performed. Moreover, the ability to solder onto sloped surfaces without component slippage was not quantified and may require additional adhesives to hold parts in place. Understanding this will enable the creation of truly 3D packages.

Another feature that aids with solderability in conventional PCB's is the application of a solder mask that prevents solder spreading along the tracks and pads from bridging across one another. These are usually applied and etched using lithographic techniques that share the same disadvantages as PCB etching, making them incompatible with this process. Further hybridisation with DW methods such as AJP [266] offers a potential solution due to the wide range of printable viscosities and usable standoff heights.

With respect to PEI printing, improvements to the mechanical strength and warping performance were seen with elevated chamber temperatures, however neither reached their full potential. The suspected cause was the inability to reach the 200 °C build environment temperature used in industrial FFF printers, which was in large due to the circulation fan drawing cold air into the printer. The fan could not be removed as circulation over the heater is required, but a more suitable method might be to use a high-temperature recirculation blower, like those used in fan ovens. Another potential cause of the warping could be thermal gradients in the X-Y plane introduced by the positioning the heater in one corner of the chamber. There is minimal literature on the effects of lateral thermal gradients on FFF printed parts; therefore, would add value to the wider community.

Although the process was unaffected by the layer-induced roughness of the FFF substrate, some electrical applications such as high-frequency RF perform better with conductors that have a smooth surface finish. This could be optimised through tweaks in the slicer or the use of a finer nozzle; however, a high-quality surface could also be achieved with curved layer slicing [267, 268]. Selective smoothing is another option, whereby only regions that require a pristine surface are altered. Machining has been demonstrated on printed PEI [208] and could be integrated into the printer for removing layering artefacts where necessary.

In Section 5.3 two flexible devices; a sensor and an actuator, were investigated to test their feasibility. While capable of taking multiple forms, the actuator could only move in one direction limiting its useful applications. In existing designs, antagonistic pairs of SMA wires [269, 270] or bias springs [271, 272] have regularly been employed to return the device to its resting state after actuation. It may be possible however, by altering the thickness of the printed PEI to tune the stiffness of the hinge, allowing it to perform the role of a bias spring without taking additional space. Furthermore, introducing the sensor design to the same component would enable positional feedback and greater control of the device.

## References

1. Zion Market Research. *Consumer Electronics Market by Product (Smartphone, Television, DVD players, Refrigerators, Washing machines, Digital cameras, and Hard disk drives) and by Region (North America, Europe, Asia Pacific, Latin America, and the Middle East & Africa) - Global*, 2018.
2. Jon, V. Making Printed Circuit Boards, In: *Fabricating Printed Circuit Boards*. 2002, pp.69–87.
3. Tu, K.-N. *Solder Joint Technology*, New York, NY: Springer New York, 2007.
4. Tamin, M.N. and Shaffiar, N.M. *Solder Joint Reliability Assessment*, Cham: Springer International Publishing, 2014.
5. Mack, C.A. Fifty Years of Moore's Law. *IEEE Transactions on Semiconductor Manufacturing*. 2011, **24**(2), pp.202–207.
6. Li, M.-Y., Su, S.-K., Wong, H.-S.P. and Li, L.-J. How 2D semiconductors could extend Moore's law. *Nature*. 2019, **567**(7747), pp.169–170.
7. Prasad, R.P. *Surface Mount Technology*, Boston, MA: Springer US, 1997.
8. Tu, K.-N. and Liu, Y. Recent advances on kinetic analysis of solder joint reactions in 3D IC packaging technology. *Materials Science and Engineering: R: Reports*. 2019, **136**(September 2018), pp.1–12.
9. Garrou, P. Wafer level chip scale packaging (WL-CSP): an overview. *IEEE Transactions on Advanced Packaging*. 2000, **23**(2), pp.198–205.
10. Burgess, L.W. *Multilayer circuit board manufacturing*, US4642160A, 1985.
11. International Organization for Standardization. *ISO/ASTM 52900:2015. Additive Manufacturing - General Principles - Terminology*. ISO/ASTM, 2015.

12. Wohlers, T.T., Campbell, R.I. and Caffrey, T. *Wohlers Report 2016: 3D Printing and Additive Manufacturing State of the Industry: Annual Worldwide Progress Report*, Fort Collins, CO: Wohlers Associates, Inc., 2016.
13. Vaidya, S., Ambad, P. and Bhosle, S. Industry 4.0 – A Glimpse. *Procedia Manufacturing*. 2018, **20**, pp.233–238.
14. Ceruti, A., Marzocca, P., Liverani, A. and Bil, C. Maintenance in Aeronautics in an Industry 4.0 Context: The Role of Augmented Reality and Additive Manufacturing. *Journal of Computational Design and Engineering*. 2019.
15. Konzept Analytics. *Global 3D Printing (Additive Manufacturing) Market: Insights, Trends and Forecasts (2019-2023)*, 2019.
16. Global 360° Research Team (Frost and Sullivan). *Global Additive Manufacturing Market, Forecast to 2025*, 2016.
17. Ikeda, S., Akamatsu, K. and Nawafune, H. Direct photochemical formation of Cu patterns on surface modified polyimide resin. *Journal of Materials Chemistry*. 2001, **11**(12), pp.2919–2921.
18. Akamatsu, K., Ikeda, S. and Nawafune, H. Site-Selective Direct Silver Metallization on Surface-Modified Polyimide Layers. *Langmuir*. 2003, **19**(24), pp.10366–10371.
19. Nawafune, H., Nishioka, T., Tsuji, H., Mizumoto, S., Seita, M. and Kusaka, M. Basic Study for Direct Metallization Using Surface Modification of Polyimide and Epoxy Resin. *Journal of Japan Institute of Electronics Packaging*. 1999, **2**(5), pp.390–393.
20. Ji, E.S., Kim, Y.H., Kang, Y.C., Kang, Y.S. and Ahn, B.H. Plating of Copper Layers on Polyimides Using Electroless Plating by Surface Modification. *Surface Review and Letters*. 2007, **14**(04), pp.593–596.

21. Watson, D.E.G., Ng, J.H.-G., Aasmundtveit, K.E. and Desmulliez, M.P.Y. In-Situ Silver Nanoparticle Formation on Surface-Modified Polyetherimide Films. *IEEE Transactions on Nanotechnology*. 2014, **13**(4), pp.736–742.
22. Ng, J.H.-G., Desmulliez, M.P.Y., Prior, K.A. and Hand, D.P. Ultra-Violet Direct Patterning of Metal on Polyimide. *Micro & Nano Letters*. 2008, **3**(3), p.82.
23. Danto, Y., Deletage, J.Y., Verdier, F. and Fremont, H. Evolution of reliability assessment in PCB assemblies, In: *Proceedings of the SBMicroelectronics Conference*. 2001, .
24. Ikeda, S., Kobayashi, Y., Fujiwara, Y., Akamatsu, K. and Nawafune, H. All-Wet Metallization Process for Transparent Polyimide Films. *Journal of Physics: Conference Series*. 2013, **417**(1), p.012019.
25. Ng, J.H.-G., Watson, D.E.G., Sigwarth, J., McCarthy, A., Prior, K.A., Hand, D.P., Yu, W., Kay, R.W., Liu, C. and Desmulliez, M.P.Y. On the Use of Silver Nanoparticles for Direct Micropatterning on Polyimide Substrates. *IEEE Transactions on Nanotechnology*. 2012, **11**(1), pp.139–147.
26. Ng, J.H.-G., Desmulliez, M.P.Y., Lamponi, M., Moffat, B.G., Walker, A.C., McCarthy, A., Suyal, H., Prior, K.A. and Hand, D.P. UV Direct-Writing of Metals on Polyimide Substrates, In: *Proceedings - 2008 2nd Electronics Systemintegration Technology Conference, ESTC*. 2008, pp.691–694.
27. Chen, D., Lu, Q. and Zhao, Y. Laser-Induced Site-Selective Silver Seeding on Polyimide for Electroless Copper Plating. *Applied Surface Science*. 2006, **253**(3), pp.1573–1580.
28. Ng, J.H.-G., Watson, D.E.G., Sigwarth, J., McCarthy, A., Suyal, H., Hand, D.P., Hin, T.Y. and Desmulliez, M.P.Y. An Additive Method for Photopatterning of Metals on Flexible Substrates, In: Hinduja, S. and Li, L. eds. *Proceedings of the 36th International MATADOR Conference*. London: Springer London, 2010, pp.389–392.

29. Rayleigh, F.R.S. XXXI. Investigations in optics, with special reference to the spectroscope. *The London, Edinburgh, and Dublin Philosophical Magazine and Journal of Science*. 1879, **8**(49), pp.261–274.
30. Wang, Z., Furuya, A., Yasuda, K., Ikeda, H., Baba, T., Hagiwara, M., Toki, S., Shingubara, S., Kubota, H. and Ohmi, T. Adhesion Improvement of Electroless Copper to a Polyimide Film Substrate by Combining Surface Microroughening and Imide Ring Cleavage. *Journal of Adhesion Science and Technology*. 2002, **16**(8), pp.1027–1040.
31. Ng, J.H.-G., Desmulliez, M.P.Y., Lamponi, M., Moffat, B.G., McCarthy, A., Suyal, H., Walker, A.C., Prior, K.A. and Hand, D.P. A Direct-Writing Approach to the Micro-Patterning of Copper Onto Polyimide. *Circuit World*. 2009, **35**(2), pp.3–17.
32. Marques-Hueso, J., Jones, T.D.A., Watson, D.E.G., Ryspayeva, A., Esfahani, M.N., Shuttleworth, M.P., Harris, R.A., Kay, R.W. and Desmulliez, M.P.Y. A Rapid Photopatterning Method for Selective Plating of 2D and 3D Microcircuitry on Polyetherimide. *Advanced Functional Materials*. 2018, **28**(6), p.1704451.
33. Redwood, B., Schöffler, F. and Garret, B. *The 3D Printing Handbook: Technologies, Design and Applications*, 3D Hubs B.V., 2017.
34. Crump, S.S. Apparatus and method for creating three-dimensional objects, US5121329A, 1989.
35. Jones, R., Haufe, P., Sells, E., Iravani, P., Olliver, V., Palmer, C. and Bowyer, A. Reprap - The replicating rapid prototyper. *Robotica*. 2011, **29**(1 SPEC. ISSUE), pp.177–191.
36. Fiedler, M. Evaluating Tension and Tooth Geometry to Optimize Grip on 3D Printer Filament. *3D Printing and Additive Manufacturing*. 2015, **2**(2), pp.85–88.



37. Agarwala, M.K., Jamalabad, V.R., Langrana, N.A., Safari, A., Whalen, P.J. and Danforth, S.C. Structural quality of parts processed by fused deposition. *Rapid Prototyping Journal*. 1996, **2**(4), pp.4–19.
38. Volpato, N., Kretschek, D., Foggiatto, J.A. and Gomez da Silva Cruz, C.M. Experimental analysis of an extrusion system for additive manufacturing based on polymer pellets. *The International Journal of Advanced Manufacturing Technology*. 2015, **81**(9–12), pp.1519–1531.
39. Bellini, A., Shor, L. and Guceri, S.I. New developments in fused deposition modeling of ceramics. *Rapid Prototyping Journal*. 2005, **11**(4), pp.214–220.
40. Liu, X., Chi, B., Jiao, Z., Tan, J., Liu, F. and Yang, W. A large-scale double-stage-screw 3D printer for fused deposition of plastic pellets. *Journal of Applied Polymer Science*. 2017, **134**(31), p.45147.
41. Dyze Design. Pulsar Pellet Extruder: Industrial High Flow Extruder - DYZE DESIGN. [Online] 2019. [Accessed November 30, 2019]. Available from: <https://dyzedesign.com/pulsar-pellet-extruder/#plastics-other>.
42. ARBURG. freeformer system: Using tiny droplets to create fully functional parts. [Online] No date. [Accessed May 12, 2020]. Available from: <https://www.arburg.com/products-and-services/additive-manufacturing/freeformer-system/>.
43. Go, J. and Hart, A.J. Fast Desktop-Scale Extrusion Additive Manufacturing. *Additive Manufacturing*. 2017, **18**, pp.276–284.
44. Kumar, N., Jain, P.K., Tandon, P. and Pandey, P.M. Investigation on the effects of process parameters in CNC assisted pellet based fused layer modeling process. *Journal of Manufacturing Processes*. 2018, **35**(December 2017), pp.428–436.
45. Lužanin, O., Movrin, D. and Plan, M. Experimental Investigation of Extrusion Speed and Temperature Effects on Arithmetic Mean Surface Roughness in Fdm-. *Journal of Technology of Plasticity*. 2013, **38**(2), pp.179–190.

46. Zinniel, R.L. and Batchelder, J.S. Volumetric feed control for flexible filament, US6085957A, No date.
47. Bellini, A., Gucceri, S. and Bertoldi, M. Liquefier Dynamics in Fused Deposition. *Journal of Manufacturing Science and Engineering*. 2004, **126**(2), pp.237–246.
48. Saini, P., Garg, D. and Choudhury, T. 3D Printing: Factors Influencing its Quality and Nature, In: *2018 International Conference on Computational Techniques, Electronics and Mechanical Systems (CTEMS)*. IEEE, 2018, pp.480–486.
49. Rigid.Ink. Ultimate 3D Print Quality Troubleshooting Guide 2018. [Online] 2018. [Accessed Available from: .
50. Kumar, M., Singh Verma, K. and Nagpure, S. Numerical Simulation of Rep-Rap 3D Printer Liquefier to Determine the Thermal Behavior of Heat Sink. *International Journal for Scientific Research & Development*. 2017, **5**(1), pp.2321–0613.
51. Turner, B.N. and Gold, S.A. A review of melt extrusion additive manufacturing processes: II. Materials, dimensional accuracy, and surface roughness. *Rapid Prototyping Journal*. 2015, **21**(3), pp.250–261.
52. E3D-Online. E3D Experimental Nozzles | Buy Online at E3D | E3D Online. [Online] No date. [Accessed December 1, 2019]. Available from: <https://e3d-online.com/experimental-nozzles>.
53. Michaeli, W. *Extrusion Dies for Plastics and Rubber*, 3rd ed. München: Carl Hanser Verlag GmbH & Co. KG, 2003.
54. Ramanath, H.S., Chua, C.K., Leong, K.F. and Shah, K.D. Melt flow behaviour of poly-ε-caprolactone in fused deposition modelling. *Journal of Materials Science: Materials in Medicine*. 2008, **19**(7), pp.2541–2550.
55. Ultimaker BV. Ultimaker S5: Reliability at Scale. [Online] No date. [Accessed January 7, 2020]. Available from: <https://ultimaker.com/3d-printers/ultimaker-s5>.

56. Stratasys Ltd. Stratasys F123 Series Printers. [Online] No date. [Accessed January 7, 2020]. Available from: <https://www.stratasys.com/3d-printers/fl23>.
57. Griffiths, C.A., Howarth, J., Rowbotham, G. de-A. and Rees, A. Effect of Build Parameters on Processing Efficiency and Material Performance in Fused Deposition Modelling. *Procedia CIRP*. 2016, **49**, pp.28–32.
58. Coogan, T.J. and Kazmer, D.O. Bond and part strength in fused deposition modeling. *Rapid Prototyping Journal*. 2017, **23**(2), pp.414–422.
59. Raney, K., Lani, E. and Kalla, D.K. Experimental characterization of the tensile strength of ABS parts manufactured by fused deposition modeling process. *Materials Today: Proceedings*. 2017, **4**(8), pp.7956–7961.
60. Anzalone, G.C., Wijnen, B. and Pearce, J.M. Multi-material additive and subtractive prosumer digital fabrication with a free and open-source convertible delta RepRap 3-D printer. *Rapid Prototyping Journal*. 2015, **21**(5), pp.506–519.
61. Sollmann, K.S., Jouaneh, M.K. and Lavender, D. Dynamic Modeling of a Two-Axis, Parallel, H-Frame-Type XY Positioning System. *IEEE/ASME Transactions on Mechatronics*. 2010, **15**(2), pp.280–290.
62. Moyer, I.E. CoreXY Theory. [Online] 2012. [Accessed November 23, 2019]. Available from: <https://corexy.com/theory.html>.
63. Clavel, R. Device for the movement and positioning of an element in space, US4976582A, 1985.
64. Okabe, E.P. and Masarati, P. Modeling and Simulation of a 3D Printer Based on a SCARA Mechanism, In: *Computational Methods in Applied Sciences*. 2016, pp.93–114.
65. Vischer, P. and Clavel, R. Kinematic calibration of the parallel Delta robot. *Robotica*. 1998, **16**(2), pp.207–218.
66. Pierrot, F., Reynaud, C. and Fournier, A. DELTA: a simple and efficient parallel robot. *Robotica*. 1990, **8**(2), pp.105–109.

67. Smoothiware. Smoothiware - Documentation. [Online] No date. [Accessed November 23, 2019]. Available from: <http://smoothiware.org/>.
68. Duet3D. Duet 2 Wifi. [Online] No date. [Accessed November 23, 2019]. Available from: <https://www.duet3d.com/DuetWifi>.
69. Wilson, M. Industrial Robots, In: *Implementation of Robot Systems*. Elsevier, 2015, pp.19–38.
70. McClintock, H., Temel, F.Z., Doshi, N., Koh, J. and Wood, R.J. The milliDelta: A high-bandwidth, high-precision, millimeter-scale Delta robot. *Science Robotics*. 2018, **3**(14), p.eaar3018.
71. Liu, Z., Wang, Y., Wu, B., Cui, C., Guo, Y. and Yan, C. A critical review of fused deposition modeling 3D printing technology in manufacturing polylactic acid parts. *The International Journal of Advanced Manufacturing Technology*. 2019, **102**(9–12), pp.2877–2889.
72. Gordelier, T.J., Thies, P.R., Turner, L. and Johanning, L. Optimising the FDM additive manufacturing process to achieve maximum tensile strength: a state-of-the-art review. *Rapid Prototyping Journal*. 2019, **25**(6), pp.953–971.
73. Gilbert, M. and Brydson, J.A. *Brydson's Plastics Materials*, 8th ed. Elsevier, 2017.
74. Spoerk, M., Holzer, C. and Gonzalez-Gutierrez, J. Material extrusion-based additive manufacturing of polypropylene: A review on how to improve dimensional inaccuracy and warpage. *Journal of Applied Polymer Science*. 2019, **137**(12), p.48545.
75. Ligon, S.C., Liska, R., Stampfl, J., Gurr, M. and Mülhaupt, R. Polymers for 3D Printing and Customized Additive Manufacturing. *Chemical Reviews*. 2017, **117**(15), pp.10212–10290.

76. He, J., Chen, J., Hellwich, K.-H., Hess, M., Horie, K., Jones, R.G., Kahovec, J., Kitayama, T., Kratochvíl, P., Meille, S. V., Mita, I., dos Santos, C., Vert, M. and Vohlídal, J. Abbreviations of polymer names and guidelines for abbreviating polymer names (IUPAC Recommendations 2014). *Pure and Applied Chemistry*. 2014, **86**(6), pp.1003–1015.
77. 3DXTech. ThemaX™ PEI 3D Filament, Made Using ULTEM™ 9085. [Online] No date. [Accessed July 15, 2019]. Available from: <https://www.3dxtech.com/thermax-pei-3d-filament-made-using-ultem-9085/>.
78. 3DXTech. ThermaX™ PEEK 3D Printing Filament [Natural]. [Online] No date. [Accessed July 15, 2019]. Available from: <https://www.3dxtech.com/thermax-peek-3d-printing-filament-natural/>.
79. Yang, C., Tian, X., Li, D., Cao, Y., Zhao, F. and Shi, C. Influence of thermal processing conditions in 3D printing on the crystallinity and mechanical properties of PEEK material. *Journal of Materials Processing Technology*. 2017, **248**(January), pp.1–7.
80. Jin, L., Ball, J., Bremner, T. and Sue, H.-J. Crystallization behavior and morphological characterization of poly(ether ether ketone). *Polymer*. 2014, **55**(20), pp.5255–5265.
81. Panda, B.N., Shankhwar, K., Garg, A. and Jian, Z. Performance evaluation of warping characteristic of fused deposition modelling process. *The International Journal of Advanced Manufacturing Technology*. 2017, **88**(5–8), pp.1799–1811.
82. Fitzharris, E.R., Watanabe, N., Rosen, D.W. and Shofner, M.L. Effects of material properties on warpage in fused deposition modeling parts. *The International Journal of Advanced Manufacturing Technology*. 2018, **95**(5–8), pp.2059–2070.
83. Turner, B.N., Strong, R. and Gold, S.A. A review of melt extrusion additive manufacturing processes: I. Process design and modeling. *Rapid Prototyping Journal*. 2014, **20**(3), pp.192–204.

84. Singh, K. Experimental study to prevent the warping of 3D models in fused deposition modeling. *International Journal of Plastics Technology*. 2018, **22**(1), pp.177–184.
85. Wang, T.M., Xi, J.T. and Jin, Y. A model research for prototype warp deformation in the FDM process. *International Journal of Advanced Manufacturing Technology*. 2007, **33**(11–12), pp.1087–1096.
86. Swanson, W.J., Turley, P.W., Leavitt, P.J., Karwoski, P.J., LaBossiere, J.E. and Skubic, R.L. High Temperature Modeling Apparatus, US6722872B1, 2004.
87. MiniFactory. miniFactory Ultra. [Online] No date. [Accessed July 15, 2019]. Available from: <https://minifactory.fi/3d-printer/>.
88. Apium Additive Technologies GmbH. Apium P220 Series. [Online] No date. [Accessed July 15, 2019]. Available from: <https://apiumtec.com/en/industrial-3d-printer>.
89. Intamsys. FUNMAT HT. [Online] No date. [Accessed July 16, 2019]. Available from: <https://www.intamsys.com/funmat-ht-3d-printer/>.
90. Tractus3D. The most advanced High Temperature PEEK 3D printers in the market. [Online] No date. [Accessed July 16, 2019]. Available from: <https://tractus3d.com/our-industrial-3d-printers/peek-3d-printer/>.
91. Gardner, J.M., Stelter, C.J., Yashin, E.A. and Siochi, E.J. High Temperature Thermoplastic Additive Manufacturing Using Low-Cost, Open-Source Hardware. *NASA STI Program*. 2016.
92. Chuang, K.C., Grady, J.E., Draper, R.D., Patterson, C. and Santelle, T.D. Additive Manufacturing and Characterization of Ultem Polymers and Composites, In: *The Composites and Advanced Materials Expo*. 2015, p.15.
93. Halidi, S.N.A.M. and Abdullah, J. Moisture effects on the ABS used for Fused Deposition Modeling rapid prototyping machine, In: *2012 IEEE Symposium on Humanities, Science and Engineering Research*. IEEE, 2012, pp.839–843.

94. Lewis, J.A. and Gratson, G.M. Direct writing in three dimensions. *Materials Today*. 2004, **7**(7), pp.32–39.
95. Piqué, A. and Chrisey, D. *Direct-Write Technologies for Rapid Prototyping*, Elsevier, 2002.
96. Hon, K.K.B., Li, L. and Hutchings, I.M. Direct writing technology- Advances and developments. *CIRP Annals - Manufacturing Technology*. 2008, **57**(2), pp.601–620.
97. Martin, G.D., Hoath, S.D. and Hutchings, I.M. Inkjet printing - the physics of manipulating liquid jets and drops. *Journal of Physics: Conference Series*. 2008, **105**(1), p.012001.
98. Derby, B. Inkjet Printing of Functional and Structural Materials: Fluid Property Requirements, Feature Stability, and Resolution. *Annual Review of Materials Research*. 2010, **40**(1), pp.395–414.
99. Reis, N., Ainsley, C. and Derby, B. Ink-jet delivery of particle suspensions by piezoelectric droplet ejectors. *Journal of Applied Physics*. 2005, **97**(9), p.094903.
100. Antohe, B. V. and Wallace, D.B. Acoustic phenomena in a demand mode piezoelectric ink jet printer. *Journal of Imaging Science and Technology*. 2002, **46**(5), pp.409–414.
101. Kordás, K., Mustonen, T., Tóth, G., Jantunen, H., Lajunen, M., Soldano, C., Talapatra, S., Kar, S., Vajtai, R. and Ajayan, P.M. Inkjet Printing of Electrically Conductive Patterns of Carbon Nanotubes. *Small*. 2006, **2**(8–9), pp.1021–1025.
102. Smith, P.J., Shin, D.-Y., Stringer, J.E., Derby, B. and Reis, N. Direct ink-jet printing and low temperature conversion of conductive silver patterns. *Journal of Materials Science*. 2006, **41**(13), pp.4153–4158.

103. Lomakin, K., Pavlenko, T., Ankenbrand, M., Sippel, M., Ringel, J., Scheetz, M., Klemm, T., Graf, D., Helmreich, K., Franke, J. and Gold, G. Evaluation and Characterization of 3-D Printed Pyramid Horn Antennas Utilizing Different Deposition Techniques for Conductive Material. *IEEE Transactions on Components, Packaging and Manufacturing Technology*. 2018, **8**(11), pp.1998–2006.
104. Mahajan, A., Hyun, W.J., Walker, S.B., Lewis, J.A., Francis, L.F. and Frisbie, C.D. High-resolution, high-aspect ratio conductive wires embedded in plastic substrates. *ACS Applied Materials and Interfaces*. 2015, **7**(3), pp.1841–1847.
105. Lessing, J., Glavan, A.C., Walker, S.B., Keplinger, C., Lewis, J.A. and Whitesides, G.M. Inkjet printing of conductive inks with high lateral resolution on omniphobic “rF paper” for paper-based electronics and MEMS. *Advanced Materials*. 2014, **26**(27), pp.4677–4682.
106. Wilkinson, N.J., Smith, M.A.A., Kay, R.W. and Harris, R.A. A review of aerosol jet printing—a non-traditional hybrid process for micro-manufacturing. *International Journal of Advanced Manufacturing Technology*. 2019.
107. Mahajan, A., Frisbie, C.D. and Francis, L.F. Optimization of aerosol jet printing for high-resolution, high-aspect ratio silver lines. *ACS Applied Materials and Interfaces*. 2013, **5**(11), pp.4856–4864.
108. Ankenbrand, M., Scheetz, M., Franke, J., Lomakin, K., Sippel, M., Gold, G. and Helmreich, K. Generation of 3D Functional Structures for High-Frequency Applications by Printing Technologies. *2018 13th International Congress Molded Interconnect Devices, MID 2018*. 2018, pp.1–5.
109. Tait, J.G., Witkowska, E., Hirade, M., Ke, T.-H., Malinowski, P.E., Steudel, S., Adachi, C. and Heremans, P. Uniform Aerosol Jet printed polymer lines with 30µm width for 140ppi resolution RGB organic light emitting diodes. *Organic Electronics*. 2015, **22**, pp.40–43.



110. Paulsen, J.A., Renn, M.J., Christenson, K. and Plourde, R. Printing conformal electronics on 3D structures with aerosol jet technology, In: *FIIW 2012 - 2012 Future of Instrumentation International Workshop Proceedings*. IEEE, 2012, pp.47–50.
111. Mahajan, A., Francis, L.F. and Frisbie, C.D. Facile method for fabricating flexible substrates with embedded, printed silver lines. *ACS Applied Materials and Interfaces*. 2014, **6**(2), pp.1306–1312.
112. Ahn, B.Y. and Lewis, J.A. Amphiphilic silver particles for conductive inks with controlled wetting behavior. *Materials Chemistry and Physics*. 2014, **148**(3), pp.686–691.
113. Wilson, P. Printed circuits, In: *The Circuit Designer's Companion*. 3rd ed., Oxford, UK: Newnes, 2012, pp.45–84.
114. Reboun, J., Pretl, S., Navratil, J. and Hlina, J. Bending endurance of printed conductive patterns on flexible substrates, In: *2016 39th International Spring Seminar on Electronics Technology (ISSE)*. IEEE, 2016, pp.184–188.
115. Eckstein, R., Rödlmeier, T., Glaser, T., Valouch, S., Mauer, R., Lemmer, U. and Hernandez-Sosa, G. Aerosol-Jet Printed Flexible Organic Photodiodes: Semi-Transparent, Color Neutral, and Highly Efficient. *Advanced Electronic Materials*. 2015, **1**(8), p.1500101.
116. Maiwald, M., Werner, C., Zöllmer, V. and Busse, M. INKtelligent printing<sup>®</sup> for sensorial applications. *Sensor Review*. 2010, **30**(1), pp.19–23.
117. Rahman, M.T., Rahimi, A., Gupta, S. and Panat, R. Microscale additive manufacturing and modeling of interdigitated capacitive touch sensors. *Sensors and Actuators A: Physical*. 2016, **248**, pp.94–103.
118. van Hest, M.F.A.M., Habas, S.E., Underwood, J.M., Pasquarelli, R.M., Hersh, P., Miedaner, A., Curtis, C.J. and Ginley, D.S. Direct write metallization for photovoltaic cells and scaling thereof, In: *2010 35th IEEE Photovoltaic Specialists Conference*. IEEE, 2010, pp.003626–003628.

119. Platt, H.A.S., Li, Y., Novak, J.P. and van Hest, M.F.A.M. Non-contact printed aluminum metallization of Si photovoltaic devices, In: *2012 38th IEEE Photovoltaic Specialists Conference*. IEEE, 2012, pp.002244–002246.
120. Kuznetsov, A.I., Kiyan, R. and Chichkov, B.N. Laser fabrication of 2D and 3D metal nanoparticle structures and arrays. *Optics Express*. 2010, **18**(20), p.21198.
121. Kuznetsov, A.I., Evlyukhin, A.B., Reinhardt, C., Seidel, A., Kiyan, R., Cheng, W., Ovsianikov, A. and Chichkov, B.N. Laser-induced transfer of metallic nanodroplets for plasmonics and metamaterial applications. *Journal of the Optical Society of America B*. 2009, **26**(12), p.B130.
122. Serra, P. and Piqué, A. Laser-Induced Forward Transfer: Fundamentals and Applications. *Advanced Materials Technologies*. 2019, **4**(1), p.1800099.
123. Piqué, A., Arnold, C.B., Wartena, R.C., Pratap, B., Shashishekar, B., Swider-Lyons, K.E., Weir, D.W. and Kant, R.A. Laser-induced forward transfer direct-write of miniature sensor and microbattery systems, In: *SPIE Proceedings*. 2003, p.182.
124. Piqué, A., Mathews, S.A., Pratap, B., Auyeung, R.C.Y., Karns, B.J. and Lakeou, S. Embedding electronic circuits by laser direct-write. *Microelectronic Engineering*. 2006, **83**(11–12), pp.2527–2533.
125. Arnold, C.B., Serra, P. and Piqué, A. Laser Direct-Write Techniques for Printing of Complex Materials. *MRS Bulletin*. 2007, **32**(1), pp.23–31.
126. Piqué, A., Pratap, B., Mathews, S.A., Karns, B.J., Auyeung, R.C.Y., Kasser, M., Ollinger, M., Kim, H., Lakeou, S. and Arnold, C.B. Laser direct-write of embedded electronic components and circuits, In: *Photon Processing in Microelectronics and Photonics IV*. 2005, pp.1–8.

127. Wang, J., Auyeung, R.C.Y., Kim, H., Charipar, N.A. and Piqué, A. Three-Dimensional Printing of Interconnects by Laser Direct-Write of Silver Nanopastes. *Advanced Materials*. 2010, **22**(40), pp.4462–4466.
128. Skylar-Scott, M.A., Gunasekaran, S. and Lewis, J.A. Laser-assisted direct ink writing of planar and 3D metal architectures. *Proceedings of the National Academy of Sciences*. 2016, **113**(22), pp.6137–6142.
129. Li, B., Clark, P.A. and Church, K.H. Robust Direct-Write Dispensing Tool and Solutions for Micro/Meso-Scale Manufacturing and Packaging, In: *ASME 2007 International Manufacturing Science and Engineering Conference*. ASMEDC, 2007, pp.715–721.
130. Adams, J.J., Duoss, E.B., Malkowski, T.F., Motala, M.J., Ahn, B.Y., Nuzzo, R.G., Bernhard, J.T. and Lewis, J.A. Conformal printing of electrically small antennas on three-dimensional surfaces. *Advanced Materials*. 2011, **23**(11), pp.1335–1340.
131. Zhu, Z., Guo, S.Z., Hirdler, T., Eide, C., Fan, X., Tolar, J. and McAlpine, M.C. 3D Printed Functional and Biological Materials on Moving Freeform Surfaces. *Advanced Materials*. 2018, **30**(23), pp.1–8.
132. Muth, J.T., Vogt, D.M., Truby, R.L., Mengüç, Y., Kolesky, D.B., Wood, R.J. and Lewis, J.A. Embedded 3D Printing of Strain Sensors within Highly Stretchable Elastomers. *Advanced Materials*. 2014, **26**(36), pp.6307–6312.
133. Sun, K., Wei, T.S., Ahn, B.Y., Seo, J.Y., Dillon, S.J. and Lewis, J.A. 3D printing of interdigitated Li-ion microbattery architectures. *Advanced Materials*. 2013, **25**(33), pp.4539–4543.
134. Huang, Q. and Zhu, Y. Printing Conductive Nanomaterials for Flexible and Stretchable Electronics: A Review of Materials, Processes, and Applications. *Advanced Materials Technologies*. 2019, **4**(5), p.1800546.
135. Russo, A., Ahn, B.Y., Adams, J.J., Duoss, E.B., Bernhard, J.T. and Lewis, J.A. Pen-on-Paper Flexible Electronics. *Advanced Materials*. 2011, **23**(30), pp.3426–3430.

136. Junfeng Mei, Lovell, M.R. and Mickle, M.H. Formulation and processing of novel conductive solution inks in continuous inkjet printing of 3-D electric circuits. *IEEE Transactions on Electronics Packaging Manufacturing*. 2005, **28**(3), pp.265–273.
137. Rapp, L., Ailuno, J., Alloncle, A.P. and Delaporte, P. Pulsed-laser printing of silver nanoparticles ink: control of morphological properties. *Optics Express*. 2011, **19**(22), p.21563.
138. Roberson, D.A., Wicker, R.B., Murr, L.E., Church, K. and MacDonald, E. Microstructural and Process Characterization of Conductive Traces Printed from Ag Particulate Inks. *Materials*. 2011, **4**(6), pp.963–979.
139. Ahn, B.Y., Lorang, D.J. and Lewis, J.A. Transparent conductive grids via direct writing of silver nanoparticle inks. *Nanoscale*. 2011, **3**(7), p.2700.
140. Valeton, J.J.P., Hermans, K., Bastiaansen, C.W.M., Broer, D.J., Perelaer, J., Schubert, U.S., Crawford, G.P. and Smith, P.J. Room temperature preparation of conductive silver features using spin-coating and inkjet printing. *Journal of Materials Chemistry*. 2010, **20**(3), pp.543–546.
141. Dearden, A.L., Smith, P.J., Shin, D.-Y., Reis, N., Derby, B. and O'Brien, P. A low curing temperature silver ink for use in ink-jet printing and subsequent production of conductive tracks. *Macromolecular Rapid Communications*. 2005, **26**(4), pp.315–318.
142. Ahn, B.Y., Duoss, E.B., Motala, M.J., Guo, X., Park, S.-I., Xiong, Y., Yoon, J., Nuzzo, R.G., Rogers, J.A. and Lewis, J.A. Omnidirectional Printing of Flexible, Stretchable, and Spanning Silver Microelectrodes. *Science*. 2009, **323**(5921), pp.1590–1593.
143. Bohandy, J., Kim, B.F. and Adrian, F.J. Metal deposition from a supported metal film using an excimer laser. *Journal of Applied Physics*. 1986, **60**(4), pp.1538–1539.

144. Lee, J., Lee, B., Jeong, S., Kim, Y. and Lee, M. Microstructure and electrical property of laser-sintered Cu complex ink. *Applied Surface Science*. 2014, **307**, pp.42–45.
145. Yung, W.K.C., Sun, B., Meng, Z., Huang, J., Jin, Y., Choy, H.S., Cai, Z., Li, G., Ho, C.L., Yang, J. and Wong, W.Y. Additive and Photochemical Manufacturing of Copper. *Scientific Reports*. 2016, **6**(December 2015), p.39584.
146. Min, H., Lee, B., Jeong, S. and Lee, M. Laser-direct process of Cu nano-ink to coat highly conductive and adhesive metallization patterns on plastic substrate. *Optics and Lasers in Engineering*. 2016, **80**, pp.12–16.
147. Grouchko, M., Kamyshny, A. and Magdassi, S. Formation of air-stable copper-silver core-shell nanoparticles for inkjet printing. *Journal of Materials Chemistry*. 2009, **19**(19), pp.3057–3062.
148. Lee, Y., Choi, J., Lee, K.J., Stott, N.E. and Kim, D. Large-scale synthesis of copper nanoparticles by chemically controlled reduction for applications of inkjet-printed electronics. *Nanotechnology*. 2008, **19**(41), p.415604.
149. Ko, S.H., Pan, H., Grigoropoulos, C.P., Luscombe, C.K., Fréchet, J.M.J. and Poulidakos, D. All-inkjet-printed flexible electronics fabrication on a polymer substrate by low-temperature high-resolution selective laser sintering of metal nanoparticles. *Nanotechnology*. 2007, **18**(34), p.345202.
150. Nur, H.M., Song, J.H., Evans, J.R.G. and Edirisinghe, M.J. Ink-jet printing of gold conductive tracks. *Journal of Materials Science: Materials in Electronics*. 2002, **13**(4), pp.213–219.
151. Stringer, J., Althagathi, T.M., Tse, C.C.W., Ta, V.D., Shephard, J.D., Esenturk, E., Connaughton, C., Wasley, T.J., Li, J., Kay, R.W. and Smith, P.J. Integration of additive manufacturing and inkjet printed electronics: a potential route to parts with embedded multifunctionality. *Manufacturing Review*. 2016, **3**, p.12.

152. Huang, L., Huang, Y., Liang, J., Wan, X. and Chen, Y. Graphene-based conducting inks for direct inkjet printing of flexible conductive patterns and their applications in electric circuits and chemical sensors. *Nano Research*. 2011, **4**(7), pp.675–684.
153. Kamyshny, A. and Magdassi, S. Conductive Nanomaterials for Printed Electronics. *Small*. 2014, **10**(17), pp.3515–3535.
154. Shin, D.-H., Woo, S., Yem, H., Cha, M., Cho, S., Kang, M., Jeong, S., Kim, Y., Kang, K. and Piao, Y. A Self-Reducible and Alcohol-Soluble Copper-Based Metal–Organic Decomposition Ink for Printed Electronics. *ACS Applied Materials & Interfaces*. 2014, **6**(5), pp.3312–3319.
155. Walker, S.B. and Lewis, J.A. Reactive Silver Inks for Patterning High-Conductivity Features at Mild Temperatures. *Journal of the American Chemical Society*. 2012, **134**(3), pp.1419–1421.
156. McKerricher, G., Vaseem, M. and Shamim, A. Fully inkjet-printed microwave passive electronics. *Microsystems & Nanoengineering*. 2017, **3**, p.16075.
157. Roberson, D.A., Wicker, R.B. and Macdonald, E. Ohmic curing of printed silver conductive traces. *Journal of Electronic Materials*. 2012, **41**(9), pp.2553–2566.
158. Roberson, D.A., Wicker, R.B. and MacDonald, E. Ohmic Curing of Three-Dimensional Printed Silver Interconnects for Structural Electronics. *Journal of Electronic Packaging*. 2015, **137**(3), p.031004.
159. Perelaer, J., de Gans, B.-J. and Schubert, U.S. Ink-jet Printing and Microwave Sintering of Conductive Silver Tracks. *Advanced Materials*. 2006, **18**(16), pp.2101–2104.
160. Mu, Q., Lei, M., Roach, D.J., Dunn, C.K., Kuang, X., Yuan, C., Wang, T. and Qi, H.J. Intense pulsed light sintering of thick conductive wires on elastomeric dark substrate for hybrid 3D printing applications. *Smart Materials and Structures*. 2018, **27**(11), p.115007.

161. Das, S., Cormier, D. and Williams, S. Potential for Multi-functional Additive Manufacturing Using Pulsed Photonic Sintering, In: *43rd Proceedings of the North American Manufacturing Research Institution of SME*. Elsevier B.V., 2015, pp.366–377.
162. Leigh, S.J., Bradley, R.J., Pursell, C.P., Billson, D.R. and Hutchins, D.A. A Simple, Low-Cost Conductive Composite Material for 3D Printing of Electronic Sensors. *PLoS ONE*. 2012, 7(11), pp.1–6.
163. Flowers, P.F., Reyes, C., Ye, S., Kim, M.J. and Wiley, B.J. 3D printing electronic components and circuits with conductive thermoplastic filament. *Additive Manufacturing*. 2017, **18**, pp.156–163.
164. American Society for Testing and Materials. ASTM E1004 - 17. *Standard Test Method for Determining Electrical Conductivity Using the Electromagnetic (Eddy Current) Method*. ASTM, 2017.
165. Kwok, S.W., Goh, K.H.H., Tan, Z.D., Tan, S.T.M., Tjiu, W.W., Soh, J.Y., Ng, Z.J.G., Chan, Y.Z., Hui, H.K. and Goh, K.E.J. Electrically conductive filament for 3D-printed circuits and sensors. *Applied Materials Today*. 2017, **9**, pp.167–175.
166. Dorigato, A., Moretti, V., Dul, S., Unterberger, S.H. and Pegoretti, A. Electrically conductive nanocomposites for fused deposition modelling. *Synthetic Metals*. 2017, **226**, pp.7–14.
167. Kim, M.J., Cruz, M.A., Ye, S., Gray, A.L., Smith, G.L., Lazarus, N., Walker, C.J., Sigmarsson, H.H. and Wiley, B.J. One-step electrodeposition of copper on conductive 3D printed objects. *Additive Manufacturing*. 2019, **27**(November 2018), pp.318–326.
168. Lopes, L.R., Silva, A.F. and Carneiro, O.S. Multi-material 3D printing: The relevance of materials affinity on the boundary interface performance. *Additive Manufacturing*. 2018, **23**, pp.45–52.

169. Mu, Q., Wang, L., Dunn, C.K., Kuang, X., Duan, F., Zhang, Z., Qi, H.J. and Wang, T. Digital light processing 3D printing of conductive complex structures. *Additive Manufacturing*. 2017, **18**, pp.74–83.
170. McKerricher, G., Perez, J.G. and Shamim, A. Fully inkjet printed RF inductors and capacitors using polymer dielectric and silver conductive ink with through vias. *IEEE Transactions on Electron Devices*. 2015, **62**(3), pp.1002–1009.
171. Nano Dimension Ltd. DragonFly™ LDM Brochure. [Online] 2019. [Accessed November 24, 2019]. Available from: <https://www.nano-di.com/nano-dimension-brochures>.
172. Nano Dimension Ltd. Nano Dimension - Conductive & Insulating Inks for Printed Electronics. [Online] 2019. [Accessed November 24, 2019]. Available from: <https://www.nano-di.com/materials>.
173. Nano Dimension Ltd. The DragonFly LDM™ System. [Online] 2019. [Accessed November 24, 2019]. Available from: <https://www.nano-di.com/dragonfly-ldm-3d-printer>.
174. Yim, B.-S.S., Kwon, Y., Oh, S.H., Kim, J.J.-M.M., Shin, Y.-E.E., Lee, S.H. and Kim, J.J.-M.M. Characteristics of solderable electrically conductive adhesives (ECAs) for electronic packaging. *Microelectronics Reliability*. 2012, **52**(6), pp.1165–1173.
175. Sealy, M.P., Madireddy, G., Williams, R.E., Rao, P. and Toursangsaraki, M. Hybrid Processes in Additive Manufacturing. *Journal of Manufacturing Science and Engineering*. 2018, **140**(6), p.060801.
176. Hoerber, J., Glasschroeder, J., Pfeffer, M., Schilp, J., Zaeh, M. and Franke, J. Approaches for additive manufacturing of 3D electronic applications. *Procedia CIRP*. 2014, **17**, pp.806–811.



177. Mostafaei, A., Stevens, E.L., Hughes, E.T., Biery, S.D., Hilla, C. and Chmielus, M. Powder bed binder jet printed alloy 625: Densification, microstructure and mechanical properties. *Materials & Design*. 2016, **108**, pp.126–135.
178. Gokuldoss, P.K., Kolla, S. and Eckert, J. Additive Manufacturing Processes: Selective Laser Melting, Electron Beam Melting and Binder Jetting— Selection Guidelines. *Materials*. 2017, **10**(6), p.672.
179. Gibson, I., Rosen, D.W. and Stucker, B. *Additive manufacturing technologies: Rapid prototyping to direct digital manufacturing*, Boston, MA: Springer US, 2010.
180. Friel, R.J. Power ultrasonics for additive manufacturing and consolidating of materials, In: *Power Ultrasonics*. Elsevier, 2015, pp.313–335.
181. Siggard, E.J., Madhusoodanan, A.S., Stucker, B. and Eames, B. Structurally embedded electrical systems using ultrasonic consolidation (UC), In: *17th Solid Freeform Fabrication Symposium, SFF 2006*. 2006, pp.70–83.
182. Robinson, C., Stucker, B., Branch, K.C., Palmer, J., Strassner, B., Allen, S., Bugos, R., Navarrete, M., Lopes, A., Macdonald, E., Medina, F. and Wicker, R.B. Fabrication of a Mini-Sar Antenna Array Using Ultrasonic Consolidation and Direct-Write, In: *2nd International Conference on Rapid Manufacturing*. Loughborough, UK: 2007, p.30.
183. Medina, F., Lopes, A.J., Inamdar, A. V., Hennessey, R., Palmer, J.A., Chavez, B.D., Davis, D., Gallegos, P. and Wicker, R.B. Hybrid Manufacturing: Integrating Direct-Write and Stereolithography, In: *Proceedings of the 2005 Solid Freeform Fabrication Symposium*. 2005, pp.39–49.
184. Navarrete, M., Lopes, A.J., Acuna, J., Estrada, R., Macdonald, E., Palmer, J.A. and Wicker, R.B. Integrated Layered Manufacturing of a Novel Wireless Motion Sensor System With Gps, In: *Proceedings of the 18th Annual Solid Freeform Fabrication Symposium*. 2007, pp.575–585.

185. Lopes, A.J., Navarrete, M., Medina, F., Palmer, J.A., Macdonald, E. and Wicker, R.B. Expanding Rapid Prototyping for Electronic Systems Integration of Arbitrary Form, In: *Proceedings of the 2006 Solid Freeform Fabrication Symposium*. 2006, pp.644–655.
186. Wasley, T.J., Li, J., Ta, V.D., Shephard, J.D., Stringer, J., Smith, P.J., Esenturk, E., Connaughton, C. and Kay, R.W. Additive Manufacturing of High Resolution Embedded Electronic Systems, In: *Solid Freeform Fabrication 2016: Proceedings of the 26th Annual International Solid Freeform Fabrication Symposium – An Additive Manufacturing Conference*. 2016, pp.1838–1855.
187. Li, J., Wasley, T.J., Nguyen, T.T., Ta, V.D., Shephard, J.D., Stringer, J., Smith, P.J., Esenturk, E., Connaughton, C. and Kay, R.W. Hybrid additive manufacturing of 3D electronic systems. *Journal of Micromechanics and Microengineering*. 2016, **26**(10), p.105005.
188. Li, J., Wasley, T.J., Ta, D., Shephard, J., Stringer, J., Smith, P., Esenturk, E., Connaughton, C., Harris, R.A. and Kay, R.W. Micro electronic systems via multifunctional additive manufacturing. *Rapid Prototyping Journal*. 2018, **24**(4), pp.752–763.
189. Lopes, A.J., Lee, I.H., Macdonald, E., Quintana, R. and Wicker, R.B. Laser curing of silver-based conductive inks for in situ 3D structural electronics fabrication in stereolithography. *Journal of Materials Processing Technology*. 2014, **214**(9), pp.1935–1945.
190. Optomec Inc. Revolutionary “Smart Wing” Created for UAV Model Demonstrates Groundbreaking Technology. [Online] 2013. [Accessed October 6, 2019]. Available from: <https://www.optomec.com/revolutionary-smart-wing-created-for-uav-model-demonstrates-groundbreaking-technology/>.

191. Vogeler, F., Verheecke, W., Voet, A. and Valkenaers, H. An Initial Study of Aerosol Jet® Printed Interconnections on Extrusion-Based 3D-Printed Substrates. *Strojniški Vestnik – Journal of Mechanical Engineering*. 2013, **59**(11), pp.689–696.
192. Macy, B. Capability assessment of hybrid components utilizing fused deposition modeling and aerosol jet technologies, In: *44th International SAMPE Technical Conference*. 2012, .
193. Lu, B.-H., Lan, H.-B. and Liu, H.-Z. Additive manufacturing frontier: 3D printing electronics. *Opto-Electronic Advances*. 2018, **1**(1), pp.17000401–17000410.
194. Ota, H., Emaminejad, S., Gao, Y., Zhao, A., Wu, E., Challa, S., Chen, K., Fahad, H.M., Jha, A.K., Kiriya, D., Gao, W., Shiraki, H., Morioka, K., Ferguson, A.R., Healy, K.E., Davis, R.W. and Javey, A. Application of 3D Printing for Smart Objects with Embedded Electronic Sensors and Systems. *Advanced Materials Technologies*. 2016, **1**(1), p.1600013.
195. Swensen, J.P., Odhner, L.U., Araki, B. and Dollar, A.M. Printing Three-Dimensional Electrical Traces in Additive Manufactured Parts for Injection of Low Melting Temperature Metals. *Journal of Mechanisms and Robotics*. 2015, **7**(2), p.021004.
196. Swensen, J.P., Odhner, L.U., Araki, B. and Dollar, A.M. Injected 3D electrical traces in additive manufactured parts with low melting temperature metals, In: *2015 IEEE International Conference on Robotics and Automation (ICRA)*. IEEE, 2015, pp.988–995.
197. Ota, H., Chao, M., Gao, Y., Wu, E., Tai, L.-C., Chen, K., Matsuoka, Y., Iwai, K., Fahad, H.M., Gao, W., Nyein, H.Y.Y., Lin, L. and Javey, A. 3D Printed “Eearable” Smart Devices for Real-Time Detection of Core Body Temperature. *ACS Sensors*. 2017, **2**(7), pp.990–997.
198. Liu, T., Sen, P. and Kim, C.-J. Characterization of Nontoxic Liquid-Metal Alloy Galinstan for Applications in Microdevices. *Journal of Microelectromechanical Systems*. 2012, **21**(2), pp.443–450.

199. Saari, M. Design and Control of Fiber Encapsulation Additive Manufacturing, Southern Methodist University, 2019.
200. Kim, C., Espalin, D., Liang, M., Xin, H., Cuaron, A., Varela, I., Macdonald, E. and Wicker, R.B. 3D Printed Electronics With High Performance, Multi-Layered Electrical Interconnect. *IEEE Access*. 2017, **5**, pp.25286–25294.
201. Saari, M., Galla, M., Cox, B., Richer, E., Krueger, P.S. and Cohen, A.L. Active Device Fabrication Using Fiber Encapsulation Additive Manufacturing, In: *Proceedings of the International Solid Freeform Fabrication Symposium*. 2015, pp.26–39.
202. Liang, M., Shemelya, C., MacDonald, E., Wicker, R.B. and Xin, H. 3-D printed microwave patch antenna via fused deposition method and ultrasonic wire mesh embedding technique. *IEEE Antennas and Wireless Propagation Letters*. 2015, **14**, pp.1346–1349.
203. Cox, B., Saari, M., Xia, B., Richer, E., Krueger, P.S. and Cohen, A.L. Fiber Encapsulation Additive Manufacturing: Technology and Applications Update. *3D Printing and Additive Manufacturing*. 2017, **4**(2), pp.116–119.
204. Saari, M., Cox, B., Richer, E., Krueger, P.S. and Cohen, A.L. Fiber Encapsulation Additive Manufacturing: An Enabling Technology for 3D Printing of Electromechanical Devices and Robotic Components. *3D Printing and Additive Manufacturing*. 2015, **2**(1), pp.32–39.
205. Florencio Díaz, R., Rodríguez Boix, R., Carrasco Yépez, F., Encinar Garcinuño, J., Barba Gea, M. and Pérez Palomino, G. Broadband reflectarrays made of cells with three coplanar parallel dipoles. *Microwave And Optical Technology Letters*. 2014, **56**(3), pp.748–753.
206. Kim, C., Espalin, D., Cuaron, A., Perez, M.A., Lee, M., MacDonald, E. and Wicker, R.B. Cooperative Tool Path Planning for Wire Embedding on Additively Manufactured Curved Surfaces Using Robot Kinematics. *Journal of Mechanisms and Robotics*. 2015, **7**(2), p.021003.

207. Espalin, D., Ramirez, J., Medina, F. and Wicker, R.B. Multi-Material, Multi-Technology FDM System. *23rd Annual International Solid Freeform Fabrication Symposium - An Additive Manufacturing Conference, SFF 2012*. 2012, pp.828–835.
208. Espalin, D., Muse, D., MacDonald, E. and Wicker, R.B. 3D Printing multifunctionality: Structures with electronics. *International Journal of Advanced Manufacturing Technology*. 2014, **72**(5–8), pp.963–978.
209. Shemelya, C., Banuelos-Chacon, L., Melendez, A., Kief, C., Espalin, D., Wicker, R.B., Krijnen, G.J.M. and Macdonald, E. Multi-functional 3D printed and embedded sensors for satellite qualification structures. *2015 IEEE SENSORS - Proceedings*. 2015, pp.1422–1425.
210. MacDonald, E. and Wicker, R.B. Multiprocess 3D printing for increasing component functionality. *Science*. 2016, **353**(6307), p.aaf2093.
211. Wu, S.-Y., Yang, C., Hsu, W. and Lin, L. 3D-printed microelectronics for integrated circuitry and passive wireless sensors. *Microsystems and Nanoengineering*. 2015, **1**(April), pp.1–9.
212. Chang, Y.-H., Wang, K., Wu, C., Chen, Y., Zhang, C. and Wang, B. A facile method for integrating direct-write devices into three-dimensional printed parts. *Smart Materials and Structures*. 2015, **24**(6), p.065008.
213. Goth, C. and Kuhn, T. MID Technology and Mechatronic Integration Potential, In: *Three-Dimensional Molded Interconnect Devices (3D-MID)*. München: Carl Hanser Verlag GmbH & Co. KG, 2014, pp.1–21.
214. Yan, H., Chen, J. and Zhao, J. 3D-MID manufacturing via laser direct structuring with nanosecond laser pulses. *Journal of Polymer Engineering*. 2016, **36**(9), pp.957–962.
215. Schramm, R. Structuring and Metallization, In: *Three-Dimensional Molded Interconnect Devices (3D-MID)*. München: Carl Hanser Verlag GmbH & Co. KG, 2014, pp.63–108.

216. LPKF Laser & Electronics. 3D-MID Technology with Laser Direct Structuring (LDS). [Online] No date. [Accessed September 30, 2019]. Available from: <https://www.lpkf.com/en/industries-technologies/electronics-manufacturing/3d-mids-with-laser-direct-structuring-lds/>.
217. LPKF Laser & Electronics. Approved LDS Materials. [Online] 2020. [Accessed May 5, 2020]. Available from: [https://jp.lpkf.com/\\_mediafiles/2074-approved-plastics-lpkf-lds.pdf](https://jp.lpkf.com/_mediafiles/2074-approved-plastics-lpkf-lds.pdf).
218. LPKF Laser & Electronics Design rules for laser direct structured MID components. *LDS MID Design Rules*. 2010.
219. Amend, P., Pscherer, C., Rechtenwald, T., Frick, T. and Schmidt, M. A fast and flexible method for manufacturing 3D molded interconnect devices by the use of a rapid prototyping technology. *Physics Procedia*. 2010, 5(PART 2), pp.561–572.
220. Prater, T., Werkheiser, N., Ledbetter, F., Timucin, D., Wheeler, K. and Snyder, M. 3D Printing in Zero G Technology Demonstration Mission: complete experimental results and summary of related material modeling efforts. *The International Journal of Advanced Manufacturing Technology*. 2019, **101**(1–4), pp.391–417.
221. Snyder, M., Dunn, J. and Gonzalez, E. The Effects of Microgravity on Extrusion Based Additive Manufacturing, In: *AIAA SPACE 2013 Conference and Exposition*. Reston, Virginia: American Institute of Aeronautics and Astronautics, 2013, pp.1–6.
222. Dunn, J.J., Hutchison, D.N., Kemmer, A.M., Ellsworth, A.Z., Snyder, M., White, W.B. and Blair, B.R. 3D Printing in Space : Enabling New Markets and Accelerating the Growth of Orbital Infrastructure. 2010.
223. Holman, J.P. *Heat Transfer*, 10th ed. Boston, MA: McGraw-Hill Education, 2010.

224. Stratasys Ltd. Fortus® 450mc 3D Production System User Guide. [Online] 2015. [Accessed July 17, 2019]. Available from: <http://articles.stratasys.com/en/articles/2043364-fortus-450mc-k0-series-user-guide>.
225. Moylan, S., Slotwinski, J., Cooke, A., Jurrens, K. and Donmez, M.A. Proposal for a Standardized Test Artifact for Additive Manufacturing Machines and Processes, In: *Solid Freeform Fabrication Symposium*. 2012, pp.902–920.
226. Rebaioli, L. and Fassi, I. A review on benchmark artifacts for evaluating the geometrical performance of additive manufacturing processes. *The International Journal of Advanced Manufacturing Technology*. 2017, **93**(5–8), pp.2571–2598.
227. Johnson, W.M., Rowell, M., Deason, B. and Eubanks, M. Comparative evaluation of an open-source FDM system. *Rapid Prototyping Journal*. 2014, **20**(3), pp.205–214.
228. Minetola, P., Iuliano, L. and Marchiandi, G. Benchmarking of FDM Machines through Part Quality Using IT Grades. *Procedia CIRP*. 2016, **41**, pp.1027–1032.
229. Byun, H.-S. and Lee, K.H. Design of a New Test Part for Benchmarking the Accuracy and Surface Finish of Rapid Prototyping Processes, In: Kumar, V., Gavrilova, M.L., Tan, C.J.K., and L'Ecuyer, P. eds. *Computational Science and Its Applications - ICCSA 2003*. Berlin, Heidelberg: Springer Berlin Heidelberg, 2003, pp.731–740.
230. Tymrak, B.M., Kreiger, M. and Pearce, J.M. Mechanical properties of components fabricated with open-source 3-D printers under realistic environmental conditions. *Materials & Design*. 2014, **58**, pp.242–246.
231. Keleş, Ö., Blevins, C.W. and Bowman, K.J. Effect of build orientation on the mechanical reliability of 3D printed ABS. *Rapid Prototyping Journal*. 2017, **23**(2), pp.320–328.

232. Lanzotti, A., Grasso, M., Staiano, G. and Martorelli, M. The impact of process parameters on mechanical properties of parts fabricated in PLA with an open-source 3-D printer. *Rapid Prototyping Journal*. 2015, **21**(5), pp.604–617.
233. Akande, S.O., Dalgarno, K.W. and Munguia, J. Low-Cost QA Benchmark for Fused Filament Fabrication. *3D Printing and Additive Manufacturing*. 2015, **2**(2), pp.78–84.
234. American Society for Testing and Materials. ASTM D638 - 14. *Standard Test Method for Tensile Properties of Plastics*. ASTM, 2014.
235. International Organization for Standardization. ISO 527-1:2012(en). *Plastics - Determination of Tensile Properties - Part 1: General Principles*. ISO, 2012.
236. Kuznetsov, V., Solonin, A., Urzhumtsev, O., Schilling, R. and Tavitov, A. Strength of PLA Components Fabricated with Fused Deposition Technology Using a Desktop 3D Printer as a Function of Geometrical Parameters of the Process. *Polymers*. 2018, **10**(3), p.313.
237. Mizera, A., Bednarik, M., Mizera, M., Tomanova, K. and Mohorko, M. Tensile impact behaviour of 3D printed parts on FFF/FDM printer Zortrax M200, In: Mastorakis, N., Mladenov, V., and Bulucea, A. eds. *MATEC Web of Conferences*. 2018, p.04049.
238. Fernandez-Vicente, M., Calle, W., Ferrandiz, S. and Conejero, A. Effect of Infill Parameters on Tensile Mechanical Behavior in Desktop 3D Printing. *3D Printing and Additive Manufacturing*. 2016, **3**(3), pp.183–192.
239. Alsoufi, M.S. and El-sayed, A. Warping Deformation of Desktop 3D Printed Parts Manufactured by Open Source Fused Deposition Modeling ( FDM ) System. *International Journal of Mechanical & Mechatronics Engineering*. 2017, **17**(04), pp.7–16.



240. Micro-Epsilon. scanCONTROL // 2D/3D laser scanner (laser profile sensors). [Online] No date. [Accessed July 18, 2019]. Available from: <https://www.micro-epsilon.co.uk/download/products/cat-scancontrol/dax--scanCONTROL-29x0--en.html#page=2&zoom=Fit>.
241. Cruz Sanchez, F.A., Boudaoud, H., Muller, L. and Camargo, M. Towards a standard experimental protocol for open source additive manufacturing. *Virtual and Physical Prototyping*. 2014, **9**(3), pp.151–167.
242. Anoop, M.S. and Senthil, P. Homogenisation of elastic properties in FDM components using microscale RVE numerical analysis. *Journal of the Brazilian Society of Mechanical Sciences and Engineering*. 2019, **41**(12), p.540.
243. LPKF Laser & Electronics ProtoPlate LDS User manual. 2015.
244. Brandt, M., ed. *Laser Additive Manufacturing: Materials, Design, Technologies, and Applications*, 1st ed. Elsevier, 2017.
245. Bernhard, T., Bamberg, S., Brüning, F., Brüning, R., Gregoriades, L.J., Sharma, T., Brown, D., Klaus, M. and Genzel, C. Analysis of stress/strain in Electroless Copper Films. *International Symposium on Microelectronics*. 2013, **2013**(1), pp.000026–000030.
246. Siegman, A.E. *Lasers*, Sausalito, CA: University Science Books, 1986.
247. Bridge, L. Haldor Topsoe “Geometric Factors in Four Point Resistivity Measurement.” [Online] 1968. [Accessed November 3, 2019]. Available from: <http://four-point-probes.com/haldor-topsoe-geometric-factors-in-four-point-resistivity-measurement/#hal>.
248. American Society for Testing and Materials. ASTM D3359 - 17. *Standard Test Methods for Rating Adhesion by Tape Test*. 2017.
249. Wen, F.B., Krishnan, S. and Chan, Y.M. Lead-free solder paste selection and solder joint reliability for copper stud flip chip, In: *2008 International Conference on Electronic Materials and Packaging*. IEEE, 2008, pp.80–83.

250. Lewis, A. Formulation Considerations for Automated Dispensing of Lead Free Solder Paste, In: *Proceedings of IPC/JEDEC 5th International Conference on Lead Free Electronic Assemblies and Components*. San Jose: 2004, pp.1-10.
251. Lee, N.-C. Surface Mount Assembly Processes, In: *Reflow Soldering Processes*. Elsevier, 2001, pp.57-89.
252. CHIPQUIK. SMD4300SNLI0T5 Solder Paste Datasheet. [Online] No date. [Accessed November 6, 2019]. Available from: <http://www.chipquik.com/datasheets/SMD4300SNLI0T5.pdf>.
253. Lee, N.-C. Optimizing a Reflow Profile Via Defect Mechanisms Analysis, In: *Reflow Soldering Processes*. Elsevier, 2001, pp.239-250.
254. Dai, J. and Ludois, D.C. A Survey of Wireless Power Transfer and a Critical Comparison of Inductive and Capacitive Coupling for Small Gap Applications. *IEEE Transactions on Power Electronics*. 2015, **30**(11), pp.6017-6029.
255. Komoda, N., Nogi, M., Suganuma, K., Kohno, K., Akiyama, Y. and Otsuka, K. Printed silver nanowire antennas with low signal loss at high-frequency radio. *Nanoscale*. 2012, **4**(10), p.3148.
256. Le Sage, G.P. 3D Printed Waveguide Slot Array Antennas. *IEEE Access*. 2016, **4**, pp.1258-1265.
257. Huang, R., Robl, W., Detzel, T. and Ceric, H. Modeling of stress evolution of electroplated Cu films during self-annealing, In: *2010 IEEE International Reliability Physics Symposium*. IEEE, 2010, pp.911-917.
258. Felton, S.M., Tolley, M.T., Demaine, E.D., Rus, D. and Wood, R.J. A method for building self-folding machines. *Science*. 2014, **345**(6197), pp.644-646.
259. Felton, S.M., Tolley, M.T., Shin, B., Onal, C.D., Demaine, E.D., Rus, D. and Wood, R.J. Self-folding with shape memory composites. *Soft Matter*. 2013, **9**(32), pp.7688-7694.

260. Zarek, M., Layani, M., Cooperstein, I., Sachyani, E., Cohn, D. and Magdassi, S. 3D Printing: 3D Printing of Shape Memory Polymers for Flexible Electronic Devices. *Advanced Materials*. 2016, **28**(22), pp.4166–4166.
261. Ge, Q., Sakhaei, A.H., Lee, H., Dunn, C.K., Fang, N.X. and Dunn, M.L. Multimaterial 4D Printing with Tailorable Shape Memory Polymers. *Scientific Reports*. 2016, **6**(1), p.31110.
262. Khoo, Z.X., Teoh, J.E.M., Liu, Y., Chua, C.K., Yang, S., An, J., Leong, K.F. and Yeong, W.Y. 3D printing of smart materials: A review on recent progresses in 4D printing. *Virtual and Physical Prototyping*. 2015, **10**(3), pp.103–122.
263. Garner, L.J., Wilson, L.N., Lagoudas, D.C. and Rediniotis, O.K. Development of a shape memory alloy actuated biomimetic vehicle. *Smart Materials and Structures*. 2000, **9**(5), pp.673–683.
264. Dong, Y., Zhaobo, C., Boming, Z., Yinghou, J. and Longxue, J. Shape Memory Alloy Driven Two-way Deformation Structure Design. *Applied Mechanics and Materials*. 2013, **435**, pp.2129–2133.
265. Jones, T.D.A., Ryspayeva, A., Esfahani, M.N., Shuttleworth, M.P., Harris, R.A., Kay, R.W., Desmulliez, M.P.Y. and Marques-Hueso, J. Direct metallisation of polyetherimide substrates by activation with different metals. *Surface and Coatings Technology*. 2019.
266. Wu, Y. and Halfyard, K. Solder mask compositions for aerosol jet printing, US9540529B2, 2016.
267. Llewellyn-Jones, T., Allen, R. and Trask, R. Curved Layer Fused Filament Fabrication Using Automated Toolpath Generation. *3D Printing and Additive Manufacturing*. 2016, **3**(4), pp.236–243.
268. Allen, R.J.A. and Trask, R.S. An experimental demonstration of effective Curved Layer Fused Filament Fabrication utilising a parallel deposition robot. *Additive Manufacturing*. 2015, **8**, pp.78–87.

269. Georges, T., Brailovski, V. and Terriault, P. Characterization and design of antagonistic shape memory alloy actuators. *Smart Materials and Structures*. 2012, **21**(3), p.035010.
270. Wang, T.-M., Shi, Z.-Y., Liu, D., Ma, C. and Zhang, Z.-H. An Accurately Controlled Antagonistic Shape Memory Alloy Actuator with Self-Sensing. *Sensors*. 2012, **12**(6), pp.7682–7700.
271. Shayanfard, P., Kadkhodaei, M. and Jalalpour, A. Numerical and Experimental Investigation on Electro-Thermo-Mechanical Behavior of NiTi Shape Memory Alloy Wires. *Iranian Journal of Science and Technology, Transactions of Mechanical Engineering*. 2019, **43**(S1), pp.621–629.
272. Li, J., Sun, M., Wu, Z. and Yin, H. Design, Analysis, and Grasping Experiments of a Novel Soft Hand: Hybrid Actuator Using Shape Memory Alloy Actuators, Motors, and Electromagnets. *Soft Robotics*. 2020, **00**(00).

## Appendix A

### Values Used in Heat Transfer Calculations

Table A.1: Heat Transfer Calculation Values

Component		Thickness (m)	A (m <sup>2</sup> )	V (m <sup>3</sup> )	$\rho$ (kg/m <sup>3</sup> )	$C_p$ (J/kg.K)	k (W/m.K)	$\epsilon$
Bed	Aluminium	$3 \times 10^{-3}$	0.053	$1.59 \times 10^{-4}$	2,707.0	896.0	204.0	0.09
	Glass	$3 \times 10^{-3}$	0.053	$1.59 \times 10^{-4}$	2,230.0	900.0	1.09	0.90
Ceiling	Aluminium	$5 \times 10^{-3}$	0.101	$5.05 \times 10^{-4}$	2,707.0	896.0	204.0	0.09
	Foam	$1.6 \times 10^{-2}$	0.101	$1.62 \times 10^{-3}$	256.3	1,260.0	0.06	-
	Air Gap	$2.1 \times 10^{-2}$	0.101	$2.12 \times 10^{-3}$	1.2	1,024.8	0.04	-
Full Walls	Aluminium	$3 \times 10^{-3}$	0.138	$4.14 \times 10^{-4}$	2,707.0	896.0	204.0	0.09
	Foil	$3 \times 10^{-5}$	0.138	$4.14 \times 10^{-6}$	2,707.0	896.0	204.0	0.09
	Foam	$8 \times 10^{-3}$	0.138	$1.01 \times 10^{-3}$	256.3	1,260.0	0.06	-
	Air Gap	$6 \times 10^{-3}$	0.138	$8.28 \times 10^{-4}$	1.2	1,024.8	0.04	-
Belt Covers	Aluminium	$3 \times 10^{-3}$	0.044	$1.32 \times 10^{-4}$	2,707.0	896.0	204.0	0.09
	Foil	$3 \times 10^{-5}$	0.044	$1.32 \times 10^{-6}$	2,707.0	896.0	204.0	0.09
	Foam	$8 \times 10^{-3}$	0.044	$3.52 \times 10^{-4}$	256.3	1,260.0	0.06	-
	Air Gap	$6 \times 10^{-3}$	0.044	$2.64 \times 10^{-4}$	1.2	1,024.8	0.04	-
Door and Frame	Aluminium	$3 \times 10^{-3}$	0.111	$3.33 \times 10^{-4}$	2,707.0	896.0	204.0	0.09
	Foil	$3 \times 10^{-5}$	0.111	$3.33 \times 10^{-6}$	2,707.0	896.0	204.0	0.09
	Foam	$8 \times 10^{-3}$	0.111	$8.88 \times 10^{-4}$	256.3	1,260.0	0.06	-
	Air Gap	$6 \times 10^{-3}$	0.111	$6.66 \times 10^{-4}$	1.2	1,024.8	0.04	-
Window	Glass	$3 \times 10^{-3}$	0.027	$8.10 \times 10^{-5}$	2,230.0	900.0	1.09	0.90

## Appendix B

### Convective Heat Transfer Coefficient Calculations

To calculate the convective heat transfer coefficient  $h$  using Equation (B.1), the Nusselt number  $\overline{Nu}_f$  were first found using Equation (B.2).

$$h = \frac{\overline{Nu}_f \cdot k}{L} \quad (B.1)$$

$$\overline{Nu}_f = C(Gr_f \cdot Pr_f)^m \quad (B.2)$$

The subscript  $f$  denoted that this must be performed at the film temperature, which was defined as the mean temperature between the solid and the fluid. The length scale  $L$  depended on the orientation of the surface. For vertical plates it was defined as the height of the surface, whereas for horizontal plates it was the area of the surface divided by its perimeter.

$C$  and  $m$  were also determined by the orientation as well as which direction with respect to gravity the heat was convected from. The three situations used in this work are shown in Table B.1.

*Table B.1: C and m values for Nusselt number calculations*

<b>Condition</b>	<b>C</b>	<b>m</b>
Vertical plate	0.59	0.25
Horizontal plate – upper surface	0.15	0.33
Horizontal plate – lower surface	0.58	0.20

The other values in the Nusselt number calculation were the Grashof and Prandtl numbers. These were found using Equations (B.3) and (B.4).

$$Gr_f = \frac{g\beta\Delta TL^4}{\nu^2} \quad (B.3)$$

$$Pr_f = \frac{C_p\mu}{k} \quad (B.4)$$

Where:

- $Gr_f$  is the Grashof number
- $g$  is gravitational acceleration ( $9.81 \text{ m/s}^2$ )
- $\beta$  is the coefficient of thermal expansion
- $\Delta T$  is the temperature change in K
- $L$  is the length scale in m
- $\nu$  is the dynamic viscosity of air in  $\text{kg/m.s}$
- $Pr_f$  is the Prandtl number
- $C_p$  is specific heat of air in  $\text{J/kg.K}$
- $\mu$  is the kinematic viscosity of air in  $\text{m}^2/\text{s}$
- $k$  is the thermal conductivity in  $\text{W/m.K}$

The thermodynamic properties of air for the two film temperatures used in the calculations can be seen in Table B.2.  $110 \text{ }^\circ\text{C}$  was used for boundaries between operating air temperature ( $200 \text{ }^\circ\text{C}$ ) and the ambient environment ( $20 \text{ }^\circ\text{C}$ ).  $50 \text{ }^\circ\text{C}$  was used between the external surfaces ( $80 \text{ }^\circ\text{C}$  assumption) and the environment.

*Table B.2: Thermodynamic properties of air*

<b>Property</b>	<b>50 °C</b>	<b>110 °C</b>
Specific Heat (J/kg.K)	$1.01 \times 10^3$	$1.01 \times 10^3$
Thermal Conductivity (W/m.K)	$2.80 \times 10^{-2}$	$3.24 \times 10^{-2}$
Kinematic Viscosity ( $\text{m}^2/\text{s}$ )	$1.80 \times 10^{-5}$	$2.42 \times 10^{-5}$
Dynamic Viscosity (kg/m.s)	$1.95 \times 10^{-5}$	$2.21 \times 10^{-5}$

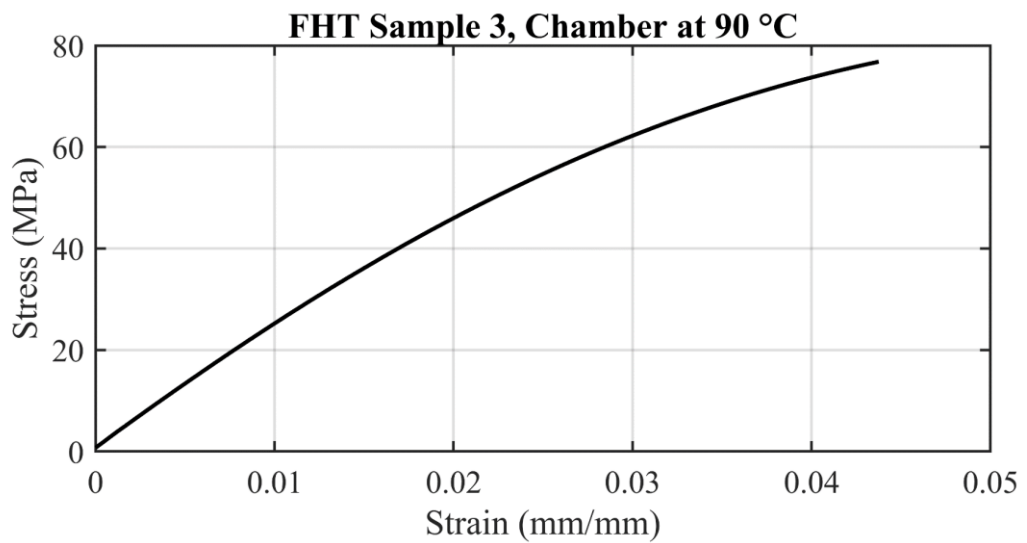
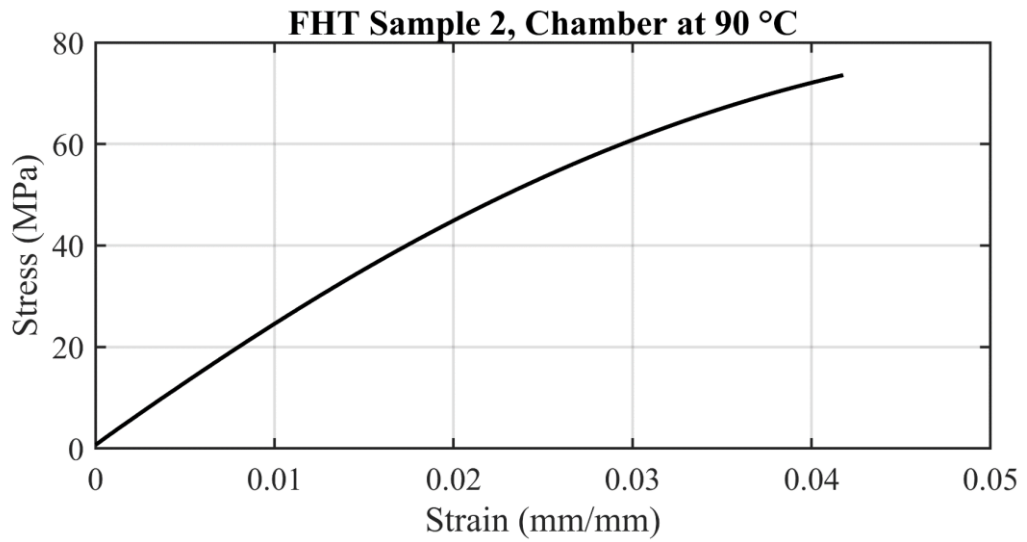
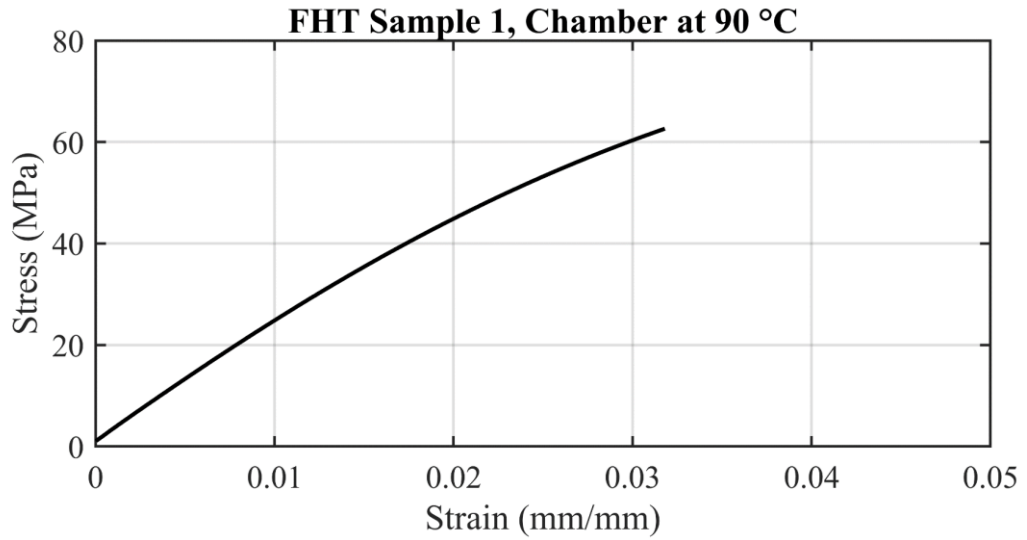
The results of the convective heat transfer coefficient calculations for the scenarios encountered in the design are detailed in Table B.3.

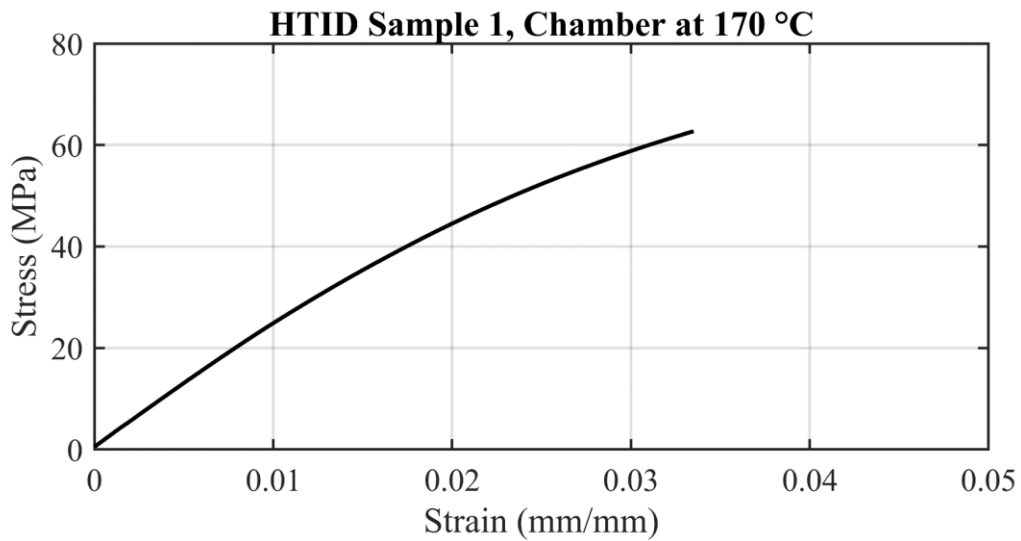
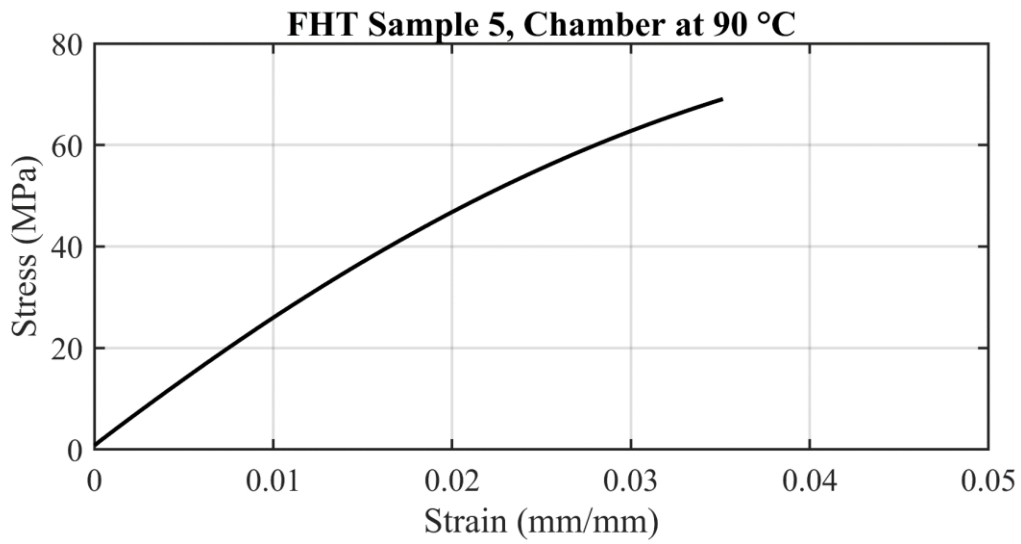
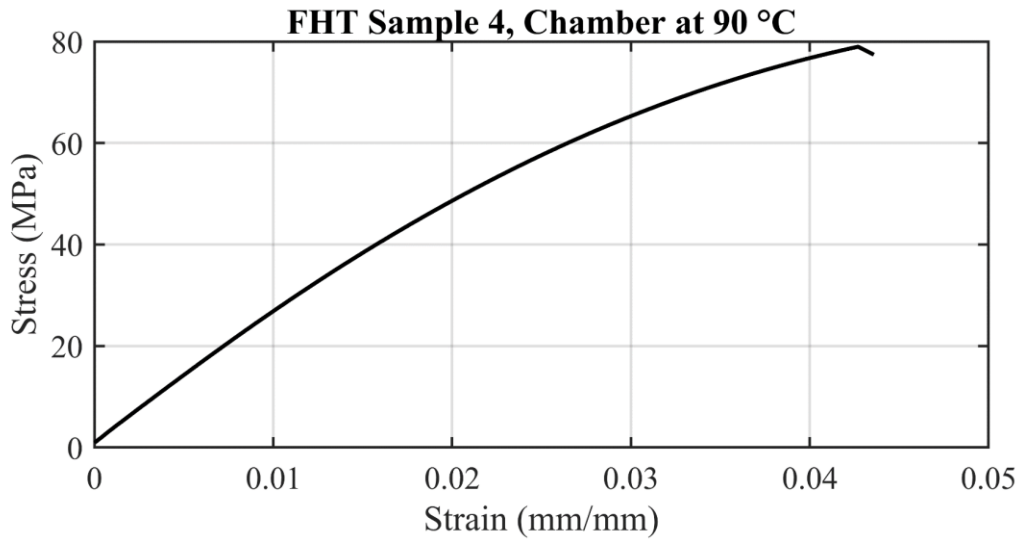
Table B.3: Convective heat transfer coefficients

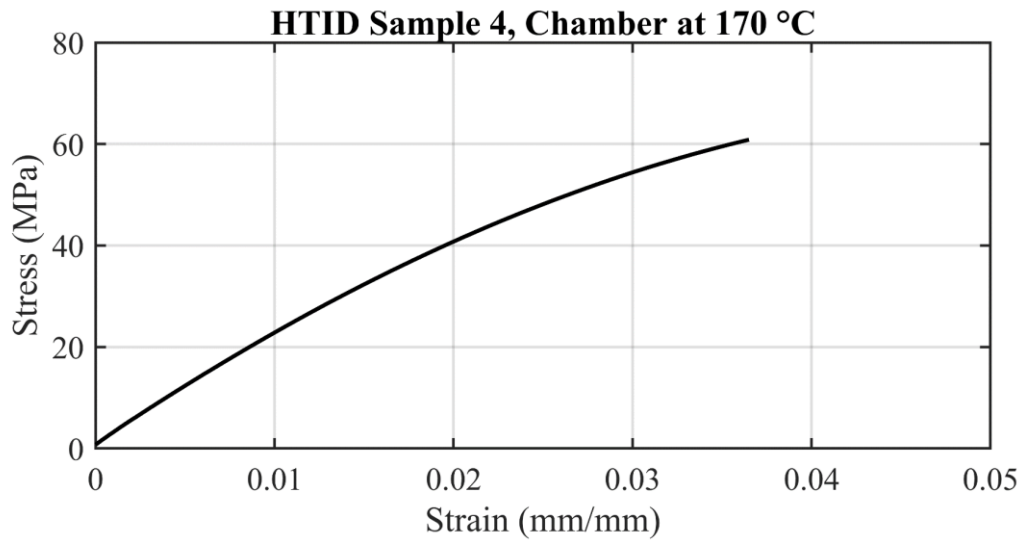
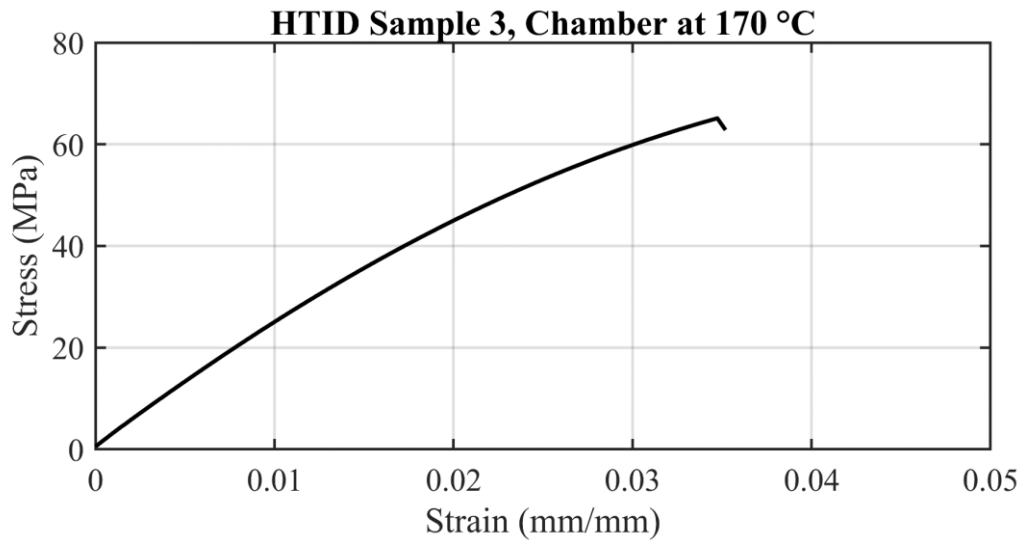
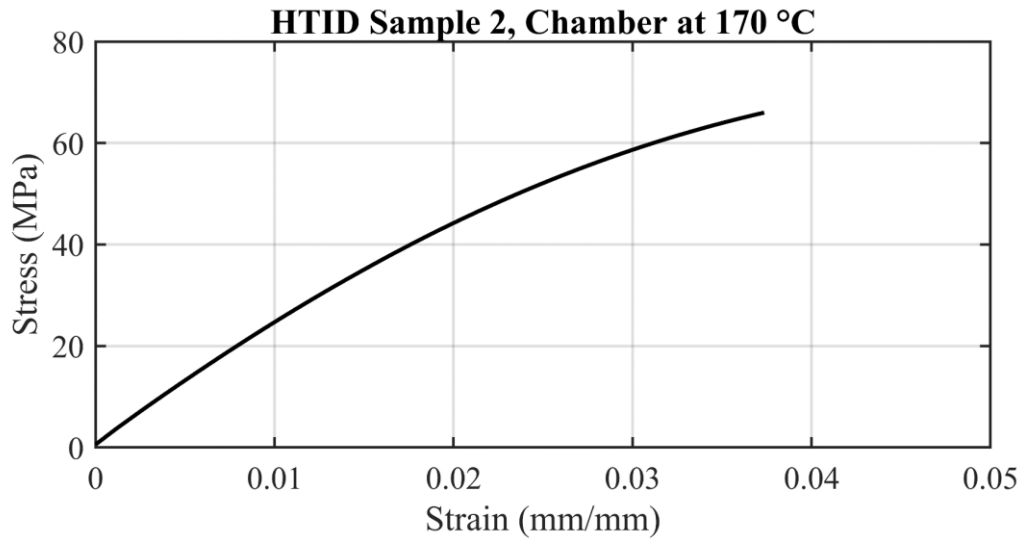
Scenario	Condition	$T_f$ (°C)	$\Delta T$ (°C)	L (m)	$Pr_f$	$Gr_f$	C	m	$Nu_f$	h
Bed – Topside	Horizontal Plate – Upper Surface	110	180	0.07	0.691	$1.68 \times 10^5$	0.15	0.33	7.31	3.65
Bed - Underside	Horizontal Plate – Lower Surface	110	180	0.07	0.691	$1.68 \times 10^5$	0.58	0.20	5.97	2.98
Chamber – Ceiling	Horizontal Plate – Upper Surface	50	60	0.08	0.702	$1.39 \times 10^5$	0.15	0.33	6.64	2.38
Chamber – Solid Walls	Vertical Plate	50	60	0.35	0.702	$5.57 \times 10^7$	0.59	0.25	46.66	3.73
Chamber – Belt Covers	Vertical Plate	50	60	0.35	0.702	$5.57 \times 10^7$	0.59	0.25	46.66	3.73
Chamber – Door and Frame	Vertical Plate	50	60	0.35	0.702	$5.57 \times 10^7$	0.59	0.25	46.66	3.73
Chamber – Window	Vertical Plate	50	60	0.15	0.702	$1.88 \times 10^6$	0.59	0.25	20.00	3.73
Chamber – Open Side	Horizontal Plate – Lower Surface	110	180	0.08	0.691	$3.51 \times 10^5$	0.58	0.20	6.92	2.48

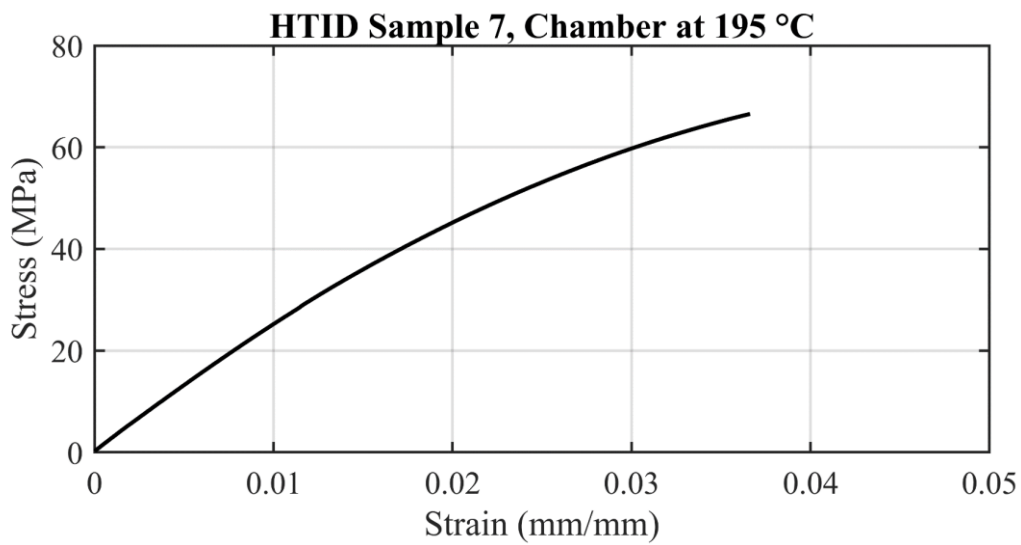
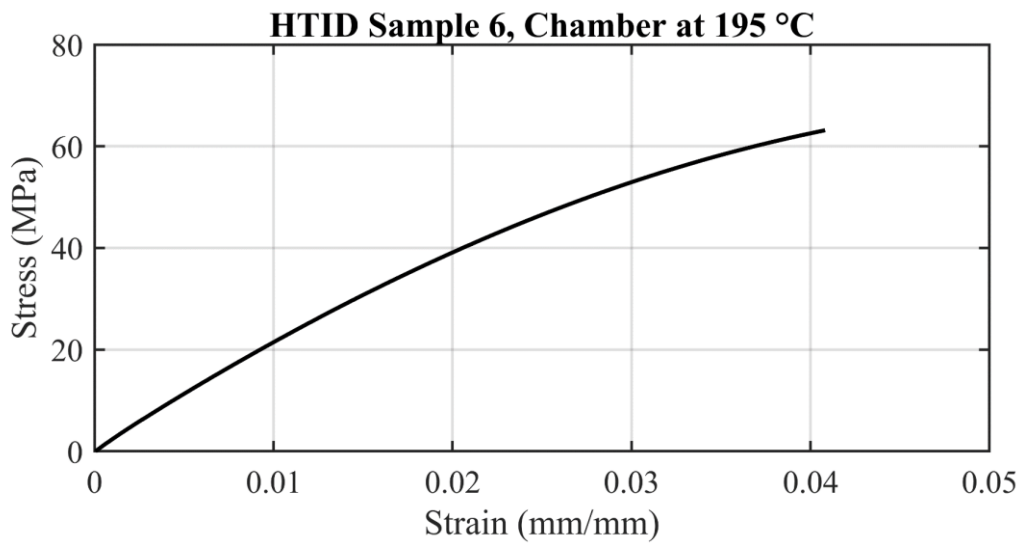
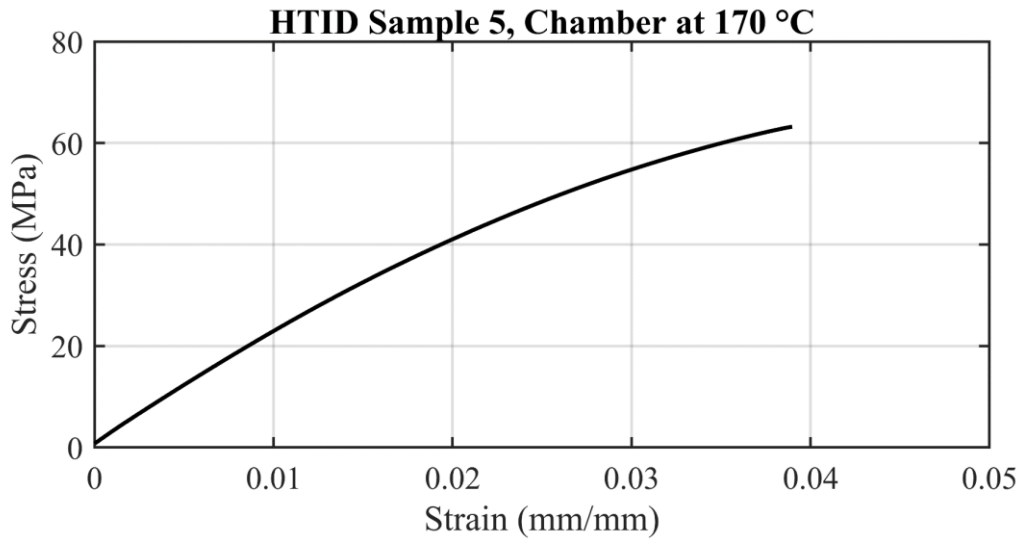


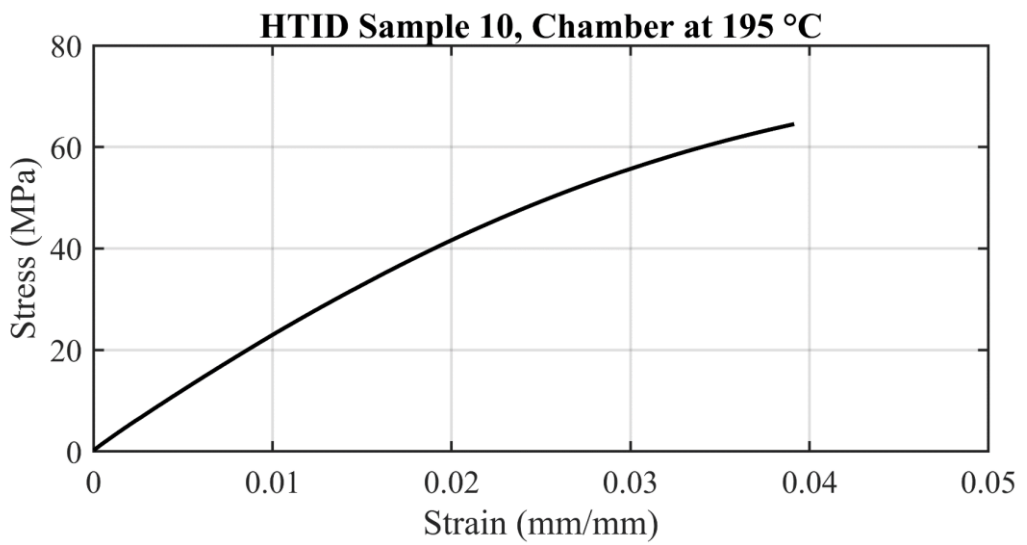
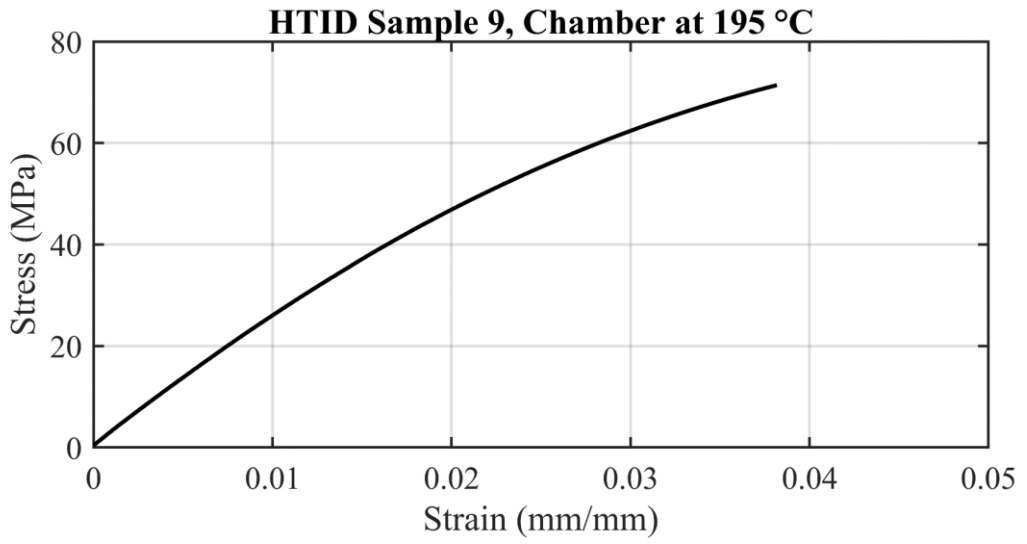
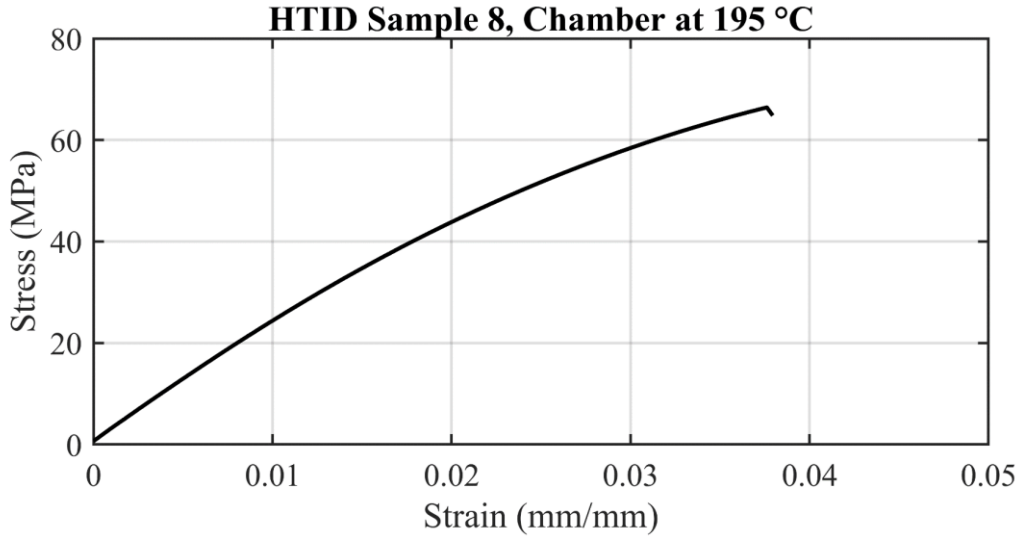
## Appendix C

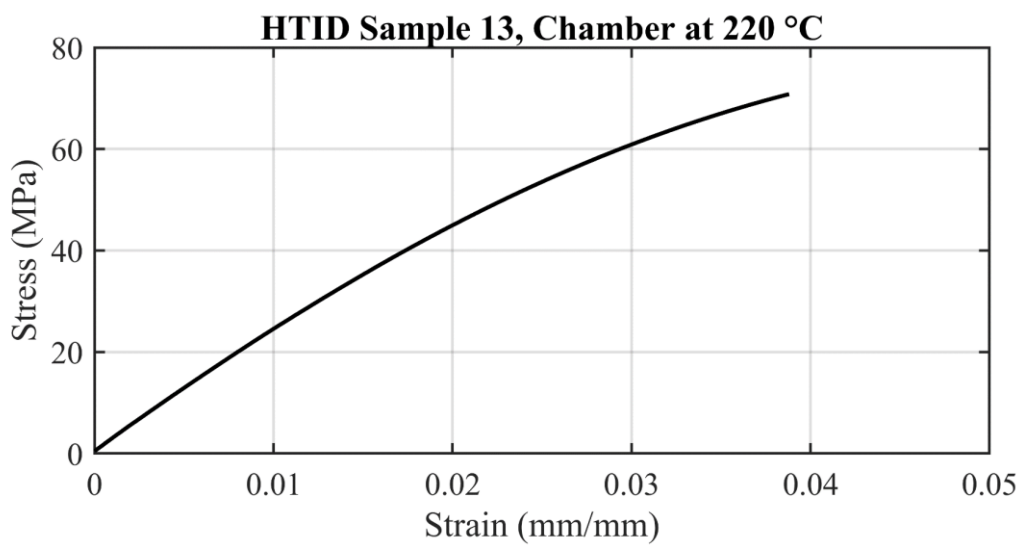
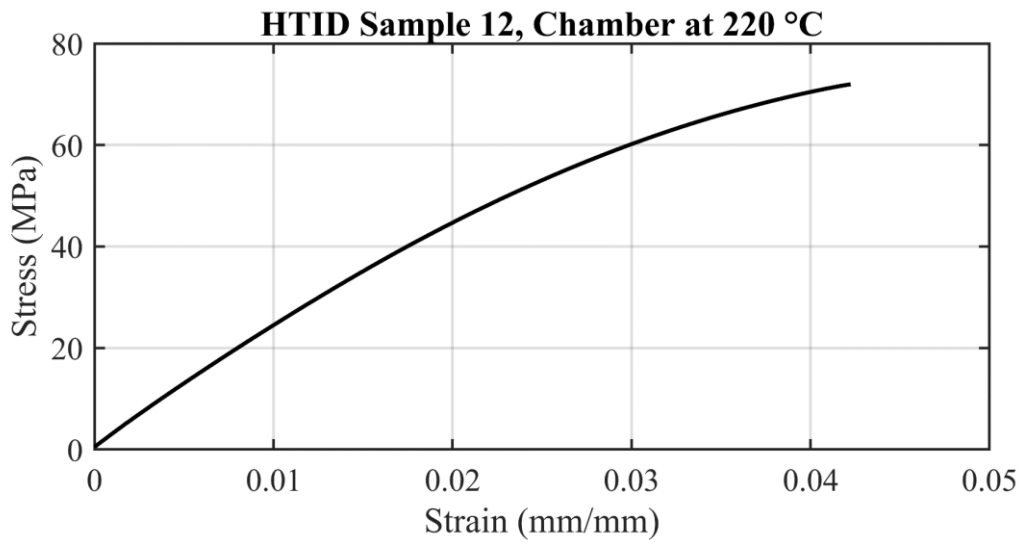
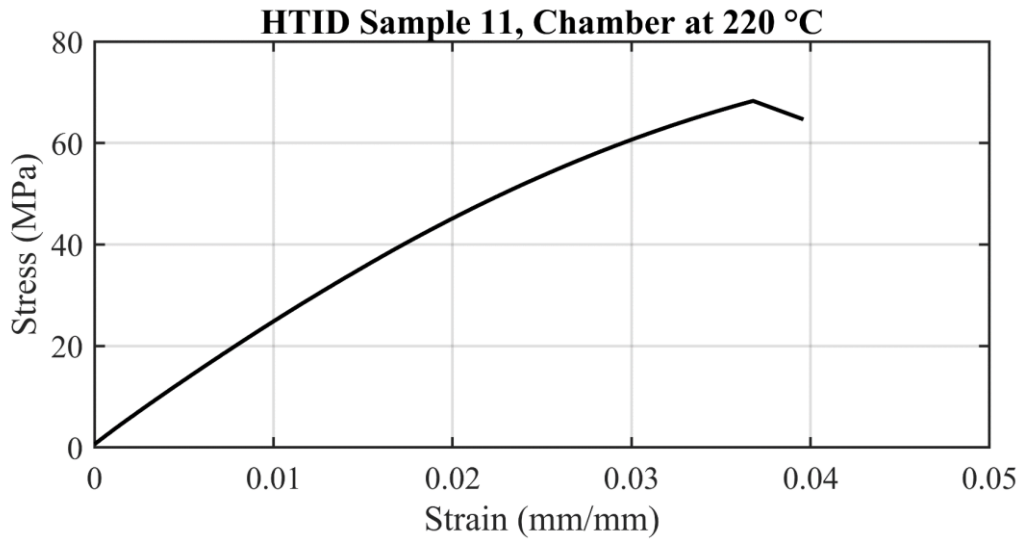


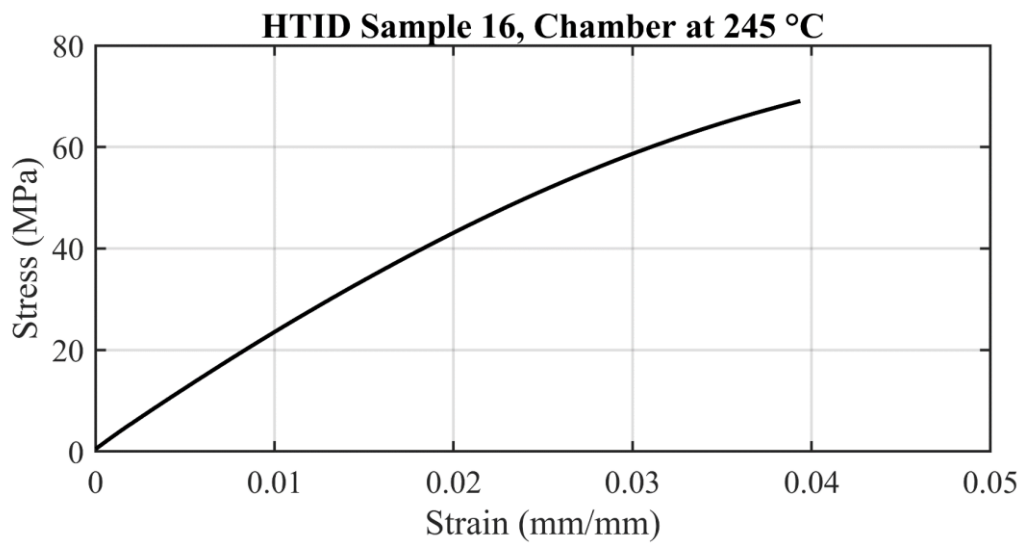
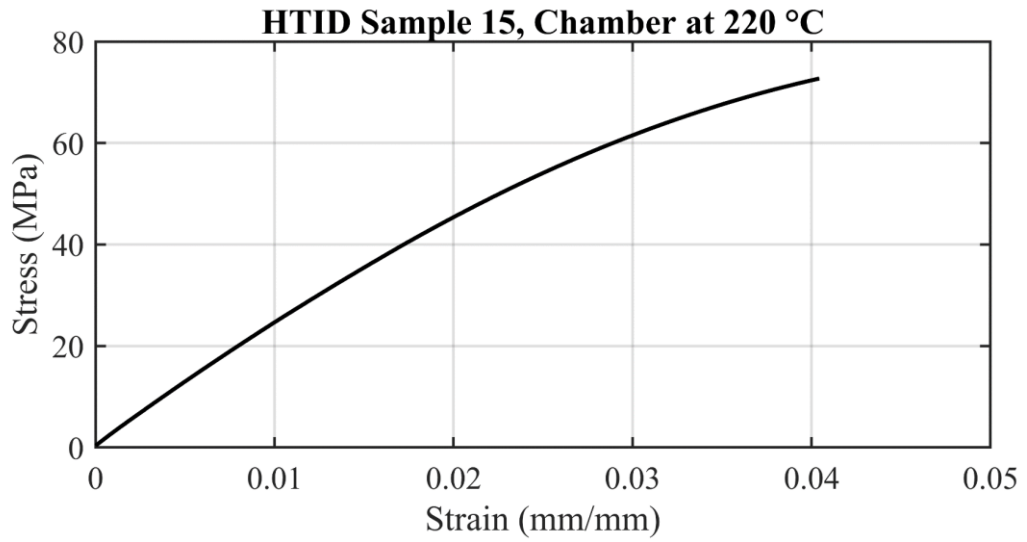
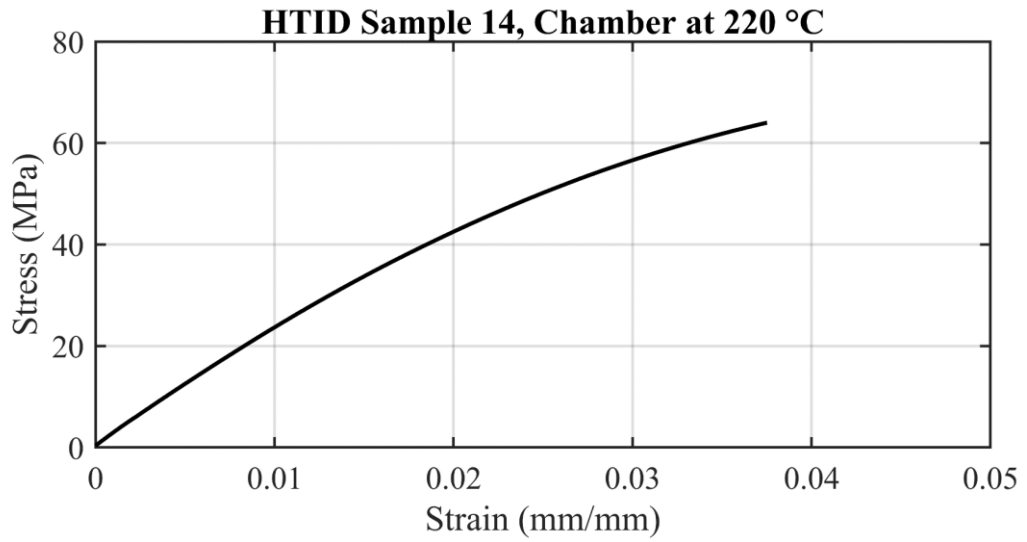


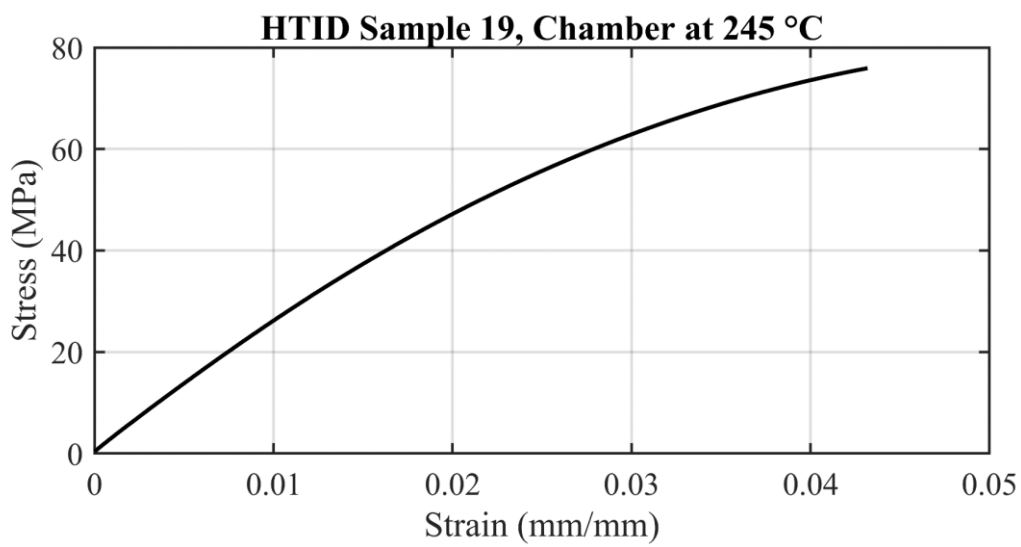
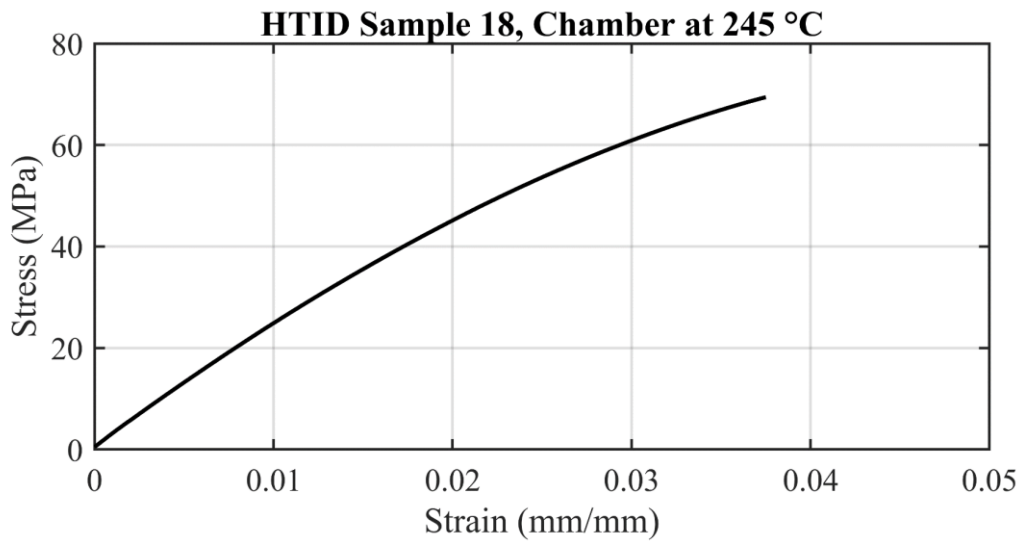
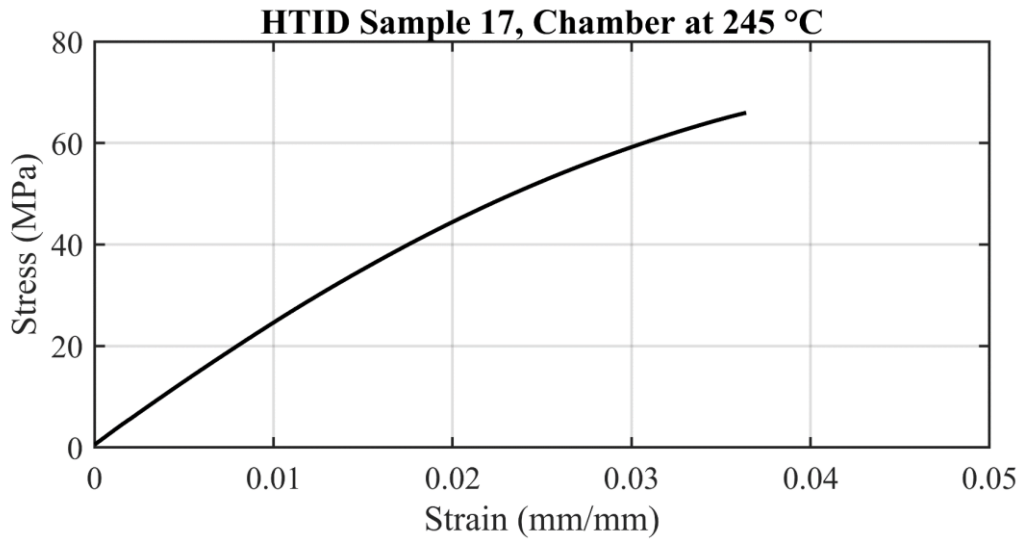




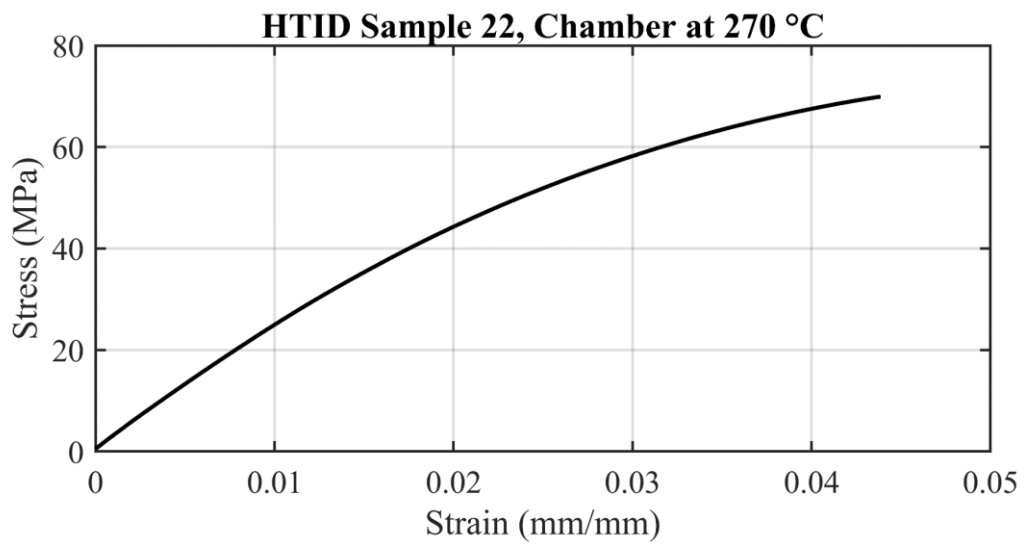
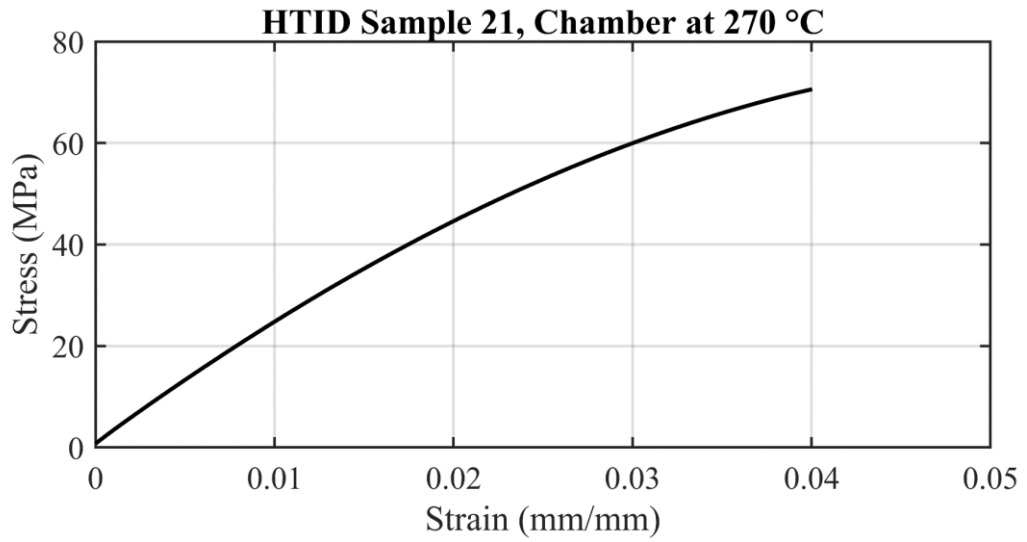
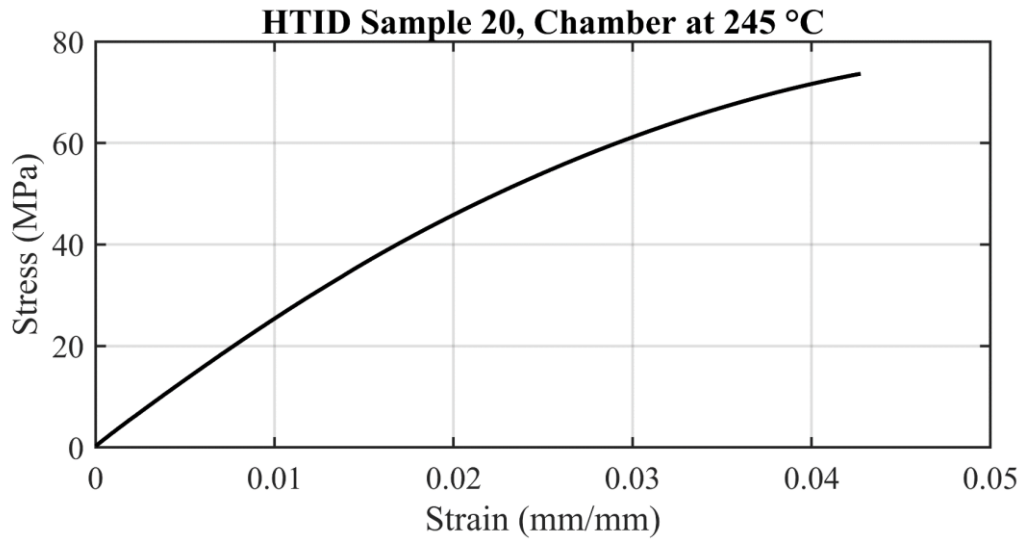


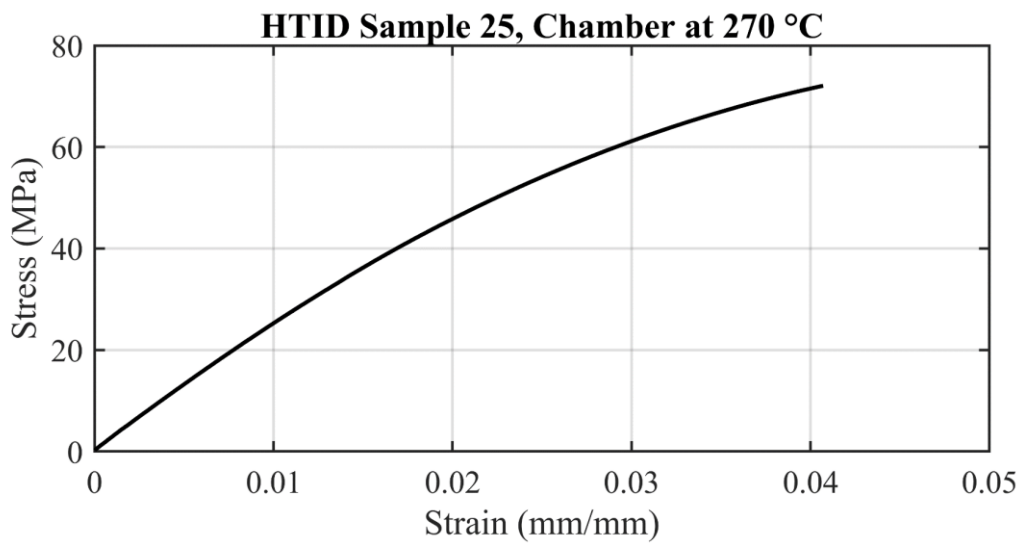
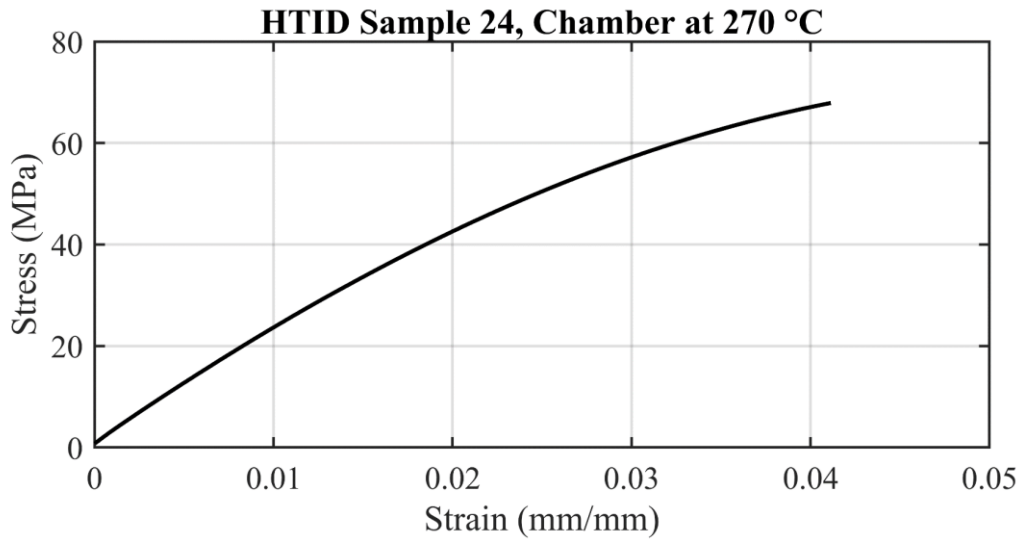
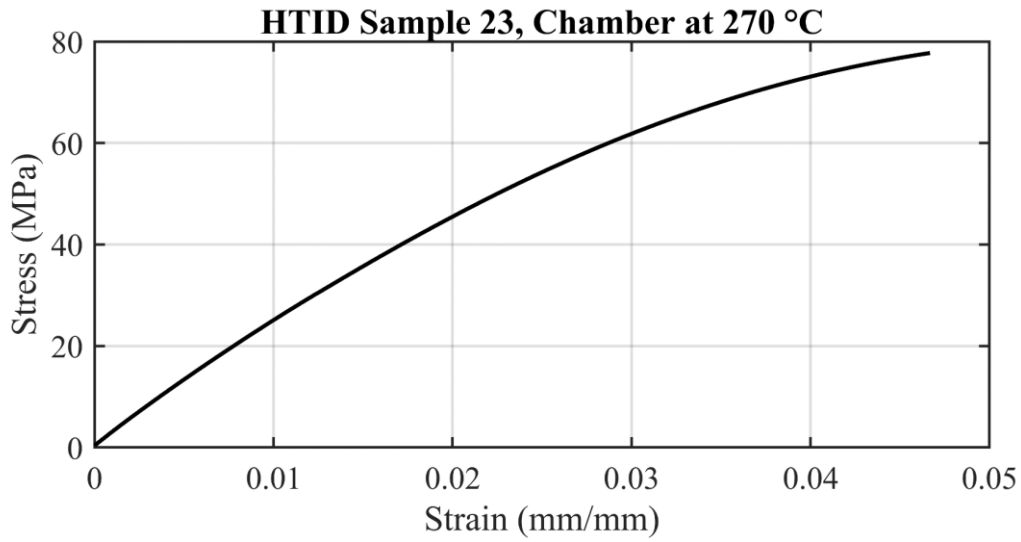






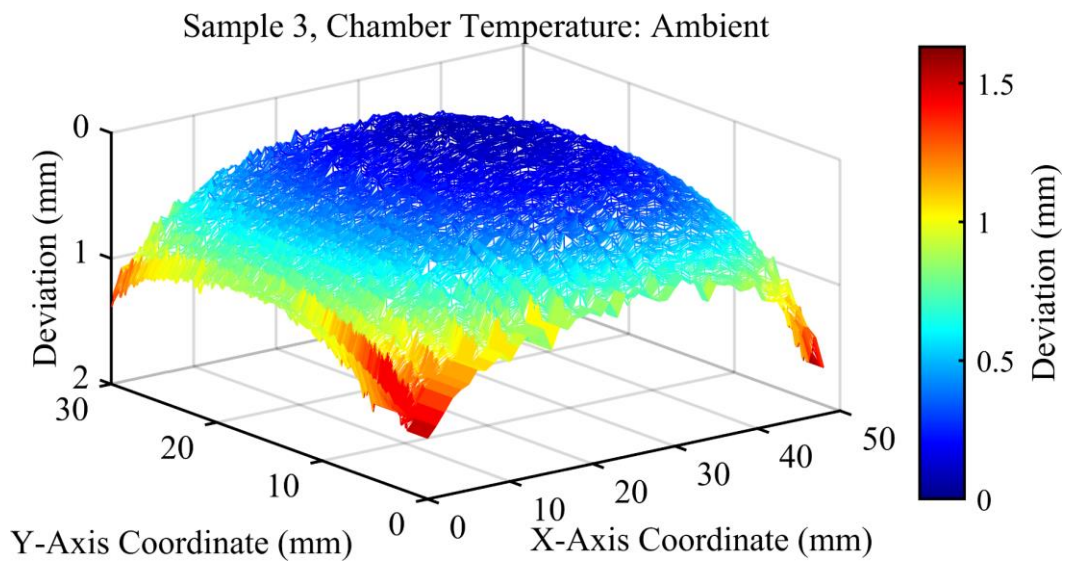
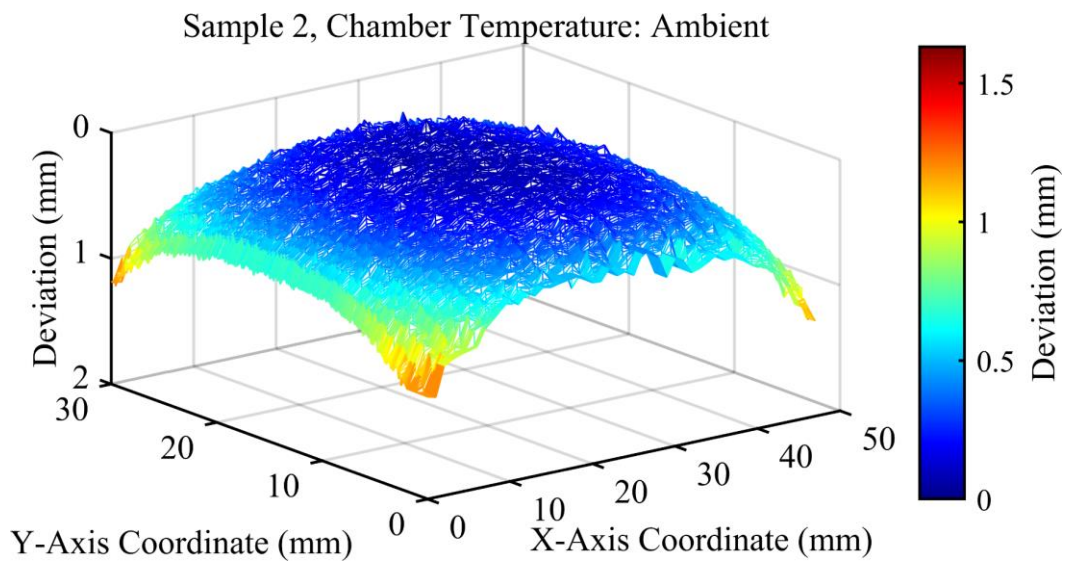
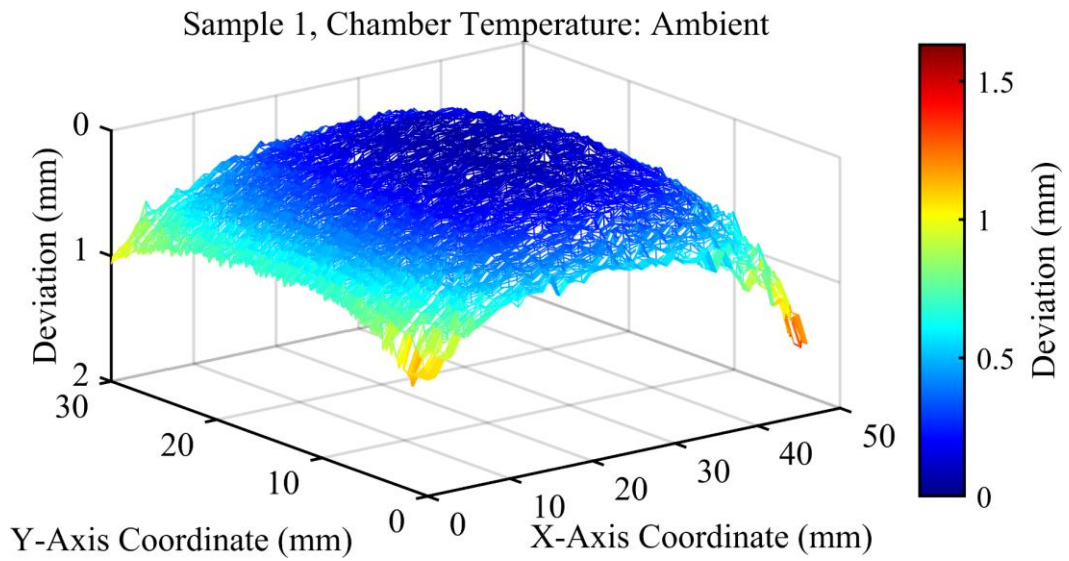




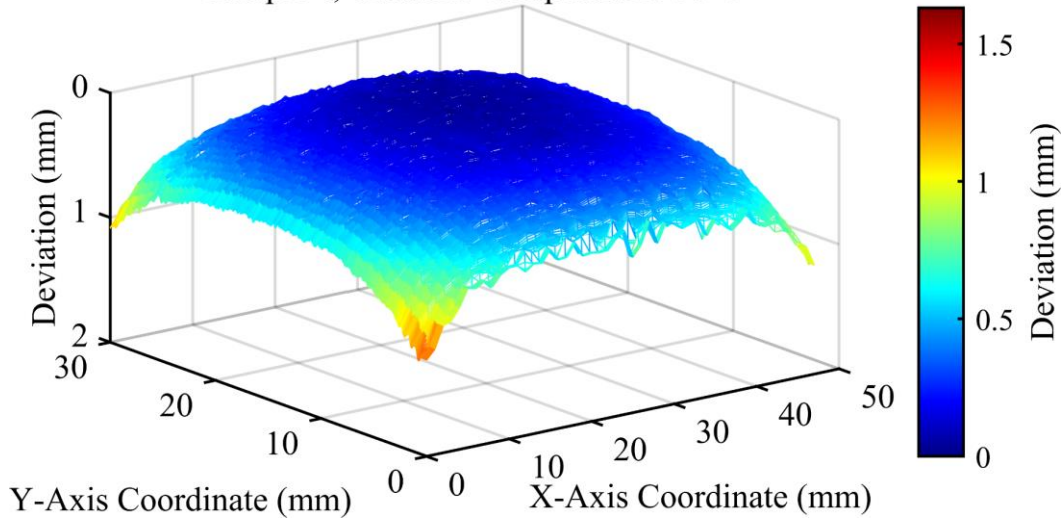


## Appendix D

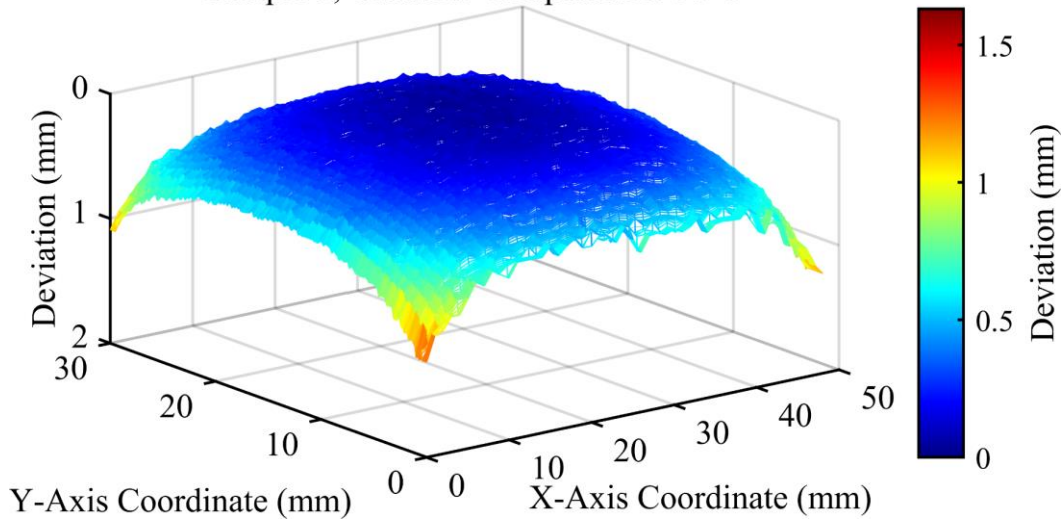
### Warping Surface Profiles



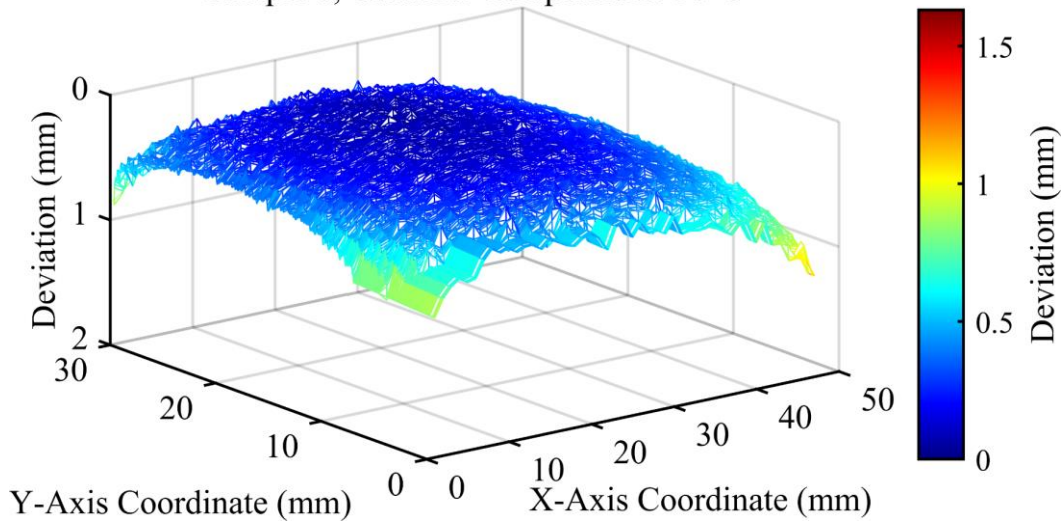
Sample 4, Chamber Temperature: 90°C



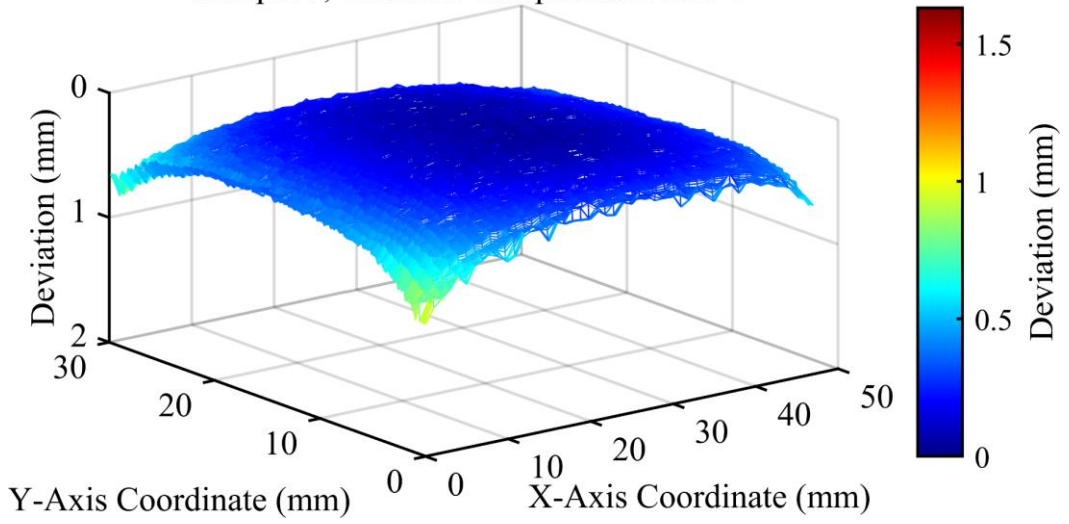
Sample 5, Chamber Temperature: 90°C



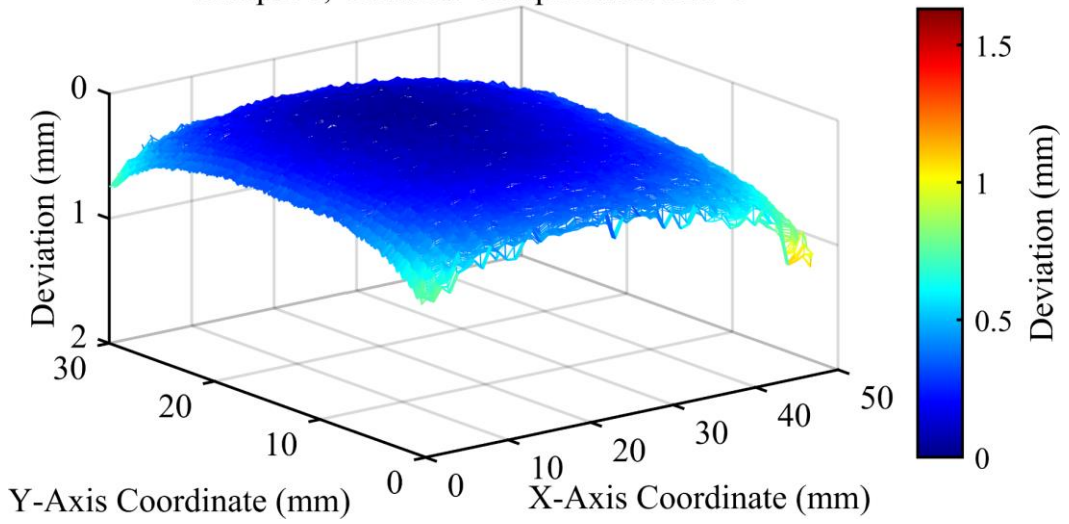
Sample 6, Chamber Temperature: 90°C



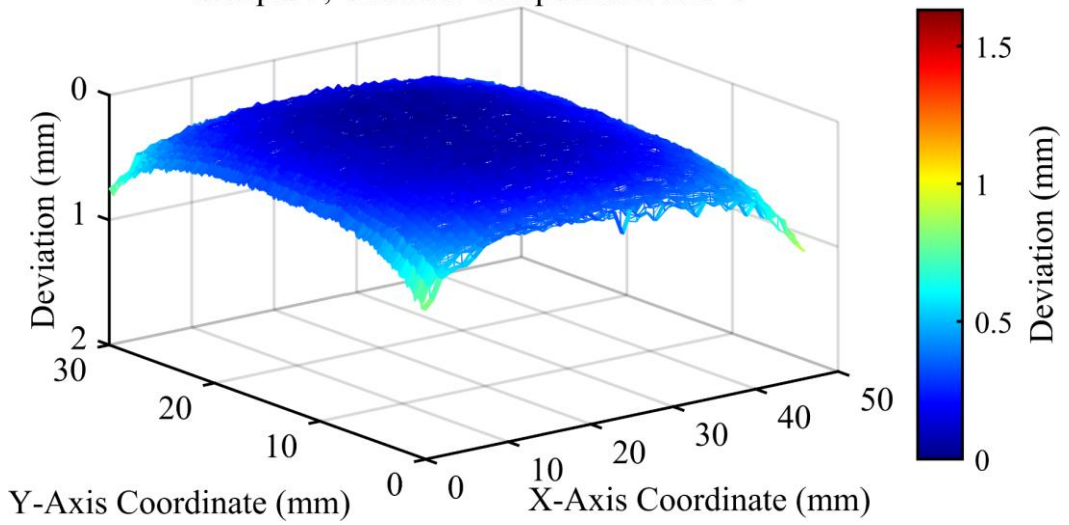
Sample 7, Chamber Temperature: 120°C



Sample 8, Chamber Temperature: 120°C



Sample 9, Chamber Temperature: 120°C



## **Appendix E**

### **Enthone MacDermid Metex 9962 Copper Plating Solution**

#### **Bath Composition by Volume**

- 75% Deionised water
- 15% Metex Copper Concentrate 9962-A
- 10% Metex Copper Reducer 9962-C

#### **Operating Conditions**

- Temperature: 20-32 °C. Optimum 24 °C.
- Immersion time: 6 – 15 minutes depending upon thickness desired and the operating temperature selected. See plating rates below.

#### **Plating Rate**

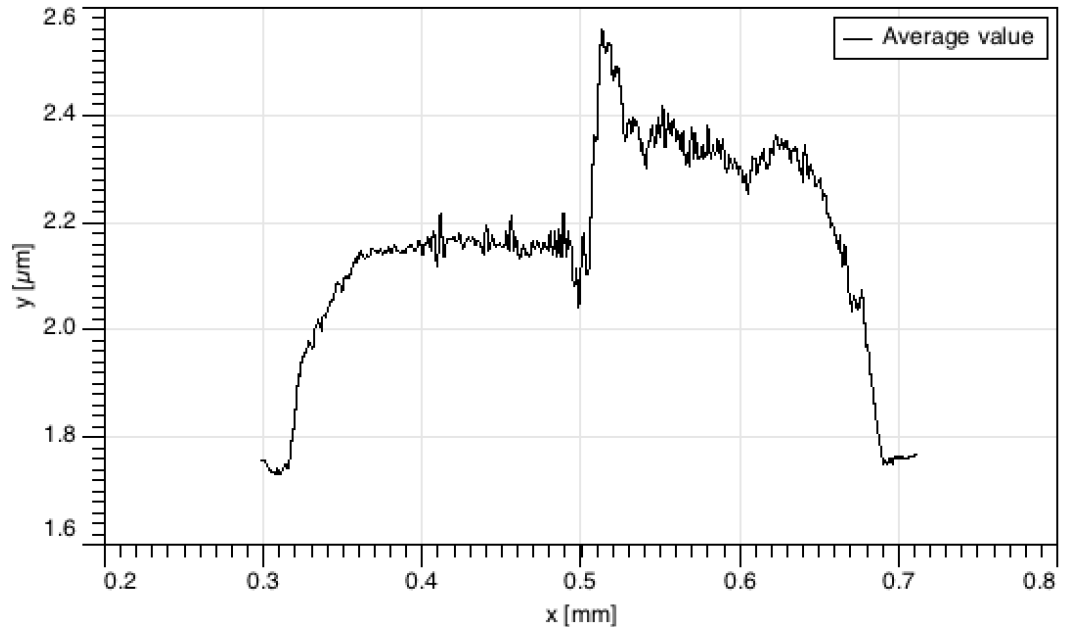
- 7 minutes = 0.425  $\mu\text{m}$
- 10 minutes = 0.55  $\mu\text{m}$
- 15 minutes = 0.65  $\mu\text{m}$

Bath loading: Up to 4.0  $\text{dm}^2/\text{L}$

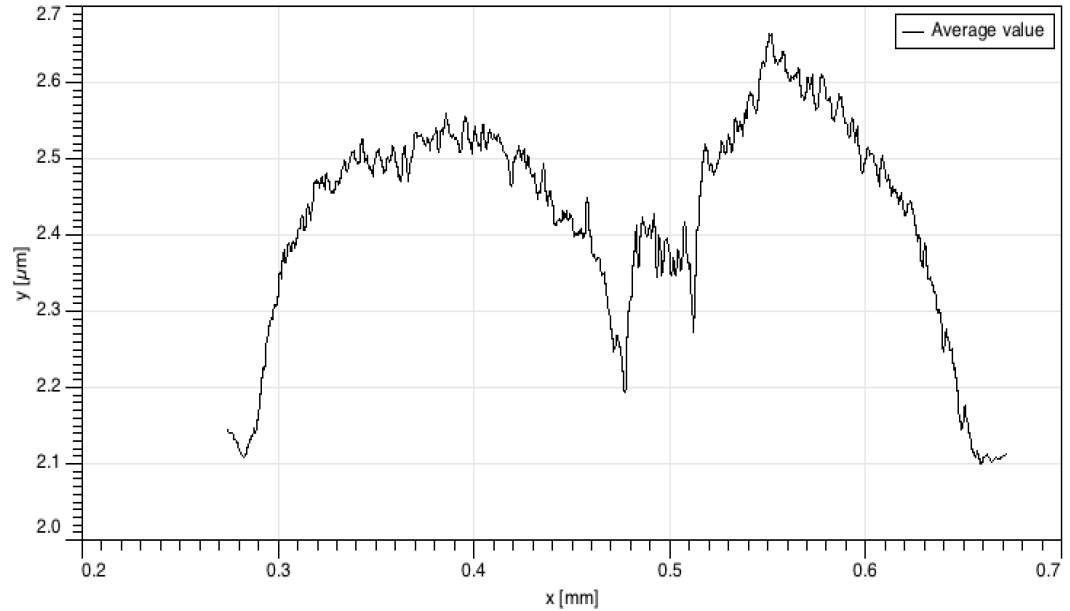
## Appendix F

### Full White-Light Interferometry Data Set

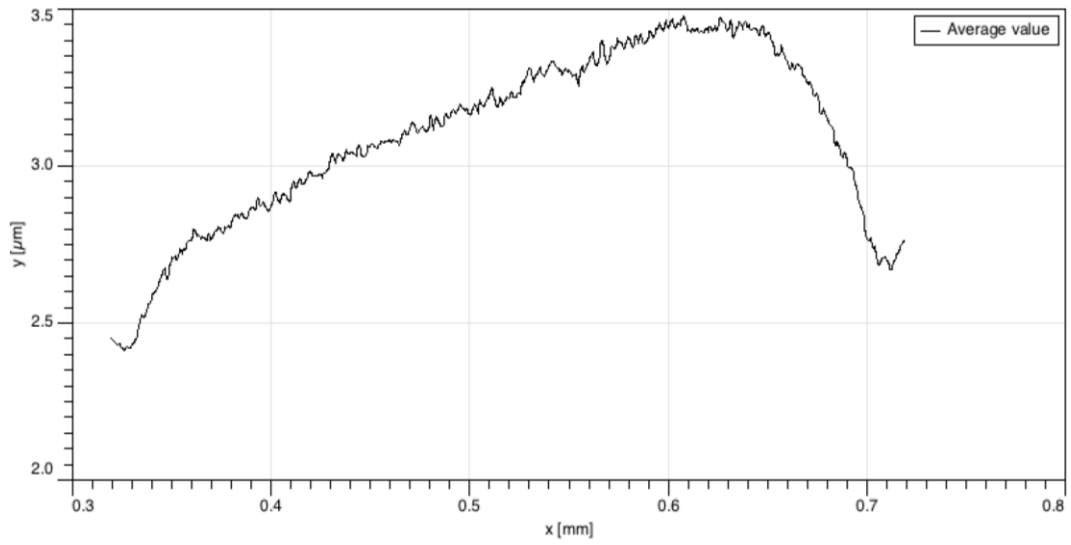
#### Scan 1



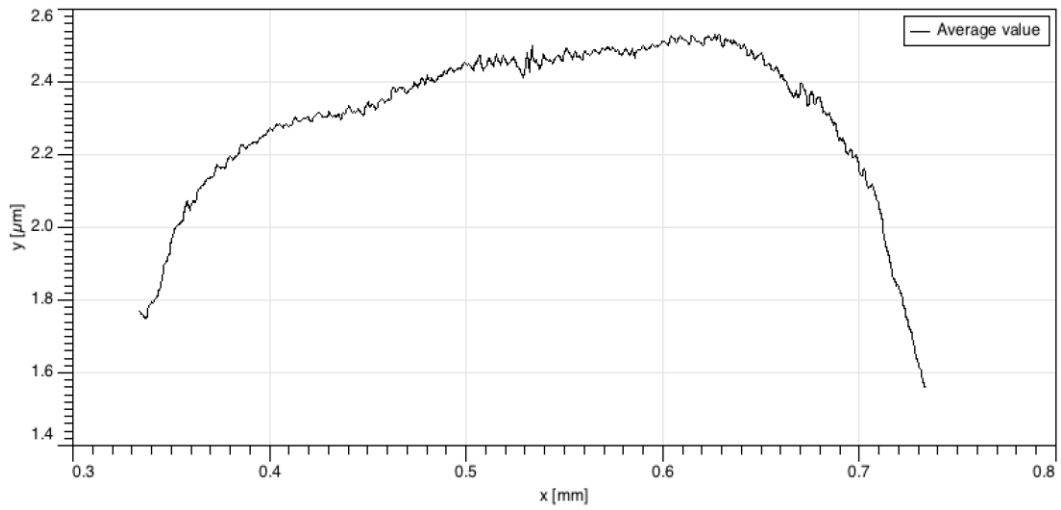
#### Scan 2



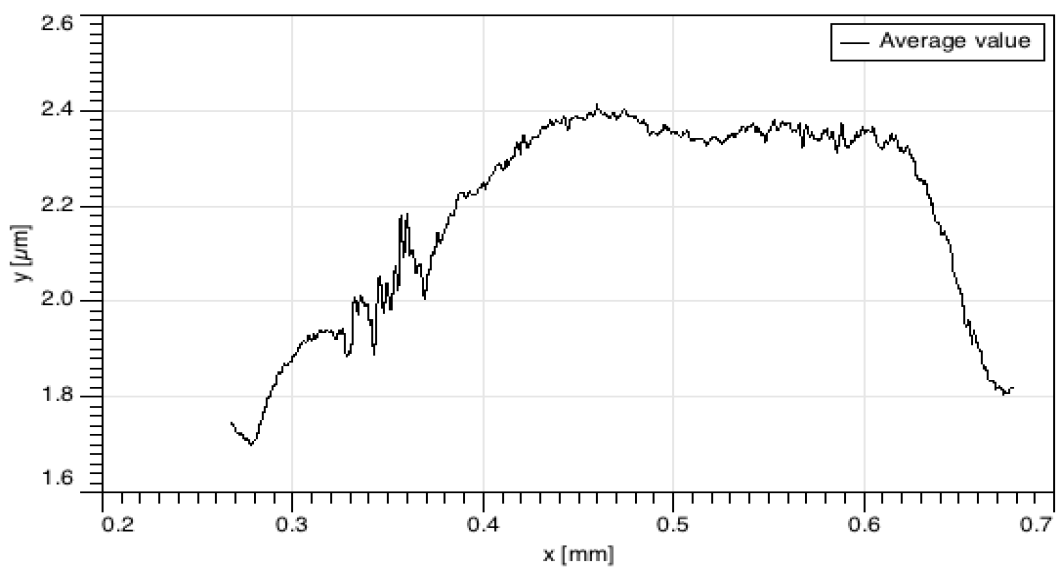
### Scan 3



### Scan 4

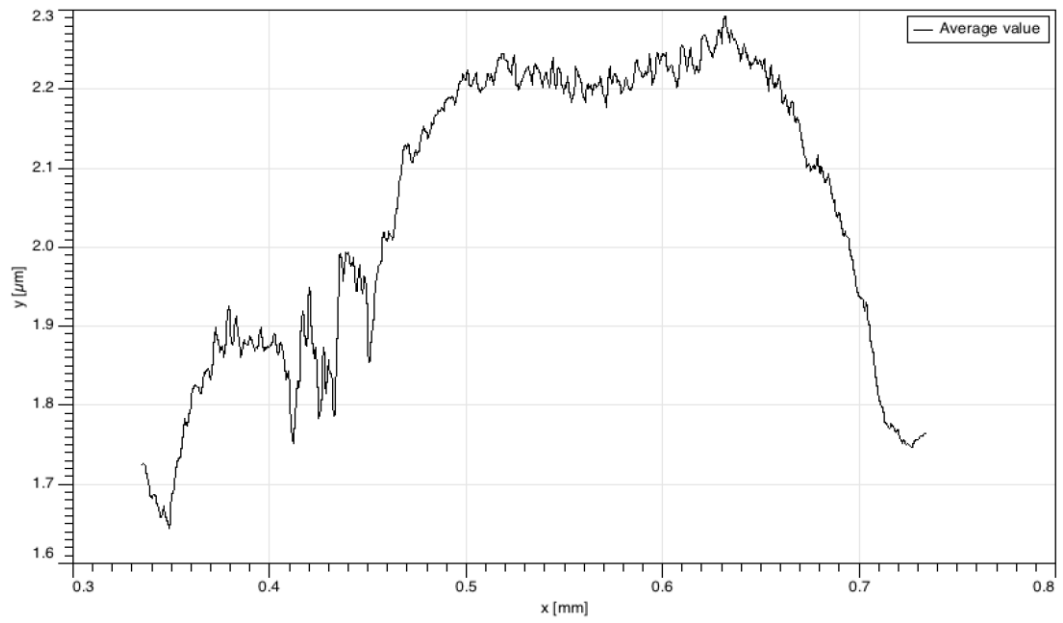


### Scan 5

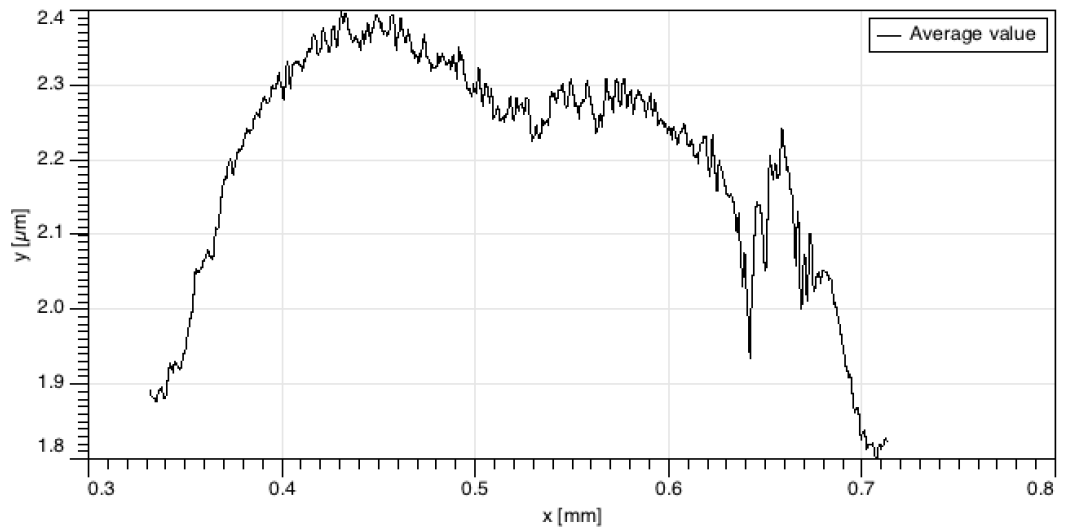




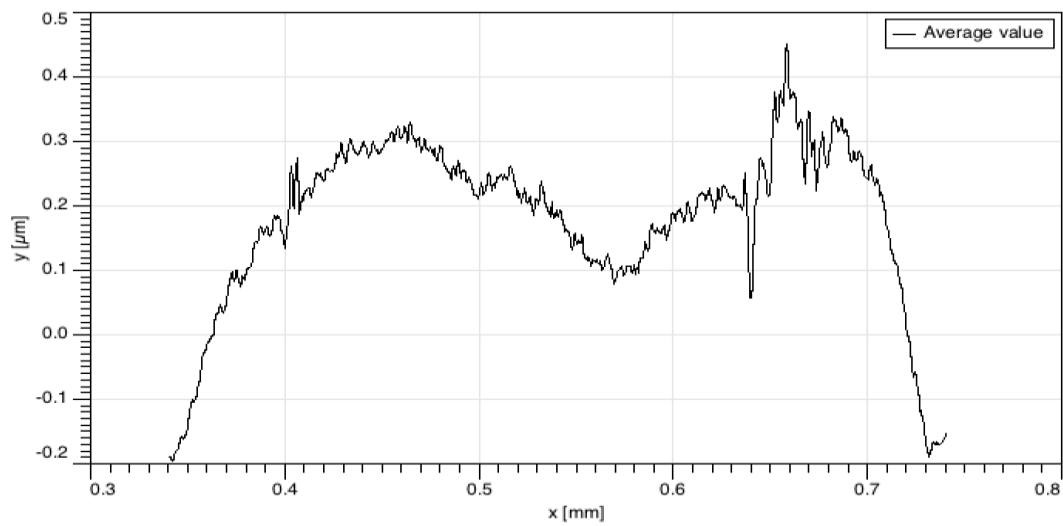
### Scan 6



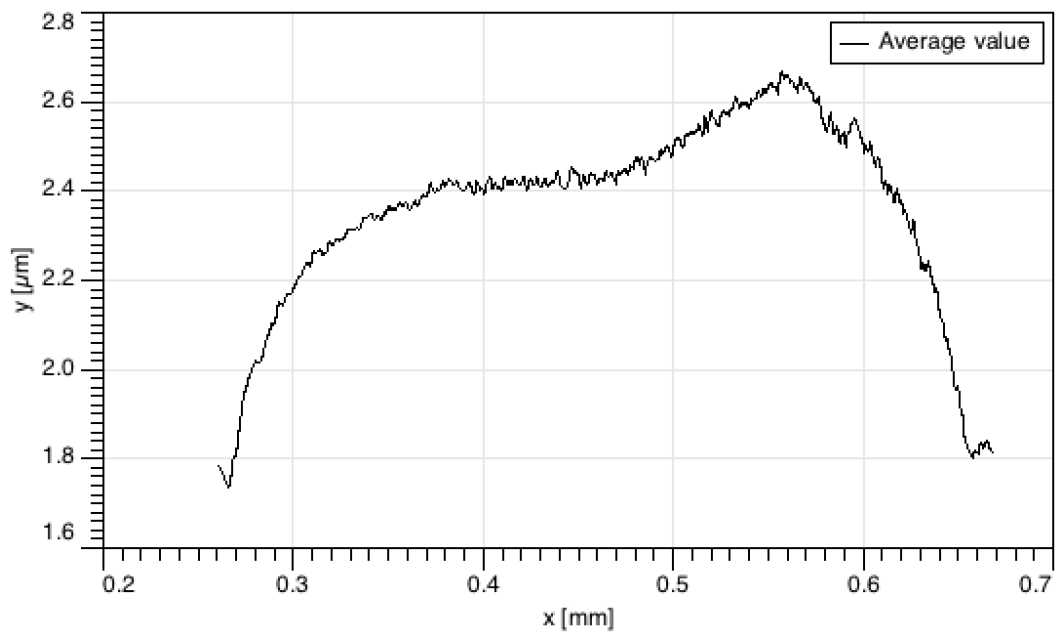
### Scan 7



### Scan 8



### Scan 9



### Scan 10

